

# Seismic behaviour and analysis of U-shaped RC walls

THÈSE N° 7133 (2016)

PRÉSENTÉE LE 26 AOÛT 2016

À LA FACULTÉ DE L'ENVIRONNEMENT NATUREL, ARCHITECTURAL ET CONSTRUIT  
LABORATOIRE DU GÉNIE PARASISMIQUE ET DYNAMIQUE DES STRUCTURES  
PROGRAMME DOCTORAL EN GÉNIE CIVIL ET ENVIRONNEMENT

ÉCOLE POLYTECHNIQUE FÉDÉRALE DE LAUSANNE

POUR L'OBTENTION DU GRADE DE DOCTEUR ÈS SCIENCES

PAR

**Raluca-Tereza CONSTANTIN**

acceptée sur proposition du jury:

Prof. A. Nussbaumer, président du jury  
Prof. K. Beyer, directrice de thèse  
Prof. B. Stojadinovic, rapporteur  
Prof. S. Sriharan, rapporteur  
Prof. A. Muttoni, rapporteur



ÉCOLE POLYTECHNIQUE  
FÉDÉRALE DE LAUSANNE

Suisse  
2016



---

## Preface

Research on the seismic assessment of buildings that are braced by reinforced concrete walls has long focused on the in-plane response of walls with rectangular cross sections. As a result, we have today a good understanding of the force-displacement response of such walls for most failure modes that can develop. In real buildings, however, many walls have not a rectangular section but are composed of two or more wall sections that form L-, T-, U- or more complex shapes. The behaviour of these walls when subjected to bidirectional loading come into the focus of seismic engineering research on reinforced concrete walls.

Raluca Constantin's thesis contributes to this research line by studying the behaviour of U-shaped walls. In her work, Raluca focuses on the response of these walls under loading in the diagonal direction. This loading direction is often disregarded but she shows that it can lead to the smallest displacement capacity and to failure modes not observed for other loading directions. Raluca advanced the knowledge on the seismic response of U-shaped walls through an experimental and a numerical study. She tested two U-shaped walls that differed with regard to the applied axial load. Raluca's tests are intensively instrumented using conventional and optical measurement techniques and the data is made available to the research community. In addition to the experimental study, Raluca investigated the response of U-shaped walls through detailed numerical shell element models. These models were used to develop new analytical formulations that can be used in the early stages of the design process. The main contributions concern the modification of effective stiffness estimates, yield displacement formulations that account further for shear deformations, which are particularly important for U-shaped walls, and plastic hinge lengths for different loading directions.

Lausanne, July 2016

Katrin Beyer



---

## Acknowledgements

First and foremost, I would like to express my heartfelt gratitude to my thesis supervisor Prof. Katrin Beyer. I appreciated your continuous interest in my research, your availability but also your constant encouragement, especially in the most difficult times. Your expertise, your feedback and your insightful questions contributed significantly to the quality of this thesis. Your energy and your dedication to research are an inspiration. Thank you!

I would also like to thank the members of my jury: Prof. Aurelio Muttoni, Prof. Sri Sritharan and Prof. Bozidar Stojadinovic, for their genuine interest in my work and their valuable feedback. Additionally, I would like to acknowledge Prof. Alain Nussbaumer for his service as president of the jury but also for his feedback on the design of the laboratory reaction wall.

The funding for this project was partially provided by the Swiss National Science Foundation (Grant No. 20021\_132315/1) and it is gratefully acknowledged. Special thanks to Prof. Frank J. Vecchio for making freely available the VecTor4 software to us and to Dr. Trevor Hrynyk who helped me get started on the numerical modelling with this software.

The experimental part of this research was carried out at the structural testing laboratory in EPFL and would not have been possible without the help of the technical staff. Many thanks to Armin Krkic and Gérald Rouge who provided important help with the test set-up, but also to Gilles Guignet, Sylvain Demierre and Frédérique Dubugnon. It was a real pleasure working with you in the lab. Many students helped with the experimental work. I am grateful to all of them, especially to Alex Moraru, Efthymios Papoutsis and Hugues Vincent for their hard work. Many thanks also to the IT support who were always prompt to solve any IT issue, especially to Nicolas Dubois and Stefano Nepa.

Current and former EESD members have provided help and feedback during various stages of this project, as well as a great atmosphere at the office and outside. Thanks to Pia Hannewald, Alessandro Paparo and Sarah Petry with whom I started this journey and who provided valuable advice on the experimental work and not only. Thanks also to Angelica Rosso and Danilo Tarquini for their help during the experimental testing while putting up with a very stressed version of myself. I am particularly grateful to João Almeida for patiently going through my written work and providing valuable feedback. Thanks to Alessandro Paparo and Francesco Vanin for translating the Italian abstract. Further thanks to Georgia Angeli, Ovidiu Prodan, Marco Tondelli and Bastian Wilding. Special thanks to my 'grandson' Ale, my office mate for so many years, for the lively office atmosphere and all the special times in our office and outside work. Special thanks also to my 'newest' office mate Shenghan Zhang for the always positive attitude and all the interesting philosophical and technical discussions, mostly the former. Finally, thanks to Marie-Madeleine Gruaz and Yvonne Buehl who made my life easier when it came to administrative things.

---

I would like to thank also the friends and colleagues from the other research groups for the many enjoyable moments spent together from lunch or coffee breaks to hiking or skiing trips. Thanks to Carlos, Dan, Galina, Ioannis, Filip, Francisco, Hadi, João, Jürgen, Maléna, Marie-Rose, Michael and Stefan but also to the many other fun and smart people that I have met in EPFL. Thanks also to my team mates and friends from the Lausanne Table Tennis Club who provided a good balance to my university life. Further thanks to the ex-EPFL Romanian group of friends who always offered encouragement and advice, especially to Ramona and Mihai. Also I would also like to thanks my friends back home in Romania for always being there for me.

Finally, I would like to thank my family for their unconditional support and encouragement. I am particular grateful to Mum, Dad and my big brother Dragoş for allowing me to do whatever I wanted to do and wherever I wanted to do it. Thanks also to Andrei for his help with mathematical statistics. And last but certainly not least, I am extremely grateful to my husband Ionuţ who eagerly got involved in this project and contributed with anything from proof-reading my English and the French abstract to helping me with the test set-up. Thank you for your unconditional love and patience!

Lausanne, July 2016

Raluca Constantin

---

## Abstract

In many countries of moderate to high seismicity, reinforced concrete (RC) core walls are used as lateral bracing systems in mid- to high-rise buildings where they typically accommodate lift shafts or stair cases. Unlike planar walls which provide horizontal strength and stiffness mainly in the in-plane direction of the wall, core walls provide bidirectional strength and stiffness. This feature complicates their inelastic behaviour which is not yet fully understood as experimental and numerical studies are still rather scarce when compared to planar walls. Therefore, current design codes use findings from planar walls while specific guidelines for the design and analysis of core walls are still lacking. In addition, simple analysis tools widely used by design engineers such as the plastic hinge model, have been derived and calibrated for columns, beams or planar walls and their suitability for core walls has been only marginally verified. For these reasons the current study focuses on: (1) improving the knowledge on the inelastic behaviour of U-shaped walls under bidirectional loading and (2) on extending easily applicable engineering type models, such as the plastic hinge model, to the analysis of U-shaped walls. The scope of the thesis is limited to U-shaped walls, which is the simplest type of core wall that still retains the key characteristics of such walls.

The first part of the thesis focuses on understanding the behaviour of U-shaped walls under loading along the geometric diagonal of the section. This loading direction is not typically considered in the design process but it was found to determine the shear design of the flanges while the displacement capacity for this direction might be the lowest of all the loading directions. In order to address the behaviour under diagonal loading, two large-scale quasi-static cyclic tests on U-shaped walls were carried out. Failure mechanisms specific to diagonal loading and possible critical design aspects related to these failure modes were identified from the experimental results. In addition, the influence of the longitudinal reinforcement distribution on the wall behaviour was investigated.

The second part of the thesis focuses on adapting equations used in plastic hinge model for the analysis of U-shaped walls. Plane section analyses and a shell element model validated against the experimental data were used to perform parametric studies on U-shaped walls. From the results of the parametric studies a new equation for the yield curvature for any direction of horizontal loading was proposed as well as a modified yield displacement equation that accounts for the partially cracked wall height at yield. With this equation, predictions of yield displacements were improved especially for very slender walls. Quantities that rely on the yield displacement, such as the effective stiffness of the wall were also better predicted when the cracked height was accounted for in the prediction. And finally, plastic hinge length equations were also modified to account for the variation with the different loading directions.

Key words: U-shaped walls, diagonal loading, plastic hinge model, yield displacement, plastic hinge length





---

## Résumé

Dans de nombreux pays avec une sismicité modérée ou forte, les murs noyau en béton armé (BA) sont utilisés en tant que systèmes de contreventement latéral dans des bâtiments de hauteur moyenne ou grande où typiquement ils entourent des cages d'ascenseur ou d'escaliers. Contrairement aux murs rectangulaires qui fournissent une résistance horizontale et une rigidité principalement dans le plan du mur, les murs noyau fournissent une résistance et une rigidité bidirectionnelle. Cette propriété complique leur comportement inélastique qui n'est aujourd'hui pas entièrement compris car les études expérimentales et numériques sont encore plutôt rares comparées aux murs rectangulaires. Par conséquent, les codes de dimensionnement actuels utilisent les résultats des murs rectangulaires alors que des lignes directrices spécifiques pour le dimensionnement et l'analyse des murs noyau sont encore manquantes. De plus, des outils d'analyse simples largement utilisés par les ingénieurs de conception tels que le modèle de la rotule plastique, ont été dérivés et calibrés pour des colonnes, poutres ou murs rectangulaires et leur pertinence pour des murs noyau n'a été que partiellement vérifiée. Pour ces raisons l'étude actuelle se concentre sur : (1) améliorer la connaissance sur le comportement inélastique des murs noyau soumis à une charge bidirectionnelle et (2) sur étendre des modèles type d'ingénierie facilement applicables, tel que le modèle de la rotule plastique, pour l'analyse des murs noyau. Le cadre de cette thèse se limite aux murs avec une section en forme de U, qui est le plus simple type de mur noyau mais qui conserve encore les principales caractéristiques d'un tel mur.

La première partie de la thèse porte sur la compréhension du comportement des murs avec une section en forme de U, soumis à une charge le long de la diagonale géométrique de la section. Cette direction de chargement n'est généralement pas considérée dans le processus de dimensionnement, mais elle est déterminante pour le dimensionnement en cisaillement des ailes du mur alors que la capacité de déplacement pour cette direction pourrait être la plus faible de toutes les directions de chargement. Afin d'investiguer le comportement sous un chargement selon la direction diagonale, deux tests cycliques et quasi-statiques à large ont été effectués sur des murs avec une section en forme de U. Les mécanismes de ruptures spécifiques à un chargement selon la direction diagonale ainsi que des aspects de dimensionnement critiques liés à ces modes de défaillance ont été identifiés suite aux tests expérimentaux. En outre, l'influence de la distribution de l'armature longitudinale dans la section a été investiguée.

La deuxième partie de la thèse porte sur l'adaptation des équations utilisées dans le modèle de rotule plastique à l'analyse des murs avec une section en forme de U. Deux modèles numériques, un modèle basé sur l'hypothèse des sections planes et un modèle avec des éléments de coque, ont été validés avec les données expérimentales et ensuite ont été utilisés pour réaliser des études paramétriques sur des murs avec une section en forme de U.

---

Avec les résultats des études paramétriques, une nouvelle équation pour la courbure d'écoulement pour toute direction d'un chargement horizontal a été proposée ainsi qu'une nouvelle équation pour le déplacement d'écoulement qui considère que le est mur partiellement fissuré sur l'hauteur à l'écoulement. Les quantités qui dépend du déplacement d'écoulement, tels que la rigidité effective du mur, ont également été mieux prédites lorsque l'hauteur fissuré a été prise en compte dans la prédiction. Et finalement, les équations de la longueur de la rotule plastique ont été modifiées pour tenir compte de la variation avec la direction de chargement.

Mots clefs : Murs avec une section en forme de U, chargement dans la direction diagonale, modèle de la rotule plastique, déplacement d'écoulement

---

## Riassunto

In molti paesi a moderata ed alta sismicità, nuclei portanti in cemento armato, contenenti vani scala o ascensori, vengono spesso usati come elementi sismo-resistenti per edifici medio-alti. Diversamente dai setti rettangolari, che garantiscono rigidezza e resistenza orizzontale nella sola direzione del loro piano, le pareti non rettangolari offrono rigidezza e resistenza bidirezionali. Tale caratteristica rende più complesso lo studio del loro comportamento inelastico, che non è attualmente compreso nella sua completezza, essendo poche le ricerche sperimentali e numeriche condotte finora. Per tale motivo le norme attuali sono basate su risultati ricavati per muri rettangolari, mentre linee guida specifiche per muri non rettangolari sono tuttora mancanti. Inoltre, semplici modelli largamente utilizzati in ambito professionale, come il modello di cerniera plastica, sono stati ricavati e calibrati per colonne, travi o muri rettangolari e la loro applicabilità a muri non rettangolari è stata solo in parte verificata. Per tali ragioni questo studio si concentra su: (1) migliorare la conoscenza del comportamento inelastico di muri ad U sollecitati da azioni bidirezionali ed (2) estendere i modelli ingegneristici per muri rettangolari, come ad esempio quello di cerniera plastica, all'analisi di muri ad U. Tale studio è limitato a muri ad U, trattandosi del modello più semplice di muro non rettangolare che tuttavia mantiene le caratteristiche chiave di tali elementi strutturali.

La prima parte della tesi si concentra sullo studio del comportamento di muri ad U sollecitati da forze dirette secondo la diagonale geometrica della sezione. E' stato trovato che tale direzione di carico, non considerata in genere nella progettazione, può determinare la resistenza a taglio delle ali. In aggiunta a ciò, anche la capacità di spostamento in tale direzione può risultare determinante. Per studiare il comportamento sotto azioni diagonali, sono stati condotti due test quasi-statici a grande scala su muri ad U. Sono stati identificati i meccanismi di rottura relativi alla direzione diagonale e possibili aspetti critici per la progettazione legati a tale meccanismo di rottura. Inoltre, è stata studiata l'influenza della distribuzione dell'armatura longitudinale sul comportamento sismico.

La seconda parte della tesi si concentra su come adattare il modello di cerniera plastica all'analisi di muri ad U. Modelli numerici che utilizzano l'ipotesi di sezione piana ed elementi finiti di tipo shell, validati rispetto ai risultati sperimentali, sono utilizzati al fine di condurre un'analisi parametrica su muri ad U. Dai risultati di tale studio è stata ricavata una nuova equazione per calcolare la curvatura di snervamento relativa ad una generica direzione di carico. Viene inoltre proposta un'equazione per valutare lo spostamento a snervamento che considera la parziale fessurazione della parete lungo la sua altezza. Con tale equazione viene migliorata la stima dello spostamento equivalente, in particolare per pareti molto snelle. Considerando la zona fessurata del muro si possono quindi meglio valutare le grandezze correlate allo spostamento a snervamento, come la rigidezza effettiva della parete. Infine, sono state modificate le equazioni per valutare l'estensione della cerniera plastica in modo tale da considerare le diverse direzioni di carico.

Parole chiave: muri ad U, carico diagonale, modello di cerniera plastica, spostamento a snervamento, estensione della cerniera plastica.



# Contents

<b>Preface</b>	<b>i</b>
<b>Acknowledgements</b>	<b>iii</b>
<b>Abstract</b>	<b>v</b>
<b>1 Introduction</b>	<b>1</b>
1.1 Background and problem statement . . . . .	1
1.2 Objectives and scope of the study . . . . .	2
1.3 Organisation of the thesis . . . . .	3
<b>2 Review on the seismic behaviour of U-shaped walls and modelling approaches</b>	<b>5</b>
2.1 Seismic behaviour of non-planar walls . . . . .	5
2.1.1 Experimental tests on non-planar walls . . . . .	5
2.1.2 Observations from experimental tests on U-shaped walls . . . . .	7
2.1.3 Bidirectional loading history . . . . .	11
2.1.4 Distribution of longitudinal reinforcement . . . . .	15
2.2 Modelling of U-shaped walls . . . . .	16
2.2.1 Modelling approaches for U-shaped walls . . . . .	17
2.2.1.1 Simplified models . . . . .	17
2.2.1.2 Macro models . . . . .	19

## Contents

---

2.2.1.3	Detailed FE models . . . . .	24
2.2.1.4	Summary of modelling approaches . . . . .	25
2.2.2	Estimates of quantities for plastic hinge model . . . . .	25
2.2.2.1	Yield curvature . . . . .	26
2.2.2.2	Yield displacement . . . . .	28
2.2.2.3	Plastic hinge length . . . . .	28
2.2.2.4	Shear displacements . . . . .	31
2.2.3	Ultimate limit strains . . . . .	33
2.2.4	Effective stiffness of RC walls . . . . .	35
<b>3</b>	<b>Quasi-static tests of two U-shaped walls under diagonal loading</b>	<b>39</b>
3.1	Introduction . . . . .	39
3.2	Test units, set-up, instrumentation and loading history . . . . .	39
3.2.1	Geometry of the test units . . . . .	40
3.2.2	Material properties . . . . .	40
3.2.3	Description of test set-up and instrumentation . . . . .	41
3.2.4	Loading history . . . . .	44
3.3	Test results . . . . .	46
3.3.1	Failure mechanisms and hysteretic behaviour . . . . .	46
3.3.1.1	TUC . . . . .	47
3.3.1.2	TUD . . . . .	50
3.3.2	Crack patterns . . . . .	51
3.3.3	Local deformation response specific to diagonal loading . . . . .	56
3.3.3.1	Vertical strains on the inner and outer side of the flange ends	56
3.3.3.2	Vertical strains at the base of the wall . . . . .	56
3.3.4	Shear to flexural displacements ratios . . . . .	62

3.3.5	Comparison of experimentally determined moment capacities with section analysis estimates . . . . .	65
3.4	Conclusions . . . . .	67
3.5	Dataset . . . . .	68
<b>4</b>	<b>Experimentally derived quantities for the plastic hinge model</b>	<b>69</b>
4.1	Introduction . . . . .	69
4.2	Experimentally determined displacement components . . . . .	70
4.3	Yield curvature . . . . .	73
4.3.1	Definition . . . . .	73
4.3.2	Determining the experimental first yield point . . . . .	74
4.3.2.1	Strains at base of the wall . . . . .	74
4.3.2.2	Procedures for determining first yield . . . . .	74
4.3.2.3	Curvature profiles and cracked height at first yield . . . . .	75
4.3.2.4	Alternative procedure based on strains . . . . .	78
4.3.3	Comparison of experimental results with estimates and section analysis results . . . . .	78
4.4	Yield displacement . . . . .	82
4.4.1	Experimental yield displacement . . . . .	82
4.4.2	Yield displacement estimates . . . . .	83
4.4.2.1	Flexural displacements due to wall deformation . . . . .	83
4.4.2.2	Flexural displacements due to strain penetration . . . . .	88
4.4.3	Comparison of experimental yield displacements with estimates . . . . .	88
4.5	Plastic hinge length . . . . .	92
4.5.1	Estimates for plastic hinge lengths from experimental results . . . . .	92
4.5.1.1	Equations for plastic hinge lengths in the literature . . . . .	92
4.5.1.2	Particularities for diagonal loading . . . . .	93

## Contents

---

4.5.2	Experimentally determined plastic hinge lengths . . . . .	93
4.5.2.1	Plastic hinge lengths back-calculated from top displacement .	94
4.5.2.2	Plastic hinge lengths calculated from height of plastic zone .	96
4.5.2.3	Variations and trends of the experimentally determined plastic hinge lengths . . . . .	99
4.5.3	Discussion . . . . .	103
4.6	Ultimate limit strains . . . . .	104
4.6.1	Introduction . . . . .	104
4.6.2	Experimentally determined ultimate limit strains and curvatures . . . . .	105
4.6.3	Comparison with limit strain estimates . . . . .	105
4.7	Shear displacements . . . . .	109
4.7.1	Experimentally determined shear to flexural displacement ratios . . . . .	109
4.7.1.1	Experimental determination . . . . .	109
4.7.1.2	Variation of shear displacements with displacement ductility	109
4.7.2	Estimates for the shear displacements in the inelastic range . . . . .	110
4.7.3	Estimates for the shear displacements at yield . . . . .	114
4.8	Effective stiffness of RC walls . . . . .	118
4.9	Conclusions . . . . .	120
<b>5</b>	<b>Validation of two numerical models for U-shaped walls</b>	<b>123</b>
5.1	Plane section analysis . . . . .	124
5.1.1	Model set-up . . . . .	124
5.1.2	Model validation . . . . .	125
5.1.2.1	Experimental determination of moment-curvature relationship	125
5.1.2.2	Moment capacity . . . . .	128
5.1.2.3	Moment capacity accounting for the effective flange width .	129
5.1.2.4	Yield curvature . . . . .	132



5.1.3	Summary of findings from plane section analysis . . . . .	135
5.2	Shell element model . . . . .	135
5.2.1	VecTor4 software . . . . .	136
5.2.2	Model set-up . . . . .	138
5.2.2.1	Reference model: geometry, mesh and material models . . .	138
5.2.2.2	Mesh sensitivity . . . . .	140
5.2.2.3	Material models and analysis options: sensitivity studies . . .	147
5.2.2.4	Material properties . . . . .	156
5.2.2.5	Load application and load history . . . . .	161
5.2.3	Model validation . . . . .	161
5.2.3.1	Force-displacement curves . . . . .	162
5.2.3.2	Yield curvature . . . . .	162
5.2.3.3	Yield displacement . . . . .	168
5.2.3.4	Effective stiffness . . . . .	170
5.2.3.5	Plastic hinge length . . . . .	171
5.2.3.6	Ratio of shear to flexural displacements . . . . .	174
5.2.4	Influence of the loading history . . . . .	177
5.2.4.1	Introduction . . . . .	177
5.2.4.2	Wall strength . . . . .	178
5.2.4.3	Yield curvature, yield displacement and effective stiffness . .	178
5.2.4.4	Plastic hinge length . . . . .	183
5.2.4.5	Ratio of shear to flexural displacements under monotonic loading	183
5.3	Conclusions . . . . .	189
<b>6</b>	<b>Yield and ultimate displacement of U-shaped walls</b>	<b>191</b>
6.1	Introduction . . . . .	191

## Contents

---

6.2	Design of the parametric study . . . . .	191
6.2.1	Design of the U-shaped RC walls . . . . .	192
6.2.1.1	General design considerations and parameters of the study . .	192
6.2.1.2	Design procedure steps . . . . .	194
6.2.1.3	Confinement lengths . . . . .	195
6.2.2	Numerical models . . . . .	195
6.2.2.1	Plane section analysis . . . . .	195
6.2.2.2	Shell element model . . . . .	197
6.3	Yield curvature . . . . .	197
6.3.1	Results from plane section analysis . . . . .	199
6.3.2	Comparison with existing estimates . . . . .	200
6.3.3	New estimates for yield curvature for any loading direction . . . . .	204
6.3.3.1	Derivation of yield curvature estimates for any loading direction	205
6.3.4	Comparison of section analysis and shell element model results . . . .	210
6.4	Yield displacement . . . . .	210
6.5	Effective stiffness ratio . . . . .	216
6.5.1	Comparison with existing estimates . . . . .	216
6.5.2	Trends of effective stiffness with the different loading positions . . . .	217
6.5.3	Modified equation for effective stiffness ratio . . . . .	218
6.6	Plastic hinge lengths . . . . .	227
6.6.1	Inelastic curvature profiles . . . . .	227
6.6.2	Displacement capacity . . . . .	227
6.6.3	Plastic hinge length . . . . .	236
6.6.3.1	Trends with wall length, shear span, axial load ratio and shear stress . . . . .	236
6.6.3.2	New estimates for plastic hinge lengths . . . . .	236

6.7	Conclusions . . . . .	243
<b>7</b>	<b>Summary, conclusions and outlook</b>	<b>245</b>
7.1	Summary and conclusions . . . . .	245
7.2	Outlook . . . . .	249
	<b>Appendix</b>	<b>251</b>
	<b>Notations</b>	<b>263</b>
	<b>Bibliography</b>	<b>274</b>



# 1. Introduction

## 1.1 Background and problem statement

In seismic prone areas, many medium to high-rise buildings use reinforced concrete (RC) core walls as the main lateral load resisting element. Core walls are structural elements composed of several rectangular wall segments, termed webs or flanges, that are connected at the vertical edges and are closing the wall section on three sides. The fourth side of the section can be either open or partially closed by deep beams. Due to their cross-section shape, core walls are commonly used to accommodate lift shafts or staircases.

Despite the popularity of the core walls in practice, their inelastic behaviour under seismic loading is not yet well understood as experimental tests on core walls are scarce when compared to the number of tests carried out on planar walls. Extensive experimental research on planar RC walls has led to the identification of the parameters controlling their seismic behaviour and provided data for derivation and calibration of analytical tools and design guidelines. For core walls, lack of experimental data has delayed the development of design guidelines. Design codes are therefore mostly based on findings from planar wall tests, leaving to the design engineer the difficult task of extrapolating these guidelines to core walls.

The following reasons explain the more complex seismic behaviour of core walls when compared to that of planar walls:

- Planar walls provide horizontal strength and stiffness mainly in the in-plane direction of the wall while core walls provide strength and stiffness in all horizontal directions. For planar walls, only the in-plane direction of loading is considered in design, but for core walls the designer needs to consider in addition to the principal axes of the cross-section also other horizontal directions that could be critical for design.
- The shear lag effect limits the effectiveness of web and flanges when in tension, and hence the wall strength is reduced when compared to the wall strength derived from a plane section analysis [Kwa96]. The shear lag effects in core walls are further exacerbated by the rather large shear deformations experimentally observed even for slender core walls. Experimental tests on core walls have shown that the shear deformations are particularly large in the wall parts that are mostly in tension when carrying significant shear loads [BDP11].

- Due to their cross-sectional geometry, core walls provide also torsional strength and stiffness and hence the interaction of torsion, bending and shear should be considered. While the wall is linear elastic, the shear centre position is fixed. In the inelastic range, however, the position of the shear centre migrates towards the parts of the section that are in compression, complicating thus further the evaluation of the torsional response of the core wall [IR05].

One of the simplest types of core walls possessing all the characteristics enumerated above are U-shaped walls and experimental studies on core walls that have been carried out in the past focused therefore on this type of core wall. Previous research on U-shaped walls has shown the complex behaviour that such walls exhibit under bidirectional loading. The diagonal loading direction, which is not typically considered in design, has been identified as a particular critical direction. This is for the following reasons: the displacement capacity is often smaller than for principal directions, the distribution of the shear forces between the different planar wall parts is complex and the load transfer mechanism from the wall to the foundation is unclear [BDP08b]. These unknowns raise also questions about the failure mechanisms that govern the wall behaviour under diagonal loading. Shear failures in the web and compression failures in the flange ends are among the most common ones observed in previous studies. This study will show that also the out-of-plane bending of the flanges and the resulting strain gradient across the flange width can influence the failure mode.

Despite previous experimental research on core walls focusing on U-shaped walls, the available data is still rather scarce and it has not allowed the in-depth validation of analytical tools for such walls. Engineering type models, such as the plastic hinge model, have been developed and calibrated against experimental data on columns, beams or planar walls. Their applicability to U-shaped walls has been only marginally verified. It remains therefore unclear if and how these models can be applied to U-shaped walls for the different loading directions.

## 1.2 Objectives and scope of the study

The objective of this study is to make a contribution to the performance-based seismic design of U-shaped RC core walls. The study aims at: (1) providing high quality experimental data for the validation of numerical and analytical models, (2) improving the knowledge on the behaviour of U-shaped walls under bidirectional loading with focus on the diagonal direction and (3) extending easily applicable engineering type models, such as the plastic hinge model, to the analysis of U-shaped walls.

In order to reach the first objective a new experimental campaign was performed in which two U-shaped walls were tested under horizontal diagonal loading. The second objective was achieved by interpreting the new experimental data and by identifying deformation behaviour and failure mechanisms specific to diagonal loading. The third objective focuses on the extension of the plastic hinge model to core walls by verifying existing estimates against experimental data and results from advanced non-linear simulations and by proposing new estimates where necessary.

The scope of this study is limited to the flexural and the shear behaviour of U-shaped walls while the torsional behaviour was not specifically addressed. For all U-shaped walls in this study, investigated experimentally or numerically, loading was applied at the height of the shear span under the form of imposed displacements while the rotation of the wall in the cross-section plane was always restrained at this height. The U-shaped walls discussed within this study are isolated cantilever walls, while entire buildings including U-shaped walls were not considered.

### 1.3 Organisation of the thesis

This section provides a brief description of the topics covered in each chapter of the thesis. The thesis comprises seven chapters.

Chapter 2 presents a review of previous tests on core walls and other non-planar walls. Previous tests on U-shaped walls are discussed and key points of their non-linear behaviour are identified as well as needs of further research identified. Different loading protocols previously applied in experimental tests of non-planar walls are reviewed. In addition, the influence of the longitudinal reinforcement distribution within the section on the wall behaviour is discussed.

In the second part of this Chapter 2 a review of modelling approaches for U-shaped walls is presented. The reviewed modelling approaches are divided into three categories: simplified models based on empirical and mechanical principles, macro models and detailed finite element models. The models are discussed with respect to their capability to capture the inelastic behaviour of U-shaped walls under bi-directional loading.

Chapter 3 describes the experimental tests of two U-shaped walls tested under quasi-static cyclic loading. The test set-up, loading history and the main experimental results are included in this chapter. The walls were tested mainly under loading in the direction of the diagonal of the section. This allowed the identification of failure mechanisms and design issues specific to diagonal loading of U-shaped walls. In addition, the influence of the longitudinal reinforcement distribution on the behaviour of the wall was investigated through these tests.

In Chapter 4, the experimental results from Chapter 3 together with results from a previous similar test campaign are investigated further. Quantities necessary in the application of the plastic hinge model are derived from the experimental results and compared to estimates. These quantities are: yield curvature, yield displacement, plastic hinge length, shear deformations and ultimate strain limits. In addition, the effective stiffness ratio is investigated. From the comparison between experimentally derived values and estimates, quantities that need further investigation or cases where estimates are missing are identified. Particular emphasis is placed on the yield displacement, for which new estimates are proposed based on the experimentally observed curvature profiles at yield.

## Chapter 1. Introduction

---

In order to validate the new equations for the plastic hinge model, the available experimental data on U-shaped walls is not sufficient. Therefore, a detailed shell element model was validated against the experimental data in Chapter 5 and then it was further used for parametric studies in Chapter 6. This latter chapter discusses in detail the setting-up of the model for U-shaped walls and the modelling choices made. In addition, results from plane section analyses are compared in this chapter to the experimental data in terms of wall strength and yield curvature, and discrepancies are discussed.

In Chapter 6, a parametric study is performed for U-shaped walls with different geometries using the validated shell element model and plane section analyses. The design of the parametric study as well as the design of the U-shaped walls used in the study, are discussed in this chapter. From the results of the parametric study, new estimates for yield curvatures for any loading direction, new estimates for the effective stiffness of walls and new equations for the plastic hinge length are proposed.

The final Chapter 7 presents a summary of the main contributions of the thesis and the conclusions of the study. Based on the findings of this report, several directions for further research are presented.



## **2. Review on the seismic behaviour of U-shaped walls and modelling approaches**

This chapter is comprised of two main parts. The first part reviews experimental campaigns of non-planar reinforced concrete (RC) walls, i.e., walls designed to carry shear forces in both horizontal directions such as walls with L-, T-, I-, U-, C-shaped cross sections. Key findings from these campaigns and state-of-the-art knowledge on the seismic behaviour of RC core walls are summarised in this part (Section 2.1). The second part 2.2 presents a review of numerical modelling approaches for U-shaped walls and identifies advantages and drawbacks of each approach.

### **2.1 Seismic behaviour of non-planar walls**

#### **2.1.1 Experimental tests on non-planar walls**

This section reviews experimental tests on U-shaped or C-shaped walls that are documented in the literature. In addition, experimental campaigns on isolated non-planar walls tested under quasi-static cyclic bidirectional loading are also included to investigate effects of loading history on the wall behaviour. The tests included in this selection are limited to non-planar walls with open cross-section, except one campaign on box-shaped walls which was included as it is the most comprehensive experimental investigation of the loading history effects to date.

In Table 2.1, the test series fulfilling the outlined criteria are grouped on thematic test campaigns and then in chronological order. The findings from these tests are discussed in more detail in the following sections focusing on test observations for U-shaped walls, bidirectional loading histories and the influence of the distribution of the longitudinal reinforcement on the wall behaviour.

## Chapter 2. Review on the seismic behaviour of U-shaped walls and modelling approaches

Year	Reference	C-S shape	Prototype structure	Loading pattern	Scale	No./ Name of test units	Shear span M/V [m]	Shear span ratio H/L	L/t	Axial load ratio N/fc*Ac	Main investigated parameter	Failure modes/comments
1993	University of Illinois [SW93]	C-shaped	-	unidirectional, along symmetry axis (parallel to flanges)	1:4	CLS CMS	2.74 2.74	1.8 1.8	20 20	0.06 0.07	Influence of web reinforcement amount on wall behaviour	Both CLS and CMS failed due to concrete crushing in the flange ends and extension of crushing over the length of the flanges
2001	CEA Saclay [CCM99]	U-shaped	1 person lift shaft	Shake table test: unidirectional, along symmetry axis (parallel to flanges)	1:1.67	No. 3	3.90	4.33	6	0.1	Influence of stirrup spacing; Validation of EC8 design rules	Poor ductility properties of the longitudinal reinforcement bars ( $\epsilon_{sr} = 2.5 - 2.6\%$ ) lead to premature bar fracture and wall failure
2001	Ispra [PP+00a] [PP+00c] [PP+00d] [PP+00b]	U-shaped	1 person lift shaft	Parallel to web Parallel to flanges Clover leaf Pattern	1:1	Wall 1 Wall 2 Wall 3	3.9 3.9 3.9	2.6 2.6 2.6	6 6 6	0.1- 0.12	Influence of loading history; Validation EC8 design rules	Wall 1: Bar buckling where one stirrup was forgotten; Wall 2: Bar fracture after buckling; Wall 3: Bar fracture after buckling; shear failure of the flange in compression at loading with one flange end in compression
2008	ETHZ [BDP08b]	U-shaped	Core wall in mid-rise building	Complex bidirectional	1:2	TUA TUB	2.95/ 3.35	2.81 2.58	8.67 13	0.02 0.04	Influence of wall thickness and loading history	TUA: Bar fracture after buckling; TUB: Crushing of diagonal compression struts in the web
2013	University of Washington [LL+13]	C-shaped	Core wall in mid-rise building	Parallel to web Bidirectional Bidirectional	1:3	Wall 6 Wall 7 Wall 8	5.00 5.00 Variable	1.64 1.64 (1.64)	20 20 20	0.05 0.05 Variable	Influence of loading history	Wall 6: sliding at the base; Wall 7: Bar fracture after buckling; Wall 8: Concrete crushing and bar fracture (variable axial load and shear span)
1994-2003	Japan [HK+00] [HK+01] [OS+04] [KN+07]	Box-shape Cylinder shape	Nuclear reactor building	Diagonal Rectangular Cross Circular	1:5	No. 15	0.6- 1	0.67	21	15	Influence of loading history	Comprehensive study on the influence of loading history
2009	University of Minnesota [Bru09]	T-shaped	Core wall in mid-rise building	Complex bidirectional	1:2 3:4	NTW1 NTW2	7.36 7.36	3.20 3.20	15.1 15.1	0.032 0.035	Influence of reinforcement detailing	NTW1: Longitudinal reinforcement concentrated in flange end; NTW2: Longitudinal reinforcement distributed over flange width; Both units failed due to crushing of the web end.

**Table 2.1:** Selected experimental tests on non-planar RC walls

### 2.1.2 Observations from experimental tests on U-shaped walls

- **University of Illinois (UoI) tests**

Two C-shaped wall were tested at the University of Illinois under quasi-static reversed cyclic loading [SW93] (Figure 2.1). unidirectional loading was applied in the direction of the symmetry axis of the C-shaped section, i.e, parallel to the two flanges (Figure 2.2). The objectives of the study were: to investigate the cyclic response of non-planar walls, to study the influence of the reinforcement amount in the unconfined concrete parts of the wall on the wall behaviour, to determine the effective stiffness of non-planar walls at different displacement levels and to provide data to verify numerical models. The main varying parameter between the two tested walls was the amount of longitudinal and transversal reinforcement in the unconfined parts of the web and the flanges. The first test unit (CLS) had a 0.0025 longitudinal reinforcement content while the second one (CMS) had the double of CLS. Longitudinal and transversal reinforcement contents were equal and the reinforcement was placed only in one layer over the wall thickness, except for the boundary elements where two layers were used. Failure for both walls was reached due to confined concrete crushing and bar buckling in the boundary elements of the flange ends at  $\sim 1.8\%$  drift. Upon further loading, crushing extended in nearly the entire length of the flanges. Based on numerical results of models validated with the experimental data, the study concluded that all the reinforcement in the web was effective in tension. Additionally, the reinforcement amount in the unconfined wall parts was found to not have a significant influence on the magnitude of shear displacements. The influence of the reinforcement in the unconfined parts of the wall is discussed in more detail in Section 2.1.4.

- **Ispra and Saclay tests**

The Ispra and Saclay tests were part of a joint test campaign on U-shaped walls [CCM99], which investigated the detailing rules of EC8 [CEN01] for RC walls. unidirectional shake table tests were performed on three U-shaped walls in Saclay, while another three walls were tested under quasi-static cyclic loading in Ispra. In the Saclay tests, the wall behaviour was dominated by the rupture of the longitudinal reinforcement bars which fractured prematurely due to their very small ultimate strain capacity, i.e., 2.5 – 2.6%. Therefore limited data was gathered on the inelastic behaviour of the U-shaped walls.

The Ispra tests, investigated in addition to EC8 detailing rules, also the effect of the loading history on the wall behaviour. All three walls were identical (Figure 2.1). Only the loading pattern was different. Wall 1 was tested under unidirectional loading, in the direction parallel to the web of the wall, Wall 2 was tested in the direction of the symmetry axis (parallel to flanges) and Wall 3 underwent loading following a clover leaf pattern (Figure 2.2). Wall 1 failed due to bar buckling followed by concrete crushing in the boundary element at the end of one of the flanges, where one stirrup was missing. Wall 2 failed due to fracture of previously buckled bars in one of the flanges. Wall 3 reached failure when loading with one flange end in compression, due to fracture of previously buckled bars, followed by shear compression failure of the flange in compression.

## Chapter 2. Review on the seismic behaviour of U-shaped walls and modelling approaches

The main findings of the tests were summarised by [RF01]. The displacement capacity in the principal directions was reduced for the bidirectional test as compared to the unidirectional tests, but if the capacity in the diagonal direction is considered then all units reached a similar lateral drift of  $\sim \delta = 3\%$ . When the displacement loading branches were orthogonal to the previous loading branch in the bidirectional test, they introduced an important strength reduction in the orthogonal direction, e.g., when the wall was first pushed to position D, then to F (Figure 2.2), the force in the web direction was reduced as compared to the web force from the unidirectional tests. The bidirectional test was also characterised by a more severe concrete degradation.

For the bidirectional test, when loading with one flange end in compression, almost the entire shear resistance in the direction of the flanges was provided by the flange in compression. The flange which was in tension at this loading position carried only a small amount of the total shear force in the direction of the flanges. The implication in design of this observation is to design each of the two flanges to carry the entire shear force in the direction of the flanges [IR05].

- **ETHZ tests**

Two half scale U-shaped walls were tested under quasi-static complex bidirectional cyclic loading at ETHZ (Figure 2.1 and [BDP08b]). The objectives of the test campaign were to: identify most likely failure mechanisms for U-shaped walls, investigate strength, stiffness and displacement capacity for different loading directions, determine the magnitude of the different displacement components and investigate the torsional stiffness.

The main parameter varied between the tests was the wall thickness. The complex bidirectional loading applied in both tests was based on a load protocol previously applied in the testing of box-shaped piers by [HDS06]. For the U-shaped walls, at each displacement ductility reverse loading cycles were applied in the following order: one cycle parallel to the web, one cycle parallel to flanges, one cycle in the direction of the geometric diagonal of the section and a "sweep" cycle (Figure 2.2).

The wall with the larger thickness, TUA, failed in a ductile manner due to fracturing of previously buckled reinforcement bars in the boundary element at the flange ends when loading with corner web-flange in compression. TUB failed when loading parallel to the web due to crushing of the compression diagonals in the unconfined concrete of the web, despite the wall having been designed to prevent web crushing according to EC8 [CEN03]. The failure of TUB was attributed to the excessive spalling of the unconfined part of the web under the bidirectional loading history which significantly reduced the thickness of the web [BDP08b]. When loading parallel to the web, the web shear force was larger than the web shear force under any other loading position.

ETHZ tests confirmed findings of the bidirectional Ispra test concerning the distribution of the shear forces between the two flanges when loading with one flange end in compression, i.e., flange in compression carries almost the entire shear force in the direction of the flanges. In addition, [BDP08b] found that shear displacements were particularly large in the wall parts which were mostly in tension and carried significant shear force (i.e., web at position A), and the magnitude of the shear displacements depended on the loading direction.

When comparing the wall strength with estimates from a plastic hinge model and a cyclic wide-column model (WCM), [BDP08b] found that for the diagonal direction (i.e., flange end in compression or corner web-flange in compression), the maximum wall strength was never reached. This was attributed to the significant stiffness degradation induced by the first cycles in the principal directions which always preceded the diagonal cycles. Displacement estimates for the two tested walls, using a plastic hinge analysis, indicated that the displacement capacity in the diagonal direction was smaller than for any of the principal directions [BDP08b].

- **University of Washington (UoW) tests**

Three identical one-third scale C-shaped walls were recently tested under quasi-static cyclic loading at the University of Washington [LL<sup>+</sup>13] (Figure 2.1). The test campaign investigated the effects of the loading history and of the coupling beams on the wall behaviour. Two walls (Wall 6 and Wall 7) were tested under constant axial load ratio and shear span, while for the third wall (Wall 8), both values were varied to simulate the influence of the coupling beams. Wall 6 was tested under a unidirectional loading pattern parallel to the wall web, while Wall 7 and 8 were tested under bidirectional loading. Wall 8 and initial cycles of Wall 7 were displaced according to a criss cross pattern along the two principal axes of the C-shaped section (Figure 2.2). When loading was applied in the direction of one principal axis, the displacement in the orthogonal direction was zero. In the inelastic loading cycles of Wall 7, the wall was displaced in the direction of the web while the displacement in the orthogonal direction (direction of the flanges) was kept constant to values of 1.1 – 2% drift.

Failure of Wall 6 occurred due to concrete crushing and sliding at the wall base in the construction joint while Wall 7 failed due to buckling of the longitudinal reinforcement and subsequent rupture when loading with the corner web-flange in compression. Wall 8 failed due to loss of confinement and confined concrete crushing in the boundary elements, when loading with increased axial load ratio.

Based on the experimental observations, [LL<sup>+</sup>13] concluded that the displacement capacity in the direction of the web is not affected by the bidirectional cross pattern when displacement in the orthogonal direction is zero, but is reduced when this displacement is non-zero. This is consistent with findings from [RF01]. However if the displacement in the diagonal direction is considered, then the displacement capacity is larger for the bidirectional test than for the unidirectional test (diagonal drift capacity bidirectional  $\delta_{SRSS} = 2.5\%$  compared to unidirectional drift capacity along web  $\delta = 2.2\%$ ). Bidirectional loading with non-zero orthogonal displacement was also found to reduce the wall stiffness in the direction of the web, which is again consistent with findings from [RF01].

### Conclusions

The findings of previous experimental campaigns can be summarised in terms of the failure modes of U-shaped walls and their corresponding loading directions:

## Chapter 2. Review on the seismic behaviour of U-shaped walls and modelling approaches

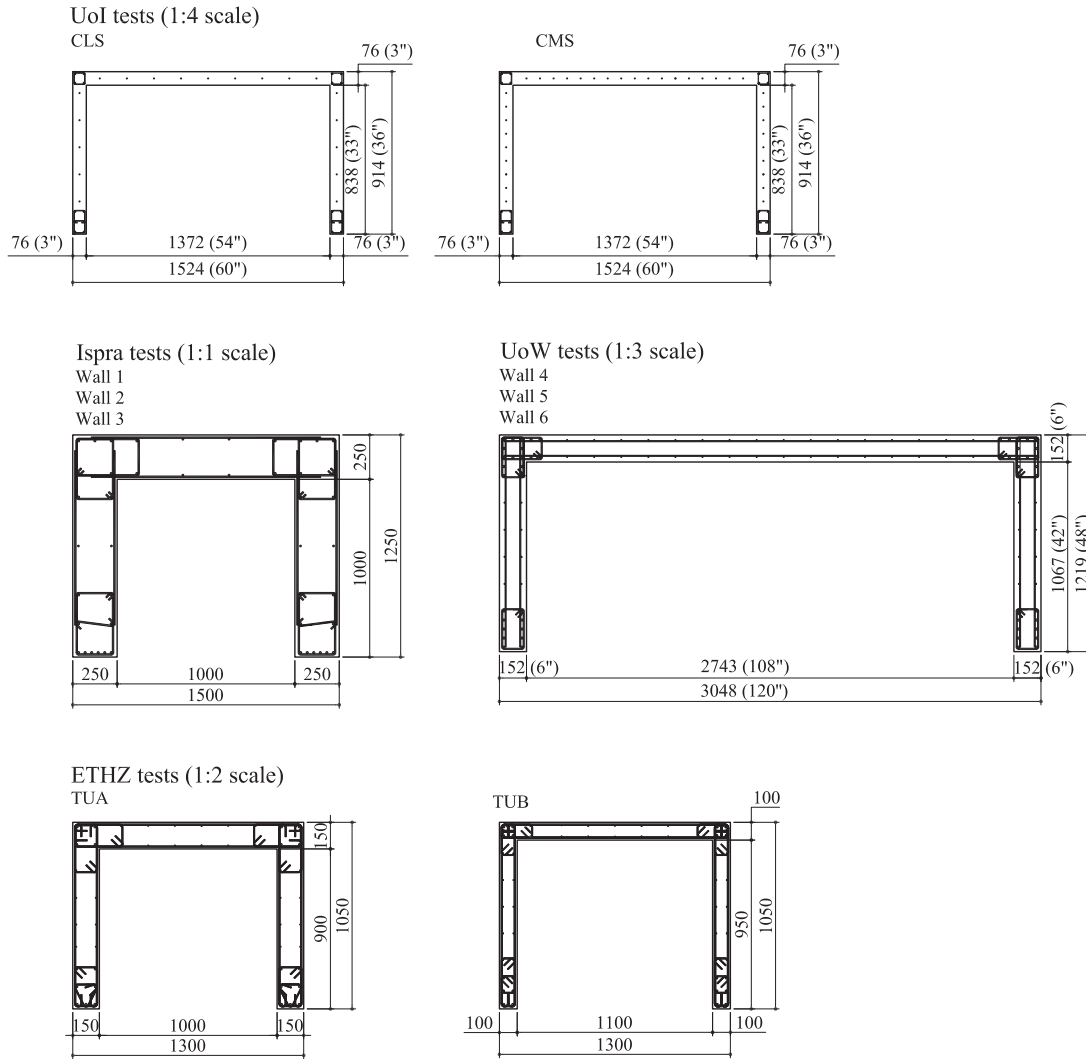


**Figure 2.1:** U-shaped and C-shaped wall sections of tests specimens from previous experimental campaigns. Dimensions are in mm, unless otherwise specified.

## 2.1. Seismic behaviour of non-planar walls

---

- Failure of the compression struts in the web determined by loading parallel to the web (position A - Figure 2.2), e.g., TUB (ETHZ tests). Since the shear force taken by the web is the largest of all the considered loading directions, the reinforcement in the web should be determined from this loading case.
- Shear compression failure in the flange determined by loading in the diagonal direction with the flange end in compression (position E - Figure 2.2), e.g., Wall 3 (Ispra tests). The compressed flange carries the majority of the shear force in the direction of the flanges at this loading position.
- Damage in the boundary elements of the flange ends (confined concrete crushing, bar buckling, bar fracture after buckling) determined by loading in the diagonal direction with the flange end in compression (position E - Figure 2.2) or with the flange end in tension (position F), e.g., Wall 7 (UoW tests) and TUA (ETHZ tests). Due to the longer wall length in the diagonal direction (i.e., wall diagonal length), for the same base curvature the diagonal loading imposes larger strain demands on the boundary elements than loading in the principal directions.
- Damage in the boundary elements of at the corner web-flange determined by loading in the diagonal direction at position E or F, e.g., Wall 3 (Ispra tests).

Based on the above conclusions, the diagonal loading direction warrants hence further attention as it is determinant for many of the failure modes for U-shaped walls. In addition, several other reasons outline the need to investigate the diagonal direction.

- The distribution of shear forces between the two flanges is complex under diagonal loading [RF01], [BDP08b].
- The transfer of the shear forces from wall to foundation is unclear since most of the wall section is expected to be in tension when loading to diagonal positions. Hence locations where the shear forces can be transferred to the foundation, i.e., compression zones, are limited [BDP08b].
- It is unclear whether the wall displacement capacity is smaller for the diagonal direction than for the principal directions. While numerical studies indicate this to be the case [BDP08b], the experimental results are contradictory as the drift capacity in the diagonal direction was found to be: smaller than for the principal loading directions (e.g., TUA from ETHZ tests), the same as for the principal directions (e.g., Wall 3 from Ispra tests) or larger than for the principal direction (e.g., Wall 7 from UoW tests).

### 2.1.3 Bidirectional loading history

This section presents a review of bidirectional loading patterns which have been previously tested on non-planar walls. The different loading patterns are discussed in terms of their suitability to investigate the U-shaped wall behaviour under diagonal loading.

## Chapter 2. Review on the seismic behaviour of U-shaped walls and modelling approaches

- Clover leaf pattern

One of the U-shaped wall specimens from the Ispra experimental campaign was tested according to a square clover leaf pattern as shown in Figure 2.2 [PP<sup>+</sup>00b]. To reach a diagonal position with this loading pattern, the load path is comprised of two consecutive displacement branches: one parallel to the web and one parallel to the flanges, i.e. two branches orthogonal to each other. As already mentioned in Section 2.1.2 test results indicated that when displacement loading branches were orthogonal to the previous loading branch, they introduced important strength reduction in the orthogonal direction [RF01]. Therefore it is likely that such a loading pattern would reduce the wall strength and stiffness for the diagonal loading direction and therefore the full wall strength in the diagonal direction might not be reached.

- Bidirectional pattern by [HDS06]

[HDS06] developed a bidirectional diagonal and "sweep" pattern for cyclic tests of box section piers. The same pattern was used for the two U-shaped walls from the ETHZ tests. In addition, the diagonal and the sweep cycles were preceded by one cycle parallel to the web and one parallel to the flanges (Figure 2.2). A shortcoming of this loading pattern is that it can provide displacement capacity only for one loading direction, that of failure. In addition, as previously mentioned, the loading cycles in the principal directions preceding the diagonal ones at the same displacement ductility level, softened the wall considerably so that the full wall strength in the diagonal direction was not reached (see Section 2.1.2 and [BDP08b]). In order to eliminate this effect and reach the full wall strength for the diagonal direction, the diagonal cycles should be the ones cycled first at a new drift level.

- Criss cross pattern with non-zero orthogonal displacement

Wall 7 from University of Washington tests [LL<sup>+</sup>13] was loaded in the inelastic cycles following a criss cross pattern with non-zero orthogonal displacement, i.e., loading was applied in the direction of the web while the displacement in the direction of the flanges was non-zero and was kept constant (Figure 2.2). This loading pattern can be considered as variation of the clover leaf pattern and hence all conclusions mentioned from the clover leaf pattern apply.

- Hourglass pattern

A complex bidirectional loading history, including an hourglass pattern, was applied in the quasi-static cyclic testing of two T-shaped walls at the University of Minnesota (UoM) [Bru09]. One of the main objectives of the test campaign was to investigate the behaviour of non-planar walls under bidirectional loading. The applied loading pattern in the inelastic range was comprised of the following cycles (see Figure 2.2):

- in the principal directions of the T-shaped section, i.e. parallel to the web and parallel to the flange (for T-shaped sections, the web is the wall part with the largest plane dimension in the direction of the symmetry axis)
- at 45° from the principal axes starting at zero deformation
- at ~ 20° or 70° from the principal axes which resulted from the 100% + 30% combination of displacements on the principal axes according to IBC 2003 [ICC03]
- following an hourglass pattern



## 2.1. Seismic behaviour of non-planar walls

---

[Bru09] compared the wall strength for the different loading directions with results from a monotonic flexural plane section model and found that the plane section model overestimated the strength significantly for the flange direction and for the skew loading directions. This was attributed to the sequence of loading cycles (see Figure 2.2). More specifically inelastic web cycles at a maximum 2% drift softened the wall considerably so that the skew cycles and the flange cycles that followed did not increase the longitudinal strain demands beyond those previously applied by the web cycles [Bru09]. This was despite imposing in the flange direction maximum drifts twice as large as those previously imposed for the web direction. Similarly to the bidirectional loading pattern applied in the ETHZ tests (Figure 2.2), the complex loading pattern applied in the UoM tests significantly softened the wall, and therefore the full wall strength was reached only for the first direction first cycled at significant inelastic drift level.

- Diagonal pattern

Diagonal criss cross loading pattern was one of the loading patterns used for the testing of squat box and cylinder walls [HK<sup>+</sup>00], [OS<sup>+</sup>04], [KN<sup>+</sup>07]. The test campaign was one of most comprehensive ones to investigate the effects of the loading history on non-planar walls, despite the very specific test units (very squat and closed section) which were representative for walls of reactor buildings. Other loading patterns investigated within this campaign were: a rectangular pattern, a criss cross pattern with zero orthogonal displacement and a circular pattern (Figure 2.2). In addition, box walls were tested also under unidirectional diagonal loading.

Force-displacement responses from the different loading patterns were then compared and conclusions were drawn on the influence of the load path and the influence of bidirectional loading. [KN<sup>+</sup>07] reported that the loading path does not influence the maximum attained force and displacement capacity for the diagonal direction. In addition, the bidirectional loading was found increase the maximum attained force as compared to the unidirectional loading in the diagonal direction. However, despite the comprehensive investigation (large number of test specimens and of investigated loading histories), the findings of this campaign cannot be readily extrapolated to non-planar slender walls with open cross-section, such as the U-shaped walls.

## Chapter 2. Review on the seismic behaviour of U-shaped walls and modelling approaches

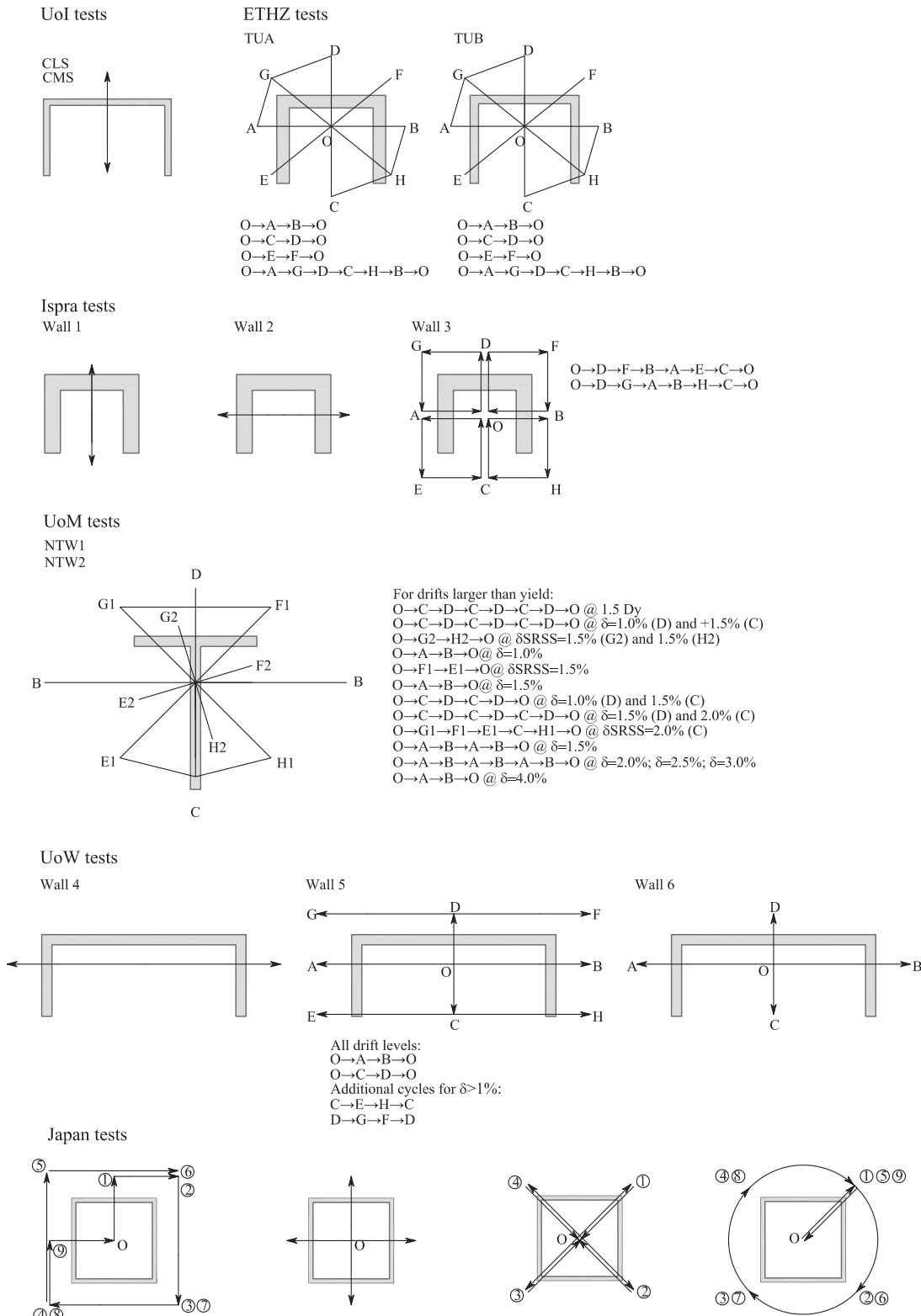


Figure 2.2: Bidirectional loading histories applied to non-planar walls.

### Conclusions on loading history

Test campaigns on the bidirectional response of non-rectangular walls have employed different types of loading histories. These loading histories vary with respect to the number of loading directions considered, load paths and number of cycles per displacement level. Since the focus of the tests campaign to be performed within this study is to investigate the behaviour in the diagonal direction of the U-shaped walls, loading will be applied only in the diagonal direction (E-F or H-G) in one diagonal displacement branch passing through zero deformation. Reaching the diagonal position through two consecutive displacement branches (i.e. clover leaf or hourglass pattern) reduces the wall stiffness and strength in the diagonal direction.

Diagonal loading can be applied unidirectionally, i.e., along one geometric diagonal of the U-shaped section or bidirectionally, i.e., along both geometric diagonals in a criss cross pattern (Figure 2.2 Japan tests). The second option is more appealing since applying such a load history would allow the investigation of an additional parameter through the experimental tests, namely the distribution of the longitudinal reinforcement, which is discussed in the following section.

#### 2.1.4 Distribution of longitudinal reinforcement

For non-planar walls the shear lag effects are important and the shear displacements are particularly large even for slender walls [Bru09], [BDP08a], [ZL14]. Both effects reduce the wall stiffness and large shear displacements can result in shear failures. It is therefore desirable to reduce these effects. One possible way of doing so is to distribute the longitudinal reinforcement uniformly over the wall section instead of concentrating it in the boundary elements.

[Bru09] investigated experimentally the influence on the wall behaviour of the distribution of longitudinal reinforcement within the wall section. One of the two T-shaped walls tested (NTW1), had the flange detailed with longitudinal reinforcement concentrated in the boundary elements and minimal reinforcement content in the rest of the flange. The second wall (NTW2) had the longitudinal reinforcement uniformly distributed across the flange. This resulted in reinforcement contents in the unconfined part of the flange of 0.6% for NTW1 and 2.2% for NTW2. The unconfined part of the web was detailed for both test units with minimal longitudinal reinforcement content.

The shear lag effects were found to be reduced by uniformly distributing the reinforcement in the flange. The shear lag effects (expressed as the difference between plane section analysis estimates of moment and measured moment for a given steel strain) when loading in the direction of the web with the flange in tension were increased by 60% for displacement of up to 2.5 times the yield displacement when the flange of NTW1 was in tension as compared to NTW2.

The crack spacing and width was also reduced by the uniformly distributed reinforcement. The crack pattern observed for the flange of NTW1 and the webs of both NTW1 and NTW2 showed closely spaced and narrow flexural cracks in the region of the confined boundary elements while in the unconfined part, cracks were steeper, wider and their spacing was larger. For the flange of NTW2 detailed with uniformly distributed reinforcement, the cracks were closely spaced and narrow over the entire flange length.

## Chapter 2. Review on the seismic behaviour of U-shaped walls and modelling approaches

Despite the wider and the more inclined cracks in the unconfined concrete of the flange of NTW1 than for the flange of NTW2, [Bru09] concluded that the longitudinal reinforcement distribution had no significant influence on the magnitude of shear displacements. This is consistent with findings by [SW93]. However if one considers the measured deformation components of the two T-shaped walls for loading in the flange direction, for NTW1 the average shear displacements of the first storey in the inelastic range (drift  $\geq 1.5\%$ ) account for  $\sim 39\%$  of the total deformation of this story while for NTW2, they account for only  $\sim 27\%$  of the deformations of the first storey. This difference means an increase of  $\sim 44\%$  in the contribution of the shear displacements to the total deformation of the first storey. A similar difference can be computed for the contribution of the shear displacements in the second storey. Therefore based on these measurements, it can be concluded that uniformly distributing the reinforcement within the wall section does reduce the contribution of the shear deformation to the total deformation as compared to when the reinforcement is concentrated in the boundary elements. This conclusion is consistent with results from numerical studies on rectangular walls [SB<sup>+</sup>14].

In addition, previous research indicates that the wall failure modes can also depend on the distribution of the longitudinal reinforcement. Shear sliding failure or out-of-plane buckling of the boundary element seem to be favoured by the concentration of reinforcement in the boundary elements [PP92], [RA<sup>+</sup>14], [SB<sup>+</sup>14].

Based on these considerations it was decided to investigate the influence of the distribution of the longitudinal reinforcement distribution experimentally, through the test campaign performed within this study. Capturing of failure modes, especially involving out-of-plane behaviour, by means of numerical analyses is often challenging and hence experimental studies are necessary.

### 2.2 Modelling of U-shaped walls

Modelling approaches of different complexities have been developed by several research groups for the analysis of non-planar walls. According to their complexity, the modelling approaches for RC walls could be divided into three categories:

- Simplified models which are based on mechanical principles and/or empirical data
- Macro models which use a combination of different element types (e.g., beam elements, trusses, links, springs) to account for the different wall responses (e.g., flexural, axial, shear)
- Detailed finite element (FE) models with shell or solid elements

In the following, selected models from each category are compared in Section 2.2.1 with regard to their ability to capture key issues of the non-linear behaviour of U-shaped walls such as: wall strength, displacement capacity, the prediction of the different displacement components and capturing the distribution of shear forces between the web and two flanges.

In addition, previous studies where these models have been applied to non-planar walls are briefly discussed. From the models compared in Section 2.2.1, the plastic hinge model and its application to non-planar walls is discussed at length in a separate section (Section 2.2.2). Special emphasis is given to the plastic hinge model, which is one of the most popular simplified models used by design engineers because it is easy to use and provides reliable estimates of the displacement capacity.

For each of the models presented in Section 2.2.1 the displacement capacity is typically determined based on limits of reinforcement and concrete strains, which are associated with certain types of failure of reinforcement bars and concrete. The selection of appropriate strain limits is discussed in Section 2.2.3.

In addition, this section addresses the effective stiffness of RC walls which is typically used in linear seismic analyses to estimate the effective period of the RC building. The effective stiffness of RC walls, defined as the stiffness at first yield, is hence an important input parameter in seismic assessment, and for this reason state-of-the-art estimates are discussed in Section 2.2.4.

### 2.2.1 Modelling approaches for U-shaped walls

#### 2.2.1.1 Simplified models

Simplified models for RC walls are typically based on empirical data or on mechanical principles or a combination of both, e.g., plastic hinge models [PP87], [PCK07] or three-parameter kinematic theory model [MHB16]. One of the most popular simplified models is the plastic hinge model. This model is based on the idea that the force-displacement response of a RC wall that forms a flexural mechanism can be obtained from the moment-curvature relationship of the section subjected to the largest moment demand. While the shear force can be readily obtained by dividing the moment through the shear span  $H$ , determining the displacement from the curvature requires several assumptions.

The flexural displacement is computed as the sum of elastic and plastic displacements (Equation 2.1, where the elastic displacement is approximated with the yield displacement  $\Delta_y$  of the wall. The elastic curvatures, i.e., curvatures lower than yield curvature  $\phi_y$ , are assumed to follow a linear variation along the wall shear span. The plastic curvatures are assumed to be concentrated in a limited region called the equivalent plastic hinge length where their variation is considered constant [PP87] (Figure 2.3). The flexural displacements are then obtained by the integration of the assumed curvature profiles over the wall height (Equation 2.2 and Equation 2.3).

In the plastic hinge model, the displacements due to strain penetration into the foundation are typically included in the flexural displacements. This is done for the plastic flexural displacements through the inclusion of a strain penetration term in the plastic hinge length equation.

## Chapter 2. Review on the seismic behaviour of U-shaped walls and modelling approaches

The shear displacements  $\Delta_s$  can be added to the flexural ones, and they are accounted for through semi-empirical models that relate the shear and the total flexural deformations  $\Delta_f$ . The total displacement can then be written as in Equation 2.4.

$$\Delta = \Delta_y + \Delta_p \quad (2.1)$$

$$\Delta_y = \phi_y \frac{H^2}{3} \quad (2.2)$$

$$\Delta_{p,f} = \phi_p L_{ph} H \quad (2.3)$$

$$\Delta = \Delta_y + \Delta_{p,f} (1 + \Delta_s / \Delta_f) \quad (2.4)$$

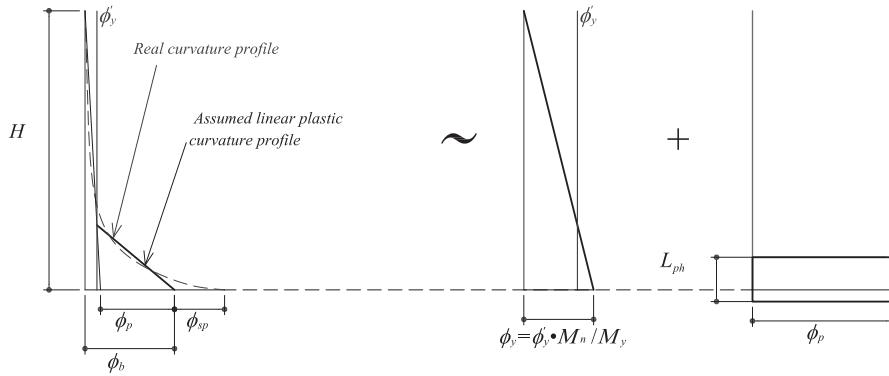


**Figure 2.3:** Linear approximations of the real curvature profile and assumptions for the plastic hinge model. The plastic hinge length  $L_{ph}$  includes the strain penetration length  $L_{ph}$ .

This section, presented briefly the concept of the plastic hinge model. A more detailed discussion of the quantities involved in the application this model and the assumptions behind them is given in Section 2.2.2. In the following, the application of the plastic hinge model to U-shaped walls and findings from this model are presented.

The plastic hinge model was applied by [BDP08a] to predict the behaviour of the two U-shaped walls tested at ETHZ (see Section 2.1.2 and [BDP08a]). Monotonic moment-curvature analyses were performed for each loading position (see Figure 2.2) using a zero-length element with a fibre section in the Opensees software [MMG09]. The behaviour of the reinforcement bars was modelled with the Giuffre-Menegotto-Pinto model [MP73]. Popovics' equation was used to model the concrete behaviour, while the confined concrete was modelled using with the Mander model [Pop73]. The strain limits for bar fracture after buckling and confined concrete crushing were defined using recommendations by [PCK07].

For the determination of the force-displacement curve, the yield displacement was computed using a modified equation accounting for a partially cracked wall at yield (i.e., elastic curvature profile was not linear over the wall height). Shear displacements were accounted for through the ratio of shear to flexural displacements  $\Delta_s/\Delta_f$  computed from according to a semi-empirical equation newly proposed by [BDP11].

The plane section analysis predicted well the moment capacities for the principal directions of loading. For the diagonal direction of loading the moment capacity was significantly overestimated as the full moment capacity was not reached for this direction of loading [BDP08a]. The overestimation of the moment capacity in the diagonal direction was assigned to the limitation of this simplified monotonic model in capturing the cyclic stiffness degradation under bidirectional loading. One other limitation of the moment-curvature analysis is that it cannot provide the distribution of the shear forces between the two flanges, leaving such critical decisions to the design engineer.

Predictions of the displacement capacity were done using a design and an assessment approach. With the design approach, predicted displacement capacities were smaller than those experimentally observed while with the assessment approach predictions were typically larger. However, the displacement capacities for the different loading directions could not be exactly verified since the walls failed only in one direction and experimental data was therefore limited. The inherent assumption of plane sections remaining plane which can differ significantly from the real response of the section of non-planar walls, is another limitation of the plastic hinge model.

### 2.2.1.2 Macro models

Macro modelling approaches refer within this study to models that use a combination of different types of elements such as beams, trusses, links or springs to model the different responses of a RC wall such as flexural, axial, shear or torsion. In the following, the most common macro models used for the modelling of RC walls are briefly discussed. These models are:

- Beam-column element models
- Wide-column models
- Truss models (or lattice models)
- Macro model with "wall element"

## **Chapter 2. Review on the seismic behaviour of U-shaped walls and modelling approaches**

### **Beam-column element model**

In beam-column element models the wall section is modelled by a single element. Important aspects for the characterisation of the different models are the formulation of the beam element used and the discretisation choices, e.g., number of elements over the wall height. The choice of the element formulation can influence the required element discretisation and the required number of integration points per element.

Two types of beam elements can be distinguished according to their formulation: displacement-based and force-based elements. In displacement-based elements, the displacement field is imposed, with forces computed based on energy balance considerations while in the force-based elements, the force field is imposed with element displacements obtained by work equivalence balance [CAP10]. For displacement-based elements, the curvature is often assumed to vary linearly over the element height, while for force-based elements the moment varies linearly over the wall height. Hence, several displacement-based elements over the height are required for the realistic modelling of a wall, while a single force-based element can be used for this task. However, the displacement-based elements are significantly more popular in practice. For a detailed discussion on the advantages and drawbacks of each of the two formulations the reader is referred to [CAP10] and [ATB16].

In order to model the wall behaviour, the beam elements allow the distribution of plasticity over the element height and are assigned a fibre-section that implicitly captures the axial-flexural interaction. With beam element models, the shear displacements are generally either neglected or modelled as linear elastic displacement components. The shear behaviour is hence decoupled from the axial and flexural one. The same applies to the torsional behaviour. Incorporating the axial-flexure-shear-torsion interaction for beam elements is an active research topic which most often concentrates on passing from Euler-Bernoulli beam theory to higher order beam theories [CAP15]. The effect of strain penetration can be modelled by introducing a zero-length rotational spring at the wall base.

To assess the displacement capacity of beam-column element models, numerical strains at integration points are compared to ultimate limit strains. However, the post-peak strains obtained at the integration points are sensitive to the discretisation and the type of element formulation. The length of the element where inelastic strains concentrate has a major impact on the numerically obtained strains. For this reason, this element is typically assigned a length related to the expected physical spread of plasticity. The equivalent plastic hinge length is often used as first approximation [ATB16].

The material models used with fiber sections are typically one-dimensional and thus relatively simple and straightforward to use. However, concrete behaviour such as confinement or lateral expansion cannot be directly modelled, and are accounted for in a simplified manner.



## 2.2. Modelling of U-shaped walls

---

While the behaviour of planar RC walls can be relatively well approximated by beam-column models, for non-planar walls, a fibre section cannot yield the distribution of shear forces between the different wall flanges and web. Beam-element models are often used for modelling walls within a building due to their reduced computational effort. However when modelling U-shaped walls that have an inherent torsional resistance, the designer needs to decide on the in-plane position of the beam element model representing the wall. The element can be placed for example at the centroid of the wall section or at the shear centre of the elastic section. [RF01] recommends to place the beam element model of the wall at the centroid of the wall section only if the torsional resistance of the wall is small.

[MK<sup>+</sup>06] and [Wau09] have modelled isolated non-planar walls subjected to bidirectional loading using beam-column element models. [MK<sup>+</sup>06] used a displacement-based beam element based on Timoshenko beam theory to model the U-shaped wall tested under bidirectional loading in Ispra [RF01] (see Section 2.1.1). To model the behaviour of concrete under cyclic loading a damage model with two damage variables, one for concrete in compression and one in tension, was used [LBMPC92]. Shear and torsion were modelled as linear and were decoupled from the axial and flexural behaviour. Global force-displacement results matched relatively well the experimental behaviour, but the displacement capacity or the local results were not evaluated.

[Wau09] used a force-based beam element implemented in Opensees software [MMG09] to model the T-shaped walls tested under complex bidirectional loading at the University of Minnesota [Bru09] (see Section 2.1.1). The T-shaped wall was modelled using force-based elements with fibre sections to model the axial-flexural behaviour and a zero-length element with stress-slip properties for the strain penetration. Additionally, a force-deformation shear model was aggregated at the section level to account for shear displacements, i.e., equivalent to having shear springs in parallel with the beam element. The force-deformation shear model was fitted with the experimental data. After accounting for the shear displacements, the model captured well the global force-displacement behaviour of the wall. However, the monotonic analyses significantly overestimated the peak moments for low and medium ductilities. This difference was attributed to the modelling of accumulated cyclic damage in steel and concrete [Wau09].

### Wide-column models

In the wide-column analogy, the non-planar walls are divided into the composing web and flange sections. Each web and flange section is represented by a vertical beam element located at the centroid of these sections. The beam elements are then connected through horizontal links, parallel to the weak axis of the sections, which connect in common nodes at the intersection between web and flange.

Wide-column models (WCM) with inelastic properties for U-shaped walls have been only briefly discussed by [RF01] and more thoroughly investigated by [BDP08d]. In the latter study, the two U-shaped walls from the ETHZ tests [BDP08b] have been modelled using the wide-column models. Following the set-up of the model based on existing recommendations, [BDP08d] performed sensitivity studies regarding the geometry of the WCM, the shear and torsional properties of the vertical elements as well as the properties of the horizontal links and updated the model based on their findings. The WCM described in the following and whose results are discussed herein refers to the updated model.

## **Chapter 2. Review on the seismic behaviour of U-shaped walls and modelling approaches**

The WCM was set-up in Opensees software [MMG09]. The three vertical elements corresponding to the web and the two flanges were modelled using nonlinear displacement-based beam elements with fibre-sections. A number of eight beam elements were used over the height of the wall below the collar and six over the height of the collar. The in-plane and the out-of-plane shear stiffness of the vertical elements as well as the torsional stiffness were decoupled from the flexural-axial behaviour. The in-plane and the out-of-plane shear stiffness were modelled via zero-length springs inserted at the connection between two beam elements. The in-plane shear stiffness was assigned a constant value, which corresponded to about half the maximum ductility reached by the test specimen. The out-of-plane shear stiffness was assigned a quarter of the in-plane stiffness while the torsional stiffness was set to zero since the torsion was mainly restrained at the wall top during experiments.

The horizontal links were placed every two vertical elements over the wall height. They were assigned a constant torsional flexibility in order to allow warping of the section. In addition, constant in-plane shear flexibility was assigned to the links to account for the deformations due to vertical shear stresses transmitted at the interface web-flange.

The WCM captured well the moment capacity of the wall under bidirectional loading. The in-plane shear flexibility assigned to the vertical elements was found to be of paramount importance in the prediction of the experimentally attained moment capacity. Previous WCM where the shear stiffness of the vertical elements was taken as equal to the shear stiffness of the elastic section significantly overestimated this moment capacity. Since it relies on beam elements, the displacement capacity of the wall requires assigning a suitable length to the element where inelastic strains concentrate.

The WCM is one of the simplest models for non-planar walls, which directly provide the distribution of the shear forces between the individual wall parts, i.e, web and each of the two flanges. It is relatively simple to set-up, requires reduced computational effort and hence it could be a good modelling option for non-planar walls with more complex geometries such as E-shaped walls or modelling of non-planar walls as part of buildings. The limitations of the model draw from the limitations of the beam elements: typically shear and torsional stiffness are assigned constant values and are not function of the axial strains, the flexural strains and the state of cracking as they are in reality. Thus the stiffness degradation during the loading history can be only approximated through the assigned shear and torsional properties but it is not truly captured.

### **Truss models**

Truss models (or lattice models) use a combination of beam and truss elements to model the behaviour of RC structural elements. Typically, the RC wall is divided into several rectangular panels over the height and length. Each panel is composed of vertical, horizontal and diagonal truss and beam elements connected together at the four nodes of the panel. The vertical elements are typically modelled using beam elements with fibre sections composed of concrete and steel fibres representing the longitudinal reinforcement bars. Horizontal elements are modelled by trusses which represent the concrete and steel behaviour in the horizontal direction. Truss elements are also used for the diagonals of the panels formed by the vertical and the horizontal elements to model the diagonal field of concrete.

## 2.2. Modelling of U-shaped walls

---

A 3D nonlinear beam-truss model was recently developed by [LP12] and [LP13] for modelling of non-planar RC walls, including a U-shaped wall tested under bidirectional loading which is discussed herein (TUB from ETHZ tests see Section 2.1 and [BDP08b]). The model used nonlinear force-based beam elements with fibre sections in the vertical direction, nonlinear truss elements in the in-plane horizontal directions and nonlinear truss elements in the diagonals of the panels. In addition, linear Euler-Bernoulli beam elements were used parallel to the truss elements in the horizontal direction, in order to model the out-of-plane bending stiffness of the segments of the wall. A particularity of this model was that the diagonal nonlinear truss elements used a biaxial concrete model that accounted for compression softening [VC86] and for the dependency of the post-peak concrete strains on the mesh size.

The model of the U-shaped wall was set-up in Opensees software [MMG09]. A number of ten beam-truss panels over the height were used for the model, and four additional panels for the collar where the loads were applied. The concrete model used for the vertical and the horizontal elements was based on Fuji model [HK<sup>+</sup>97] while the reinforcing steel was modelled using the Giuffre-Menegotto-Pinto model [MP73].

The moment capacity of the U-shaped wall in the diagonal direction was relatively well captured within 8% average difference. The displacement capacity was also well captured but only when mesh-size effects were accounted for. Without the mesh-size effects, failure of the wall due to crushing in the compression diagonals of the web was predicted for a lower drift than experimentally observed, i.e., 1.8% versus 3%.

The good predictions of the strength and displacement capacity, when mesh-size effects are considered, indicate that the model is promising for predicting the behaviour of U-shaped walls under bidirectional loading. The model requires moderate computational expense and relatively moderate effort to set-up. The model accounts only elastically for the out-of-plane bending, and it does not account for the degradation of the out-of-plane shear stiffness of the wall under bidirectional loading. The out-of-plane shear stiffness of the U-shaped walls might play a role in the transfer of shear forces from wall to foundation, especially for loading positions where the compression zones are limited.

### **Macro model with "wall element"**

A macro-element model [BDP08c] was set-up using the software PERFORM3D [Com06] and results have been compared with experimental data from tests in ETHZ. Two types of macro-elements were used, namely a "shear wall element" and a "general wall element". The "shear wall element" was composed of two layers: one layer accounted for axial and flexural behaviour while the other layer accounted for shear behaviour. The "general wall element" had three additional layers to the other two already mentioned. Two of the additional layers accounted for diagonal compression struts in each of the two diagonal directions and the last layer was a horizontal fibre layer.

## **Chapter 2. Review on the seismic behaviour of U-shaped walls and modelling approaches**

In both elements, the shear layer was assigned an elastic shear stiffness corresponding to the shear stiffness experimentally determined at medium displacement ductility. All other deformation modes were assigned elastic properties. Results for the "shear wall element" under cyclic loading were generally too stiff and the distribution of the in-plane shear forces between the two flanges was not captured very well. The "general wall element" showed good agreement with the experimental data [BDP08d]. The concept of "wall element" is rather similar to a truss panel as presented in the previous section, but this study was mentioned here to complete the review of the modelling studies on U-shaped walls.

### **2.2.1.3 Detailed FE models**

Detailed FE element models are the most refined of all modelling approaches and also the most demanding in terms of computational efforts. For this reason such models are often still limited to modelling isolated walls.

Shell finite elements are considerably simpler, less computationally expensive and therefore typically preferred to solid elements when modelling RC walls. If out-of-plane behaviour of the wall is judged to be important, shell elements with multi-layers and with more complex formulations can be used. Axial, flexure, shear and torsional behaviour as well as the interaction between them are directly accounted for. Two-dimensional or three-dimensional material laws are typically used with the shell element models.

The main drawbacks of these models are the large computational times and the need for post-processing of results to obtain the quantities needed in design. The complexities of the material models and of the element formulations can render the check and interpretation of the results sometimes difficult.

[IR05] modelled the U-shaped wall tested in Ispra under bidirectional loading using a 3D shell element model [PP<sup>+</sup>00b]. The concrete was modelled by means of multi-layered thin shell elements using plane-stress assumption, while the reinforcement was modelled with truss elements. The concrete was modelled using a biaxial fixed smeared crack approach discussed in [IR00]. The reinforcement bars were modeling using a cyclic model which accounted for Bauschinger effect and bar buckling.

A good match was achieved between the numerical and the experimental results, except for the last cycles characterised by strong strength degradation. Discrepancies in the last cycles were attributed to the limitation of the shell element via the plane-stress assumption in capturing concrete crushing and bar buckling, as well as disregarding the flexibility due to strain penetration in the model [IR05].

### 2.2.1.4 Summary of modelling approaches

The modelling approaches outlined in the previous sections were used to model the nonlinear behaviour of U-shaped walls. While the plastic hinge and the beam-column element models have their merits concerning their simplicity and ease of use for design engineers, they require further developments so they can correctly model U-shaped walls under any direction of loading. It should be pointed out that even if more accurate results are obtained such models several limitations cannot be overcome.

More specifically, for the design of U-shaped walls it is important to know how the forces are distributed between by the wall parts—a result that cannot be obtained directly from plastic hinge analysis or beam-column element models. The wide-column model with inelastic properties constitutes an improvement in this direction as it can directly yield the quantities needed in design. The results obtained so far with this model are promising but further validation against experimental data and other detailed models are required.

The truss models have shown promising results in capturing the behaviour of U-shaped walls. The displacement capacity was also well predicted as long as mesh-size effects were considered. In general, except the plastic hinge model, determining the displacement capacity of any of the models reliably requires either accounting for mesh-size effects or using measures that account for the spread of inelastic strains over the element height, e.g., average rotation over the height where plasticity spreads.

Inelastic shell element models are more and more applied in engineering practice. They require considerable time to set-up and expertise in numerical modelling. However, such models can offer detailed local information and as such an insight in the complex behaviour of the core walls. Moreover, these models take directly the interaction between axial force, shear and flexure into account. This is why Chapter 5 of this report describes the setting up and validation of a shell element model which will be used for investigating particular aspects of the U-shaped wall behaviour as well as for performing parametric studies in Chapter 6.

### 2.2.2 Estimates of quantities for plastic hinge model

The concept of the plastic hinge model was briefly discussed in Section 2.2.1. This section presents the state-of-the-art estimates for the different quantities involved in the application of the plastic hinge model.

For design purposes bi-linear approximations of the moment-curvature and the corresponding force-deformation response are typically used [PCK07] (Figure 2.4). This idealisation consists of an initial "elastic" branch and a post-yield "plastic" branch. The "elastic" branch is limited by the yield curvature  $\phi_y$  in the moment-curvature response and by the yield displacement  $\Delta_y$  in the force-deformation response. The "plastic" branch is bounded by the yield point and the ultimate point defined by the ultimate curvature  $\phi_u$  or by the ultimate displacement  $\Delta_u$ . Therefore characterising the bi-linear force-deformation response requires knowledge of  $\Delta_y$  and  $\Delta_u$ , which depend on  $\phi_y$  and  $\phi_u$ .

## Chapter 2. Review on the seismic behaviour of U-shaped walls and modelling approaches

Additional quantities necessary for computing the deformation response are: the shear displacements, the plastic hinge length and the strain penetration length  $L_{sp}$  typically included in  $L_{ph}$ . All these quantities are discussed in the following, except  $\phi_u$  which is determined from the ultimate strain limits discussed in Section 2.2.3.

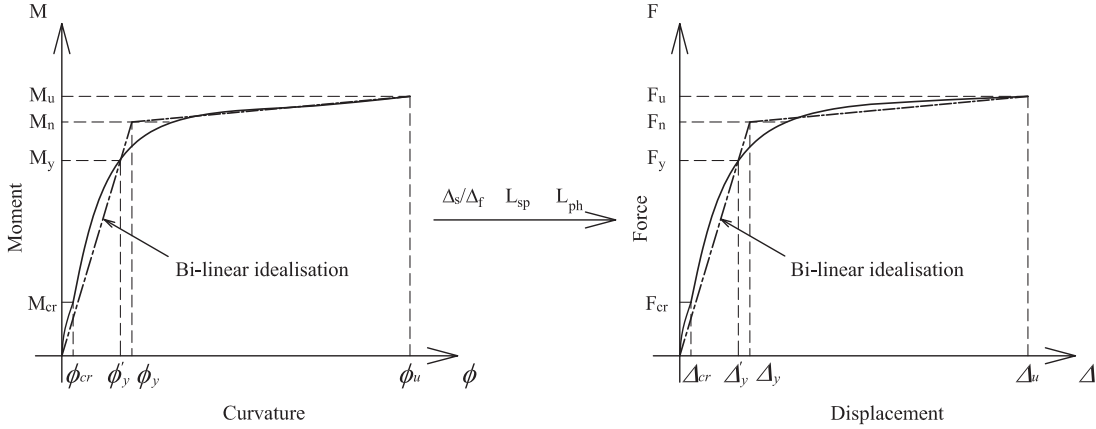


**Figure 2.4:** Plastic hinge analysis - obtaining the force-displacement response from the moment-curvature response by means of several quantities: shear to flexural deformation ratio  $\Delta_s/\Delta_f$ , strain penetration length  $L_{sp}$  and plastic hinge length  $L_{ph}$

### 2.2.2.1 Yield curvature

The nominal yield curvature is computed as in Equation 2.5 where the first yield curvature  $\phi'_y$ , the first yield moment  $M_y$  and the nominal moment  $M_n$  are determined from section analysis. Typically these quantities are computed as follows based on recommendations by [PCK07]. The first yield corresponds to the instant when the most tensioned reinforcement bar reaches its yield strain  $\epsilon_{sy}$  or when the most compressed concrete fibre reaches a compression strain of  $\epsilon_c = 0.002$ . The nominal moment  $M_n$  is determined at the serviceability limit strains (i.e., strains corresponding to residual crack widths of  $\sim 1$  mm and to the onset of concrete spalling) defined as tensile reinforcement strains of  $\epsilon_s = 0.015$  or compressive concrete strains of  $\epsilon_c = 0.004$ .

$$\phi_y = \phi'_y \frac{M_n}{M_y} \quad (2.5)$$

The yield curvature is considered to depend, for design purposes, only on the wall sectional geometry and the  $\epsilon_{sy}$  of the most tensioned reinforcement bar [PSC96]. The yield curvature can therefore be written as in Equation 2.6 [PSC96] where  $K_y$  is the dimensionless yield curvature and  $l_{wall}$  is the length (depth) of the wall.

$$\phi_y = K_y \frac{\epsilon_{sy}}{l_{wall}} \quad (2.6)$$

## 2.2. Modelling of U-shaped walls

The dimensionless yield curvature  $K_y$  was found to depend on the geometry of the wall section, the loading direction for non-planar walls, the distribution of the longitudinal reinforcement within the section and to a lesser extent on the longitudinal reinforcement content. Several researchers have derived, based on parametric sectional analysis, expressions for the  $K_y$  value for different wall shapes other than rectangular. The emphasis was placed on I-shaped or T-shaped section walls for bending along the principal directions of the sections [Pau02],[PCK07],[SS<sup>+</sup>13]. The U-shaped section walls have not been addressed directly but estimates from the I- or T-shaped walls can be used as approximations also for the principal directions of the sections of the U-shaped walls.

[BDP08b] used such estimates from [Pau02] to compare with experimental results from two U-shaped walls and found the agreement rather good. The 2012 DBD Model Code [SPC12] recommends for U-shaped/ C-shaped walls the same values as those proposed by [Pau02] but mentions that there are still uncertainties related to the simplified value of  $K_y$  for U-shaped walls and recommends performing moment-curvature analyses to verify these design values. The estimates for the different wall shapes are summarised in Table 2.2 and it is indicated how they can be used as approximations for the U-shaped walls.

**Table 2.2:** Estimates for dimensionless yield curvature  $K_y$  of RC walls

Row No.	Cross-section shape	Loading position	[Pau02]	[PCK07]	[SS <sup>+</sup> 13]	[SPC12]
1	Rectangular - concentrated reinforcement	-	1.85	1.80	-	1.85
2	Rectangular - distributed reinforcement	-	2.15	2.00	-	2.15
3	T-shaped	Parallel to web, flange in compression	1.50	1.40	1.80	1.40
4	T-shaped	Parallel to web, flange in tension	2.00	1.80	2.15	1.80
5	U-shaped	Parallel to web, one flange in tension	use values row 3			1.80
6	U-shaped	Parallel to flanges, web in tension	use values row 4			1.80
7	U-shaped	Parallel to flanges, web in compression	use values row 3			1.40

## Chapter 2. Review on the seismic behaviour of U-shaped walls and modelling approaches

Estimates by [PCK07] are  $\sim 10\%$  higher than those by [Pau02], which they attributed to the reinforcement strain hardening effect which was not considered in the analyses by [Pau02]. Estimates by [SS<sup>+</sup>13] for T-shaped walls presented in Table 2.2 in their simplified form, are in their extended form (Equation 2.7) the most complex, accounting for the longitudinal reinforcement distribution (i.e., uniformly distributed over the wall length or concentrated toward the boundary elements), the web length to flange length ratio  $A$  and the total wall longitudinal reinforcement percentage  $\rho_l$ . In Equation 2.7  $k$  varies between 1.8 and 2.0 while  $x, y$  and  $\lambda$  are variables depending on the reinforcement distribution and loading direction: flange in tension or flange in compression.

$$K_y = k + xA + y(\rho_l - \lambda) \quad (2.7)$$

The approximations of these estimates are compared to the new experimental data for U-shaped walls in Section 4.3. Note that there are currently no estimates for other loading directions than the principal ones. [BDP08b] found from comparison with two U-shaped wall tests that the sectional analysis can be used to derive the yield curvatures also for the diagonal loading directions.

### 2.2.2.2 Yield displacement

For design purposes the yield displacement is determined assuming a linear curvature profile over the wall height  $H$  which implies a fully cracked wall over the height and hence a constant wall stiffness. The yield displacement can be therefore estimated accounting also for the equivalent strain penetration length at yield  $L_{y,sp}$  [HRS04], [PCK07]:

$$\Delta_y = \phi_y \frac{(H + L_{y,sp})^2}{3} \quad (2.8)$$

[HRS04] and [PCK07] propose to determine the the first yield displacement  $\Delta'_y$  and hence also the nominal yield displacement  $\Delta_y$  by accounting for the elastic shear displacements  $\Delta_s$  and for the flexural displacements due to pre-yield strain penetration, which they found to account for a significant part of the pre-yield deformations. [BDP08b] further refined the approach by accounting for a partially cracked profile at first yield. The yield displacement could be hence evaluated as in Equation 2.9 where  $k_{cr}$  is a factor accounting for the extent of cracking over the wall height at first yield.

$$\Delta_y = \phi'_y \frac{M_n}{M_y} \left( \frac{k_{cr}}{3} H^2 + L_{y,sp} H \right) \left( 1 + \frac{\Delta_s}{\Delta_f} \right) \quad (2.9)$$

### 2.2.2.3 Plastic hinge length

State-of-the-art plastic hinge length equations for walls are reviewed in this section. Only plastic hinge lengths specifically addressing walls [BA11], [Kaz13] as well as the on of the most widely used plastic hinge length equations [PCK07] are discussed here.



## 2.2. Modelling of U-shaped walls

The plastic hinge length  $L_{ph}$  of walls is a measure of the spread of plastic strains and curvatures over the wall height. The spread of plastic strains over the wall height are the result of three phenomena [PP87]:

- moment gradient  $M_u/M_y$  and reinforcement strain hardening  $f_u/f_y$
- tension shift effects due to inclined flexure-shear cracking
- strain penetration into the foundation

One of the most well-known equation for the plastic hinge length of the walls is based on the work of Priestley, Paulay, Park and co-workers and it accounts for the sum of contributions of the three above listed phenomena. The plastic hinge length is expressed under the form of Equation 2.10 [PP87], where the term related to the wall effective height  $H$  accounts for moment gradient and strain hardening effects, the term related to the wall length  $l_{wall}$  accounts for the tension shift due to inclined shear-cracking while the term related to the longitudinal bar diameter  $d_b$  accounts for the strain penetration into the foundation.

$$L_{ph} = C_1H + C_2l_{wall} + C_3d_b \quad (2.10)$$

The coefficients of the Equation 2.10 have been expressed by [PP92] resulting in Equation 2.11. In this equation the spread of plasticity due strain hardening is directly addressed through the reinforcement properties  $k = 0.2(f_u/f_y - 1)$ . The spread of plasticity due to tension shift effects is taken as  $0.2l_{wall}$  considered as a suitable value for assessment purposes of the displacement capacity of RC walls. The equation is lower bounded by twice the strain penetration length  $L_{sp} = 0.022f_yd_b$ .

$$L_{ph} = \min(0.08, k)H + 0.2l_{wall} + 0.022f_yd_b \geq 2L_{sp} \quad (2.11)$$

Equation 2.11 has been later modified by [PCK07] for design purposes. The tension shift term was reduced to  $0.1l_w$  to introduce some degree of conservatism when determining the displacement capacity.

$$L_{ph} = \min(0.08, k)H + 0.1l_{wall} + 0.022f_yd_b \geq 2L_{sp} \quad (2.12)$$

The above  $L_{ph}$  equations are intended to be used for determining the ultimate displacement capacity of the wall as in Equation 2.4. For this purpose,  $L_{ph}$  estimates are usually combined with ultimate curvature from section analysis corresponding to different ultimate states (see Section 2.2.3).

## Chapter 2. Review on the seismic behaviour of U-shaped walls and modelling approaches

In the determination of  $L_{ph}$ , it was assumed that the center of the plastic hinge with the length  $L_{ph}$  is at the base of the wall. This is strictly true if  $L_{ph}$  is exactly twice the strain penetration term  $0.022f_yd_b$ . If strain penetration effects are negligible the centre of the plastic hinge will be located at the middle of the plastic hinge length. Computing the wall displacement, using one assumption or the other was found to lead to differences of  $\sim 10\%$  in the displacement capacity [Han13].

Recent research on the plastic hinge length of RC walls have focused on determining the  $L_{ph}$  values from numerical studies using detailed nonlinear finite element models validated against experimental data. [BA11] present the setting-up of a shell element model with VecTor2 software [WV02]. The model was validated with experimental data from a test conducted by one of the authors, in terms of global force-displacement behaviour, as well as in terms of curvature profiles over the wall height and strain profiles along the wall length at different drift levels. Then a parametric study was performed on cantilever walls to investigate the influence of shear on the  $L_{ph}$ . The  $L_{ph}$  value was determined as half of the height over which plasticity spreads, i.e., half of the height of the plastic zone  $L_{pz}$ . This choice was the result of the observation of the authors that inelastic curvatures vary linearly over  $L_{pz}$ .

The authors found that shear has a significant influence on  $L_{ph}$  especially for squat walls after onset of diagonal cracking. However, they concluded that it is not necessary to include the shear stress in the formulation of  $L_{ph}$  as long as the wall length  $l_{wall}$  and the shear span  $H$  are accounted for (Equation 4.25). The increase in axial load ratio  $N/(A_g f_c)$  was found to reduce the plastic hinge length of walls. This effect was attributed to the decreasing  $M_u/M_y$  ratio with increasing axial force.

$$L_{ph} = (0.05H + 0.2l_{wall}) \left(1 - 1.5 \frac{N}{A_g f_c}\right) \leq 0.8l_{wall} \quad (2.13)$$

The above plastic hinge length was determined at 2% global drift at the shear span of the walls. Unlike the previously discussed equations, [BA11] did not determine  $L_{ph}$  to match a displacement value but used the real spread of plasticity over the wall height. The results were interpreted as a lower bound estimate of the plastic hinge length of walls however the displacement estimates obtained with this  $L_{ph}$  value were not evaluated. No assumption was made for the centre of rotation of the plastic hinge but based on the linear assumption of the inelastic curvature profile and since strain penetration was not considered, the center is located exactly  $1/3L_{pz} = 2/3L_{ph}$  from the wall base.

In another numerical study conducted by [Kaz13], the RC walls were modelled by means of detailed FE model using ANSYS<sup>®</sup> software. The lower two stories of the wall, where inelastic strains were considered to be concentrated, were modelled using solid elements while the upper stories were modelled using Timoshenko beam elements to reduce computation time. In order to account for the influence of the floor-slabs on the shear flow in the wall, horizontal flanges were modelled at floor level for the two lower stories. The foundation was also modelled to account for the strain penetration.

The study investigated the influence of the wall length  $l_{wall}$ , the wall shear span  $H$ , the axial load ratio  $N/(A_g f_c)$ , the horizontal reinforcement ratio in the web  $\rho_{sh}$  and longitudinal reinforcement ratio in the boundary elements  $\rho_{bl}$ . The  $L_{ph}$  value corresponding to the wall displacement capacity was back-calculated from the top displacement (Equations 2.3 and Equation 2.4 without the shear displacement factor). The shear displacements were not differentiated from the flexural ones in this calculation while displacement due to strain penetration were found to be negligible and were hence not considered. Using regression analysis, Equation 4.26 was derived for  $L_{ph}$ . The obtained  $L_{ph}$  equation is intended to be used for the displacement capacity of the wall at the ultimate damage state.

$$L_{ph} = 0.27 l_{wall} \left(1 - \frac{N}{A_g f_c}\right) \left(1 - \frac{f_{yh}}{f_c}\right) (H/l_{wall})^{0.45} \quad (2.14)$$

Plastic hinge length estimates according to [PCK07] have been compared with experimental results of only two U-shaped walls [BDP08b]. In Section 4.5.2, the presented estimates will be compared with additional experimental data to conclude on their suitability for capturing the  $L_{ph}$  values for U-shaped walls for different loading directions.

### 2.2.2.4 Shear displacements

Shear displacements account for a significant portion of the total deformation of RC walls, even for relatively slender walls. For non-planar walls shear displacements are particularly large for wall parts which are in tension [BDP08b], [ZL14] and can vary with the loading direction [BDP08b]. Therefore they should be explicitly included in the modelling of non-planar RC walls.

Several modelling approaches for estimating the shear displacements of RC walls have been proposed in the framework of plastic hinge analysis [PCK07], [HRS04], [BDP11], [Han13]. Such estimates can also be used for deriving a shear stiffness value for modeling approaches where this stiffness is assigned a constant value, e.g., beam-element models or WCM. According to these estimates the main parameters influencing the magnitude of the shear displacements of RC walls are: (1) the level of axial strain on the section, (2) the cracking angle in the plastic region and (3) the shear stress demand to capacity ratio.

Shear displacements are typically expressed as a function of the flexural displacement since the ratio of shear to flexural displacements  $\Delta_s/\Delta_f$  was found to be roughly constant in the inelastic range for RC walls with non-degrading shear mechanism, i.e., flexure controlled walls [Daz00], [HRS04], [BDP11]. State-of-the-art estimates for  $\Delta_s/\Delta_f$  ratios are discussed in the following.

## Chapter 2. Review on the seismic behaviour of U-shaped walls and modelling approaches

[HRS04] derived an estimate for the  $\Delta_s/\Delta_f$  ratio (Equation 2.15a) based on the assumptions that: (1) shear to flexural displacement ratios remain constant over the inelastic range for non-degrading shear mechanisms, (2) shear deformations stem from the horizontal deformations occurring in shear cracks and (3) shear deformations concentrate between the lowest inclined crack (crack angle  $60^\circ$ ) and the highest crack which reaches the base with the  $\theta_{max}$  angle. About 35% of the total wall flexural deformations were found to be concentrated in between these two cracks based on comparison with experimental data. Hence the 0.35 term in the Equation 2.15a. The correction factor  $\alpha$  (Equation 2.15b) accounting for the shear demand to diagonal tension capacity  $V/V_n$  or shear demand to web crushing capacity  $V/V_{wc}$  was introduced to account for RC walls with low shear reinforcement content in the web or reduced web thickness for which shear displacements would have been otherwise underestimated.

$$\frac{\Delta_s}{\Delta_f} = \alpha 0.35 (1.6 - 0.2\theta_{max}) \frac{l_{wall}}{H} \quad (2.15a)$$

$$1 \leq \alpha = \left( \frac{V}{V_n} + \frac{V}{V_{wc}} \right) \leq 2 \quad (2.15b)$$

[BDP11] based their estimate on the assumptions that: (1) shear to flexural displacement ratios remain constant over the inelastic range for non-degrading shear mechanisms, (2) significant shear deformations occur only in the plastic hinge, where curvature is assumed constant and (3) strain state in the plastic hinge is homogeneous. [BDP11] used Mohr circle to describe the state of strain in the plastic region. By making the assumption that the principal compressive strain and the transversal strain are small (i.e., not a degrading shear mechanism) the shear strains were computed only as a function of the mean axial strain of the section  $\epsilon_m$ . Equation 2.16 was hence derived, considering that shear strains concentrate in the plastic hinge region over which they are constant and that the flexural displacement can be computed with a plastic hinge mechanism.

$$\frac{\Delta_s}{\Delta_f} = 1.5 \frac{\epsilon_m}{\phi \tan \theta} \frac{1}{H} \quad (2.16)$$

In the above equation,  $\phi$  is the constant curvature in the plastic hinge,  $\theta$  is the crack angle at the top of the fan-like pattern where cracks begin to be parallel and 1.5 is an empirical correction factor calibrated against test data on planar and non-planar walls.

In the application of both the previous models, it is necessary to determine the shear crack angle. Several shear crack angle estimates can be used for this task (e.g., [CM91], [BVC06]). [Han13] investigated the suitability of several crack angle estimates and proposed to use the approach by [HHF11] based on comparison with experimental data from seven RC rectangular bridge piers. This approach is based on elastic strain energy derivations and expresses the crack angle as a function of longitudinal and transversal reinforcement contents  $\rho_l$  and  $\rho_h$  respectively (Equation 2.17). In addition, the ratio between the elastic modulus of steel  $E_s$  and concrete  $E_c$  enters in the equation  $k_E = E_s/E_c$ . The angle  $\theta$  in Equation 2.17 is the crack angle relative to the longitudinal axis of the wall.

$$\tan\theta = \sqrt{\frac{\rho_h + k_E\rho_l\rho_h}{\rho_l + k_E\rho_l\rho_h}} \quad (2.17)$$

In addition, [Han13] presented a conceptual approach for determining the shear displacements based on the assumptions that: (1) shear displacements stem from rotation in shear cracks as in [HRS04] model and (2) shear displacements do not concentrate in the plastic hinge but have a linear or constant distribution over the wall height (assumption based on the experimentally observed shear strain profiles). [Han13] proposed an analytical solution for computing the shear displacement of an RC wall based on the kinematics of an idealised crack pattern (Equation 2.18). The magnitude of the shear displacements  $\Delta_s$  depends on the wall height over which cracking occurs  $H_{cr}$  and which is assumed to yield shear displacements. In addition,  $\Delta_s$  depends on the axial strain on the wall section  $\varepsilon_l(y_1)$  which varies with the wall height ( $y_1$  is the vertical coordinate). Therefore, in order to apply this approach it is necessary to estimate the height over which cracking extends  $H_{cr}$  and the distribution of the axial strain  $\varepsilon_l$  over the wall height. The model has not been validated against an experimental database but the concept seems promising.

$$\Delta_s = \frac{1}{2} \int_0^{H_{cr}} \frac{1}{0.5l_w} \int_{0.5y}^{0.5l_{cr}} \varepsilon_l(y_1) dy_1 dy \quad (2.18)$$

### 2.2.3 Ultimate limit strains

Peak strain values at the critical section of a structural element are a good indicator of the damage state of the element. Strains corresponding to ultimate damage states can hence be used to determine the displacement capacity of an element. In plastic hinge models, this is done by linking the ultimate strain to the displacement capacity via the curvature and the plastic hinge length. For capacity designed ductile walls the ultimate damage states typically accounted for are: (1) reinforcement bar fracture after previous buckling and (2) concrete crushing in the confined boundary elements of the wall.

For the reinforcement bar fracture after buckling limit state, [PCK07] recommend to account for the effects cyclic loading by reducing the ultimate steel strain under monotonic loading  $\varepsilon_{su}$  by a factor of 0.6. The steel tensile strain capacity under cyclic loading is affected by the compression strains under the reverse loading cycles and by the effects of buckling. [Res93] found that a limit on the total strain excursion  $\varepsilon_s - \varepsilon_c$  was better suited for determining the bar fracture after buckling. However such a limit is more difficult to apply to monotonic analyses.

## Chapter 2. Review on the seismic behaviour of U-shaped walls and modelling approaches

[PCK07] recommend a limit concrete strain for section analysis to account for confined concrete crushing limit state based on the model by [MPP88]. The ultimate compression state is assumed to be reached when the confining reinforcement fractures. Therefore Equation 2.19 of the concrete limit strain was derived by equating the strain energy absorbed by the concrete, above the value corresponding to the unconfined concrete to strain energy absorbed by the confinement. In the equation below,  $\rho_v$  is the volumetric ratio of the confinement reinforcement,  $f_{cc}$  is the confined concrete strength based on [MPP88] and  $f_{yv}$  the yield strength of the confinement reinforcement. The coefficients  $C_1$  and  $C_2$  depend on the stress-strain relationships of steel and concrete. An average value of the  $C_2/C_1$  ratio is 1.4.

$$\varepsilon_{cu} = 0.004 + \frac{C_2 \rho_v f_{yv} \varepsilon_{su}}{C_1 f_{cc}} = 0.004 + 1.4 \frac{\rho_v f_{yv} \varepsilon_{su}}{f_{cc}} \quad (2.19)$$

Another limit state that can be of particular interest for non-planar walls is the out-of-plane buckling of the wall. This ultimate limit state is assumed to be controlled by the maximum tensile strain [PP93], [CE99]. Under cyclic loading the edges of the wall are subjected to large tensile strains resulting in large cracks where the reinforcement bars yield. During the reverse cycle, when the wall edge is in compression, the compression resultant force not be applied eccentrically due to irregularities in the material and geometry of the wall, causing the out-of-plane buckling [PG85]. For non-planar walls, certain loading directions can impose in addition to large tensile strains at the wall edges also out-of-plane displacements at the wall top which could speed up the triggering of the out-of-plane buckling, e.g., the flange ends of U-shaped walls when loading in the diagonal direction (positions E-F Figure 2.2).

To prevent the out-of-plane buckling of walls, equations have been developed to estimate the minimum wall thickness [PP93], [CE99]. If the wall thickness is known, one can back-calculate the tensile strain triggering the out-of-plane buckling. Both models for walls were developed based on experimental tests on RC columns with pinned-pinned boundary conditions. While Equation 2.20 by [PP93] can be used for walls with both one layer and two layers of longitudinal reinforcement, Equation 2.21 by [CE99] applies only for the latter case. In the two equations,  $l_0$  can be taken as the plastic hinge length,  $\beta = 0.8$  for two-layer reinforcement and  $\xi_c$  is computed as in Equation 2.22 where  $m = \rho_b f_y / f_c$  is the mechanical reinforcement ratio of the boundary element.

$$\varepsilon_{sm} = 8\beta \left(\frac{t_{wall}}{l_0}\right)^2 \xi_c \quad (2.20)$$

$$\varepsilon_{sm} = \frac{\pi^2}{2} \left(\frac{t_{wall}}{l_0}\right)^2 \xi_c + 3\varepsilon_{sy} \quad (2.21)$$

$$\xi_c = 0.5(1 + 2.35m - \sqrt{(5.53m^2 + 4.70m)}) \quad (2.22)$$

The presented strain limits will be compared with the experimental results from U-shaped walls in Section 4.6. In plastic hinge analysis, ultimate limit strains are used with moment-section analysis to determine the ultimate curvature of the critical section. Therefore Section 4.6 will also evaluate the validity of the plane section assumption for U-shaped walls for the different loading directions, i.e., if the definition of curvature can still be used for such walls at ultimate damage state.

### 2.2.4 Effective stiffness of RC walls

The effective stiffness of RC walls is an important quantity in seismic design as it is typically used to estimate the effective period of an RC building in linear seismic analyses. The structural elements are assigned an effective stiffness typically equal to the elastic section stiffness multiplied by a reduction factor. For RC walls, this reduction factor accounts for the increased flexibility of the wall due to concrete flexural and shear cracking as well as due to anchorage (pull-out) deformations at the base of the wall.

Several equations are available in the literature for estimating the effective stiffness of RC walls (e.g., [PP92], [FB00] or [AIB07]). Most of these models account for the slender walls only for the flexural stiffness. The effective stiffness values are typically accounted for by providing estimates of the effective moment of inertia  $I_e$  or of the ratio of the effective moment to the gross moment of inertia  $I_e/I_g$ , while assuming a constant wall stiffness over the height. The main parameters found to influence the effective stiffness of RC walls are: the reinforcement yield strength  $f_y$ , the axial load ratio  $N/f_c A_g$  and the wall geometry, i.e., wall length  $l_{wall}$  or wall thickness  $t_{wall}$ . In the following, the main equations used for estimating the effective wall stiffness are briefly presented.

[PP92] recommends an effective stiffness value for slender RC walls expressed through the  $I_e$  value as in Equation 2.23a. The equation is based on an analytical study on reinforced masonry shear walls by [PH89] and corresponds to the secant stiffness of the wall at first yield of the most tensioned reinforcement bar. For less slender walls, i.e. aspect ratio  $H/l_{wall} \leq 4$ , where the shear displacements can become important, Equation 2.23b is proposed. The equation accounts for the shear displacements and makes some allowance for the anchorage deformations, i.e., strain penetration [PP92].

$$I_e = \left( \frac{100}{f_y} + \frac{N}{f_c A_g} \right) I_g \quad (2.23a)$$

$$I_w = \frac{I_e}{1.2 + F} \quad (2.23b)$$

$$F = \frac{30I_e}{H^2 l_{wall} t_{wall}} \quad (2.23c)$$

## Chapter 2. Review on the seismic behaviour of U-shaped walls and modelling approaches

[FB00] proposed Equation 4.40 to estimate the effective stiffness of slender RC walls. The equation is based on a parametric study using plane section analysis on slender rectangular walls with uniformly distributed reinforcement. The effective stiffness was defined as the secant stiffness at first yield of the most tensioned reinforcement bar. The shear displacements were neglected while the axial load was considered to be constant over the height. In addition, tension stiffening of the concrete was accounted for. The study was criticised by [FB02] for assuming a constant axial load over the wall height, for accounting for the tension stiffening of concrete and for ignoring the flexibility due to strain penetration. In multi-storey buildings the axial load varies along the wall height resulting in an increase of the cracking height and hence a reduction of the flexural stiffness [FB02].

$$I_e = 0.267 \left( 1 + 4.4 \frac{N}{f_c A_g} \right) \left( 0.62 + \frac{190}{f_y} \right) (0.76 + 0.005 f_c) I_g \quad (2.24)$$

An estimate for the flexural effective stiffness of high-rise shear walls was developed by [AIB07] based on a trilinear bending moment-curvature model calibrated with results from one experimental test on a slender wall. In order to account for the different degrees of cracking in the wall, i.e., lightly cracked or severely cracked due to cyclic loading, [AIB07] suggested two simplified equations as upper-bound and lower-bound estimates for the effective flexural stiffness of high-rise core walls (Equation 4.41a).

$$I_e = \left( 0.6 + \frac{N}{f_c A_g} \right) I_g \leq I_g \quad (2.25a)$$

$$I_e = \left( 0.2 + 2.5 \frac{N}{f_c A_g} \right) \leq 0.71 I_g \quad (2.25b)$$

Instead of using an estimate for the  $I_e$  or the  $I_e/I_g$  value, a more precise effective stiffness value can be determined by dividing the wall nominal strength  $F_n = M_n/H$  by the yield displacement  $\Delta_y$  [PCK07]. While the nominal strength can typically be determined by means of plane section analysis, the determination of the yield displacement is more complex. It requires knowledge of the yield curvature and assumptions on the curvature distribution over the height at yield, on the shear displacements at yield and on the strain penetration also at yield. Typically the yield displacement is taken as equal to the flexural displacement assuming a fully cracked wall over the height (linear curvature distribution) with the base curvature equal to yield curvature [PCK07]. A linear curvature profile will overestimate however the flexural yield displacement and the difference is partially assigned to shear displacements and flexural displacements due to strain penetration [PCK07].



## **2.2. Modelling of U-shaped walls**

---

Since most of these estimates consider only the flexural flexibility it is expected that the predicted effective stiffness values tend to be on the high side, since shear displacements have been shown to constitute a significant part of the total deformation of U-shaped wall for certain loading positions. Since both the contribution of the shear displacements to the total deformation as well as the yield curvature depend on the different loading positions of U-shaped walls, it is expected that also the effective stiffness should vary with the loading position.

However, to the best of the author's knowledge, none of the here reviewed estimates been compared with experimental results from non-planar walls loaded in different directions. For this reason in Chapter 4, the effective stiffness estimates are compared with experimental results from four U-shaped walls tested for different loading directions.



# 3. Quasi-static tests of two U-shaped walls under diagonal loading

## 3.1 Introduction

This chapter is based on experimental work performed by the author under the supervision of the thesis director in the structural testing laboratory at EPFL. The content of this chapter has been previously published as a journal article [CB16] DOI 10.1016/j.engstruct.2015.10.018.

The experimental test campaign and findings from quasi-static cyclic tests on two half-scale U-shaped reinforced concrete (RC) walls performed at EPFL are presented in this chapter. The objective of the test programme was to investigate the U-shaped wall behaviour when loaded along the geometric diagonal of the U-shaped section. More specifically, the programme focused on identifying failure mechanisms specific to diagonal loading and possible critical design aspects related to these failure modes as well as particular phenomena that could explain the load transfer mechanisms between wall sections and wall and foundation for loading in the diagonal direction.

The experimental results of the new test campaign emphasising observed phenomena typical to U-shaped walls under diagonal loading are discussed within this chapter. The chapter is organized in several sections. The test units, the test set-up, the loading history and the instrumentation are presented in Section 3.2. Section 3.3 describes the failure mechanisms, the hysteretic behaviour as well as key deformation quantities that highlight the section deformation at the wall base, the out-of-plane bending of the flange end and the shear deformations of the wall sections. Section 3.4 gives a summary of the findings concluding with recommendations for analysis and design.

## 3.2 Test units, set-up, instrumentation and loading history

The test campaign is a continuation of the previous test campaign on U-shaped walls from ETH Zurich [BDP08b]. Therefore the overall geometry of the test units is the same and the test set-up is very similar as in the previous test campaign. The two test programmes differed only with regard to the reinforcement layouts of the walls, the instrumentation and the loading history.

## Chapter 3. Quasi-static tests of two U-shaped walls under diagonal loading

---

A detailed description of the design of the test set-up and of the test units can be found in [BDP08b] and is hence not repeated herein. Therefore the following sections discuss only briefly the geometry of the new test units including reinforcement layouts (Section 3.2.1), material properties (Section 3.2.2), test set-up and the instrumentation (Section 3.2.3) as well as the loading history (Section 3.2.4).

### 3.2.1 Geometry of the tests units

The two U-shaped walls tested as part of this project were half-scale models of the lower two storeys of a prototype elevator shaft and had the same dimensions as test unit TUB in [BDP08b]. Both test units, named TUC (Test Unit C) and TUD (Test Unit D) had identical longitudinal reinforcement layouts (Figure 3.1) but differed with regard to the applied axial load ratio and shear reinforcement: TUC was subjected to an axial load ratio of 0.06 and TUD to an axial load ratio of 0.15. The higher axial load ratio was applied to account for the effects of possible increase in axial force due to the shear force transferred by coupling beams. To account for the higher shear force demand of TUD, the shear reinforcement percentage was increased by  $\sim 25\%$  as compared with TUC. To maximise the amount of experimental information collected, it was decided to modify the reinforcement layout of TUB slightly and investigate also the influence of the longitudinal reinforcement distribution on the behaviour of the two wall flanges. Therefore, for both walls one flange was detailed with longitudinal reinforcement mainly concentrated in the boundary elements while in the other flange and the web the longitudinal reinforcement was uniformly distributed along the wall section. The reinforcement layout for the two test units is shown in Table 3.1. The longitudinal reinforcement content of the two flanges in the boundary elements and in the unconfined part is given for comparison in Table 3.1, together with the reinforcement contents of the web and the entire wall.

### 3.2.2 Material properties

The material properties of both test units are given in Table 3.2 and Table 3.3. The material tests were performed in accordance with the Swiss Norm SIA262/1 [SIA03]. The concrete tensile strength  $f_t$  was derived from double-punch tests [CY80]. Concrete properties from material tests are: concrete compressive strength  $f_c$ , concrete elastic modulus  $E_c$  and the concrete tensile strength  $f_t$  correspond to properties at the day of testing, except the  $f_c$  - 28days strength, which corresponds to the cylinder concrete compressive strength at 28 days.

The yield strength  $f_y$ , the ultimate strength  $f_u$  and the ultimate strain  $\varepsilon_{su}$  of the reinforcement bars are given in Table 3.3 and correspond to properties at the day of testing. Additionally, for the D12 bars, the hardening strain is given, which marks the end of the constant strength yield plateau and the beginning of increasing strength strain-hardening zone. With values of  $f_u/f_y$  between 1.18 and 1.26 and values of  $\varepsilon_{su}$  between 6.9% and 9.6%, the D8 and D12 bars belong to “Class C” grade according to Eurocode 8 [CEN03], while the D6 bars belong to “Class B” due to the strain value  $\varepsilon_{su}$  lower than 7.5%.

### 3.2. Test units, set-up, instrumentation and loading history

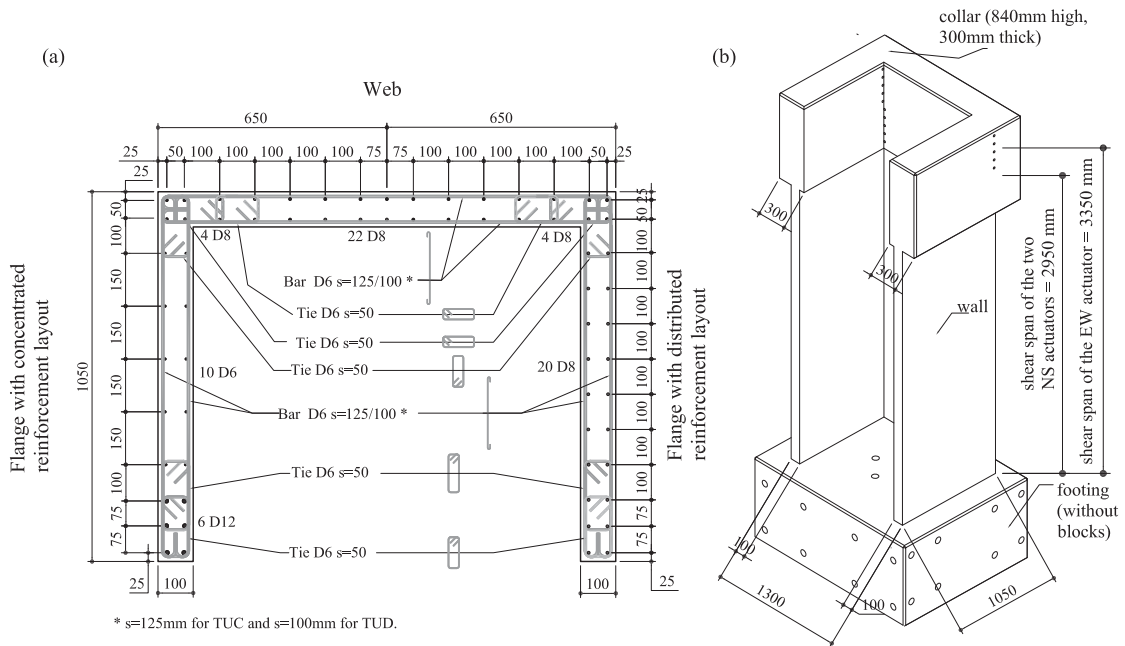


Figure 3.1: Test units TUC and TUD: cross-section and reinforcement layout (a) and elevation (b)

#### 3.2.3 Description of test set-up and instrumentation

A photo of the test set-up is shown in Figure 3.2a. As in [BDP08b], the walls were loaded horizontally with three actuators: the EW actuator loaded the webs at a height of  $h_{EW} = 3.35$  m while the NS actuators loaded the flanges of the wall at a height of  $h_{NS} = 2.95$  m from the foundation (see also Figure 3.1). The tests were performed in displacement control and rotation at the top of the wall was restrained by applying equal displacements with the NS-W and NS-E actuators. The axial load was applied by a tendon pre-tensioned by a hollow core jack located on a bream at the top of the wall (Figure 3.2a). The pressure in the hollow core jack was kept constant and therefore the test unit was subjected to a constant axial load throughout the testing (maximum variation:  $-2.5\%$  to  $6.4\%$ ). During testing, the wall behaviour was monitored through conventional instruments (linear variable differential transducers (LVDTs) and load cells) and through an optical measurement system based on triangulations of active light emitting diodes (LEDs). Photos, manual measurements of cracks and hand notes completed the data collected during the test. The layout of the measurement systems is shown in Figure 3.2b. LVDTs were used to measure global horizontal displacements at the top of the wall as well as the vertical elongation of the wall edges, which were recorded by means of four chains of eight LVDT devices each. This instrumentation is the same as the one used in [BDP08b]. One chain of four LVDTs was added on the inner side of each flange end to capture the vertical strain variation through the thickness of the flange.

### Chapter 3. Quasi-static tests of two U-shaped walls under diagonal loading

The optical measurement system Optotrak Certus [NDI10] was composed of active LEDs (466 LEDs for TUC and 510 LEDs for TUD) and three position sensors recording the 3D coordinates of the LEDs with a frequency of 2 Hz. The LEDs were glued on the outer faces of the wall in regular grids of 100x125 mm (TUC) and 100x100 mm (TUD) to match vertical and horizontal reinforcement spacing (Figure 3.2). One row of LEDs was also glued on the foundation in order to record foundation uplift and sliding. The height of the LED grid extended up to  $\sim 1.7$  m above the foundation as the main interest was to capture the plastic zone of the wall while respecting the measurement volume of the optical system.

**Table 3.1:** Longitudinal reinforcement percentages for TUC and TUD computed for the entire section and for the flanges and the web

Wall part	$\rho_l(\%)$ total	$\rho_l(\%)$ confined region	$\rho_l(\%)$ unconfined region
Flange with distributed reinforcement layout (East flange)	1.06%	1.34%	0.91%
Flange with concentrated reinforcement layout (West flange)	1.01%	2.45%	0.31%
Web	1.16%	1.25/0.90%	1.00%
Entire wall	1.09%	-	-

Total reinforcement percentage for the flanges and the web was computed by counting the corners towards the web.

Due to differences in flange reinforcement layouts, reinforcement contents of confined corner regions are slightly different.

**Table 3.2:** Mean values and standard deviations of mechanical properties of concrete

	E-modulus and compressive strength tests				Double-punch tests		
	$f_c$ - 28days [MPa]	No. of samples	$f_c$ [MPa]	$E_c$ [GPa]	No. of samples	$f_t$ [MPa]	No. of samples
TUC	$38.10 \pm 0.7$	3	$42.0 \pm 1.4$	$31.6 \pm 3.9$	3	$3.2 \pm 0.2$	4
TUD	$37.0 \pm 1.3$	3	$41.5 \pm 1.2$	$30.3 \pm 0.8$	4	$3.0 \pm 0.2$	4

### 3.2. Test units, set-up, instrumentation and loading history

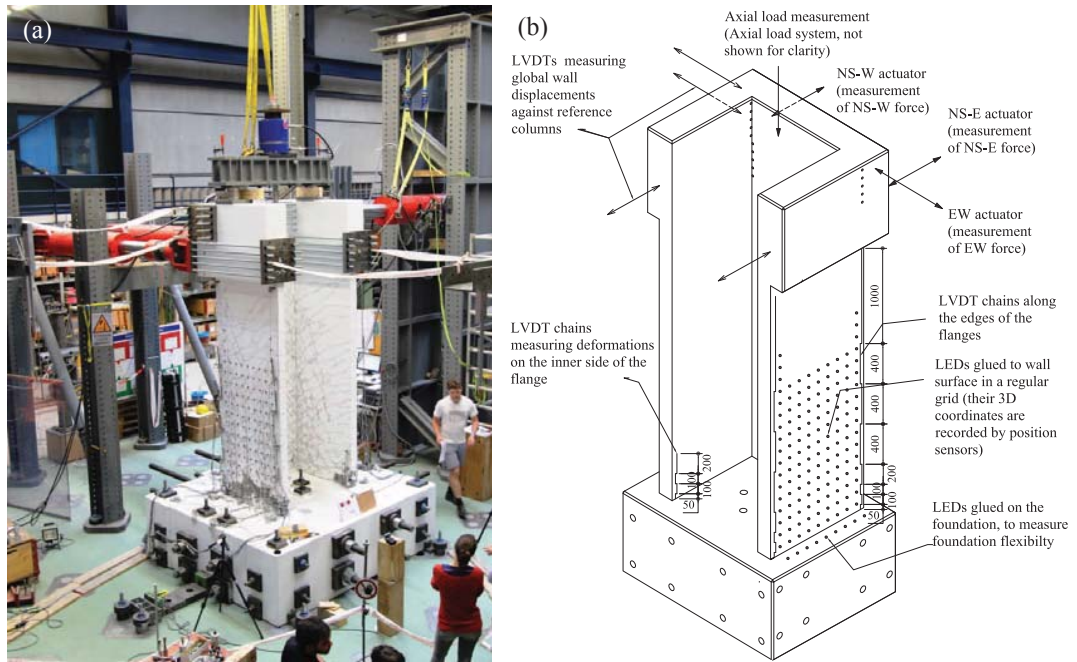


**Figure 3.2:** Photo of the test set-up (a) and location of the conventional and optical measurement devices (b)

**Table 3.3:** Mean values and standard deviations of mechanical properties of reinforcement bars used for TUC and TUD

	$f_y$ [MPa]	$f_u$ [MPa]	$f_u/f_y$ [-]	$\epsilon_{sh}$ [%]	$\epsilon_{su}$ [%]	No. of samples
D6mm bars	492±5.1	623±8.7	1.26±0.02	-	6.8±0.9	6
D8mm bars	563±26.6	663±6.5	1.18±0.05	-	7.9±0.8	7
D12mm bars	529±4.7	633±3.9	1.19±0.01	2.4±0.25	9.6±1.2	3

The yield strength  $f_y$  was determined at the 0.2% strain offset (0.2% proof stress).

### 3.2.4 Loading history

As stated in the introduction, the key objective was to understand the behaviour of the wall under diagonal loading. Hence, the main cycles were applied along the two geometric diagonals of the U-shaped section. The direction of the geometric diagonal joins the outer corner between web and flange with the outer edge of the flange end (Figure 3.3b – directions E-F and H-G). Cycles along the principal directions, i.e., loading parallel to the web (EW direction with positions A and B - Figure 3.3) or loading parallel to the flanges (NS direction with positions C and D - Figure 3.3), were also added at small drift levels in order to check the strength capacity of the wall in these directions, as past tests have shown that for these directions the strength capacity can be predicted using the plane section hypothesis [BDP08b]. The loading positions are shown in Figure 3.3b while the loading history of the test units is described below and shown in Figure 3.4:

- 0.1% drift: O-C-D-O-A-B-O
- 0.2% drift: O-C-D-O-A-B-O-E-F-O-H-G-O
- 0.3%, 0.4%, 0.6% drifts: O-E-F-O-H-G-O-C-D-O-A-B-O
- 0.8% drift: O-C-D-C-D-O-A-B-A-B-O
- 1.0%, 2.0%, 3.0% drifts: O-E-F-E-F-O-H-G-H-G-O
- 1.5%, 2.5% drifts: O-H-G-H-G-O-E-F-E-F-O

From 1.0% drift onwards, two complete reverse cycles were applied for each diagonal direction at each drift level. The orientation of the first diagonal applied at a new drift level alternated between the E-F direction and the H-G direction. Towards the end of the tests, the loading was only continued along the diagonal that led still to a stable hysteretic behaviour, as extensive wall damage had significantly reduced the stiffness in the other diagonal. The modified protocols at the end of the test were as follows: Modifications to load protocol TUC:

- 2.5% drift: O-H-G-O-E-F-O
- 3.0% drift: O-E-O-H-O (test was stopped due to loss of vertical load bearing capacity)

Modifications to load protocol TUD:

- 1.5% drift: O-H-G-H-O-E-F-E-O (test was stopped due to loss of vertical load bearing capacity)



3.2. Test units, set-up, instrumentation and loading history

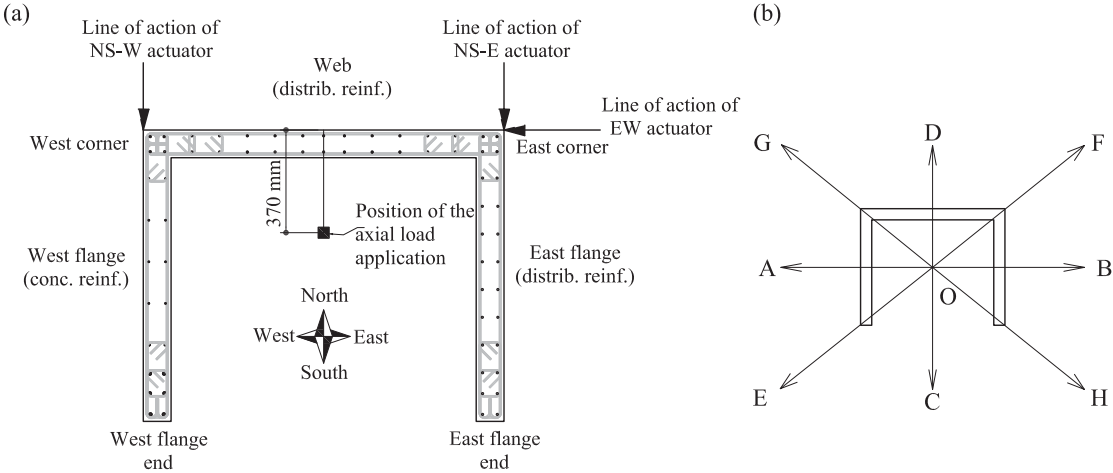


Figure 3.3: Cardinal points, sign convention for forces and displacements, denomination of wall parts (a) and loading positions (b)

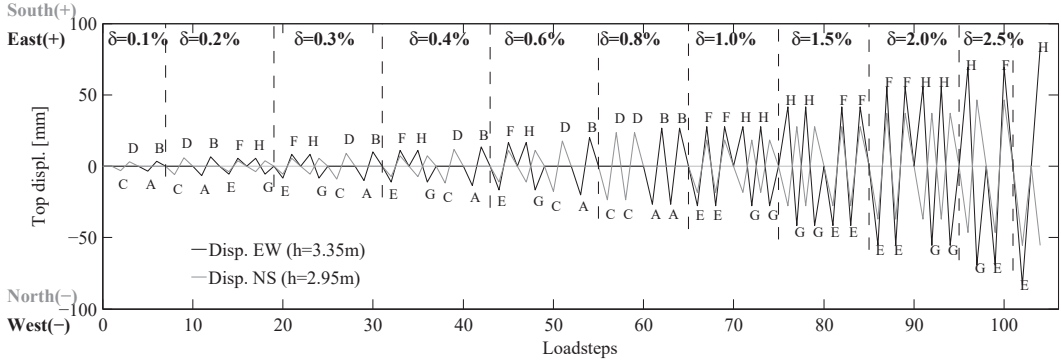


Figure 3.4: TUC loading history

### 3.3 Test results

In this section the most important findings from the tests are presented. Failure mechanisms together with hysteretic behaviour are discussed in Section 3.3.1. The influence of the reinforcement layout and of the axial load on the crack pattern and crack widths is shown in Section 3.3.2. Local deformation response specific to U-shaped walls under diagonal loading is presented in Section 3.3.3, while Section 3.3.4 investigates the influence of the longitudinal reinforcement layout and the axial load ratio on the shear to flexural deformation ratios.

#### 3.3.1 Failure mechanisms and hysteretic behaviour

The failure mechanisms of the two test units are illustrated in Figures 3.5 to 3.7 while the force-displacement hysteresees are shown in Figures 3.8 to 3.9. For the two diagonal directions individual actuator forces as well as their resultant are plotted against the wall top displacements, which were measured by means of the horizontal LVDTs recording the NS displacements at  $h_{NS} = 2.95$  m and the EW displacements at both  $h_{NS}$  and  $h_{EW} = 3.35$  m. The top displacements were corrected for the foundation flexibility (uplift and sliding) by subtracting the top displacements due to foundation flexibility.

Foundation flexibility resulted from the uplift and the sliding of the wall foundation with respect to the laboratory strong floor. The uplift and sliding of the foundation was computed from the LEDs glued on the foundation (LEDs on small steel angle in Figure 3.2). Top displacement due to uplift was computed assuming a rigid body rotation of the wall and the foundation, while the top displacement due to sliding was simply taken equal to the sliding displacement measured between the foundation and the laboratory strong floor. Top displacements due to foundation flexibility accounted for  $\sim 6 - 8\%$  of the measured top displacements at yield drift and decreased thereafter. The corrected top displacements and the forces were combined through the square root of the sum of squares (SRSS) to obtain quantities representative of the diagonal directions (Figures 3.8b-c and 3.9b-c):

$$F_{SRSS} = \sqrt{(F_{EW}^2 + F_{NS}^2)} \cdot \text{sign}(\Delta_{NS}) \quad (3.1)$$

$$\Delta_{SRSS} = \sqrt{(\Delta_{EW@2.95})^2 + \Delta_{NS}^2} \cdot \text{sign}(\Delta_{NS}) \quad (3.2)$$

where  $F_{EW}$  and  $F_{NS}$  are the forces carried by the wall in the EW and the NS direction respectively, while  $\Delta_{EW@2.95}$  and  $\Delta_{NS}$  are the wall horizontal displacements in the EW and the NS directions, both measured at  $h_{NS}$ . The SRSS values were multiplied by the sign of the NS displacement for plotting the hysteresis loops consistently.

### 3.3.1.1 TUC

*Failure mode when loading along the diagonal E-F:* Failure of TUC occurred due to out-of-plane buckling and compression failure of the flange with the concentrated reinforcement (West flange). Failure occurred during loading in the E-F diagonal direction when the flange end was in compression at position E (Figure 3.5). A maximum of 2.5% SRSS drift was reached for this direction prior to wall failure. During the last cycle, the wall stiffness was significantly reduced when loading from zero displacement towards position E, as compared to the previous cycles at the same loading position (Figure 3.8b, d-f). In this cycle the loading was stopped at only 1.0% drift due to extensive damage to the West flange and  $\sim 35\%$  drop in the SRSS force capacity as compared to the maximum reached in this last cycle at this loading position (see Figure 3.8b).

*Out-of-plane failure of plastic zone of West flange:* The failure mode of the wall, i.e. out-of-plane buckling of the wall end and compression failure of the unconfined concrete, was first experimentally investigated and reported by [PG85] for walls loaded in plane. For TUC, the evolution of wall failure can be summarised as follows: due to large displacement demands imposed on the wall at position F (i.e., 2.5% SRSS drift), large tensile strains were developed in the reinforcement bars of the West flange end resulting in wide horizontal cracks ( $\sim 4$  mm) in this region. When unloading from position F, the longitudinal bars first had to yield in compression before the cracks could close. During this stage the plastic zone had a very small stiffness and was as a result vulnerable to out-of-plane instability.

For rectangular walls loaded in plane, out-of-plane displacements are typically caused mainly by construction imperfection. Loading to position E led to a large strain gradient across the flange end (see Section 3.3.3.1), which leads to an eccentricity of the compression force acting in this region. This strain gradient is expected to have promoted the out-of-plane buckling process. As a result of the strain gradient, the flange end bulged towards the inside of the U-shaped wall, which was also the direction in which the flange failed out-of-plane (Figure 3.5b).

Based on the visual observation and the force-displacement hysteresees, the initiation of the out-of-plane buckling occurred near zero SRSS top displacement when returning to zero from the first cycle at position F with 2.5% SRSS drift. The force-displacement hysteresees show significantly reduced wall stiffness after the onset of buckling (Figure 3.8b, d-f). The fact that onset of buckling occurred near zero displacement is in line with observations from tests on thin T-shaped walls, which failed also due to out-of-plane buckling [RAB16]. It was found that at this instant, cracks are open along the entire length of the wall and the out-of-plane stiffness is therefore very small. Note that, while the out-of-plane buckling mode of TUC and the thin walls described in [RAB16] shared many similarities, the buckling mode of the thin walls involved the entire storey height and not just the plastic zone as observed for TUC.

Due to the out-of-plane buckling, the West flange end of TUC lost its compression carrying capacity. To compensate for this, the compressed depth increased into the unconfined part of the flange, leading to concrete crushing in this region and final loss of the wall force capacity both in the direction of the flanges (NS direction - Figure 3.8d-e) and also in the direction of the web (EW direction - Figure 3.8f).

### Chapter 3. Quasi-static tests of two U-shaped walls under diagonal loading

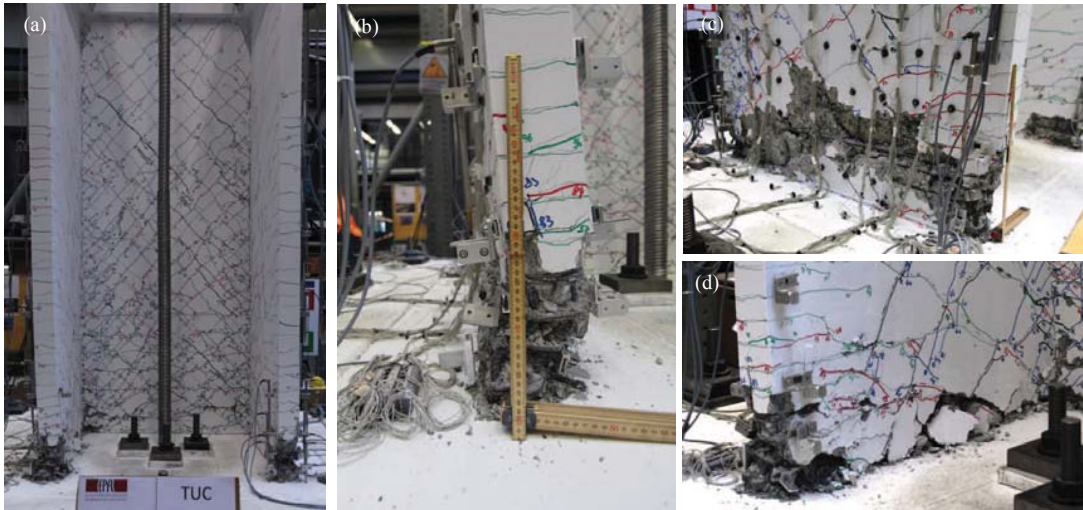


**Figure 3.5:** TUC: Out-of-plane buckling and compression failure of the concentrated reinforcement layout flange at position E (West flange end in compression) at an SRSS drift of  $\sim 1.0\%$ . Front view of the wall (a); close-up view of the buckled flange end (b); outside view (c) and inside view (d) of the West flange.

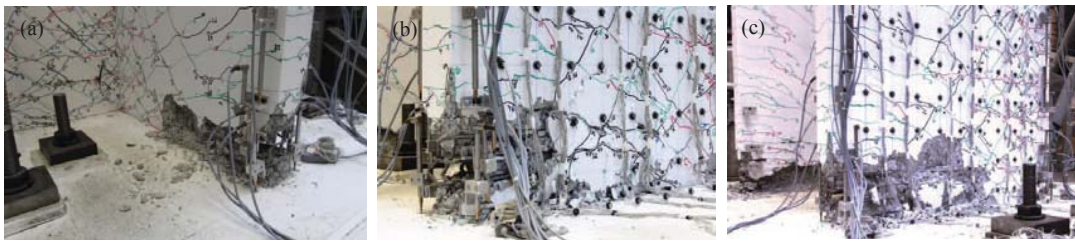


**Figure 3.6:** TUC: Crushing of the concrete in the flange with distributed reinforcement (East) at position H (East flange end in compression) at an SRSS drift of  $\sim 2.5\%$ . View for inner side of the East flange (a) and view from the outer side: far-off view (b) and close-up.

*Failure mode when loading along the diagonal H-G:* Continuing loading along the E-F diagonal would have led to a complete destruction of the West flange due to the out-of-plane buckling compression failure at 1.0% drift. For this reason, this loading cycle was not completed and the wall was cycled along the H-G diagonal instead. However, loading along this diagonal led to a compression failure of the East flange at 2.5% SRSS drift, which had already been reached in a previous cycle. At this point the test was stopped because of axial load failure (Figure 3.6 and Figure 3.8g-i).

*Influence of reinforcement layout on buckling of longitudinal bars:* Recent experimental research on rectangular walls [HM<sup>+</sup>14] concluded however that walls detailed with distributed reinforcement will reach lower ultimate drifts than walls with concentrated reinforcement, as the smaller diameter bars in the boundary elements of the former will undergo early bar buckling for the same stirrup spacing of the two walls. The failure of the U-shaped walls presented here was, however, not controlled by bar fracture. The different diameters of longitudinal reinforcement bars in the flanges with concentrated (West) and distributed reinforcement (East) had, however, an influence on the onset of bar buckling and the drift at which first bar fractures were observed.

Three of the four confined boundary elements of the U-shaped walls were detailed with D8 longitudinal reinforcement bars, i.e., the end of the flange with distributed reinforcement (East) and the two corners between a flange and the web. The fourth boundary element, i.e., the end of the flange with concentrated reinforcement (West) was detailed with D12 vertical bars. All four boundary elements featured the same stirrup spacing (Figure 3.1a). D8 bars of the boundary elements buckled indeed before any D12 bar of the West flange end buckled (Figure 3.10b): Two D8 bars first buckled in the East flange end in the first cycle at 1.5% drift at position H followed by the buckling of one D8 bar in the confined corner between East flange and web in the second cycle at 2.0% drift at position F. In the confined corner between West flange and web one D8 bar first buckled in the first cycle at 2.0% drift at position G. In the following cycles, further D8 bars buckled in these confined boundary elements. And finally, buckling initiated also in the West flange end when a D12 bar buckled in the cycle at 2.5% drift at position E. Outside the boundary elements, bar buckling occurred only in the unconfined concrete of the flange with concentrated reinforcement (West). For this flange the outer D6 bar closest to the confined flange end buckled in the first cycle at 2.5% drift at position G, hence before any buckling occurred in end of this flange.

Bar fractures first occurred in the cycle at 2.5% drift at position G when three D8 bars fractured in the East flange end. Their fracture however did not significantly affect the wall strength, i.e., the wall retained more than 80% of its SRSS force capacity (Figure 3.8c, g-i) and also of the NS force capacity (Figure 3.8d), and was hence not considered as failure. The strength drop was not significant since bar diameters are small and uniformly distributed throughout the flange.

*Influence of the reinforcement layout on the wall stability:* The observed failure modes suggested that the flange with distributed reinforcement layout (East flange) was less prone to out-of-plane buckling failure than the flange with concentrated reinforcement layout (West flange). Mechanical models by Paulay and Priestley [PP93] and Chai and Elayer [CE99] show that the lateral stability of the wall boundary element depends strongly on the maximum tensile strain the wall boundary element had been subjected to. This threshold value of tensile strain that triggers the out-of-plane instability decreases with increasing longitudinal reinforcement ratio [CE99], [MK03]. As a result, flange ends with large longitudinal reinforcement contents—such as those in sections with concentrated reinforcement layout—are more susceptible to out-of-plane buckling than flange ends of sections with lower longitudinal reinforcement contents as in distributed reinforcement layouts [MK03]. This trend is in line with the observed flange failures.

### Chapter 3. Quasi-static tests of two U-shaped walls under diagonal loading

---

*Drift capacities:* Along both diagonals, one full cycle with 2.5% SRSS drift was completed before the strength dropped by 20% or more. For the test here, the wall flange with distributed and the wall flange with concentrated reinforcement reached the same drift capacity. The failure modes attained for the two loading directions were, however, rather different and strongly influenced by the respective reinforcement layouts. Based on the test observations the reinforcement layouts influence the following phenomena:

The drift related to the onset of bar buckling and bar fracture: For distributed reinforcement layouts, the diameter of the longitudinal bars in the boundary elements is typically smaller than for concentrated reinforcement layouts. For the same stirrup spacing, bars in the distributed reinforcement layout will therefore buckle and fracture at smaller drifts.

The out-of-plane stability of the plastic zone: The larger the longitudinal reinforcement content in the boundary element, the more prone is the plastic zone to out-of-plane instability. For TUC, out-of-plane instability occurred for the West flange (concentrated reinforcement) but not for the East flange (distributed reinforcement).

The influence of the reinforcement layout on crack widths and shear deformations is discussed in Sections 3.3.2 and 3.3.4 respectively. For TUD the reinforcement layout had also an influence on the compression zone depth, which is discussed in the following section.

#### 3.3.1.2 TUD

TUD, the test unit with an axial load ratio of 0.15, failed due to an explosive compression failure of the concrete in the flange with distributed reinforcement (East flange, Figure 3.7b-c). The compression failure occurred after reaching position H in the second cycle at 1.5% drift (Figure 3.9c, g-i). The compression failure initiated in the confined part of the flange end and extended suddenly to the unconfined part of the flange. Once the behaviour stabilised again, the flange had crushed along  $\sim 80\%$  of its length (Figure 3.7c). In the previous cycle, visual inspection indicated only limited crushing of the boundary element as shown in Figure 3.7a.

The explosive failure and the extensive concrete crushing were caused by the large compression depth and significant compressive strains in the East flange at position H. Already in the first cycle at position H at 1.5% drift, the compressive strains computed from optical measurements reached for the unconfined concrete of the flange  $\sim 0.003$  (average strains over the height  $h = 75 - 200$  mm,  $h$  measured from top of foundation). Due to the larger axial load ratio the compression zone depth of TUD was larger than that of TUC. In addition, the distributed reinforcement layout in the East flange led to a larger compression zone depth for the East flange than for the West flange. But most importantly under diagonal loading with the flange end in compression (positions E and H), the compression depth of the flange end is considerably larger than in the case of orthogonal loading with both flange ends in compression (position C) as local deformation response indicates (see Section 3.3.3.2).



**Figure 3.7:** TUD: explosive compression failure of the distributed reinforcement layout flange (East flange). Wall condition at 1st cycle at position H at 1.5% drift (a-b) and wall condition after failure in the 2nd cycle at position H at 1.5% drift: view on the inner side (c) and view on the outer side (d).

For TUD, the wall failure along the H-G diagonal was marked by  $\sim 75\%$  loss in the SRSS force capacity (Figure 3.9c). The loading was therefore continued in the E-F direction, but already in the first cycle concrete crushing in the web occurred leading to a significant strength drop at a drift of  $\sim 1.0\%$  (Figure 3.9f). Moreover, the wall was no longer able to carry the nominal axial load of 1950 kN.

The shear demand on TUD (SRSS force) was on average  $\sim 36\%$  larger than on TUC due to the increased axial load ratio of the former (Figure 3.8b-c and Figure 3.9b-c). The displacement capacity of TUD on the other hand was only 1.5% drift as compared to 2.5% drift for TUC. For TUC the failure was initiated by large out-of-plane deformations of the flange at zero SRSS drift (Figure 3.5) for TUD failure occurred at peak drift of a cycle when the flange failed suddenly leading to an extensive crushing band along almost the entire length of the flange (Figure 3.7b-c).

### 3.3.2 Crack patterns

The crack patterns for a U-shaped wall tested under different loading directions have already been discussed in detail elsewhere [IR05] and [BDP08b]. Beyer et al. [BDP08b] observed in their tests, that in the web the crack patterns were similar to those encountered for typical rectangular walls while the flanges had the steepest cracks of the entire wall, which opened when the flanges were loaded along the diagonal directions towards positions E and H. The steepest cracks in the web, opened in its half upper part also at positions E and H. The same observations were found valid for the tests presented herein (Figures 3.11 and 3.12).

Since the two flanges of TUC and TUD were detailed with distributed and concentrated reinforcement layouts, the crack widths, spacing and the crack angles are of interest, as differences between the two flanges were expected. Previous numerical and experimental investigations on RC walls have shown that for concentrated reinforcement layouts, cracks in the unconfined concrete part have larger widths and larger crack spacing than in the distributed layout case [Bru09], [MK03] and [RA<sup>+</sup>14].

### Chapter 3. Quasi-static tests of two U-shaped walls under diagonal loading

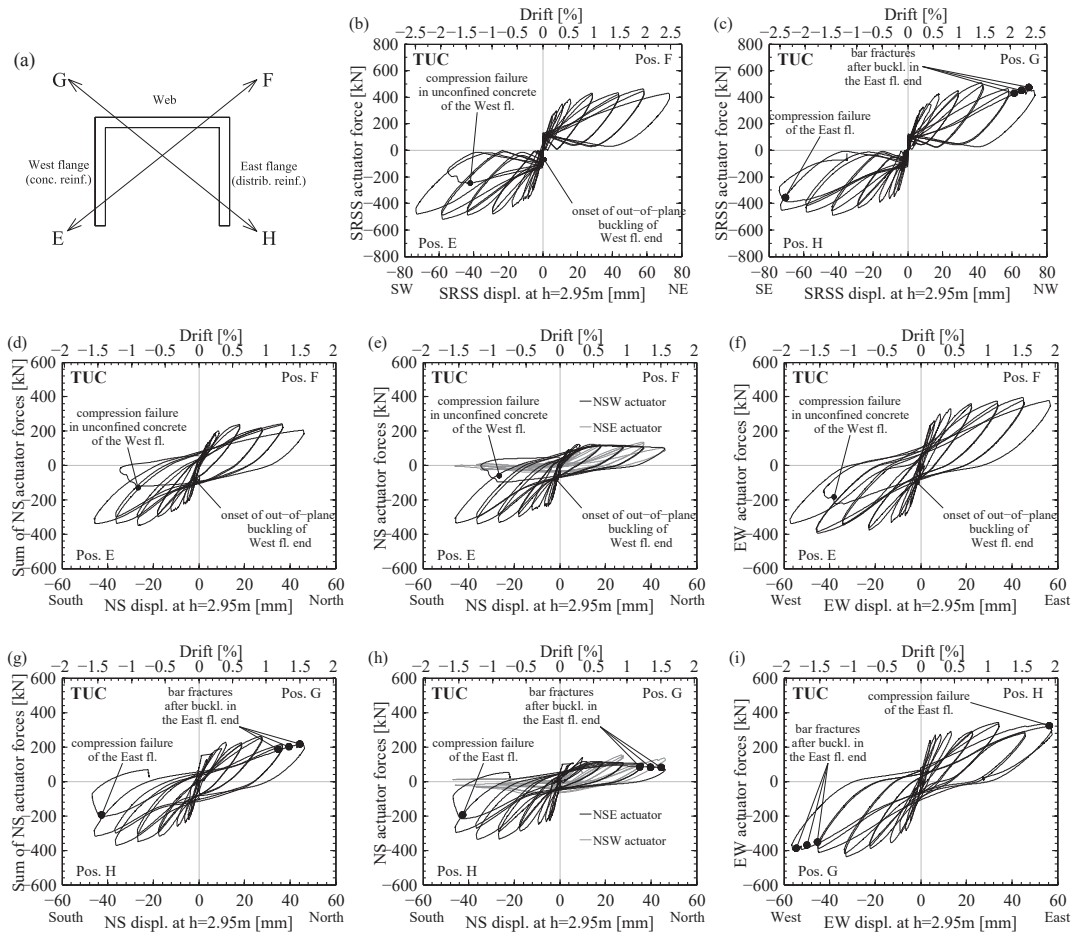


**Figure 3.8:** TUC: loading positions (a), SRSS force-displacement hysteresses (b-c) and for individual NS and EW directions (d-i).



### 3.3. Test results

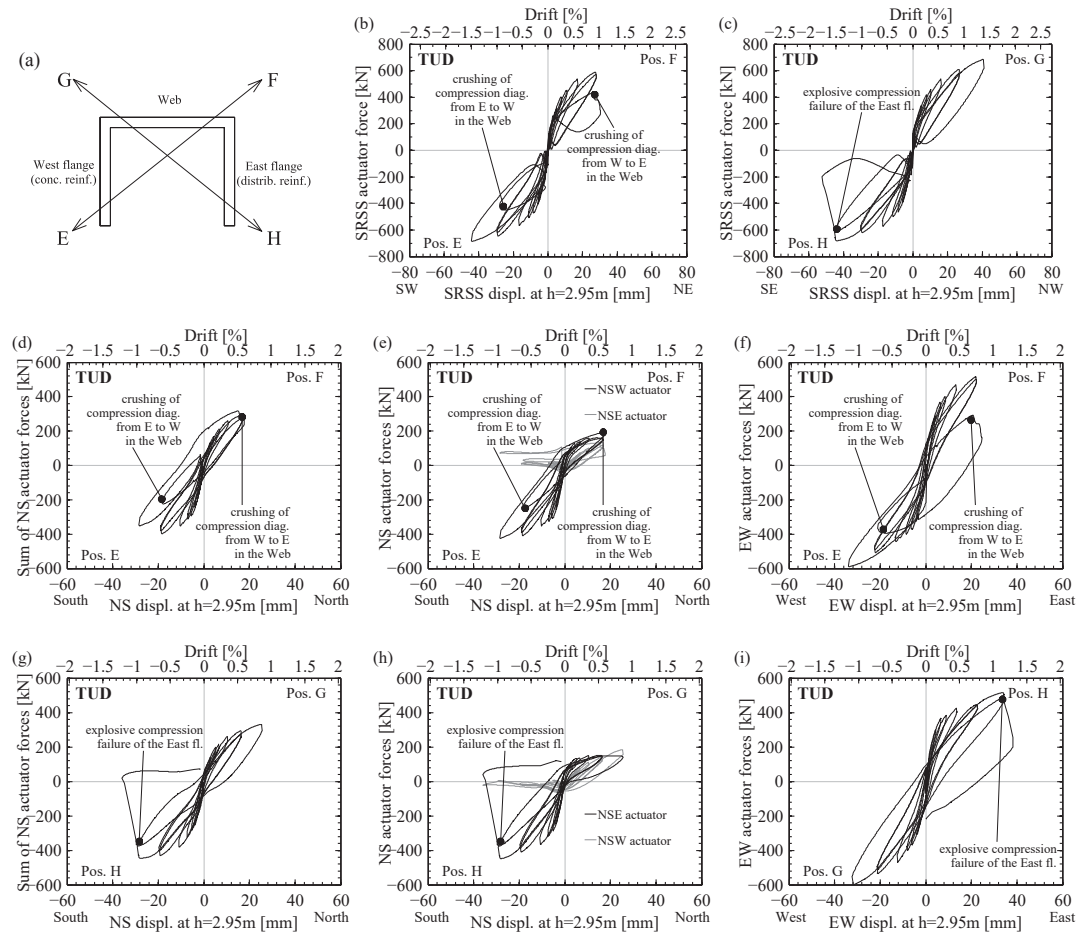


**Figure 3.9:** TUD: loading positions (a), SRSS force-displacement hysteresses (b-c) and for individual NS and EW directions (d-i).

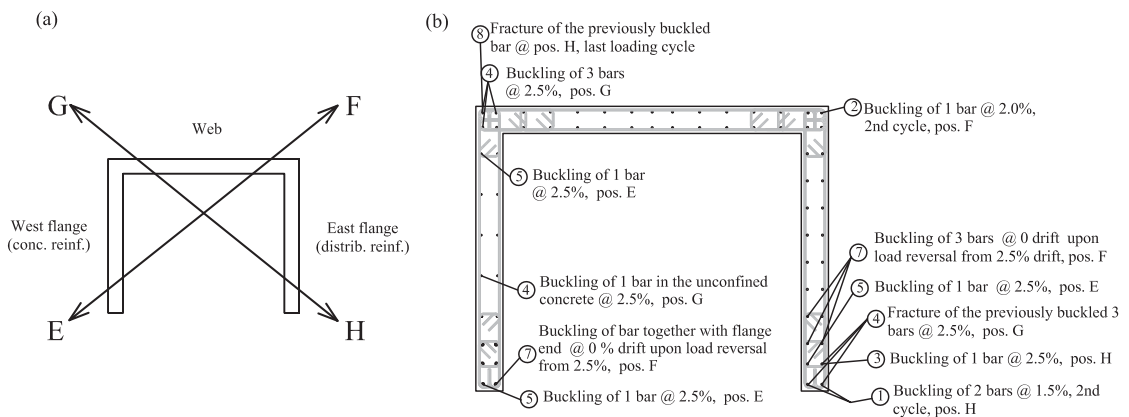


**Figure 3.10:** TUC: Sequence of bar buckling and fracture.

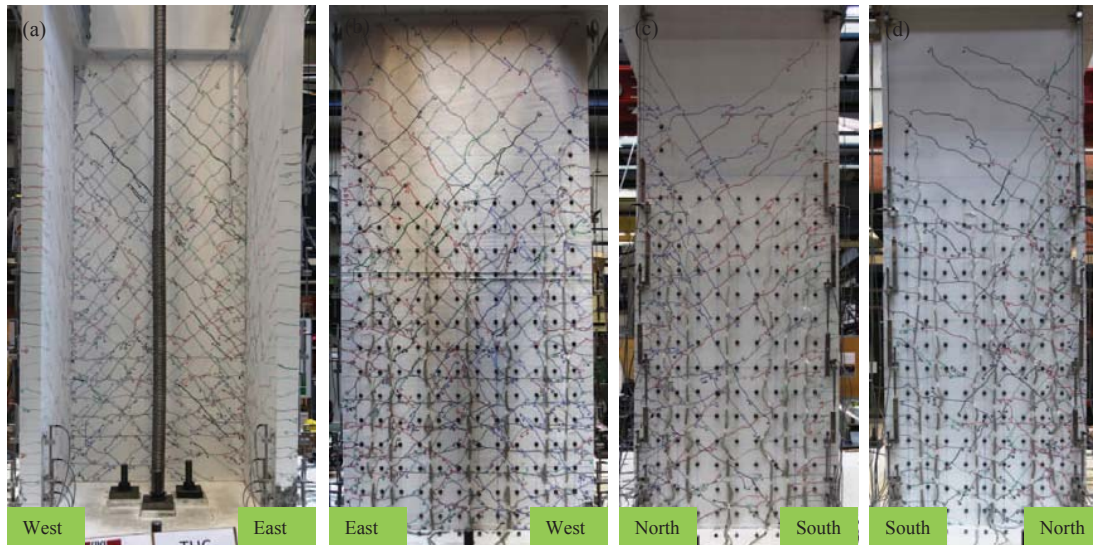


**Figure 3.11:** TUC: Crack patterns at the beginning of 1.5% drift cycles: front view (a); back view (b); view of the West flange (concentrated reinforcement) (c) and view of the East flange (distributed reinforcement) (d).

During the testing of TUC and TUD, crack widths of selected cracks were measured manually at several load steps. The comparison of maximum crack widths in the unconfined concrete part of the two flanges under symmetric loading conditions for both flanges (i.e. Position C and Position D) is shown in Figure 3.13c-d up to 0.8% drift, the last drift where loading to these positions was applied. As expected, at Positions C and D, crack widths in the flange with concentrated reinforcement layout (West flange) were on average 40% larger than in the flange with distributed reinforcement layout (East flange). The inaccuracy of manual measurements for crack widths under 1 mm, could explain the outliers in the graph: position C,  $\delta = 0.6\%$  and position D,  $\delta = 0.8\%$ . As a result of the differences in crack patterns, at the end of the test after both flanges underwent an equal number of loading cycles, the unconfined concrete of the concentrated layout flange was more damaged than the unconfined concrete of the distributed layout flange (Figure 3.13a-b).

Crack angles in the unconfined concrete part of the flanges were measured from photos, averaging the angles over the height  $h = 0 - 1.7$  m for cracks that formed for the same loading direction. Crack angles with the wall vertical axis were  $\sim 15 - 25\%$  smaller for the West flange than for the East one when flange ends were in tension due to  $\sim 15\%$  higher force capacity (and hence also higher shear demand) of the former. Crack angles varied between TUC and TUD, with  $\sim 30\%$  smaller angles with the wall vertical axis measured for TUD, indicating the increased shear demand imposed on this wall, both on the web and on the flanges (Figures 3.11 and 3.12). In addition the cracks were more closely spaced for TUD, which is probably the result of the more closely spaced shear reinforcement for this test unit.

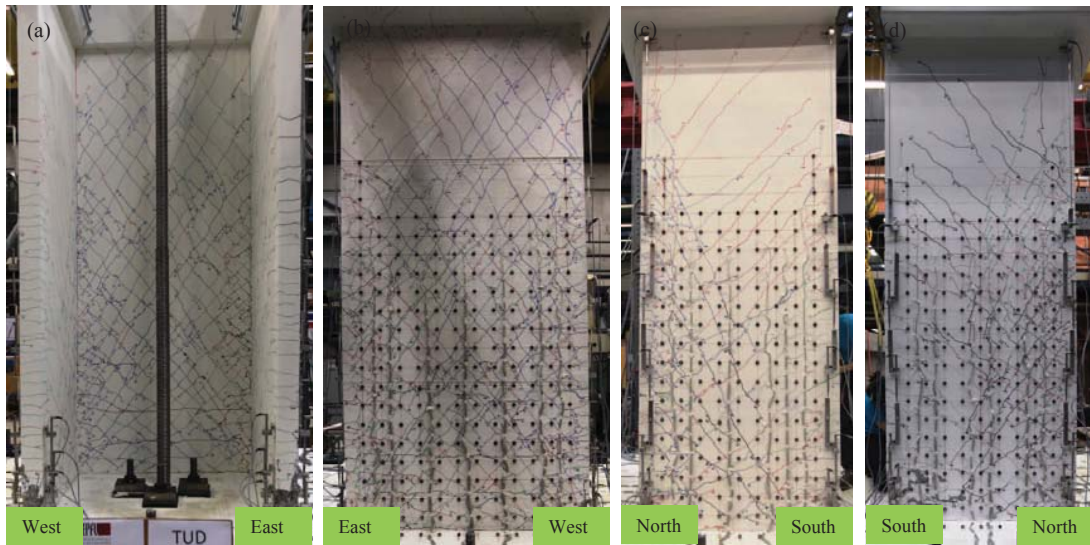


**Figure 3.12:** TUD: Crack patterns at the beginning of 1.5% drift cycles: front view (a); back view (b); view of the West flange (concentrated reinforcement) (c) and view of the East flange (distributed reinforcement) (d).

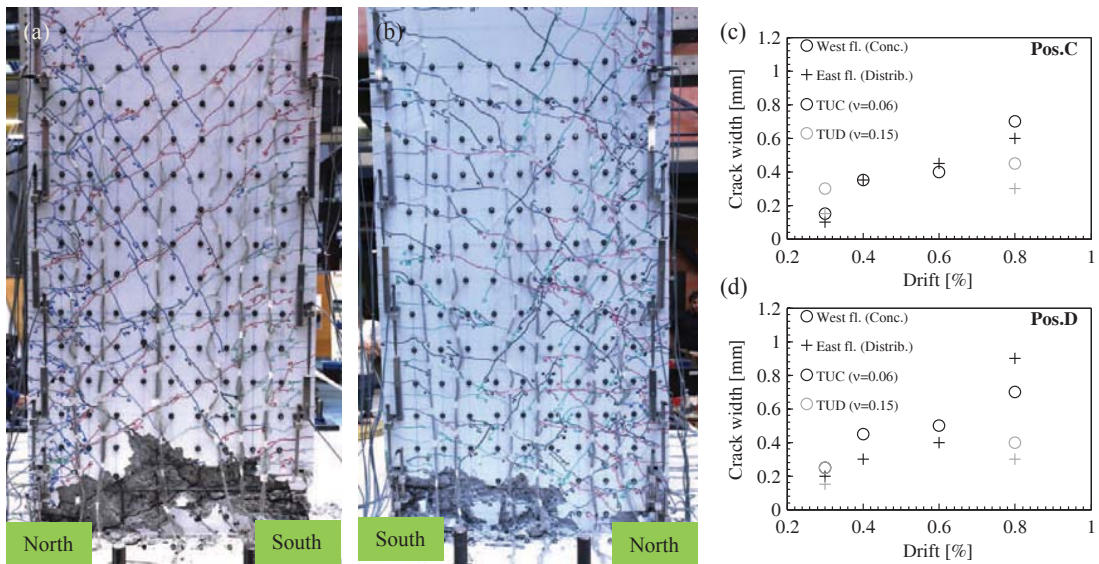


**Figure 3.13:** Influence of the longitudinal reinforcement layout on the damage to the unconfined concrete of the wall flanges. TUC wall flange condition at the end of the test: concentrated reinforcement layout (West flange) (a) and distributed reinforcement layout (East flange) (b). Maximum crack widths in the two flanges under symmetrical loading conditions (c-d).

### 3.3.3 Local deformation response specific to diagonal loading

This section presents strain profiles that illustrate the deformation response specific to U-shaped walls under diagonal loading. More specifically, the out-of-plane bending of the flanges is discussed in Section 3.3.3.1 and the section deformation at the wall base in Section 3.3.3.2.

#### 3.3.3.1 Vertical strains on the inner and outer side of the flange ends

The vertical strains on the inside and the outside of the flange ends were obtained from measurements of the LVDT chains mounted on the inner and outer sides of the flange ends (Figure 3.2b and Figure 3.14b, d). Figure 3.14 shows these vertical strains obtained for diagonal loading at drifts of 0.4% and 1.0%. The former corresponds approximately to yield drift while the latter corresponds to the largest drift that was reached by both TUC and TUD in both diagonal loading directions.

The strains shown in Figure 3.14 are computed for the inner and outer faces of the wall; for this purpose the measurements were corrected for the fact that there was an offset of approximately 4 cm between wall face and LVDT. The correction was done assuming that the strains varied linearly over the flange thickness, i.e., between the LVDT chains on the inner and the outer side of the flange end.

When the flange ends are under compression (positions E and H), the compressive strains on the outer flange face that were measured with the lowest LVDT ( $h = 50 - 150$  mm) are up to  $\sim 2.5$  times larger than on the inner flange face (Figure 3.14a-d). When the flange ends undergo tension (positions F and G) the tensile strains on the outside are again larger than on the inside but only by a factor up to  $\sim 1.4$  (Figure 3.14e-h). This strain gradient was observed also for symmetric loading positions (NS direction) but was significantly larger in the case of diagonal loading. The large strain gradient under diagonal loading promotes the out-of-plane buckling of the flange ends (Section 3.3.3.1). As discussed in Section 3.3, TUC failed after out-of-plane buckling of the West flange end. For TUD, the out-of-plane buckling was not critical since due to the increased axial load ratio the tensile strains at the flange ends, which are crucial for the triggering out-of-plane buckling [PP93], [CE99], were approximately 60% smaller than for TUC.

#### 3.3.3.2 Vertical strains at the base of the wall

The vertical strains at the base of the wall, which are discussed in this section, were derived from the optical measurement data and were therefore taken on the outer perimeter of the walls. The first two rows of LEDs, namely the row on the foundation and the first row on the wall, were used to determine average vertical strains for  $h = 0 - 75$  mm. Figure 3.15 shows these vertical strain profiles at the wall base along the perimeter of the U-shaped section for the diagonal loading directions again plotted for the two above mentioned drift levels, i.e., 0.4% and 1.0%.

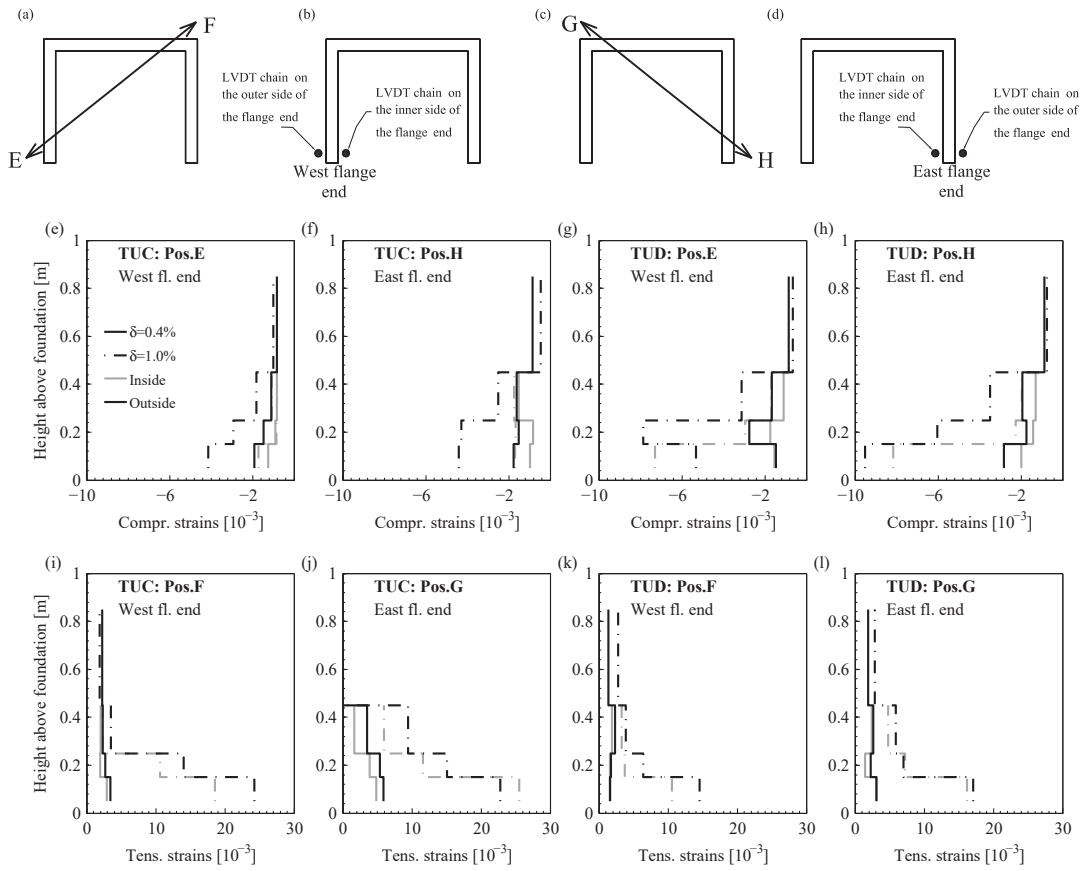


**Figure 3.14:** TUC and TUD: Vertical strains on the inside and outside of the flange ends (e-l) computed from measurements of LVDT chains mounted on the two sides of the flange ends (a-d).

### Chapter 3. Quasi-static tests of two U-shaped walls under diagonal loading

---

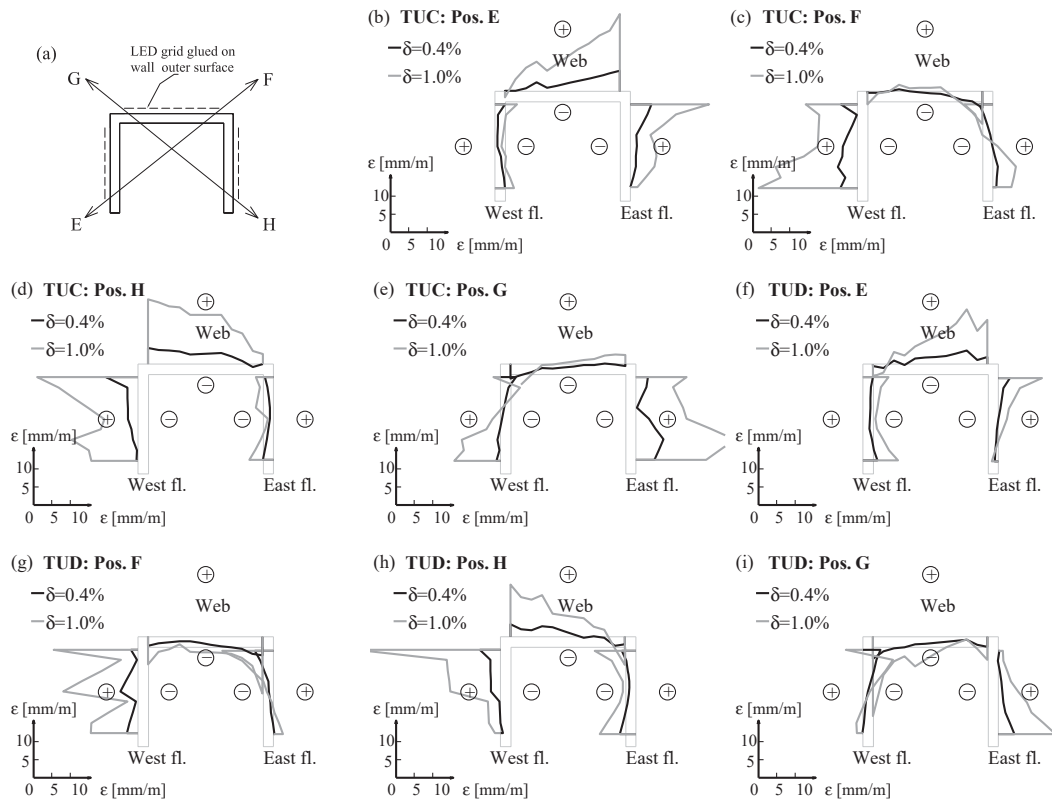
This height interval,  $h = 0 - 75$  mm, at the base of the wall represents the relevant section for the force transfer mechanism from wall to foundation. While the magnitudes of the strains over  $h = 0 - 75$  mm may be influenced by the tensile and compressive strain penetration into the foundation, the general trends in the strain distribution along the wall perimeter (i.e. whether strains are compressive or tensile) are not affected. Therefore it is possible to compare qualitatively the experimentally obtained vertical strain distribution with the one estimated using plane section analysis, a widely used analytical tool which forms the basis of most beam-column formulations. The two strain profiles: experimental and analytical are compared later in this section and the discrepancies between the two are discussed.

Figure 3.15b shows the vertical strain distribution at the wall base for loading towards position E of TUC. Peak values of compressive strains were attained—as expected—at the flange end but also near the intersection of web and West flange. This second peak compressive strain indicates the presence of a compression zone at the intersection of web and West flange which is less evident at drift levels in the elastic range (0.4% drift) and more pronounced after reaching the nominal moment capacity (1.0% drift). The presence of this compression zone is important because, it cannot be captured by a plane section analysis but might be at the core of the force transfer mechanism from wall to foundation for shear forces in the direction of the web as discussed in the following section.

#### Comparison with section analysis estimates

The plane section analysis of the U-shaped wall was performed using a zero-length fibre element in the “Opensees” software [MMG09]. The U-shaped section was divided into 212 concrete fibres and 66 reinforcement fibres. The concrete areas were grouped into different zones depending on the degree of confinement. The Concrete04 material model was used for the stress-strain behaviour of the concrete fibres, while confinement properties were computed according to Mander et al. [MPP88]. The Steel02 material model with default parameters was used for the reinforcement stress-strain behaviour. Monotonic analyses were performed in displacement control (i.e., curvature control) along the geometric diagonals of the section. Yield, nominal and ultimate strain limits were determined following recommendations by [PCK07].

Figure 3.16 compares for position E of TUC the experimentally obtained vertical strain distribution at the wall base with the one obtained from section analysis. This figure shows that section analysis fails to capture the parabolic variation of the experimental compressive strains along the West flange, with the two compressive strain peaks at the West flange end and the corner between web and West flange. As a consequence, the compression zone at the intersection of web and West flange where high compressive strains were measured (i.e., almost as high as in the West flange end) is also not captured with the plane section assumption. As previously stated, the presence of the extra compression zone at the corner web-flange plays a role in the force transfer mechanism from wall to foundation.



**Figure 3.15:** TUC and TUD: Vertical strains at the base of the wall under diagonal loading directions determined from optical measurements over the height  $h = 0 - 75$  mm above foundation on the outer perimeter of the wall. Tensile strains are plotted on the outside of the U-shaped section (positive strains) and compressive strains on the inside (negative strains). The values of the strains can be measured from the outer face of the U-shaped section using the strain scale provided in the left down corner of each subplot.

### Chapter 3. Quasi-static tests of two U-shaped walls under diagonal loading

---

Shear forces can be transferred from wall to foundation only through compression zones at the base of the wall as only small shear forces can be transferred through a tension zone. At position E, section analysis yields only one compression zone at the West flange end (Figure 3.16c). This would imply that all shear forces are transferred to the foundation at the West flange end. The shear force in East-West direction, which is originally carried by the web (Figure 3.16a), would therefore be transferred as an out-of-plane shear force through the West flange end.

The experimental vertical strain profile (Figure 3.16b) indicates however an additional compression zone at the corner between web and flange which can serve for transferring the web shear force to the foundation through a more direct in-plane force path. While the test set-up did not allow measuring the distribution of reaction forces along the base of the wall, the compression zone at the corner between web and West flange represents strong evidence that at least part of the shear force in the web is transferred to the foundation through this compression zone.

Similarly, at position F, the experimentally determined vertical strains deviate again from the plane section analysis estimates (Figure 3.17b-c) due the presence of a compression zone at the corner between West flange and web (Figure 3.17c and Figure 3.17a-b). For this case, it is the shear force from the West flange that is most likely at least partially transferred to the foundation through this corner. Analogous comments apply to positions H and G and to TUD (Figure 3.17d-i).

Another difference between the experimentally obtained vertical strain distribution at the wall base and the one obtained from section analysis at position E is the magnitude of the vertical strains at the East flange end (Figure 3.16). Although as previously stated the magnitudes of the two vertical strain distributions cannot be directly compared, it is however important to note that the magnitude of the experimentally determined strains closest to the East flange end is lower than the reinforcement yield strain even at a drift of 1.0%, i.e., approximately when the nominal moment is reached. The experimentally determined vertical base tensile strains are expected to be influenced by tensile strain penetration into the foundation which increases the values of the tensile base strains [HRS04]. However, the experimentally determined strains are still about four times lower than the section analysis strains at the East flange end (Figure 3.16c). This clearly indicates that the experimentally determined tensile strains in the East flange end are significantly lower than section analysis predictions, and hence so is the tensile force provided by the reinforcement in this region. Therefore, the contribution of the tension reinforcement in the East flange to the wall strength is significantly lower than what section analysis suggests, i.e., not all reinforcement in the East flange is contributing effectively to the wall strength. Analogous comments apply to positions E and H of TUD. The previous observation on the effective contribution of the tension reinforcement does not affect positions F and G. For these positions the flange ends are the most tensioned zones of the section and hence the reinforcement in these zones contributes significantly to the wall strength. The implications of this are further discussed in Section 3.3.5.

Such significant deviations from the plane section assumption are possible due to the large shear deformations of the sections of slender core walls under diagonal loading. Shear deformations can account for up to 50% of the total wall section deformation when sections are mainly in tension [BDP08b] and [ZL14] and similar values have been found also for the U-shaped walls presented herein (see Section 3.3.4).



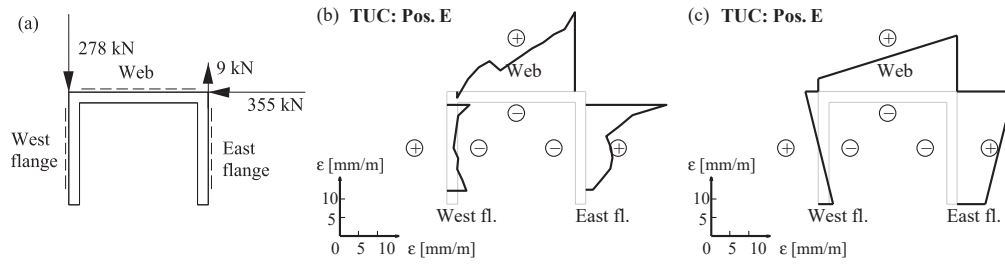


**Figure 3.16:** TUC: Compressive zones at the wall base under diagonal loading at position E at nominal point: nominal forces (a); vertical strain distribution from experimental measurements at the outer side of the wall (b) and from plane section analysis prediction also at the outer side of the wall (c). The values of the strains can be measured from the outer face of the U-shaped section using the strain scale provided in the left down corner of the subplots.

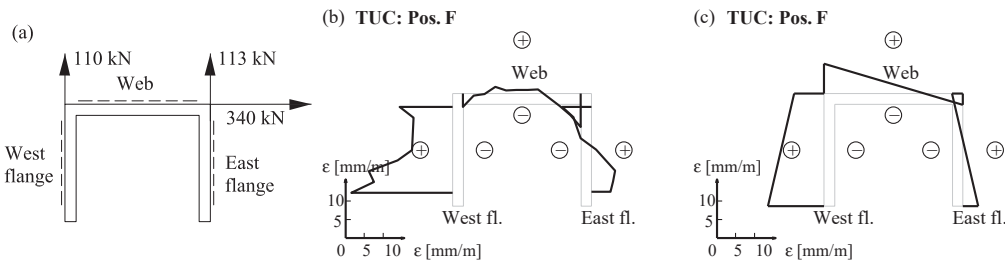


**Figure 3.17:** TUC: Compressive zones at the wall base under diagonal loading at position F at nominal point: nominal forces (a); vertical strain distribution from (b) experimental measurements and from plane section analysis prediction (c). The values of the strains can be measured from the outer face of the U-shaped section using the strain scale provided in the left down corner of the subplots.

### Influence on confinement lengths

An important issue that results from the analysis of vertical strain profiles at the wall base is the size of the compression zone at positions H shown in Figure 3.18 but also at position E. At these positions the compression zones are very deep (in particular along the outer perimeter). This large compression zone creates the potential for large compressive strains outside the confined area and hence for concrete crushing outside the confined boundary elements. Figure 3.18 compares the extent of the compressed flange zone under diagonal loading with the flange end in compression (positions H or E) against the compressed zone under symmetrical loading with both flange ends in compression (position C). The strain levels are compared for 0.6% drift which is the largest drift for which the wall was loaded to positions C and H.

Both experimental data and section analysis results indicate that the compression zone is significantly larger at position H (and by extension also at E) than at C. Hence the diagonal loading case with the flange ends in east compression should be the determining one for computing the confinement length of the flanges.

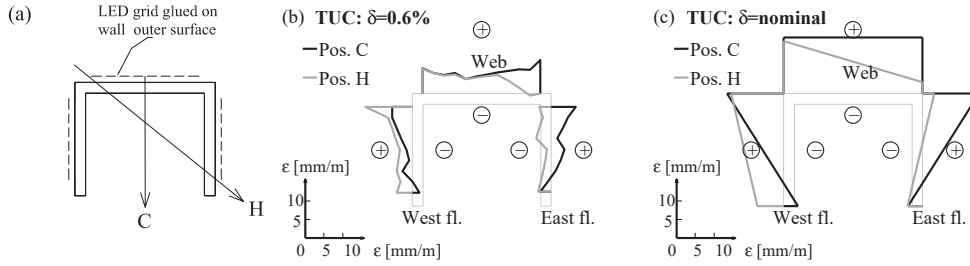


**Figure 3.18:** TUC: Vertical strains at the base of the wall for loading with the both flange ends in compression (position C) and with one flange end in compression (position H): loading positions (a), experimentally determined on the outer wall (b) and section analysis (c). Tensile strains are marked as positive and compressive strains negative. The values of the strains can be measured from the outer face of the U-shaped section using the strain scale provided in the left down corner of the subplots.

### 3.3.4 Shear to flexural displacements ratios

Typically the total horizontal displacement of a RC wall is considered to be composed of: flexural deformations (including base rotation due to strain penetration into foundation), shear deformations and sliding displacements at the wall base. In order to investigate the contribution of the shear displacements to the total displacement, the shear to flexural displacements ratio ( $\Delta_s/\Delta_f$ ) is generally used as an indicator. This ratio was found to be constant over the inelastic range for flexure-controlled walls [Daz00], [BDP11] and [ZL14].

For the two tests presented in this paper, the  $\Delta_s/\Delta_f$  ratios were determined from the optical measurement data. For each wall section component, the LED grid was divided into rectangular elements each spanning horizontally between the two outer LED columns and vertically between two consecutive LED rows. For each such rectangular element, flexural deformations were computed by double-integration of the curvatures and shear deformations were computed from the change in length of the diagonals of the elements, according to the procedure explained in more detail in [Han13]. The procedure for computing the curvatures was slightly modified by assuming a best linear fit of the vertical displacements over each row of LEDs. Flexural deformations at the height of load application were derived assuming that curvatures decrease linearly to zero from the top of the measurement grid ( $\sim 1.7$  m) to the height of load application ( $h_{EW} = 3.35$  m and  $h_{NS} = 2.95$  m). Over this same height interval shear deformations were considered to be zero, as such deformations concentrate mainly in the plastic hinge region [HRS04] and [BDP11] and hence below the height of  $\sim 1.7$  m.

The sliding displacements at the wall base were determined as the difference in horizontal displacements of the foundation row of LEDs and the first row on the wall (measuring height  $h = 0 - 75$  mm). In agreement with findings in [BDP08b], sliding displacements were small accounting for a maximum of 3.7%, 5% and 3.5% of the total top displacement for the web, West flange and East flange respectively for TUC at 2.5% drift and accounted for less than 2% for all wall sections of TUD. Therefore the sliding displacements were included in the computation of the shear displacements.

Previous experimental research on RC core walls by [BDP08b] and [ZL14] found that the contribution of shear displacements to the total displacements depends strongly on the loading direction, with the largest contribution being when wall sections (flanges or web) are under net tension. For U-shaped walls, this is the case for the web at positions E and H, the West flange at position F and the East flange at position G. The shear displacements for these loading cases were found to be significantly larger than those for typical slender rectangular walls ([BDP08b] and [ZL14]). These trends are confirmed also by the two wall tests presented herein (Figure 3.19b, c and Table 3.4). The shear deformations are as large as  $\sim 50 - 70\%$  of the flexural deformations for the web at positions E and H (Figure 3.19c – left), and as large as  $\sim 60 - 100\%$  of the flexural deformations for the flange under tension at diagonal loading: positions F and G (Figure 3.19b – right). For both the flanges and the web mainly in tension at these loading positions, the contribution of the shear deformations to the total deformation increased with higher axial load ratio (Figure 3.19b-c). Higher axial load ratio leads to higher shear demand on the wall sections, hence smaller crack angles with vertical axis of the wall (Section 3.3.2) and therefore larger shear deformations [HRS04], [BDP11], [Han13].

The longitudinal reinforcement layout (concentrated or distributed) also influences the contribution of the shear displacements to the total displacements:  $\Delta_s/\Delta_f$  ratios are larger for the flange with concentrated reinforcement layout than for the flange with distributed reinforcement layout case [Bru09] and [RA<sup>+</sup>14]. Also this trend is confirmed by results from TUC and TUD, by comparing the two flanges with concentrated (West) and distributed (East) longitudinal reinforcement distribution under symmetric loading conditions. More precisely  $\Delta_s/\Delta_f$  ratios are compared for the NS cycles – positions C and D (Figure 3.19d) and for the diagonal cycles – West flange at positions E and F with East flange at positions H and G (Figure 3.19b).  $\Delta_s/\Delta_f$  ratios are averaged over the drift range over which the  $\Delta_s/\Delta_f$  ratios are approximately constant, i.e., 0.6% to 2.0% drift or 1.0% – 2.0% drift (flange in tension at positions F and G) (Figure 3.19), are given in Table 3.4.

The flange with concentrated reinforcement layout (West flange) leads to larger  $\Delta_s/\Delta_f$  ratios than the flange with distributed reinforcement layout (East flange). The difference in  $\Delta_s/\Delta_f$  ratios results from the different longitudinal reinforcement ratios of the wall section between the boundary elements, which is smaller for the concentrated reinforcement layout. As a result, crack widths are larger in this area (Section 3.3.2) and so are shear deformations. This holds for either test units irrespective of whether the flange is mainly under tension (positions F, G and D) or compression (positions C, E and H). While the difference in percentages is substantial ( $\sim 14\%$  to  $\sim 44\%$ ), the absolute difference in  $\Delta_s/\Delta_f$  ratios between the two flanges is only significant when the flanges are in tension and the wall is loaded in the diagonal direction (difference in  $\Delta_s/\Delta_f$  ratios of 0.20 and 0.29) and relatively small when the flanges are in compression, i.e., as small as 0.06 (Table 3.4).

### Chapter 3. Quasi-static tests of two U-shaped walls under diagonal loading

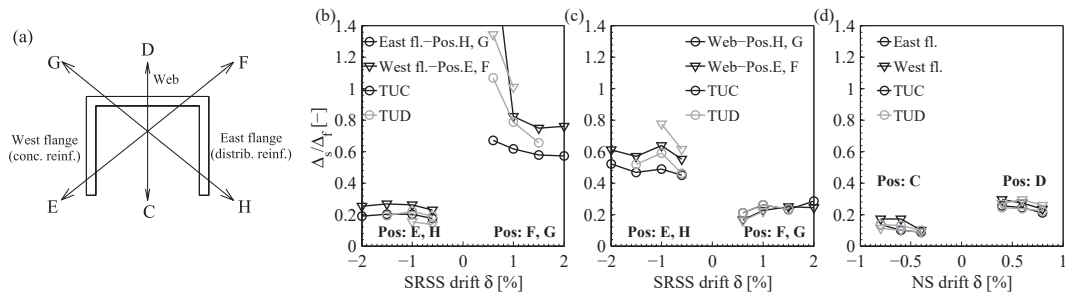


**Figure 3.19:** TUC and TUD: shear to flexural displacement ratios for: the flange under compression at position E and H (a), web under compression at positions F and G and under tension at E and H (b) and both flanges at positions C and D (c)

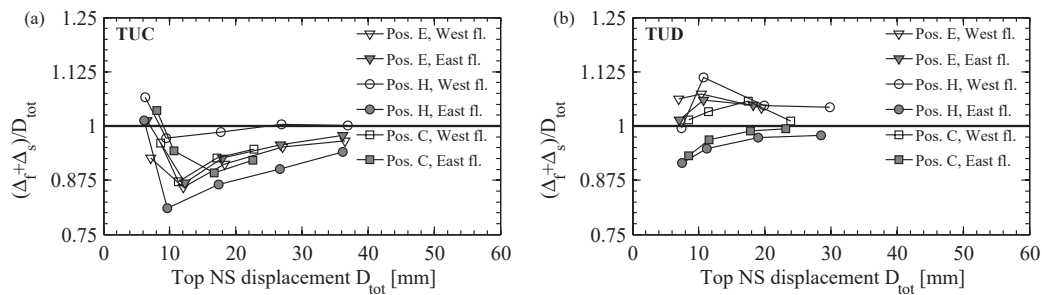


**Figure 3.20:** TUC and TUD: comparison of the top displacement obtained as the sum of flexural and shear displacements, derived from the LED measurements, with the top displacements  $D_{tot}$  as measured by the top LVDTs and corrected for foundation flexibility. Comparison is done for the two wall flanges, West and East at positions E, H and C.

This does, however, not apply to TUD when the flanges are in compression: here the  $\Delta_s/\Delta_f$  ratios are slightly larger for the flange with distributed reinforcement (East flange) than for the flange with concentrated reinforcement (West flange). It is postulated that this small difference stems from the assumptions behind the derivation of the flexural displacements: the flexural displacements were computed fitting a linear strain profile over the flange length, which yields for the concentrated reinforcement layout under high axial forces a poorer fit than for the other cases. As a result, the flexural displacements as well as the total displacements tend to be overestimated (Figure 3.20).

**Table 3.4:** Average shear to flexural deformation ratios: comparison between symmetric loading positions for the two flanges with concentrated and distributed reinforcement

Flange	Flange in compression		Flange in tension	
	Pos. E/H	Pos. C	Pos. F/G	Pos. D
TUC				
Distrib. (East)	0.18	0.10	0.54	0.21
Conc. (West)	0.24	0.14	0.74	0.24
Difference distr.-conc.	0.06	0.04	0.20	0.03
Percentage difference [%]	33%	40%	37%	14%
TUD				
Distrib. (East)	0.19	0.11	0.69	0.22
Conc. (West)	0.13	0.09	0.98	0.26
Difference distr.-conc.	-0.06	-0.02	0.29	0.04
Percentage difference [%]	-32%	-18%	42%	18%

### 3.3.5 Comparison of experimentally determined moment capacities with section analysis estimates

The U-shaped wall strength capacity under diagonal loading was shown to be significantly overestimated by a plane section analysis, especially for loading with one flange end in compression (positions E and H) [BDP08b]. For the two U-shaped wall tests presented here, the experimentally determined moment-curvature hysteresses are compared with the values obtained from section analysis (Figure 3.21). The numerical model used for the section analysis was briefly described in Section 3.3.3.2. The experimental curvature was determined from the LVDT measurements, corrected to filter-out the influence of tensile and compressive strain penetration. For this, the procedure used by Hines et al. [HRS04] was employed. The best linear fit line of the curvature profile over the height interval  $h=50-850$  mm was extrapolated to the wall base and the intersecting value was taken as the experimental base curvature (Figure 3.20d). The SRSS moment was computed as:

$$M_{SRSS} = \sqrt{(M_{EW}^2 + M_{NS}^2)} \cdot sign(\Delta_{NS}) \quad (3.3)$$

where  $M_{EW}$  and  $M_{NS}$  are the moments at the base of the wall for bending around the axis perpendicular to the web and parallel to the web respectively. The SRSS value was multiplied by the sign of the NS displacement for plotting the hysteresis loops consistently.

### Chapter 3. Quasi-static tests of two U-shaped walls under diagonal loading

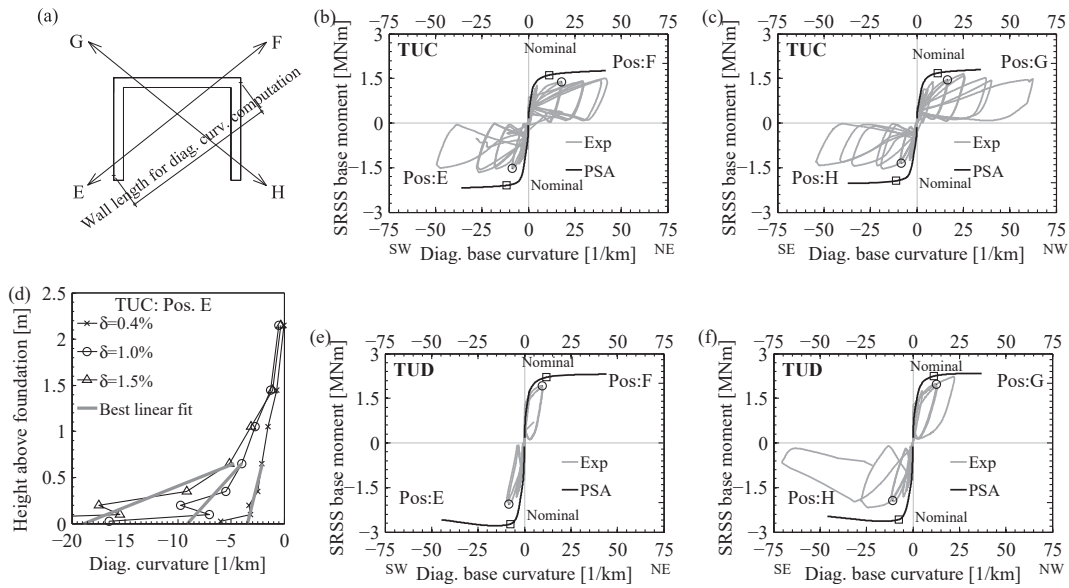


**Figure 3.21:** Comparison between the experimentally determined moment-curvatures and results from plane section analysis (PSA) for the diagonal loading directions (a) for TUC (b-d) and TUD (e-i). The position of the nominal point is indicated in the moment-curvature relationships for both experimental (round marker) and plane section analysis (square marker).

For both test units, section analysis overestimates the SRSS moment at positions E and H by  $\sim 15$  to  $25\%$ . For position F of TUC and G of both TUC and TUD the match is relatively good (less than  $10\%$  overestimation) (Figure 3.21 b-c, e-f). For position F of TUD the overestimation is slightly higher ( $\sim 12\%$ ) but this is because the maximum moment capacity was most likely not reached for this position due to prior wall failure in the other diagonal direction (see Section 3.3.1.2 and compare Figure 3.21e and f). The SRSS moment capacity is overestimated by section analysis because it fails to capture the experimentally determined vertical strain distribution at the base of the wall under diagonal loading (see discussion in Section 3.3.3.2).

More specifically, plane section analysis overestimates the flange width over which the tension reinforcement contributes effectively to the strength capacity of the wall and hence overestimates also the wall moment capacity. This effect was found to be important at positions E and H (see Section 3.3.3.2) and hence explains the larger moment overestimations at these loading positions. In addition, plane section analysis does not capture the extra compression zone at the corner web-flange (see Section 3.3.3.2). Wall moment capacity estimated with plane section analysis accounts for this zone as being in tension and hence the reinforcement in this corner contributes to the wall strength which should not be the case as these zones are in compression (Figure 3.16 and Figure 3.17). This compression zone is again more evident at positions E and H (Figure 3.15 b, d, f, h) and less important for position F and G (Figure 3.15 c, e, g, i) hence also the relatively smaller moment overestimations for the latter loading positions.

## 3.4 Conclusions

This chapter presented results from the experimental tests of two U-shaped walls under quasi-static loading along the diagonal directions of the section, which were loaded up to axial load failure. The main objective was to investigate the specific behaviour of U-shaped walls under diagonal loading. In addition, the effect of distributing the longitudinal reinforcement along the wall length instead of concentrating it in the boundary elements was studied. From the experimental measurements and observations the following conclusions concerning the behaviour of U-shaped walls under diagonal loading were drawn:

- The plane section assumption, which is the basis of simple analysis tools for RC walls, does not hold for the U-shaped walls under diagonal loading since it fails to capture the presence of additional compression zones at the corners between web and flange. Moreover plane section analysis overestimates the width of the flange over which the tension reinforcement contributes to the wall moment capacity. Both these effects result in overestimations of the moment capacity of U-shaped walls with plane section analysis for diagonal loading with largest overestimations for loading with the flange end in compression.
- Flanges of U-shaped wall subjected to bidirectional loading seem prone to out-of-plane buckling. For rectangular walls loaded in-plane, the out-of-plane instability is mainly caused by construction imperfections. For flanges of U-shaped walls, out-of-plane buckling of the flange ends is in addition promoted by the significant vertical strain gradient across the flange width when the wall is subjected to diagonal loading, which leads to an eccentricity of the axial force acting on the boundary element.
- The compression depth of the flange ends is the largest under diagonal loading with one flange end in compression, and hence the confinement length of the flange end should be estimated from this loading case. Particular attention should be given to adapt the confinement reinforcement to the longitudinal reinforcement layout used, as distributed reinforcement layout will generally require smaller stirrup spacing due to the smaller vertical bar diameter and longer confinement lengths.
- The axial load ratio, which was the main varying parameter between the two tests, was found to influence the wall ultimate displacement and the failure mode. The higher axial load ratio reduced the ultimate displacement capacity of the wall as the failure modes of both test units were compression-controlled. Both walls failed under diagonal loading with one flange end in compression, and their failure modes involved concrete crushing in the flange unconfined part. All these observations underline: (1) the importance of proper confinement of the flange ends to ensure the wall displacement ductility as well as (2) the importance of distributing more than the minimum required longitudinal reinforcement content within the unconfined concrete part of the wall to delay or avoid excessive concrete crushing in these regions.

### Chapter 3. Quasi-static tests of two U-shaped walls under diagonal loading

---

The experiments showed that the longitudinal reinforcement layout influenced the following mechanisms:

**Bar buckling** : For distributed reinforcement layouts, the diameter of the longitudinal bars in the boundary elements is typically smaller than for concentrated reinforcement layouts. For the same stirrup spacing, bars in the distributed reinforcement layout will therefore buckle and fracture at smaller drifts.

**Out-of-plane buckling of the boundary element over the height of the plastic zone** : Mechanical models have shown that the larger the longitudinal reinforcement content of the boundary element, the more prone it is to buckling. This was confirmed by the failure mode of TUC, where only the flange with the concentrated reinforcement developed an out-of-plane failure. Hence, one possible way of minimising the potential for out-of-plane buckling of the flange ends is to distribute the longitudinal reinforcement along the wall length.

**Compression zone depth** : Distributed reinforcement layouts lead to larger compression zone depths, which increases the susceptibility to concrete crushing. This was observed for TUD, where the compression depth extended into the non-confined part and a sudden crushing of the entire flange with distributed reinforcement was observed.

**Crack widths** : A distributed reinforcement layout features higher reinforcement contents in the wall section between the boundary elements than a concentrated reinforcement layout. The experiments showed that the increased reinforcement content helps controlling the crack widths in this area.

**Shear deformations** : As a result of the smaller crack widths, distributing the longitudinal reinforcement reduced also the shear deformations. This seems particularly important for U-shaped walls as shear deformations can account for up  $\sim 40 - 50\%$  of the total deformation when the flanges or the web are mainly in tension.

The experimental data gathered from the two tests will complement the limited database of core walls subjected to bidirectional loading. This data will serve as validation for future numerical and mechanical models.

## 3.5 Dataset

The experimental data from the two quasi-static cyclic tests was made publicly available. The Appendix of this report contains the link where the data can be downloaded and it also describes how the data is organised.



# 4. Experimentally derived quantities for the plastic hinge model

## 4.1 Introduction

Most of the equations for quantities involved in plastic hinge (PH) analysis are empirical or semi-empirical and have been mainly developed for rectangular walls or even for beams and columns (see Section 2.2.2). The suitability of these equations for the plastic hinge analysis of core walls has been only marginally assessed [BDP08b], [SS<sup>+</sup>13] despite the popularity of the plastic hinge method within the design engineering community. Therefore, in this section, existing estimates of plastic hinge quantities are compared to experimental results from four U-shaped wall tests, namely to two quasi-static cyclic tests presented in Section 3 (TUC and TUD) and to two previous tests by [BDP08b] (TUA and TUB), with the following objectives in mind:

- assess suitability of the state-of-the-art PH estimates for application to U-shaped walls and establish if new estimates are required
- derive experimental quantities for PH analysis using a consistent approach in order to allow validation with numerical models

The findings in this section aim to complement the previous study by [BDP08b] on the suitability of the state-of-the-art PH estimates for application to U-shaped walls. Note that some of the experimentally derived quantities for TUA and TUB might be different from the original reference since procedures for their derivation were modified in this chapter. Besides the comparison with the estimates, the experimental results will also be used in Chapter 5 to validate two numerical models for U-shaped walls, which in turn will be used for parametric studies in Chapter 6. Therefore the derivation procedures of the PH quantities from experimental results required a more consistent approach. These procedures will be presented throughout this chapter for each investigated quantity.

## Chapter 4. Experimentally derived quantities for the plastic hinge model

---

In the application of the PH analysis, the force-displacement relationship is obtained from a moment-curvature response of the wall base section using estimates for the shear to flexural displacements ratio  $\Delta_s/\Delta_f$ , the plastic hinge length  $L_{ph}$  and the strain penetration length  $L_{sp}$  (Figure 4.1). The moment-curvature response can be obtained from section analysis or its bi-linear idealisation can be directly obtained from estimates of the key quantities, such as for example the yield curvature  $\phi_y$ . Therefore, in this section the following experimentally derived quantities are compared to the estimates:

- Yield curvature  $\phi_y$
- Yield displacement  $\Delta_y$
- Plastic hinge length  $L_{ph}$
- Ultimate strain limits
- Shear displacements  $\Delta_s$

In addition, the effective stiffness  $K_{eff}$  of the U-shaped walls is investigated for the different loading positions. Although  $K_{eff}$  is not a necessary quantity in the application of the PH model it can be derived straightforwardly from PH quantities as the ratio between first yield force and first yield displacement  $K_{eff} = F_y/\Delta'_y$ . This is equivalent to the ratio of between nominal force and nominal yield displacement  $K_{eff} = F_n/\Delta_y$ . The effective stiffness  $K_{eff}$  is an useful quantity in the analysis and design of buildings with RC walls, e.g. in linear analyses of RC buildings with walls for estimating the period of the structure.

The chapter starts with Section 4.2 which presents the derivation of the displacement components, i.e., flexural and shear displacements, necessary in the further derivation of the PH quantities. The experimental PH quantities are then compared to estimates in the order listed above. Particular emphasis is placed on the yield displacement  $\Delta_y$  results and the corresponding estimates (Section 4.4). The assumption of a linear curvature profile at first yield [PCK07] and modifications to account for the extent of cracking over the wall height are also investigated. The chapter ends with a section on the effective stiffness of U-shaped walls (Section 4.8).

### 4.2 Experimentally determined displacement components

During the testing of test unit C (TUC) and test unit D (TUD) (Section 3), the wall behaviour was monitored by means of two different measuring systems, namely: (1) a conventional measurement system composed of linear variable differential transducers (LVDTs) and load cells and (2) an optical measurement system composed of active light emitting diodes (LEDs) glued to the outer surface of the wall and three cameras tracking their displacements during the test. The two systems are presented in detail in Section 3. While the conventional measurement system was also used for the monitoring of TUA and TUB ([BDP08b]), the optical measurement system was newly introduced for TUC and TUD. A similar optical measurement system was previously used for rectangular RC walls by [Han13], which presents also procedures for derivation of displacement components from such measurements.

## 4.2. Experimentally determined displacement components

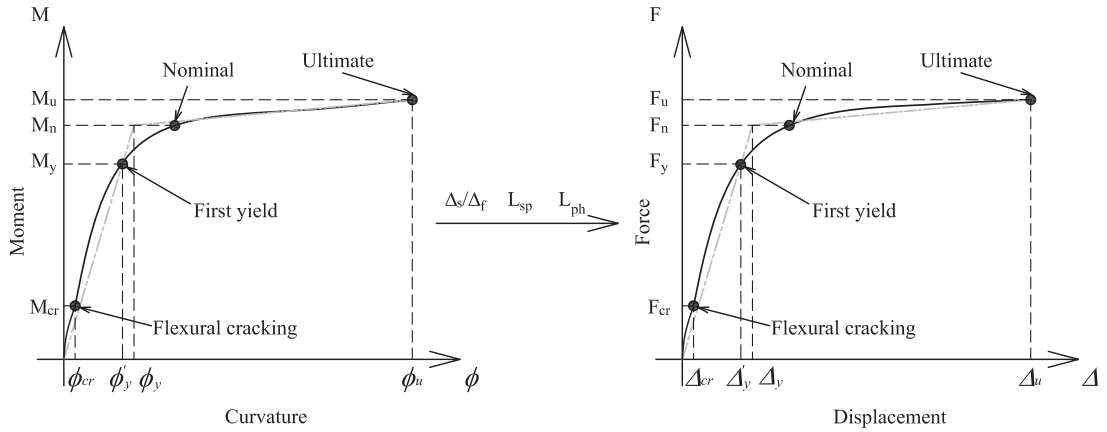


**Figure 4.1:** Plastic hinge analysis - obtaining the force-displacement response from the moment-curvature response by means of several quantities: shear to flexural displacements ratio  $\Delta_s/\Delta_f$ , strain penetration length  $L_{sp}$  and plastic hinge length  $L_{ph}$

Having two independent measuring systems has allowed the computation of the displacement components in two different ways and hence the cross-checking the experimentally derived data. This section explains how the displacements components of TUC and TUD have been derived from the two measurements systems.

Typically the total horizontal displacement of a RC wall is considered to be composed of: flexural displacements (including base rotation due to strain penetration into foundation) and shear displacements (including sliding displacements at the wall base). In general, the flexural displacements can be determined by double-integration of the average curvatures over the height of the wall. The shear displacements can then be computed through the so-called "indirect" method: by subtracting the flexural displacements from the measured top horizontal displacement. Alternatively, if the measurement system permits, the shear displacements can be computed directly from the shear distortion of instrumented rectangular panels on the surface of the wall. All these methods are further explained in the following.

For the conventional measuring system, curvatures were determined from the average strains of the LVDT chains mounted at the outside edges of the wall for each wall section (web or flanges) and also for the diagonal directions. Curvatures along the wall height for the East flange were computed, for example, as in [BDP08b]:

$$\phi = \frac{\delta_{SE,i}/dh_{LVDT,i} - \delta_{NE,i}/dh_{LVDT,i}}{l_w'} \quad (4.1)$$

where  $\delta_{SE,i}$  and  $\delta_{NE,i}$  are the measured displacements in the  $i$ -th instrument from the wall base,  $dh_{LVDT,i}$  is the measuring base length of the  $i$ -th instrument and  $l_w'$  is the horizontal distance between the  $SE$  and  $NE$  LVDT chains.

## Chapter 4. Experimentally derived quantities for the plastic hinge model

The shear displacements were determined from the conventional measurement system through the indirect method: by subtracting the flexural displacements from the total top horizontal displacements. Shear displacements were computed in this manner for all wall sections, i.e., web, West flange and East flange, and also for the diagonal direction of the wall.

Flexural and shear displacements were also computed from the optical measurement system. For each wall section component, the LED grid was divided into rectangular elements each spanning horizontally between the two outer LED columns ( $d = 8 \times 100$  mm for the web and  $d = 11 \times 100$  mm for the flanges) and vertically between two consecutive LED rows ( $dh_{LED,i} = 125$  mm for TUC and  $dh_{LED,i} = 100$  mm for TUD) (Figure 4.2). Flexural displacements were computed as in Equation 4.2a, assuming a constant curvature over the height of the rectangular element  $dh_{LED,i}$ . Due to premature loss of LEDs from the outer columns of the wall section, the curvatures were computed using a best linear fit of the vertical displacements over each row of LEDs. The shear displacements were also computed from the rectangular LED elements from the change in length of the element diagonals (Equation 4.2b). No correction with curvature was performed for the shear deformations as it was assumed that curvatures are constant over the height  $dh_{LED,i}$ , for which the shear displacements were computed [Hir84].

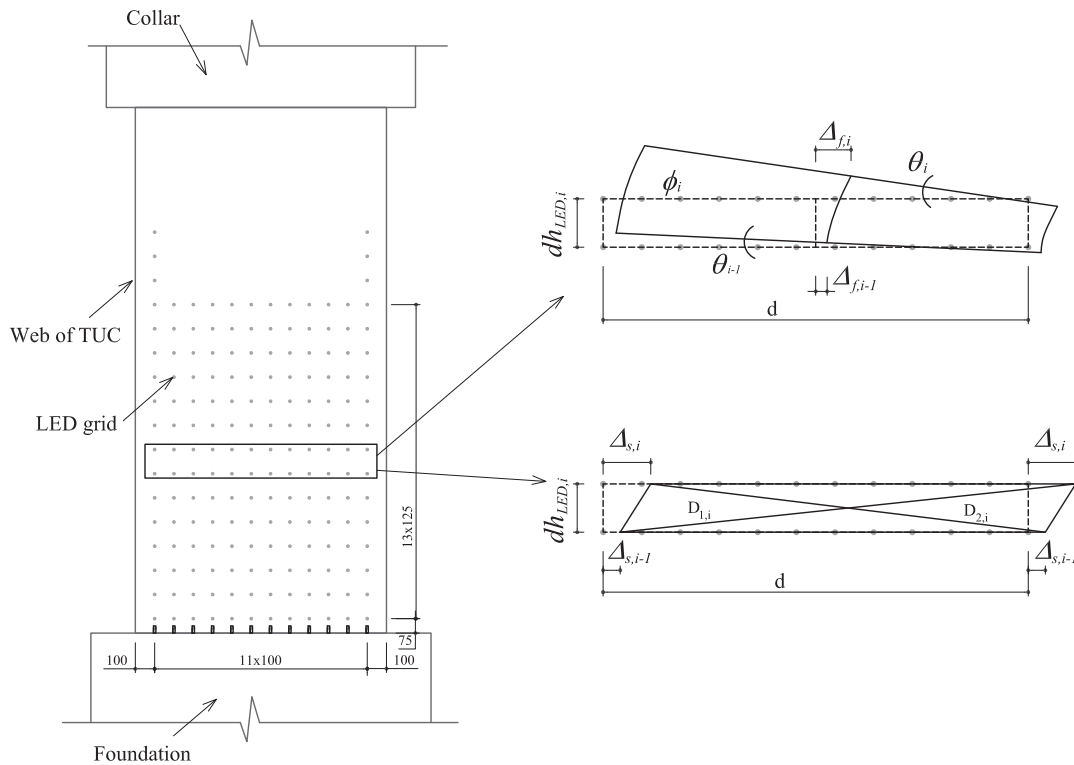


**Figure 4.2:** Sketch for the calculation of flexural and shear displacements from the optical measurement data, for one rectangular element. A rectangular element taken from the LED grid on the web of TUC is given as an example.

$$\Delta_{f,i} = \Delta_{f,i-1} + \theta_{i-1}dh + \frac{\phi_i dh^2}{2} \quad (4.2a)$$

$$\Delta_{s,i} = \Delta_{s,i-1} + \frac{D_{1,i}^2 - D_{2,i}^2}{4d} \quad (4.2b)$$

For both measuring systems, flexural displacements at the height of load application were derived assuming that curvatures decrease linearly to zero from the top of the measurement grid ( $\sim 1.7$  m for the LED grid and 2.65 m for the LVDT chains) to the height of load application ( $h_{EW} = 3.35$  m and  $h_{NS} = 2.95$  m). Over this same height interval for the LED grid, the shear displacements were considered to be zero, as such deformations concentrate mainly in the plastic hinge region [BDP11], [HRS04] and hence below the height of  $\sim 1.7$  m.

The sliding displacements at the wall base of TUC and TUD could be determined only from the optical measuring system as the difference in horizontal displacements of the foundation row of LEDs and the first row on the wall (measuring height  $h = 0 - 75$  mm). In agreement with findings in [BDP08b], sliding displacements were small accounting for a maximum of 3.7%, 5% and 3.5% of the total top displacement for the web, West flange and East flange respectively for TUC at 2.5% drift and accounted for less than 2% for all wall sections of TUD. Therefore the sliding displacements were included in the computation of the shear displacements.

All deformation quantities of TUC and TUD were corrected for foundation flexibility, i.e., sliding and uplift of the wall foundation with respect to the strong-floor of the testing laboratory. Top displacements due to foundation flexibility were derived from the optical measurement data, and accounted for 6 – 8% of the top displacements at yield drift and decreased thereafter.

## 4.3 Yield curvature

### 4.3.1 Definition

Yield curvature is a concept introduced for design purposes and it marks the boundary between elastic and inelastic phase in a bi-linear moment-curvature relationship describing the flexural behaviour of an RC wall (Figure 4.1). It is defined as in Equation 4.3 where  $\phi'_y$  and  $M_y$  are the curvature and respectively the moment corresponding to first yield, while  $M_n$  is the moment corresponding to nominal point or to serviceability limit state (Figure 4.1).

$$\phi_y = \phi'_y \frac{M_n}{M_y} \quad (4.3)$$

### 4.3.2 Determining the experimental first yield point

Typically the first yield point is defined for section analysis as the point on the moment-curvature response when the most tensioned reinforcement first reaches the yield strain or when the most compressed concrete fibre reaches a strain of  $-0.002$ , whichever occurs first [PCK07]. When assessing the first yield point from experimental data, the question arises which experimental strains should be taken for the comparison with these limit state strains.

#### 4.3.2.1 Strains at base of the wall

Comparing the experimental strains recorded near the wall base (the section of the largest moment demand) with plane section analysis strains will only lead to unreliable results as anchorage deformation (or strain-penetration effects) heavily influences the magnitude of these strains. The term "strain penetration" describes the following phenomena: (1) the tensile strains in the longitudinal reinforcement do not drop to zero immediately below the wall base, but decrease gradually with depth into the foundation and (2) similarly, on the compressed side of the wall, below the wall base, the concrete compressive strains also dissipate with depth into the foundation [PCK07]. As a consequence, the measured tensile and compressive strains near the base of the wall are not representative for the deformation of the wall section itself but contain also the deformation due to strain penetration into the foundation, e.g. [HRS04], [BDP08b]. For the cases of TUA to TUD, the vertical strain measurements from the first LVDT above the wall base over the height  $h = 0 - 50$  mm and the first row of LEDs (for TUC and TUD only) from the base ( $h = 0 - 75$  mm) included this strain penetration effect.

#### 4.3.2.2 Procedures for determining first yield

However, different procedures can be used to estimate the first yield point and/or the corresponding curvature  $\phi'_y$  from the experimental data. For example, [BDP08b] determined the first yield point of TUA and TUB, based on the comparison of the average LVDT strains measured over  $h = 50 - 250$  mm, i.e., just above the base strains, with the limit strains. The first yield curvature was then computed as the extrapolation to the wall base of the best-linear fit of the curvature profile over the height of  $h = 50 - 1650$  mm, interval over which the experimental curvatures were found to be linear. A procedure of computing the base curvature from the curvature measurements above the base with a best linear fit was suggested by [HRS04].

Another possible procedure to find the first yield point is the one used by [DBB09] to relate different serviceability and ultimate limit states to section analysis strains. More precisely, [DBB09] related the curvature obtained from section analysis with the experimental base curvature, which was taken as the extrapolation to the wall base of the best-linear fit of the curvature profile over the plastic zone length  $L_{pz}$  (i.e., height over which curvatures were larger than the yield curvature). If the experimental base curvature would be computed as in the procedure by [HRS04], then this curvature can be compared with the one from section analysis to determine the first yield point.

In order to derive the first yield curvature with any of the above procedures, it is necessary to check the height over which the curvature profile can be considered as linear. Therefore, the experimental curvature profiles at first yield are discussed in the following section.

### 4.3.2.3 Curvature profiles and cracked height at first yield

An initial determination of the first yield point was done for all test units using the procedure by [BDP08b], i.e., by comparing the average LVDT strains above the wall base ( $h = 50 - 250$  mm) with the limit strains previously mentioned. The LVDT strains at the wall base ( $h = 0 - 50$  mm) were not considered due to the inclusion of the strain penetration effect, as previously mentioned. Instead, the strains averaged over the second LVDT ( $h = 50 - 150$  mm) and the third ( $h = 150 - 250$  mm) LVDT from the base were taken for the comparison based on the crack spacing at first yield [BDP08b].

The experimentally determined curvature profiles from all test units and for all loading positions, obtained at first yield determined as above, are plotted in Figures 4.3 and 4.4 for all four test units. The shape of the curvature profile at first yield is clearly not linear over the shear span of the wall  $H$ , i.e.,  $H = 3.35$  m for the EW direction and  $H = 2.95$  m for all other loading directions. The shape of these curvature profiles can be approximated by a rather bi-linear trend: linear from base up to about half the shear span, then again linear but with a different slope up to the shear span. The linear branch from the wall base to about half the shear span, corresponds approximately to the height of the wall which is cracked at first yield  $H_{cr}$ , while the upper part of the wall remains uncracked.

In Figures 4.3 and 4.4, the extent of cracking over the wall height at first yield  $H_{cr}$  was computed assuming a linear moment profile over the wall height.  $H_{cr}$  was determined as the maximum value between the height where the moment equals the cracking moment  $M_{cr}$  and the wall length  $l_{wall}$  which was included to account for tension shift effects (Equation 4.4).  $M_{cr}$  is the analytical cracking moment derived as in Equation 4.5 [PP75],  $M_y$  is the experimentally determined moment corresponding to the first yield point and  $H$  is the wall shear span depending on the loading direction.

$$H_{cr} = \max(l_{wall}; (1 - M_{cr}/M_y)H) \quad (4.4)$$

where

$$M_{cr} = (f_t + \frac{N}{A_g}) \frac{I_g}{y_t} \quad (4.5)$$

where  $f_t = 0.33\sqrt{f_c}$  is the tensile strength of concrete, with  $f_c$  as the concrete compressive strength at the day of testing, where  $N/A_g$  is the absolute value of the axial load ratio with  $N$  as the axial load and  $A_g$  as the gross wall section area, and where  $I_g$  is the moment of inertia of the wall section and  $y_t$  is the distance between the gravity centre of the cross-section and the extreme tensioned fibre, both latter quantities depending on the loading direction.

## Chapter 4. Experimentally derived quantities for the plastic hinge model

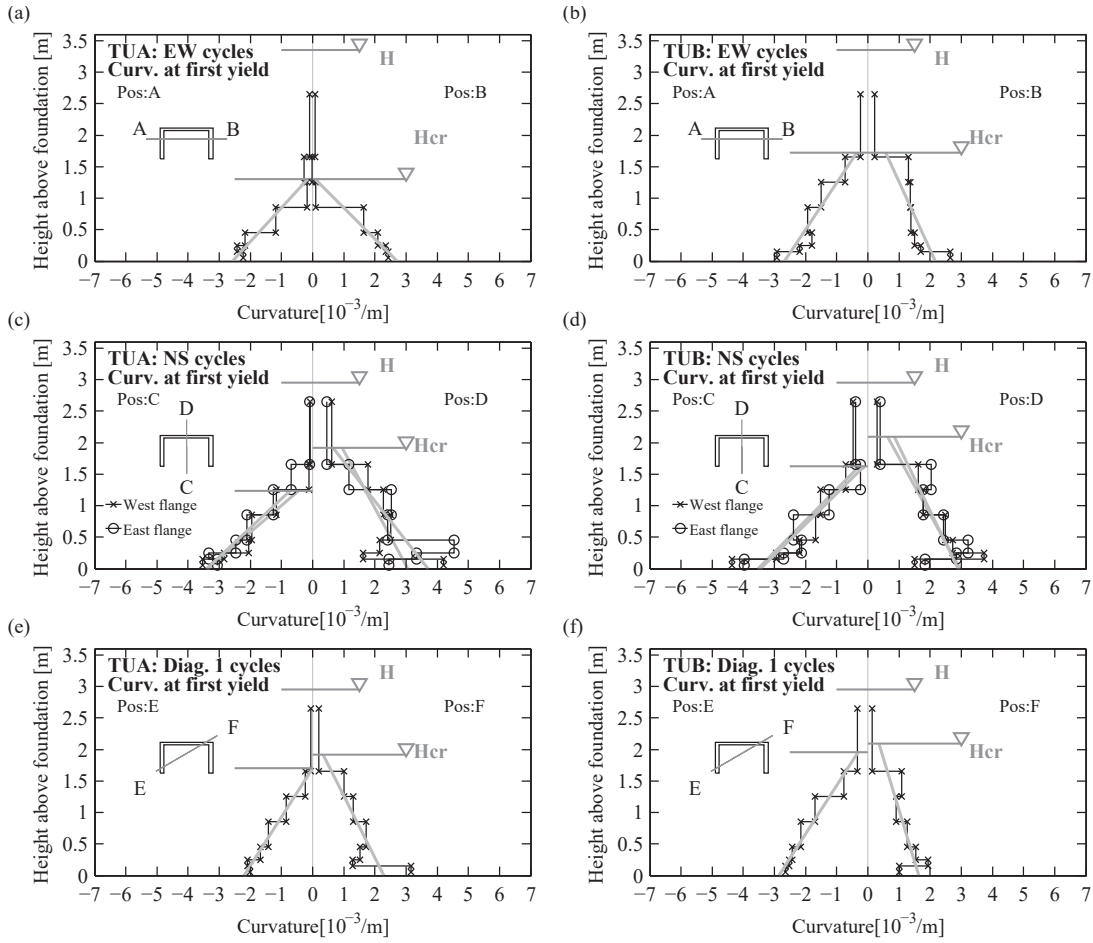


**Figure 4.3:** TUA and TUB: experimentally derived curvature profiles at first yield over  $h = 50 - 2650$  mm for all loading positions. The curvature at the wall base over  $h = 0 - 50$  mm was not plotted here as it captures mainly the strain penetration effects and affects the readability of the graph due to its comparable large value.

The extent of cracking determined analytically could not be verified by means of experimentally determined strains since the cracking strain corresponded to vertical displacements of 0.02 to 0.06 mm. Such displacements represent approximately 1 to 6 ‰ of the LVDT measurement range and hence the reliability of such measurements seems questionable. However, the analytically computed  $H_{cr}$  does seem to provide in most cases an approximately good estimate of the height over which the curvatures are linear from the base up the wall.



### 4.3. Yield curvature

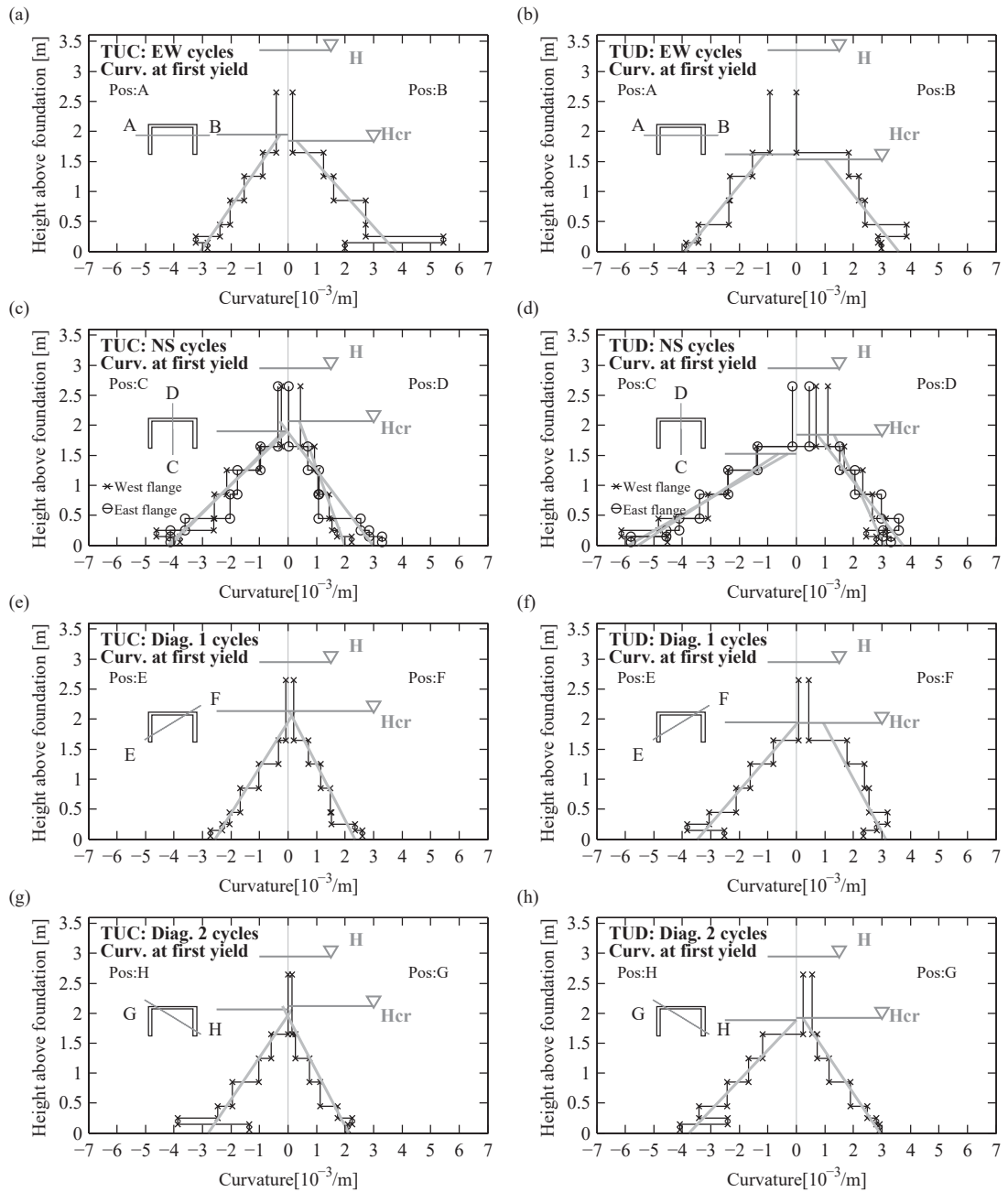


**Figure 4.4:** TUC and TUD: experimentally derived curvature profiles at first yield over  $h = 50 - 2650$  mm for all loadings. The curvature at the wall base over  $h = 0 - 50$  mm was not plotted here as it captures mainly the strain penetration effects and affects the readability of the graph due to its comparable large value.

### 4.3.2.4 Alternative procedure based on strains

As stated in the Introduction (Section 4.1), the experimentally derived PH quantities will be used for validation purposes with a detailed numerical model in Section 5.2, and next the validated numerical model will be used for parametric studies for walls with varying height, cross-section geometry and axial load ratio (Section 6). Using the strains over the height  $h = 50 - 250$  mm to determine the first yield point of all the different wall models seems hardly sound. Therefore, it is necessary to use a standardised procedure for determining first yield point, which can be applied irrespective of the wall height, section geometry or axial load ratio.

A procedure which links experimental results with section analysis through local deformations such as strains or curvatures is desirable as it allows the comparison of corresponding global quantities such as wall yield displacement or stiffness with estimates or with numerical results. Since the interest is also to compare the yield curvatures from section analysis with those experimentally obtained, the experimentally determined vertical strains will be used for determining the first yield. As previously discussed, the strains recorded at the base of the wall include the effect of the strain penetration. Hence a similar procedure to the one applied for determining the base curvature can be applied also for determining the base strains, i.e., base strain is determined as the intersection between the best linear fit of the strains over the cracked wall height at first yield and the wall base. Then, the first yield is determined at the instant when this base strain reaches first one of the first yield limit strains:  $-0.004$  concrete strain or  $\epsilon_{sy}$  reinforcement yield strain. The strain profiles and the corresponding linear fit are shown in Figures 4.5 and 4.6.

While the assumption of linearity over the cracked height has a physical meaning mainly for the tensile strains, it does seem to provide a good approximation also for the compressive strains at first yield although the compressive strains tend to typically concentrate towards the base of the wall (Figures 4.5 and 4.6). The first yield is triggered by the reinforcement strain in all cases except at position C and H of TUD due to the large axial load ratio of this test unit. These results are confirmed by moment-curvature (plane section) analysis. The model used for the section analyses is described in detail in Chapter 5 but some results will be anticipated in this section.

### 4.3.3 Comparison of experimental results with estimates and section analysis results

Using the procedure for determining first yield instant previously outlined, based on the linear fit of strains above the wall base, the experimental yield curvatures are evaluated. The first yield curvatures are derived from the curvatures above the wall base at first yield as described in Section 4.3.2.3 while the nominal to yield moment ratio  $M_n/M_y$  is computed from section analyses (see Chapter 5). The experimental yield curvatures are compared to estimates and to section analysis results under the form of dimensionless yield curvatures  $K_y$  ( $K_y = \phi_y l_{wall} / \epsilon_{sy}$ ) in Table 4.1. For improved readability, the results are shown also in graphical form in Figure 4.7.

### 4.3. Yield curvature

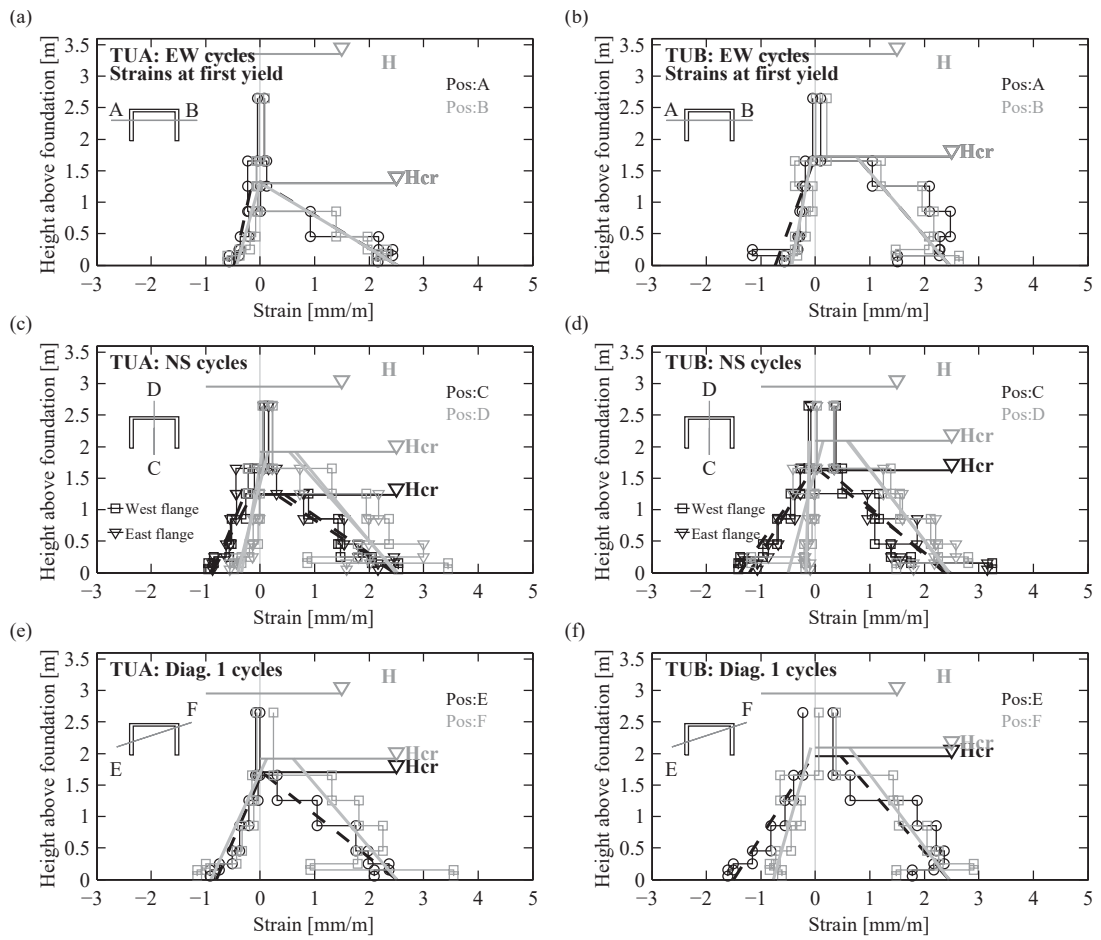


**Figure 4.5:** TUA and TUB: experimentally derived strain profiles at first yield over  $h = 50 - 2650$  mm for all loading positions

## Chapter 4. Experimentally derived quantities for the plastic hinge model

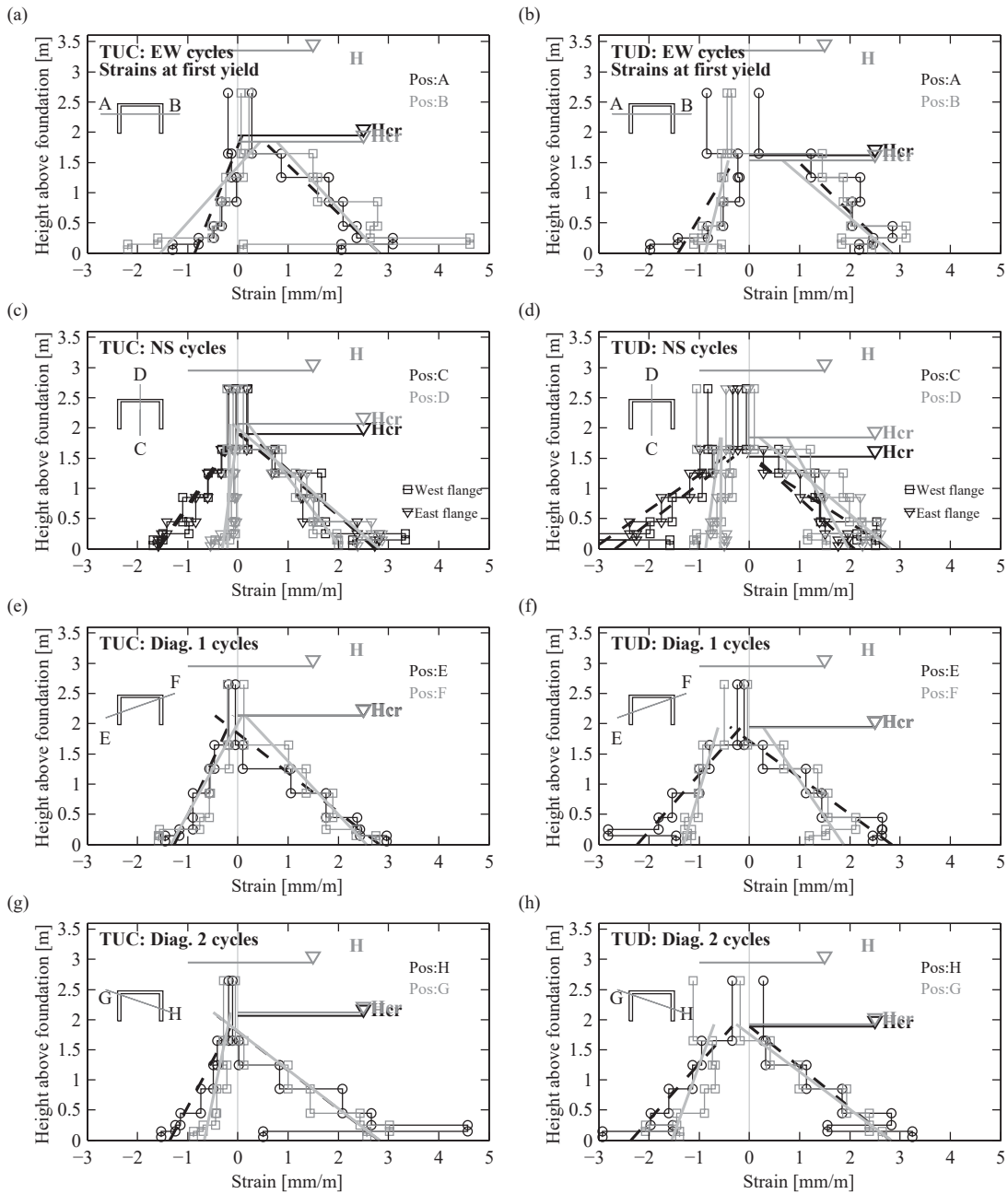


**Figure 4.6:** TUC and TUD: experimentally derived strain profiles at first yield over  $h = 50 - 2650$  mm for all loading positions

### 4.3. Yield curvature

When computing  $K_y$ , the wall length  $l_{wall}$  was taken as the length of the web  $l_{web}$  for loading along the web, as the length of the flanges  $l_{fl}$  for loading along the flanges, and as the geometric diagonal of the wall  $l_{diag} = \sqrt{l_{web}^2 + l_{fl}^2}$  for loading along the diagonal direction. The experimental results for  $K_y$  are compared to section analysis predictions, again anticipated here from Section 5.1, as well as to existing estimates for core walls (Section 2.2.2). The estimates from [Pau02], [PCK07] and [SS<sup>+</sup>13] are all derived from section analyses and yield rather similar values between each other.

The section analysis predictions match very well the existing estimates for the principal loading positions (A, B, C and D). No estimates for diagonal loading directions are currently available. Except at position B of TUC where the experimentally determined yield curvature is rather high ( $\sim 36\%$  difference with section analysis and also large value as compared with other experimental values at positions A or B), the difference between the experimentally determined yield curvatures and the section analysis predictions are below 15% and the match is hence fairly good. Therefore the experimental  $\phi_y^l$  and  $K_y$  determined with this approach will be used from here on in determining further experimental PH quantities.

**Table 4.1:** TUA to TUD: comparison of the experimentally determined dimensionless yield curvatures  $K_y$  with section analysis results and existing estimates

Pos.	Experiment				Section analysis				Estimates		
	TUA	TUB	TUC	TUD	TUA	TUB	TUC	TUD	[Pau02]	[PCK07]	[SS <sup>+</sup> 13]
A	1.41	1.42	1.60	1.80	1.36	1.35	1.53	1.64	1.40	1.50	-
B	1.39	1.28	1.95	1.59	1.36	1.35	1.43	1.53	1.40	1.50	-
C	1.66	1.76	1.94	2.36	1.62	1.74	2.00	2.05	1.80	1.85/ 2.15*	2.06/ 2.09*
D	1.46	1.33	1.30	1.42	1.46	1.41	1.49	1.55	1.40	1.50	1.55/ 1.65*
E	1.96	2.19	2.13	2.35	1.90	2.00	2.25	2.31	-	-	-
F	2.05	1.80	2.14	2.19	1.85	1.88	1.98	2.04	-	-	-
H	-	-	2.19	2.43	-	-	2.26	2.32	-	-	-
G	-	-	1.96	2.21	-	-	2.20	2.21	-	-	-

<sup>1</sup>\* Values for concentrated/distributed reinforcement layout.

The overall match between experimentally determined and section analysis predictions for the yield curvatures is further improved if the  $M_n/M_y$  values from section analysis used for the experimental determination of yield curvatures are replaced by the experimentally determined  $M_n/M_y$  values (see Figure 5.7). Using the  $M_n/M_y$  values from section analyses here, allowed to obtain yield curvatures also for the principal loading directions of TUC and TUD, which did not reach their nominal moment during the experiments as will be discussed in Section 5.1.2.4. These results are presented in detail in Section 5.1.2.4 but they are anticipated here to conclude that the sectional analyses can be used to estimate the yield curvature for U-shaped walls for the principal as well as for the diagonal loading directions.

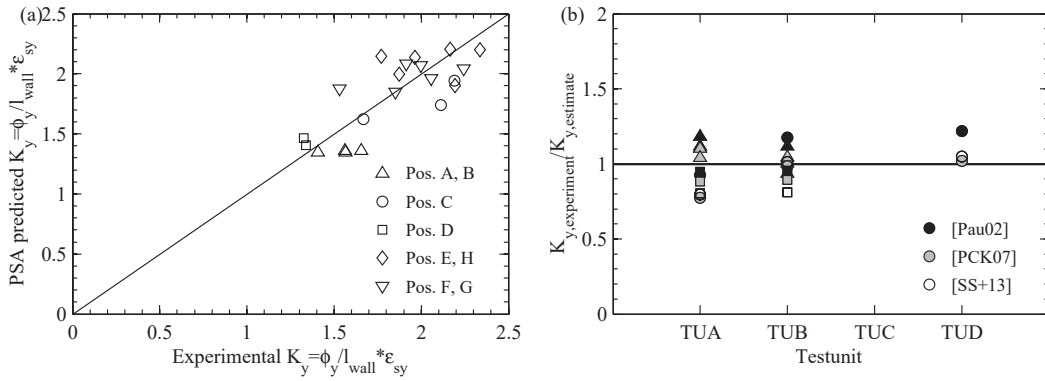


**Figure 4.7:** TUA to TUD: comparison of the experimentally determined dimensionless yield curvatures  $K_y$  with section analysis results (PSA) in (a) and with existing estimates in (b)

As a consequence, also existing estimates for yield curvatures of core walls under the principal loading directions derived from section analyses, provide good estimates of yield curvatures for U-shaped walls. These conclusions are in line with previous findings for TUA and TUB [BDP08b].

## 4.4 Yield displacement

### 4.4.1 Experimental yield displacement

Analogous to the yield curvature, the yield displacement  $\Delta_y$  marks the boundary between elastic and inelastic phase in a bi-linear force-displacement curve (Figure 4.1b) and it can be computed according to Equation 4.6 as the first yield displacement  $\Delta'_y$  times the nominal to yield moment ratio  $M_n/M_y$ . The experimental first yield displacement can be taken as the top wall displacement (i.e., at  $h_{NS} = 2.95$  m,  $h_{EW} = 3.35$  m and  $h_{diag} = 2.90$  m height above wall foundation) at the instant of reaching the first yield based on strain limits as explained in the previous section (Section 4.3). Then to obtain the experimental yield displacement, predictions of  $M_n/M_y$  values from section analyses (Chapter 5) can be used. The experimental yield displacements determined in this manner are given in Table 4.2 for TUA to TUD together with their corresponding top drifts, e.g.,  $\delta_{y,NS} = \Delta_{y,NS}/h_{NS}\%$ . Note that the yield displacements for TUA and TUB have slightly different values than those given in [BDP08b] due to the different procedure for determining the first yield point.

$$\Delta_y = \Delta'_y \frac{M_n}{M_y} \tag{4.6}$$

## 4.4. Yield displacement

**Table 4.2:** TUA, TUB, TUC and TUD: experimentally determined yield displacements  $\Delta_y$  and yield drifts  $\delta_y$  at the height of the shear span H.

Pos.	$\Delta_y$ [mm]				$\delta_y$ [%]			
	TUA	TUB	TUC	TUD	TUA	TUB	TUC	TUD
A	6.0	12.4	13.8	18.3	0.18	0.37	0.41	0.55
B	6.7	11.7	14.6	16.6	0.20	0.35	0.44	0.49
C	9.2	12.0	16.1	16.2	0.31	0.41	0.54	0.55
D	14.3	13.2	10.7	16.1	0.48	0.45	0.36	0.54
E	7.9	13.5	11.3	13.1	0.27	0.46	0.38	0.44
F	12.5	13.4	10.2	18.8	0.42	0.45	0.35	0.64
H	-	-	8.8	12.7	-	-	0.30	0.43
G	-	-	9.0	12.7	-	-	0.31	0.43

### 4.4.2 Yield displacement estimates

Two approaches are possible for estimating the wall yield displacement, starting from the first yield displacement. In the most common used approach by [PCK07], it is assumed that the wall is fully cracked over the height at first yield, i.e., a linear curvature profile over the height is assumed (Figure 4.8a). While it is acknowledged that the wall is not fully cracked at first yield, the intention of the linear curvature profile assumption is to compensate for the strain penetration into the foundation to some extent for the shear displacements, while for shear critical RC elements, the shear displacements could be added to this yield displacement [PCK07].

In the second approach, the yield displacement is estimated by predicting the individual displacements components: flexural displacements including strain penetration and shear displacements [HRS04], [BDP08b]. In the following sections, the estimates of the individual displacement components are discussed with respect to the experimentally derived displacement components.

#### 4.4.2.1 Flexural displacements due to wall deformation

The flexural first yield displacement  $\Delta'_{y,f}$  was experimentally determined by double-integration of the mean curvatures obtained from the LVDT measured strains (Section 4.2). In order to compare with estimates, the displacement due to strain penetration  $\Delta'_{y,sp}$  (Table 4.3) was subtracted from the total flexural displacements.

## Chapter 4. Experimentally derived quantities for the plastic hinge model

The flexural first yield displacement was estimated first by assuming a fully cracked profile over the height of the wall (Figure 4.8b and corresponding Equation 4.7 according to [PCK07]). A more accurate estimation of the flexural displacements can be obtained if the assumption of a partially cracked curvature profile is used (Figure 4.8c and Equation 4.8 according to [BDP08b]). By examining the experimental curvature profiles at first yield (see Figures 4.3 and 4.4), the assumption of a bi-linear curvature profile at first yield can also be used (Figure 4.8d and again Equation 4.7 but with a different factor  $k$  accounting for the shape of the curvature profile). The second assumption of the bi-linear curvature profile will result in the lowest top flexural displacement estimate since the area of the curvature profile is the smallest (Figure 4.8d).

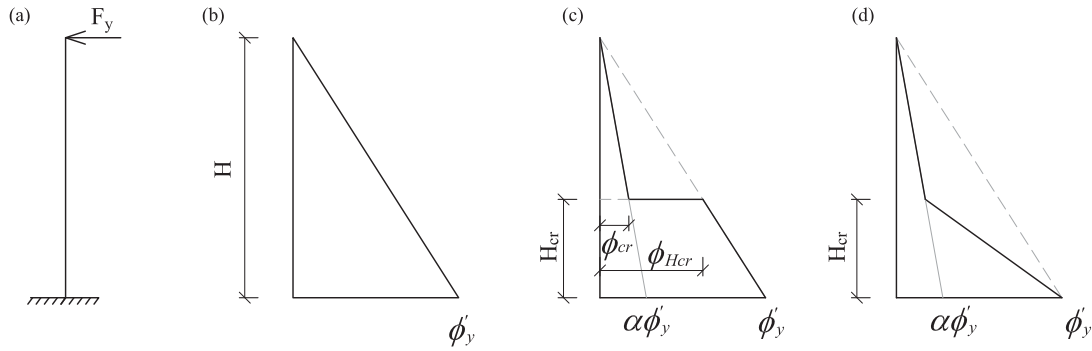


**Figure 4.8:** Assumed shape of the curvature profile at first yield over the height of a cantilever wall under a lateral point load: linear profile accounting for a fully cracked wall(b); offset bi-linear curvature profile accounting for a partially cracked wall (c) (adapted from [BDP08b]); and continuous bi-linear profile based on experimental curvature profiles also accounting for a partially cracked wall(d).

$$\Delta'_{yf,1L} = \phi'_y \frac{H^2}{3} \quad (4.7)$$

where  $\phi'_y$  is the first yield curvature and  $H$  is the wall shear span depending on the loading direction.

$$\Delta'_{yf,2L} = k_{cr} \phi'_y \frac{H^2}{3} \quad (4.8)$$

where  $k_{cr}$  is factor accounting for the extent of the cracking over the height of the wall at first yield and the assumed shape of the curvature profile.

The factor  $k_{cr}$  in Equation 4.8 can be computed in a similar fashion for the two assumed curvature profiles which account for the extent of cracking. The factor  $k_{cr}$  corresponding to a bi-linear profile with an offset at the cracking height (Figure 4.8c) will be termed  $k_1$  while the one corresponding to a continuous bi-linear profile (Figure 4.8d) will be termed  $k_2$ . For both cases, the value  $\alpha$  in Figures 4.8c,d is the ratio of the cracked to uncracked flexural wall stiffness ( $EI_{cr}/EI_g$ ). The stiffness of the uncracked wall section  $EI_g$  was taken as the gross sectional stiffness depending on the loading direction, while the stiffness of the cracked section was taken as  $EI_{cr} = M_y/\phi'_y$ . The cracked height was computed analytically as in Equations 4.4 and 4.5.



**Derivation of  $k_1$**  The flexural displacement corresponding to the curvature profile in Figure 4.8c can be estimated by integration of the curvature profile over  $H$  or in a simplified manner as:

$$\Delta_{f,1} = \phi'_y \frac{H^2}{3} - \phi_{H_{cr}} \frac{(H - H_{cr})^2}{3} + \phi_{cr} \frac{(H - H_{cr})^2}{3} \quad (4.9)$$

From same triangles,  $\phi_{cr}$  and  $\phi_{H_{cr}}$  can be written as :

$$\phi_{cr} = \alpha \phi'_y \frac{(H - H_{cr})}{H} \quad (4.10)$$

$$\phi_{H_{cr}} = \phi'_y \frac{(H - H_{cr})}{H} \quad (4.11)$$

Finally, combining Equation 4.9 with Equations 4.8, 4.10 and 4.11 and re-arranging, it results:

$$k_1 = \alpha + (1 - \alpha) \left( \frac{H_{cr}^3}{H^3} - \frac{3H_{cr}^2}{H^2} + \frac{3H_{cr}}{H} \right) \quad (4.12)$$

**Derivation of  $k_2$**  The flexural displacement corresponding to the curvature profile in Figure 4.8d can be also estimated from the integration of the assumed curvature profile over  $H$  as in Equation 4.13 as the sum of: (1) the flexural displacement from the curvature over the cracked height  $H_{cr}$  of the wall  $\Delta_{f,H_{cr}}$ , (2) the flexural displacement due to the rotation over the cracked height  $\theta_{H_{cr}}$  and (3) the flexural displacement from the curvature over the uncracked part of the wall.

$$\Delta_{f,2} = \Delta_{f,H_{cr}} + \theta_{H_{cr}}(H - H_{cr}) + \phi_{cr} \frac{(H - H_{cr})^2}{3} \quad (4.13)$$

In order to obtain the flexural displacement and the rotation at the cracked height, a reduced cantilever structure is used (Figure 4.9b). By writing the Euler-Bernoulli beam equation (Equation 4.14) of the reduced cantilever structure and by applying the corresponding boundary conditions (i.e., displacement and rotation at the base are zero) one obtains the rotation and the displacement at any height of the reduced structure (Equations 4.15a and 4.15b).

$$M(x) = -EI \frac{d^2 \Delta_f(x)}{d^2 x} \quad (4.14)$$

where  $x$  is the height coordinate measured from the top of the cantilever,  $M(x) = F_r x$  is the moment depending on  $x$  for the case of the reduced cantilever structure in Figure 4.9b and  $\Delta_f(x)$  is the lateral displacement of the cantilever depending on  $x$ . The height of the reduced cantilever structure  $H_r$  can be computed from Figure 4.9a, from same triangles as in Equation 4.16.

## Chapter 4. Experimentally derived quantities for the plastic hinge model

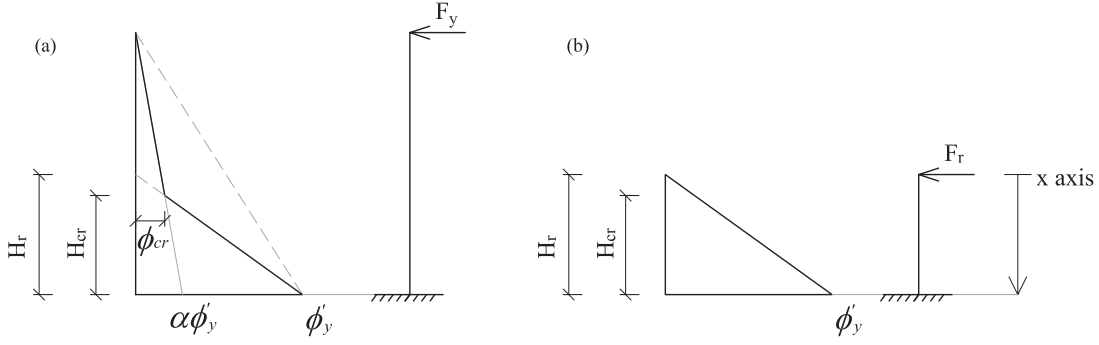


**Figure 4.9:** Bi-linear curvature profile assumption at first yield over the height of a cantilever wall: full cantilever wall under lateral point load (a); and reduced cantilever structure for computing the flexural displacement  $\Delta_{f,H_{cr}}$  and the rotation  $\theta_{H_{cr}}$  over the cracked height (b).

$$\Delta_f(x) = \frac{F_r}{EI} \frac{x^3}{6} - \frac{F_r H_{cr}^2}{2EI} x + \frac{F_r H_{cr}^3}{3EI} \quad (4.15a)$$

$$\theta(x) = \frac{F_r}{EI} \frac{x^2}{2} - \frac{F_r H_{cr}^2}{2EI} \quad (4.15b)$$

$$H_r = \frac{H_{cr} \phi'_y}{\phi'_y - \phi_{cr}} \quad (4.16)$$

If Equations 4.15a and 4.15b are evaluated for  $x = H_r - H_{cr}$  on the reduced cantilever structure, one obtains the displacement  $\Delta_{f,H_{cr}}$  and the rotation  $\theta_{H_{cr}}$  at the cracked height for the full cantilever structure. If  $H_r$  and  $\phi_{cr}$  computed as in 4.16 and 4.10, respectively are replaced in Equation 4.15a and 4.15b, while taking  $EI = EI_{cr}$  and  $F_r H_r / EI_{cr} = \phi'_y$ , one obtains:

$$\Delta_{f,H_{cr}} = \frac{\phi'_y H_{cr}^2}{6} \left( 2 + \alpha - \alpha \frac{H_{cr}}{H} \right) \quad (4.17a)$$

$$\theta_{H_{cr}} = \frac{\phi'_y H_{cr}}{2} \left( 1 + \alpha - \alpha \frac{H_{cr}}{H} \right) \quad (4.17b)$$

Finally, combining Equations 4.17a, 4.17b, 4.10 and 4.13, and re-arranging, one obtains factor  $k_2$  equal to  $k_{cr}$  in Equation 4.8:

$$k_2 = \alpha + 0.5(1 - \alpha) \left( -\frac{H_{cr}^2}{H^2} + \frac{3H_{cr}}{H} \right) \quad (4.18)$$

**Comparison of experimental flexural displacements with estimates** In order to judge which assumption fits better with the experimentally determined values, the experimental flexural displacements are compared with estimates computed according to the three curvature profile assumptions in Figure 4.8b, c, d. Note that for this comparison the experimentally derived curvature was used in the derivation of the estimates. The results are plotted in Figure 4.10 for all test units.

Indeed, assuming a linear curvature profile over the height leads to flexural displacement estimates  $\Delta'_{yf,1L}$  which are in most cases significantly larger than the experimental flexural displacements (i.e., up to  $\sim 50\%$ ). The two assumptions accounting for the cracking height lead to improved estimates of the flexural displacements due to wall deformation. However, the displacement derived with the continuous bi-linear profile (Figure 4.8d) provides overall a better match with the experimental results.

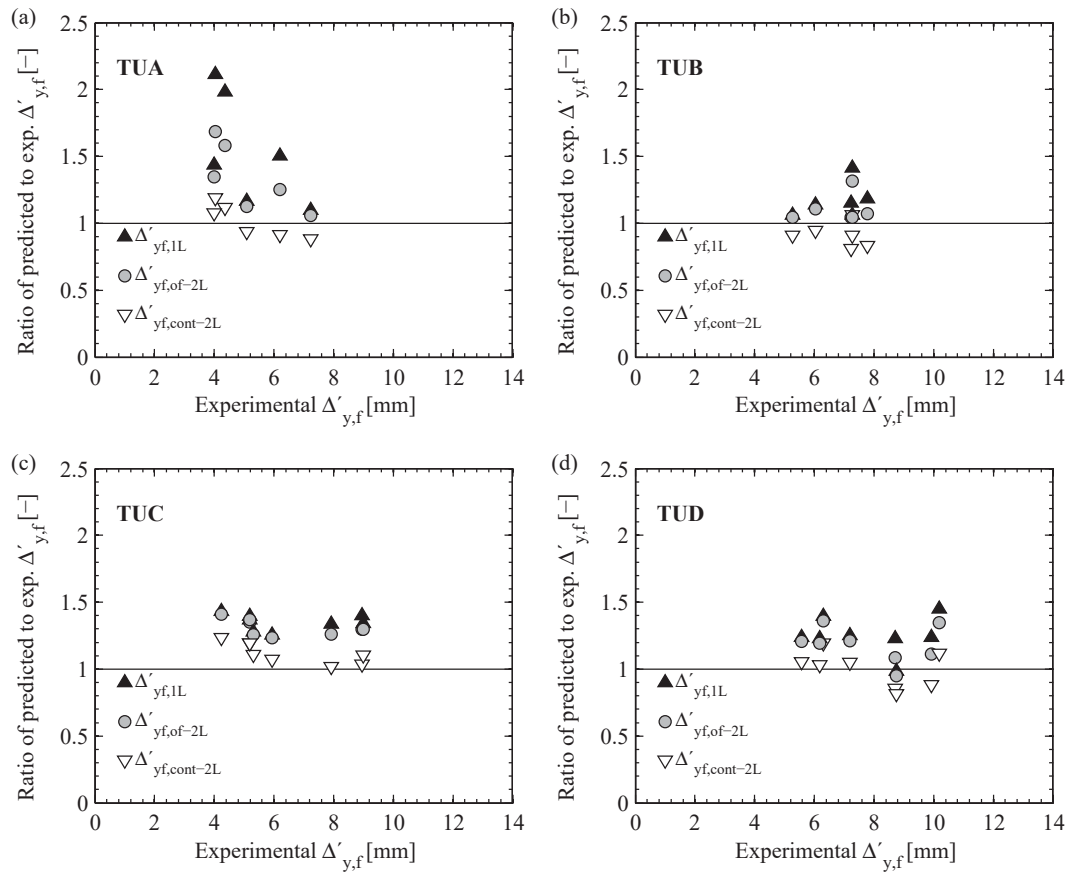


**Figure 4.10:** Comparison of experimentally determined flexural displacements with estimates (a-d). Estimates are based on different curvature profile assumptions: linear curvature profile  $\Delta'_{yf,1L}$ , bi-linear curvature profile with an offset at the cracking height  $\Delta'_{yf,of-2L}$  and continuous bi-linear profile  $\Delta'_{yf,cont-2L}$ .

#### 4.4.2.2 Flexural displacements due to strain penetration

The flexural displacements due to strain penetration into the foundation can be computed by assuming that strain penetration effects produce a rigid body rotation of the wall above the wall base. It is therefore necessary to know the base rotation  $\theta'_{y,sp}$  which is assigned to the strain penetration. This rotation can be computed as the difference between the measured base curvature at first yield  $\phi'_{y,measured}$  and the base curvature  $\phi'_y$  obtained from the curvature measurements above the base (see Section 4.3), times the LVDT length over which the curvature at base was measured, i.e.,  $L_{LVDT,row1} = 50 \text{ mm}$  (Equation 4.19). The top displacement due to strain penetration at first yield, can then be computed as in Equation 4.20.

$$\theta'_{y,sp} = (\phi'_{y,measured} - \phi'_y) \cdot 50 \text{ mm} \quad (4.19)$$

$$\Delta'_{y,sp} = \theta'_{y,sp} H \quad (4.20)$$

In order to estimate the displacement due to strain penetration, the notion of strain penetration length is introduced  $L'_{y,sp}$ , over which the curvature is considered as constant and equal to the curvature at the base of the wall section  $\phi'_y$ . Hence the base rotation due to strain penetration can be computed as in Equation 4.21. While the base curvature can be predicted from section analysis, the strain penetration length is typically estimated as function of the longitudinal bar diameter  $d_b$  and the yield strength of the bar  $f_y$ . The experimentally derived values of the displacement due to strain penetration and the strain penetration length are given in Table 4.3.

$$\theta'_{y,sp} = L'_{y,sp} \phi'_y \quad (4.21)$$

$L'_{y,sp}$  values normalised by the bar diameter and yield strength (Table 4.3 columns 10 to 13) are on average equal to 0.006 for TUA, to 0.010 for TUB, 0.009 for TUC and 0.019 for TUD. These values are all smaller than the constant 0.022 proposed by Paulay and Priestley [PP92]. The difference stems most likely from the pre-stressing of the foundation of the test units which reduced the strain penetration effects [HRS04], [BDP08b]. To account for this effect of the foundation pre-stress on the strain penetration length, [BDP08b] proposed reducing by half the constant of 0.022. A value of 0.011 agrees well with the overall average  $L'_{y,sp}/(d_b f_y)$  values for the four test units, and hence it will be used in estimating  $L'_{y,sp}$  and  $\Delta'_{y,sp}$ . The strain penetration lengths for the inelastic range are discussed together with the plastic hinge lengths in Section 4.5.

#### 4.4.3 Comparison of experimental yield displacements with estimates

Estimates from both the simplified approach, assuming a linear curvature profile over the height at yield (Equation 4.22a) and the more complex approach, accounting for shear displacements and partially cracked profile (Equation 4.22b) are compared here with the experimentally determined yield displacements. For clarity, the two equations for the yield displacement corresponding to the two prediction approaches are given below:

#### 4.4. Yield displacement

**Table 4.3:** TUA, TUB, TUC and TUD: experimentally determined flexural displacements due to strain penetration  $\Delta'_{y,sp}$  and derived strain penetration lengths  $L'_{y,sp}$

Pos.	$\Delta'_{y,sp}$ [mm]				$L'_{y,sp}$ [mm]				$L'_{y,sp}/(d_b f_y)$ [-]			
	TUA	TUB	TUC	TUD	TUA	TUB	TUC	TUD	TUA	TUB	TUC	TUD
A	0.0	0.6	0.8	1.5	3	72	79	125	0.000	0.013	0.018	0.028
B	0.4	0.5	0.8	1.6	47	68	66	158	0.008	0.012	0.015	0.035
C	0.0	0.2	0.3	0.4	4	15	25	35	0.001	0.003	0.006	0.008
D	0.5	0.3	0.3	1.0	64	37	37	107	0.011	0.007	0.008	0.024
E	0.0	0.2	0.2	0.5	2	33	32	57	0.000	0.006	0.007	0.013
F	0.6	0.6	0.1	1.0	94	108	12	126	0.016	0.019	0.002	0.020
H	-	-	0.3	0.3	-	-	35	40	-	-	0.008	0.009
G	-	-	0.3	0.7	-	-	48	82	-	-	0.011	0.018
Mean									0.006	0.010	0.009	0.019

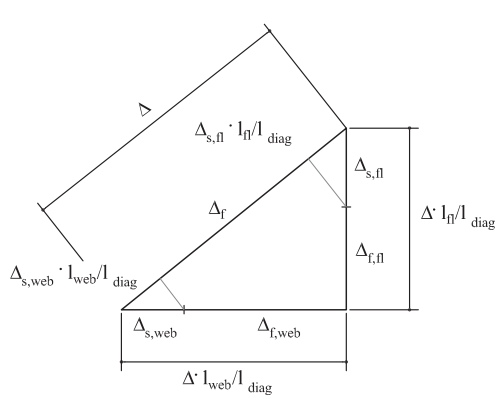
$$\Delta_{y,1L} = \phi_y \frac{H^2}{3} \quad (4.22a)$$

$$\Delta_{y,2L} = \phi_y \left( k_2 \frac{H^2}{3} + L'_{y,sp} H \right) \left( 1 + \frac{\Delta_s}{\Delta_f} \right) \quad (4.22b)$$

where  $\phi_y$  was computed from section analysis,  $L'_{y,sp} = 0.011 d_b f_y$  while  $k_2$  factor which accounts for the partially cracked profile at yield was estimated as in Equation 4.18 and  $\Delta_s/\Delta_f$  was estimated as in Section 4.7.3.

Note that for the diagonal loading direction, the shear to flexural displacements ratios were estimated as a composition of the predicted  $\Delta_s/\Delta_f$  values of the web and flanges following the procedure detailed in [BDP08b]. The procedure uses the rectangular triangle of the total top wall displacements along the web, flange and diagonal to derive geometrically the shear displacements for the diagonal direction  $(\frac{\Delta_s}{\Delta_f})_{diag}$  as the sum of projections of the shear displacements of the web and flange onto the diagonal as shown below.  $\beta = (\frac{\Delta_s}{\Delta_f})_{fl}$  is the ratio of the flange equal to the average ratio of the two flanges for position F and G, and equal to the ratio of the flange in compression at position E and H.

## Chapter 4. Experimentally derived quantities for the plastic hinge model



$$\alpha = \left(\frac{\Delta_s}{\Delta_f}\right)_{web} \quad ; \quad \Delta_{s,web} = \Delta \frac{\alpha}{1 + \alpha} \frac{l_{web}}{l_{diag}}$$

$$\beta = \left(\frac{\Delta_s}{\Delta_f}\right)_{fl} \quad ; \quad \Delta_{s,fl} = \Delta \frac{\beta}{1 + \beta} \frac{l_{fl}}{l_{diag}}$$

$$\Delta_s = \Delta_{s,web} + \Delta_{s,fl}$$

$$x = \frac{\alpha}{1 + \alpha} \left(\frac{l_{web}}{l_{diag}}\right)^2 + \frac{\beta}{1 + \beta} \left(\frac{l_{fl}}{l_{diag}}\right)^2$$

$$\left(\frac{\Delta_s}{\Delta_f}\right)_{diag} = \frac{x}{1 - x}$$

**Figure 4.11:** Derivation of shear to flexural displacements ratio for the diagonal direction (taken from [BDP08b]).

Finally, the experimental derived yield displacements are compared with the two predictions  $\Delta_{y,1L}$  and  $\Delta_{y,2L}$  in Figure 4.12. Based on the results of the four test units, none of the two approaches for predicting  $\Delta_y$  seems to be clearly superior to the other one, with both methods leading to somewhat reasonable estimates. However the linear curvature profile approach does seem in most cases to underestimate the yield displacement since the shear displacements of the U-shaped walls analysed herein are for most loading directions larger than for typical rectangular walls.

The estimate based on predicting the individual components  $\Delta_{y,2L}$  matches overall well but tends to overestimate in some cases the yield displacements (as it is the case for TUC). This overestimation can mainly be traced back to the overestimation of the flexural yield displacements (Figure 4.10). The large error at position F of TUD for both  $\Delta_{y,1L}$  and  $\Delta_{y,2L}$  is most likely due to measurement and experimental derivation method errors: the experimentally derived yield displacement is significantly larger than at the other loading position (see Figure 4.12).

As stated, none of the two approaches to estimate  $\Delta_y$  seems superior to the other for the test units analysed here in. By assuming a linear curvature profile, i.e. wall fully cracked,  $\Delta_{y,1L}$  will tend to compensate for the contribution of the shear displacements. However, if for example the shear displacements are large, as was the case for the U-shaped walls analysed here, it is expected that  $\Delta_{y,1L}$  values will underestimate the yield displacement. On the other hand, if the shear deformation are small as it is the case for rather slender walls,  $\Delta_{y,1L}$  values will most likely overestimate the yield displacements. This hypotheses will be further investigated for walls with a broader range of slenderness ratio by means of parametric studies in Chapter 6.

#### 4.4. Yield displacement

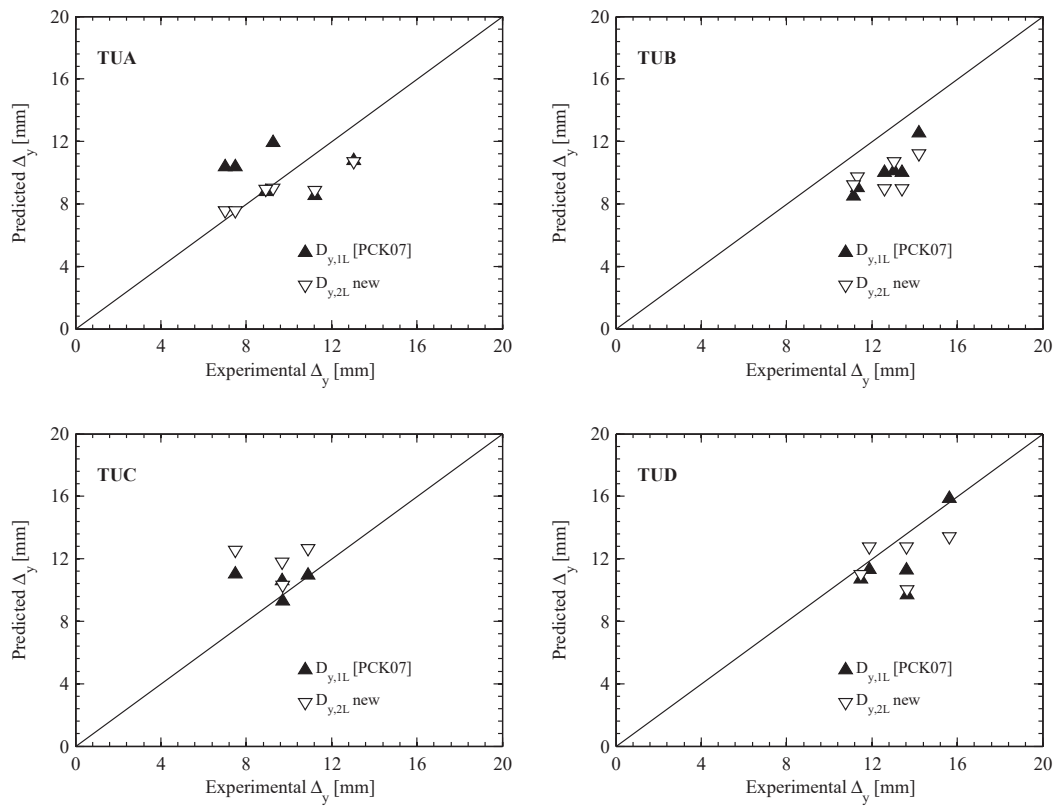


**Figure 4.12:** TUA, TUB, TUC and TUD: comparison of experimentally determined yield displacements with estimates (a-d). Estimates based on two approaches - predicting the components  $D_{y,2L}$  (Equation 4.22b) and the simple approach assuming a linear curvature profile  $D_{y,1L}$  (Equation 4.22a)

## 4.5 Plastic hinge length

The factors influencing the plastic hinge length  $L_{ph}$  have been presented and discussed in Section 2.2.2 together with state-of-the-art  $L_{ph}$  estimates for walls. This section presents the derivation of the  $L_{ph}$  values from experimental results, which are then compared to estimates in the literature. This section discusses also the influence of the loading position and ductility demand on  $L_{ph}$ . The loading positions and directions considered in the experiments are shown again for clarity in Figure 4.21.

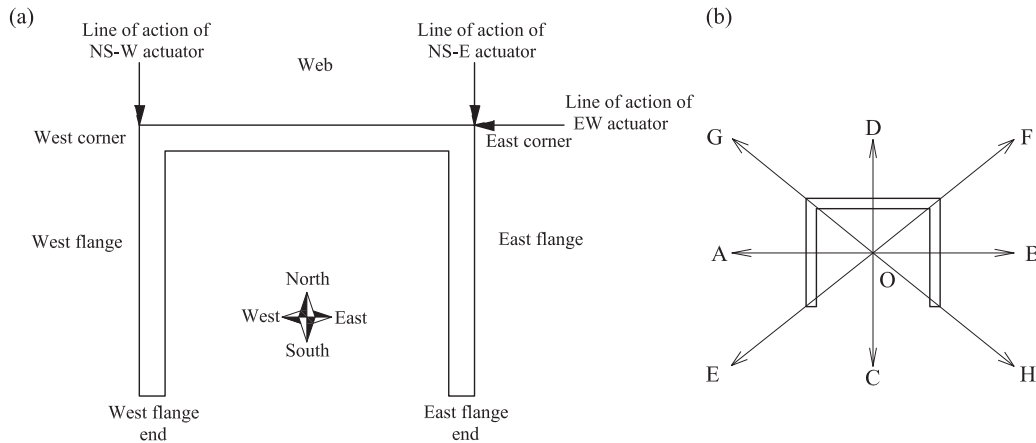


**Figure 4.13:** TUA, TUB, TUC and TUD: naming of the different wall parts and cardinal directions (a) and loading positions (b).

### 4.5.1 Estimates for plastic hinge lengths from experimental results

#### 4.5.1.1 Equations for plastic hinge lengths in the literature

State-of-the-art estimates of the plastic hinge length of RC walls have been reviewed in Section 2.2.2. For convenience, the equations that will be compared to experimental results are briefly repeated in the following.

[PCK07]a: assessment estimate which assumes the centre of rotation at the base of the wall and accounts for strain penetration

$$L_{ph} = \min(0.08, k)H + 0.2l_{wall} + 0.022d_b f_y \quad (4.23)$$

where  $k = 0.2(f_u/f_y - 1)$  with  $f_u$  and  $f_y$  equal to the ultimate and respectively yield strength of the reinforcement,  $H$  is the wall shear span,  $l_{wall}$  is the wall length and  $d_b$  is the vertical reinforcement bar diameter

[PCK07]d: design version of the [PCK07]a estimate

$$L_{ph} = \min(0.08, k)H + 0.1l_{wall} + 0.022d_b f_y \quad (4.24)$$



[BA11]: estimate intended as lower bound value of  $L_{ph}$  which does not account for strain penetration but accounts for the axial load ratio  $N/A_g f_c$  while the location of the centre of rotation is not specified, since  $L_{ph}$  was taken half the height of the plastic zone  $L_{pz}$

$$L_{ph} = (0.05H + 0.2l_{wall})\left(1 - 1.5 \frac{N}{A_g f_c}\right) \quad (4.25)$$

[Kaz13]: estimate that accounts for the axial load ratio, but does not account for strain penetration while the centre of rotation is assumed at the middle of the plastic hinge length

$$L_{ph} = 0.27l_{wall}\left(1 - \frac{N}{A_g f_c}\right)\left(1 - \frac{f_{yh}}{f_c}\right)(H/l_{wall})^{0.45} \quad (4.26)$$

where  $f_{yh}$  is the yield strength of the transverse reinforcement and  $f_c$  is the concrete compressive strength.

### 4.5.1.2 Particularities for diagonal loading

When estimating the plastic hinge length for the diagonal direction, an appropriate wall length and height need to be chosen. [BDP08b] argued that either the length of the web or the flanges should be used since the tension shift term containing the wall length is linked to the shear transfer mechanism, which mainly works in the plane of the wall sections. Similar argumentation was made for the choice of the height, and thus  $L_{ph}$  for the diagonal direction can be taken as either the  $L_{ph}$  for the EW cycles or for the NS cycles.

Since under diagonal loading the web typically carries a larger shear stress than the flange, the spread of plasticity is expected to be dictated by the web. For this reason, the wall length will be taken equal to the length of the web for the diagonal positions. The shear span will be taken as equal to  $h_{NS} = 2.95$  m since the top displacement for diagonal loading was measured at this height and the plastic flexural displacement was also derived for this height.

### 4.5.2 Experimentally determined plastic hinge lengths

As discussed in Section 2.2.2 estimates of the plastic hinge length were derived using different assumptions for the centre of rotation of the plastic hinge or for the contribution of the strain penetration term. In order to compare these estimates with experimental results, different  $L_{ph}$  values should be derived from the experimental data corresponding to the assumptions of each estimate.

In the following, two procedures for determining the experimental  $L_{ph}$  values are discussed. The first method back-calculates the  $L_{ph}$  value from the plastic flexural displacement using the plastic base curvature  $\phi_p$ , and hence corresponds the  $L_{ph}$  that best fits the top displacement. In the second procedure, the  $L_{ph}$  is simply taken as half of the height of the plastic zone  $L_{pz}$ , i.e., the  $L_{ph}$  value directly connected to the real spread of plasticity and independent of the plastic curvature. The height of the plastic zone  $L_{pz}$  corresponds to the maximum wall height where inelastic curvatures spread.

#### 4.5.2.1 Plastic hinge lengths back-calculated from top displacement

Plastic hinge lengths  $L_{ph}$  can be determined from experimental measurements by back-calculating their value from the displacements measured at the top of the wall and from the plastic curvature  $\phi_p$  [HRS04], [Han13]. The plastic part of the flexural displacement  $\Delta_{p,f}$  at the height of the shear span  $H$  stems from the plastic rotation at the wall base. Based on the assumption of the plastic hinge model (see Section 2.2.2) that the plastic curvature  $\phi_p$  is constant over the plastic hinge length,  $L_{ph}$  can be computed as in Equation 4.27 where  $\phi_p$  is the experimentally determined plastic curvature computed as in Equation 4.29 with the yield curvature  $\phi_y$  given in Table 4.1.

$$L_{ph} = \frac{\Delta_{p,f}}{\phi_p H} \quad (4.27)$$

$$\Delta_{p,f} = \Delta_f - \Delta_{y,f} \quad (4.28)$$

$$\phi_p = \phi_b - \phi_y \quad (4.29)$$

#### Base curvature

The base curvature  $\phi_b$  in Equation 4.29 is not taken directly as the measured curvature at the base of the wall (i.e., first row of LVDT from base  $h = 0 - 50$  mm) since this measurement includes the deformations due to strain penetration into the foundation. To obtain the base curvature  $\phi_b$ , [HRS04] recommends using a linear least square approximation of at least three inelastic curvature measurements above the base crack. The best linear fit is then extrapolated to the wall base to obtain the base curvature representative for the wall deformation [HRS04].

For the test units analysed here, all inelastic curvatures above the base crack were considered in the least square approximation. The height over which the inelastic curvatures spread up the wall, i.e., the height of the plastic zone  $L_{pz}$ , was determined as the height over which the curvatures were larger than the nominal yield curvature  $\phi_y$  (Figure 4.14a). In addition to this method, a second method was used to determine the base curvature  $\phi_b$ , namely by back-calculating the base curvature from the rotation above the plastic zone  $\theta_{pz}$  under the assumption of a linear curvature profile over  $L_{pz}$ . The two methods of determining the base curvature are summarised below:

$\phi_{b1}$ : obtained by best linear fit of the curvatures over the height  $h_{fit} = 50\text{mm} - L_{pz}$  and extrapolating to the base level

$\phi_{b2}$ : obtained from the rotation above the plastic zone  $\theta_{pz}$  using Equation 4.30.

$$\phi_{b2} = \frac{2\theta_{pz}}{L_{pz}} \quad (4.30)$$

where  $\theta_{pz}$  is computed from curvature integration over the plastic zone height  $L_{pz}$  after removing the curvature contribution due to strain penetration.

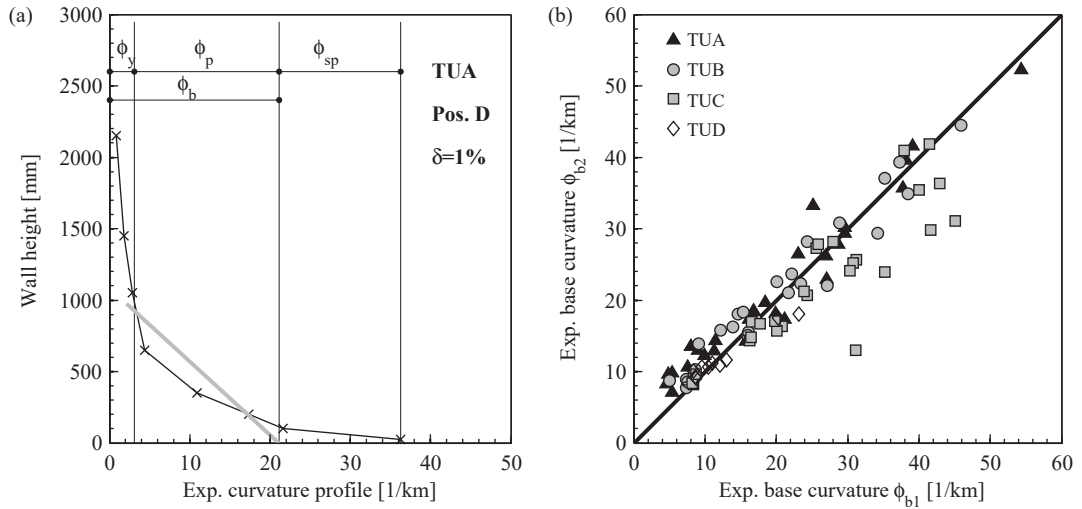


**Figure 4.14:** Wall base curvature: assumptions exemplified for TUA, position A at 1.5 % drift (a) and comparison between the base curvatures determined with the two methods  $\phi_{b1}$  and  $\phi_{b2}$

The experimental base curvatures computed with the two methods are compared in Figure 4.14b, while the assumptions behind the calculations are exemplified in Figure 4.14a. The experimental base curvatures shown here were computed at peak drifts of the inelastic cycles of all four test units and loading positions. Figure 4.14b shows that both methods of determining the base curvature yield similar results. At large peak drifts of TUC, i.e. 2.0% and 2.5% drifts, larger base curvatures are obtained with the best fit linear method  $\phi_{b1}$  than with the rotation based method  $\phi_{b2}$ . This difference is attributed to curvature concentrations towards the wall base due to significant damage at the these drift levels. Since the determination of the base curvature using the rotation above the plastic zone is less sensitive to curvature peaks than the best linear fit method, the former will be used from here on to determine the experimental plastic hinge lengths.

### Strain penetration

In Equation 4.28, the plastic flexural displacement  $\Delta_{p,f}$  includes the flexural displacements due to strain penetration and hence so will the plastic hinge length  $L_{ph}$  in Equation 4.27. Since not all estimates of  $L_{ph}$  include a strain penetration term, the contribution of the strain penetration will be removed from the experimentally determined  $L_{ph}$  in order to compare with estimates. The contribution of the strain penetration to the wall top displacement has already been discussed for the yield displacement in Section 4.4.2.2. The part of  $L_{ph}$  attributed to strain penetration, i.e., the equivalent strain penetration length  $L_{sp}$  can be computed similarly to  $L'_{y,sp}$  in Section 4.4.2.2 according to Equation 4.31. The values obtained for the experimentally determined strain penetration lengths are shown in Figure 4.15.

$$L_{sp} = \frac{1}{\phi_{b1}} (\phi_{b,measured} - \phi_{b1}) \cdot 50mm \quad (4.31)$$

## Chapter 4. Experimentally derived quantities for the plastic hinge model

---

where  $\phi_{b,measured}$  is the curvature recorded in the first LVDT from the base ( $h = 0 - 50$  mm) and includes the deformation concentrated in the base crack.

[PP92] recommends a value of  $0.022d_b f_y$  for the strain penetration length. Experimentally determined values in Figure 4.15 indicate that a value of  $0.011d_b f_y$  is more suitable for the test units discussed herein. As already mentioned in Section 4.4.2.2, the reason for these lower strain penetration lengths was the bi-axial lateral pre-stressed foundation of the test units.

Finally, after evaluating the base rotation and the strain penetration length, the plastic hinge lengths can be determined. Figure 4.16 shows the experimentally determined plastic hinge lengths  $L_{ph} - L_{sp}$ , where the strain penetration contribution was removed. The plastic hinge lengths were determined at peak drifts of the inelastic load cycles for each loading position for TUA and TUB, and only for the diagonal loading cycles for TUC and TUD. Plastic hinge lengths were not determined for the principal loading directions of TUC and TUD since the wall reached for these directions displacement ductilities of  $\mu_{\Delta} = 1.4$  to  $2.2$  and hence such values of plastic hinge lengths are of interest only if the wall is designed for low or medium ductility levels.

### 4.5.2.2 Plastic hinge lengths calculated from height of plastic zone

In the previous section, the plastic hinge length  $L_{ph}$  was back-calculated from the experimentally determined plastic flexural displacement  $\Delta_{p,f}$  (Equation 4.27). The plastic curvature used in this determination was computed assuming a linear plastic curvature profile over the height of the plastic zone  $L_{pz}$ . However, this assumption allows to compute the  $L_{ph}$  value independently of  $\Delta_{p,f}$ . The rotation above the height of the plastic zone is made equivalent to the rotation above the plastic hinge length  $L_{ph}$  where plastic curvatures are assumed constant over the height of  $L_{ph}$  (Figure 4.18). This condition yields Equation 4.32. The obtained plastic hinge lengths are also shown in Figure 4.16.

$$\frac{L_{pz}\phi_p}{2} = L_{ph}\phi_p \Rightarrow L_{ph} = \frac{L_{pz}}{2} \quad (4.32)$$

The top plastic flexural displacement can be estimated by integrating the assumed curvature profile as in Equation 4.33. Introducing Equation 4.32 into Equation 4.33,  $\Delta_{p,f}$  can be written as a function of  $L_{ph}$ .

$$\Delta_{p,f} = \frac{L_{pz}\phi_p}{2} \left( H - \frac{L_{pz}}{3} \right) \quad (4.33)$$

$$\Delta_{p,f} = L_{ph}\phi_p \left( H - \frac{2L_{ph}}{3} \right) \quad (4.34)$$

## 4.5. Plastic hinge length

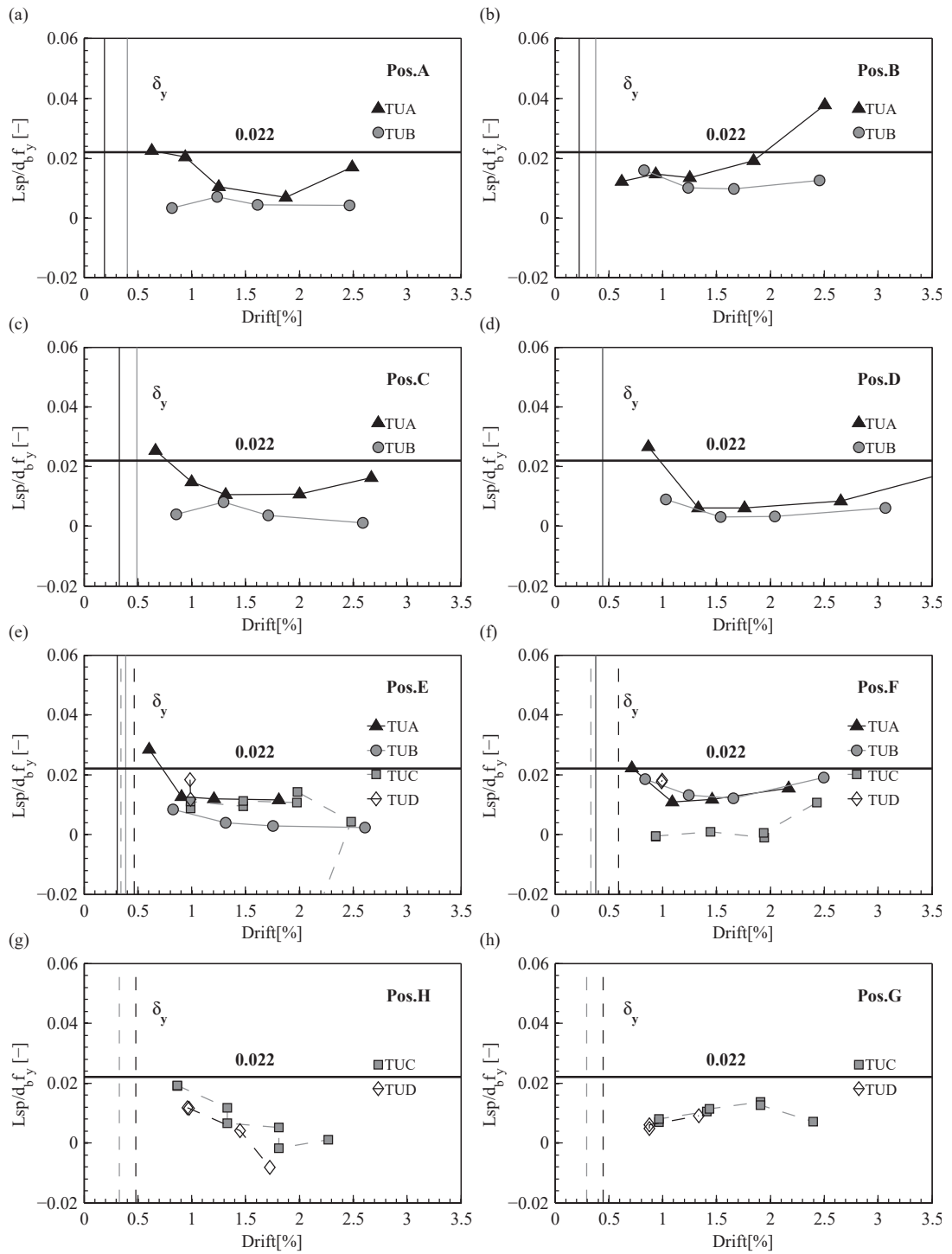


**Figure 4.15:** TUA to TUD: experimentally determined strain penetration length  $L_{sp}$  normalised by the bar diameter and yield strength of the reinforcement  $d_b f_y$ . The black vertical line, the grey line, the dashed black line and the dashed grey line indicate the values of the yield drift for TUA, TUB, TUC and TUD respectively. The black horizontal line indicates the constant value of the [PP92] estimate for  $L_{sp}/d_b f_y$  of 0.022.

## Chapter 4. Experimentally derived quantities for the plastic hinge model

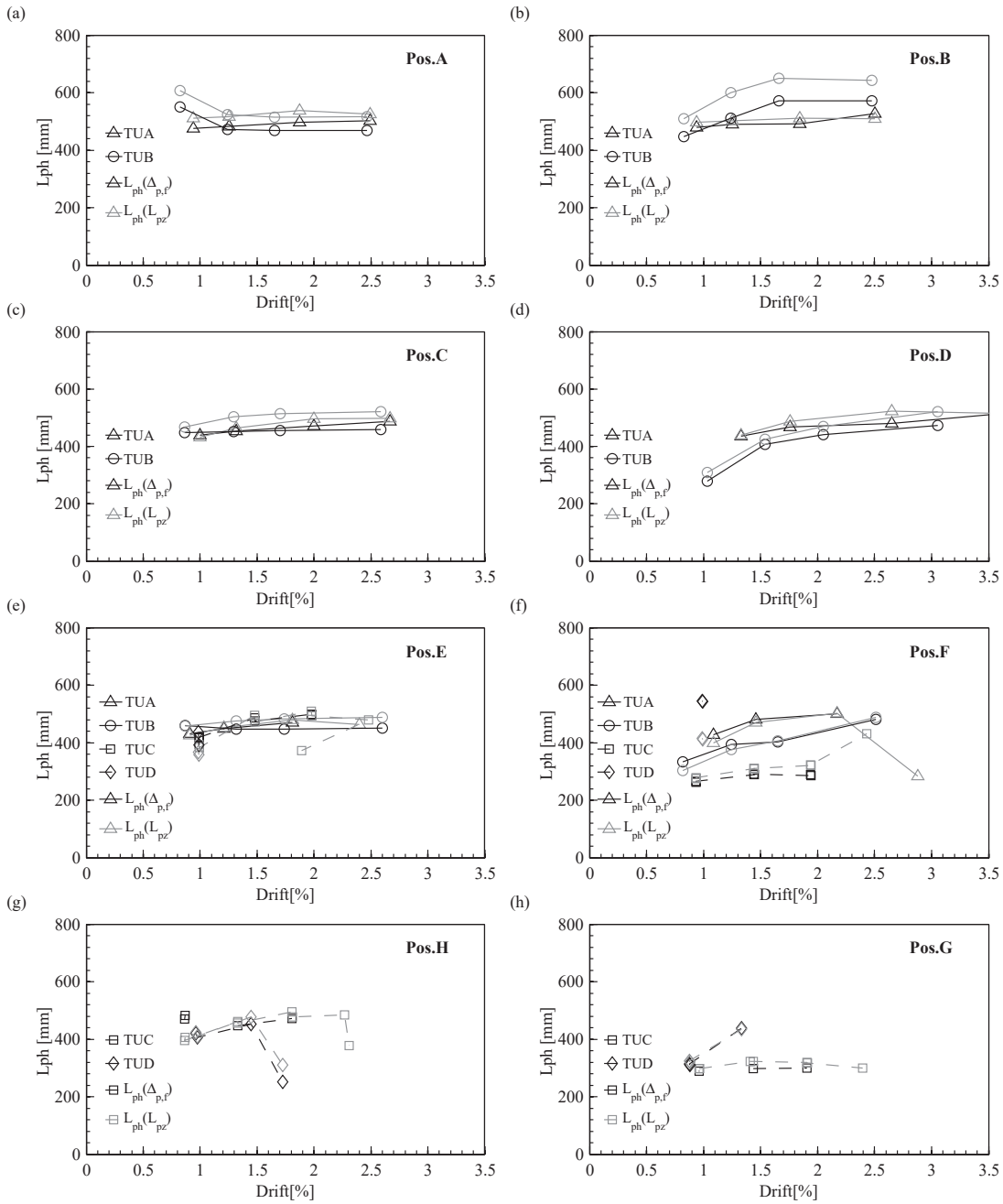


**Figure 4.16:** TUA to TUD - experimentally determined plastic hinge lengths: (1)  $L_{ph}(D_{p,f})$  back-calculated from the plastic flexural displacement using  $\phi_{b2}$  and assuming the centre of the rotation at the base of the wall (Equation 4.27) and (2)  $L_{ph}(L_{pz})$  determined as half the height of the plastic zone (Equation 4.32).

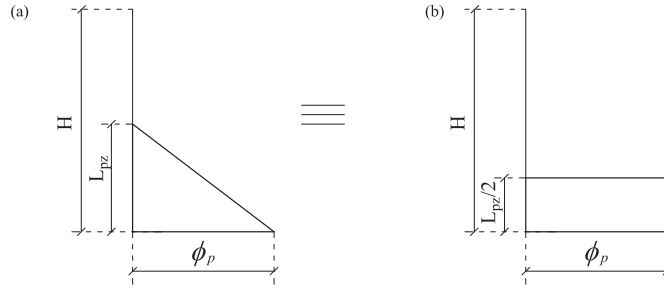


**Figure 4.17:** Assumed plastic curvature distribution: (a) linear plastic curvature profile over the height of the plastic zone  $L_{pz}$  and (b) equivalent constant plastic curvature profile over the plastic hinge length  $L_{ph}$

Note, that in the above equations, the flexural displacement due to strain penetration was not included, and can be added separately to the flexural displacement as suggested by [GF<sup>+</sup>15]. Since, the displacement due to strain penetration is treated separately, the centre of rotation of the plastic hinge can be computed exactly from curvature integration. Assumptions on the position of the centre of rotation are no longer necessary. As Equation 4.34 indicates, the centre of rotation is neither at the base of the wall nor at half the plastic hinge length from the base but at  $2/3L_{ph}$  from the wall base.

The assumption made here for the plastic curvature profile distribution can be easily verified by comparing the plastic flexural displacement estimate obtained from Equation 4.34 with the plastic flexural displacement obtained from the integration of the experimental curvature profiles. By assuming a linear distribution of the inelastic curvatures over  $L_{pz}$  (i.e., computing the plastic flexural displacement as in Equation 4.33), the actual plastic flexural displacement derived from integration of the experimental curvature is very well predicted (Figure 4.18). Hence the assumption of a linear inelastic curvature profile is rather accurate.

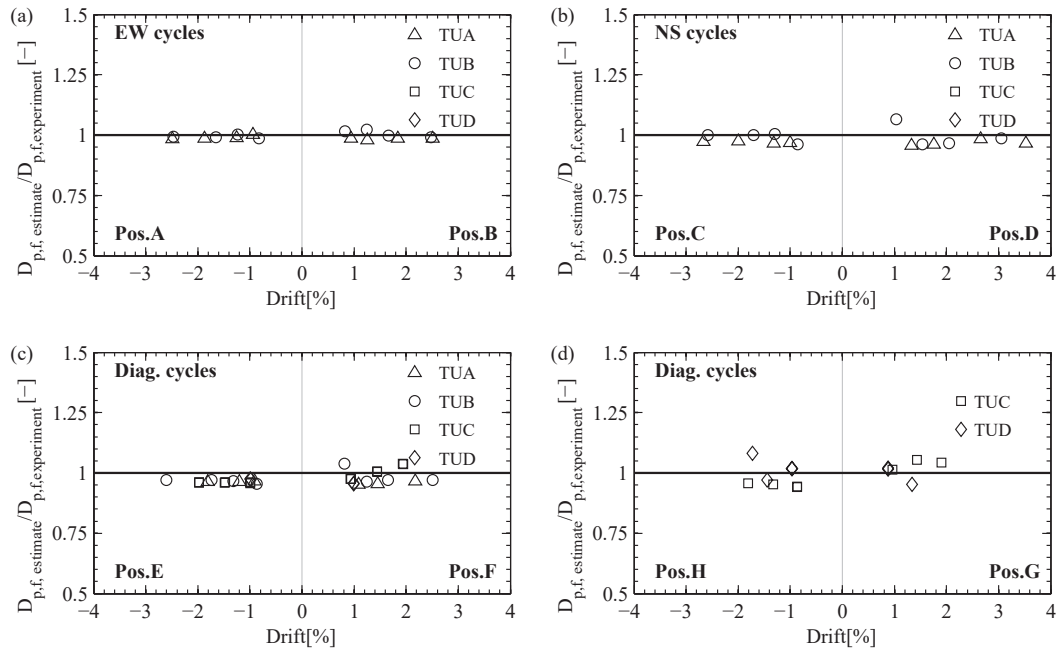
#### 4.5.2.3 Variations and trends of the experimentally determined plastic hinge lengths

Figure 4.16 indicates that for displacement ductilities larger than approximately 2 ( $\mu_{\Delta} \geq 2$ ), the plastic hinge lengths are approximately independent of the displacement ductility for all test units and loading positions, irrespective of the procedure used for their derivation. Hence a single experimental  $L_{ph}$  value can be used for  $\mu_{\Delta} \geq 2$ . For TUD at positions E, F and G (unfilled diamond marker in Figure 4.16 e-h) it is not possible to identify any trends since the wall failed at low ductilities and only one  $L_{ph}$  value could be determined.

In Equation 4.27,  $L_{ph}$  is derived by assuming that the centre of rotation of the plastic hinge is located at the base of the wall. This assumption is exact only if  $L_{ph} = 2L_{sp}$  [PCK07]. If the strain penetration length  $L_{sp}$  is small (i.e.,  $0.08H \geq L_{sp}$ ), the  $L_{ph}$  value can be obtained by assuming that the centre of rotation of the plastic hinge is located at the middle of the  $L_{ph}$ . In this case Equation 4.35 is used to derive  $L_{ph}$  values.

$$L_{ph,mid} = H - \sqrt{H^2 - \frac{2\Delta_{p,f}}{\phi_p H}} \quad (4.35)$$

## Chapter 4. Experimentally derived quantities for the plastic hinge model



**Figure 4.18:** Verification of the assumption of linear inelastic curvature profiles: comparison of plastic flexural displacement derived from integration of experimental profiles  $\Delta_{p,f,experiment}$  with the plastic flexural displacement estimated from the assumed curvature profile  $\Delta_{p,f,estimate}$



## 4.5. Plastic hinge length

$L_{ph}$  values averaged over the inelastic ductility range ( $\mu_{\Delta} \geq 2$ ) obtained with the two assumptions for the location of the plastic hinge are compared in Table 4.4. Assuming the centre of rotation of the plastic hinge is located at the wall base leads to  $L_{ph}$  values which are  $\sim 10\%$  lower than for  $L_{ph}$  derived under the assumption of the centre of rotation located at the middle of the plastic hinge length. This confirms the findings by [Han13]. In addition, the  $L_{ph}$  values derived as half of the height of the plastic zone (Equation 4.32) and averaged also for  $\mu_{\Delta} \geq 2$  are given in Table 4.4 for all the loading positions.

If the variation of the plastic hinge length is plotted with respect to the loading position (Figure 4.19), the diagonal loading positions (E-G) lead to up to 50% smaller plastic hinge lengths when compared to principal loading directions (A-D). In particular the values for the diagonal loading with the corner web-flange in compression (positions F,G) are the smallest of all loading positions. This is valid for both the plastic hinge length derived from the experimental top displacement and plastic curvature but also for the one derived directly from the spread of plasticity as half the height of the plastic zone. Lower plastic hinge length for the diagonal direction combined with the smallest curvatures of all the loading directions caused by the largest wall length for this direction ( $l_{wall} = \sqrt{l_{web}^2 + l_{fl}^2}$ ) results in the smallest displacement capacity for the diagonal direction.

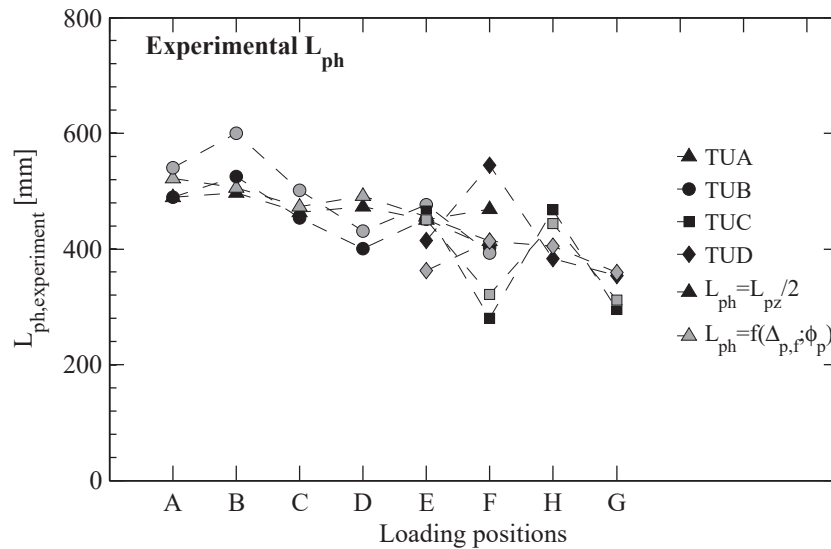


**Figure 4.19:** TUA to TUD: comparison of experimentally determined plastic hinge lengths averaged for peak displacements larger than  $\mu_{\Delta} = 2$  for the different loading positions.

## Chapter 4. Experimentally derived quantities for the plastic hinge model

**Table 4.4:** TUA to TUD - comparison between the different experimentally determined plastic hinge lengths: (1) plastic hinge lengths back-calculated from the plastic flexural displacement assuming the centre of rotation of the plastic hinge is located at the wall base (column three), (2) assuming the centre of rotation of the plastic hinge is located at the middle of the plastic hinge (column four) and (3) plastic hinge determined as half of the height of the plastic zone (column six).

		$L_{ph}(\Delta_{p,f})$			$L_{ph}(L_{pz})$	
		Eq. (4.27)	Eq. (4.35)	Difference Col.3-4	Eq. (4.32)	Difference Col.3-6
TU	Pos.	[mm]	[mm]	[%]	[mm]	[%]
TUA	A	489	548	12	523	7
	B	497	571	15	505	2
	C	463	525	13	473	2
	D	474	532	12	492	4
	E	450	507	13	456	1
	F	469	532	13	414	-12
TUB	A	490	538	10	541	10
	B	525	590	12	601	14
	C	454	500	10	502	10
	D	400	438	10	431	8
	E	451	498	10	476	6
	F	403	453	12	393	-2
TUC	E	465	521	12	450	-3
	F	280	295	5	322	15
	H	468	526	12	445	-5
	G	296	318	8	311	5
TUD	E	414	463	12	363	-12
	F	544	641	18	413	-24
	H	383	418	9	406	6
	G	354	384	8	360	2

### 4.5.3 Discussion

The experimentally derived  $L_{ph}$  values given in Table 4.4 are compared to their corresponding estimates in Figure 4.20. More precisely the  $L_{ph}$  values determined with: (1) Equation 4.27 are compared to estimates by [PCK07] both assessment and design equations, (2) Equation 4.35 are compared to estimates by [Kaz13] and (3) Equation 4.32 are compared to estimates by [BA11]. To remove the bias of the low experimentally determined strain penetration lengths, the strain penetration term is not considered in the estimates by [PCK07] (Equations 4.23 and 4.24). The other estimates used for the comparisons do not include a strain penetration effect and hence they are compared in their original form (Equations 4.25 and 4.26).

While for most loading positions the  $L_{ph}$  estimates are smaller than the experimentally determined  $L_{ph}$ , this is not the case for the diagonal loading positions (E to G) (Figure 4.20). With the exception of the design equation by [PCK07], which has the largest degree of conservatism, all other equations lead for the diagonal positions (especially F and G) to  $\sim 10 - 50\%$  larger  $L_{ph}$  values than the experimentally measured ones. For the design equation [PCK07]d the  $L_{ph}$  estimates are  $\sim 40 - 50\%$  lower than the experimental  $L_{ph}$  values, except at position F and G where the estimates are only  $\sim 30\%$  lower than the experimental values. Despite being intended as a lower bound value of the plastic hinge length, the estimates by [BA11] are also slightly larger than the experimental values at position F and G while the equation by [Kaz13] results in the largest  $L_{ph}$  estimates and hence also the largest overestimation for the diagonal loading positions. This overestimation is traced back to the lower plastic hinge lengths under diagonal loading than for the principal loading directions (Figure 4.19).

Overall, existing estimates of plastic hinge lengths are approximately 50 – 80% of the experimentally derived values for the principal loading directions (NS cycles and EW cycles). If plastic curvatures are well estimated, the wall displacement capacities obtained with such  $L_{ph}$  estimates will be lower than the actual capacity of the wall, which is desirable in design. However for the diagonal loading directions, the  $L_{ph}$  estimates are less conservative than they are for the principal directions and even overestimate the experimental values by up to 50%. The largest discrepancy is obtained for positions F and G (i.e., when corner web-flange in compression). Plastic hinge lengths estimates for the diagonal loading positions warrant hence further investigation. This topic is addressed through a parametric study on U-shaped walls in Chapter 6.

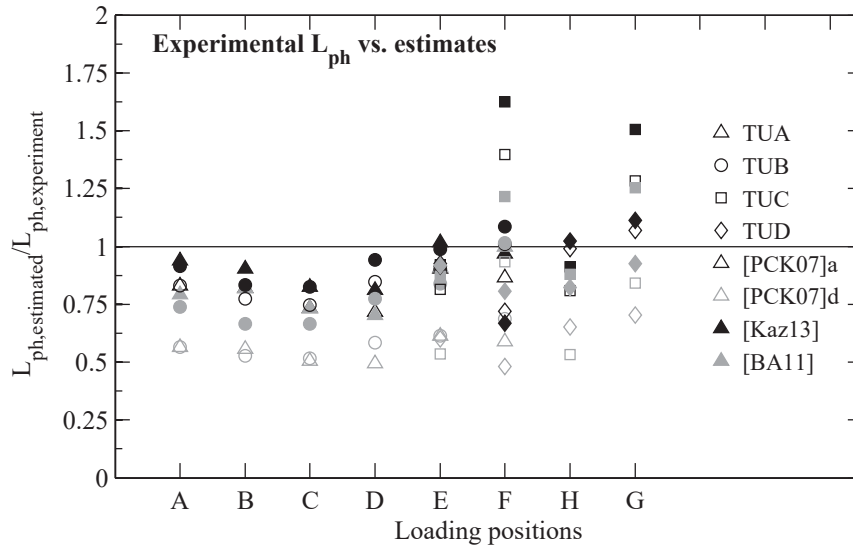


**Figure 4.20:** TUA to TUD: comparison of experimentally determined plastic hinge lengths averaged for peak displacements larger than  $\mu_{\Delta} = 2$  with corresponding estimates. The shape of the marker indicates the test unit: triangle for TUA, circle for TUB, square for TUC and diamond for TUD. The color of the marker indicates the estimate: empty black marker for [PCK07] assesment equation, empty grey marker for [PCK07] design equation, black-filled marker for [Kaz13] equation and grey-filled marker for [BA11] equation.

## 4.6 Ultimate limit strains

### 4.6.1 Introduction

To define the wall displacement capacity in the framework of PH analysis, ultimate limit strains are used with section analysis to obtain the ultimate curvature. This curvature is then combined with a plastic hinge length to obtain the displacement capacity of the wall. The prediction of the experimentally derived plastic hinge lengths has been discussed in the previous section. This section discusses the prediction of the experimentally observed ultimate limit strains and curvatures for U-shaped walls under different loading directions.

The ultimate limit states that are discussed in this section have been experimentally observed for at least one of the four discussed test units and are of interest in predicting the displacement capacity of capacity designed walls. These ultimate limit states are:

- Buckling of the boundary reinforcing bars
- Fracture of the boundary reinforcing bars
- Crushing of the confined concrete
- Out-of-plane buckling of the wall boundary element

Note that the concrete crushing in the compression diagonals of the web of TUB [BDP08b] is not discussed here as this limit state is mainly related to the force capacity of the wall. A discussion of this limit state can be found in [BDP08a].

The suitability of existing limit strain estimates to predict the ultimate limit states listed above is assessed in this section in two ways: (1) by predicting the experimental strains measured on the wall over the region where damage concentrated and (2) by predicting the experimentally derived ultimate curvature by means of section analysis.

### 4.6.2 Experimentally determined ultimate limit strains and curvatures

The experimentally derived strains were taken from the LVDT measurement at the wall edges as the average of strains over the height  $h = 50 - 150$  mm. The strain values near the base ( $h = 0 - 50$  mm) measured mainly the strain penetration effects into the foundation and hence were not considered representative for the maximum strain level in the wall itself. Instead, the average strains in the second row of LVDTs from the base were considered to represent best the actual strain state at the critical section for drifts in the inelastic range: bar buckling and fractures as well as concrete crushing occurred mainly at the level of the second LVDT. The strain values were corrected for the distance between the actual position of the LVDTs (i.e.,  $\sim 3.5$  cm from the wall surface and  $\sim 5$  cm to the edge of the wall) and the edge of the corner or of the flange end, by assuming a linear strain variation in the direction of the web and in the direction of the flanges between the LVDT chains. The experimentally derived ultimate curvatures at the wall base where computed from the rotation above the height of the plastic zone, i.e., computed as  $\phi_{b2}$  (see previous section).

### 4.6.3 Comparison with limit strain estimates

#### Longitudinal bar buckling in the boundary elements

Bar buckling in the boundary elements has been observed for all test units at different wall corners and positions (Table 4.5). The total strain excursion  $\epsilon_s - \epsilon_c$ , i.e., maximum recorded tensile strain in the steel bar  $\epsilon_s$  and minimum recorded compressive strain  $\epsilon_c$  is considered as the best criterion for assessing the onset of bar buckling [Res93]. [Hin02] suggested an interval of  $35\% \leq \epsilon_s - \epsilon_c \leq 50\%$  as limit strain for bar buckling while [DBB09] suggested a limit of  $\epsilon_s - \epsilon_c \leq 35\%$ , based on experimental tests from six rectangular walls.

The experimentally measured total strain excursions (Table 4.5 column seven) compare well with the existing estimates except for the strains in the West flange end of TUC. At this location, out-of-plane buckling of the boundary element occurred in the following loading cycle and hence LVDT measurements in the previous cycle might have been influenced by the onset of global buckling. If this case is not considered, an average value of the total strain excursion  $\epsilon_s - \epsilon_c$  of  $44\%$  can be obtained, which compares very well with the median of the strain interval proposed by [Hin02].

## Chapter 4. Experimentally derived quantities for the plastic hinge model

All total strain excursion values are larger than the 35‰ limit proposed by [DBB09]. These limit strains were derived by matching the experimental base curvature at the instant of bar buckling to the one from section analysis and back-calculating the strain value. If the same procedure is used here, the strain excursion which should be used with section analysis to match the experimental curvature, yields values close to 35‰.

For the East flange end of TUD, the measured compressive strains  $\varepsilon_c$  were larger than the maximum tensile strains  $\varepsilon_s$  recorded at this location and the former controlled the onset bar buckling. For this case, lower strain limits should be used in section analysis to predict accurately the ultimate curvature. In conclusion, the total strain excursion limit  $\varepsilon_s - \varepsilon_c = 35‰$  proposed by [DBB09] can be used with section analysis to determine the onset of buckling, as long as the tensile strains are controlling the onset of bar buckling.

**Table 4.5:** Bar buckling limit state: experimentally determined LVDT strains ( $h = 50 - 150$  mm) at the limit state and comparison of experimentally determined base curvatures  $\phi_{b2}$  to section analysis curvatures  $\phi_{PSA}$ .

TU	Location	Pos.	Drift [%]	$\varepsilon_{LVDT}$			Curvatures		
				$\varepsilon_s$ [‰]	$\varepsilon_c$ [‰]	$\varepsilon_s - \varepsilon_c$ [‰]	$\phi_{b2}$ [1/km]	$\phi_{PSA}$ [1/km]	Diff. [%]
TUA	West fl. end	E	1.8	34	-3	37	34.1	35.0	3
TUB	West fl. end	E	2.6	32	-10	42	41.7	35.0	-16
TUC	East fl. end	H	1.5	38	-10	48	23.5	21.8	-7
	Corner NE	F	2.0	20	-24	44	18.7	21.8	17
	West fl. end	E	2.5	49	-21	70	37.2	21.8	-40
TUD	Corner NW	G	2.0	44	-7	51	24.9	21.8	-12
	East fl. end	H	1.5	17	-27	44	10.7	21.8	104

### Longitudinal bar fracture in the boundary elements

Bar fracture in the boundary elements was observed only for TUA and TUC (Table 4.6). In plastic hinge analysis, the steel strain  $\varepsilon_s$  is used as a criterion for determining when bar fracture occurs. As discussed in Section 2.2.3, a strain limit equal to 50 – 60% of the ultimate steel strain  $\varepsilon_{su}$  obtained from uni-axial bar tests is recommended to account for the effect of bar buckling.

## 4.6. Ultimate limit strains

The ultimate steel strain of the D12 bars in the West flange of TUA is of  $\varepsilon_{su} = 127\%$  while for TUC the D8 bars had  $\varepsilon_{su} = 79\%$ . Hence, the average measured strains on the wall at bar fracture account for 0.62 to 0.84 % of the ultimate steel strain  $\varepsilon_{su}$  (Table 4.6 column six). Using a limit strain of  $\varepsilon_s = 0.5\varepsilon_{su}$  results in a very good match of section analysis curvatures and experimentally determined base curvatures (column nine).

**Table 4.6:** Bar fracture after buckling limit state: experimentally determined LVDT strains ( $h = 50 - 150$  mm) at the limit state and comparison of experimentally determined base curvatures  $\phi_{b2}$  to section analysis curvatures  $\phi_{PSA}$ .

TU	Loca- tion	Pos.	Drift	$\varepsilon_{LVDT}$		Curvatures		
				$\varepsilon_s$	$\frac{\varepsilon_s}{\varepsilon_{su}}$	$\phi_{b2}$	$\phi_{PSA}$ ( $\varepsilon_s = 0.5\varepsilon_{su}$ )	Diff.
			[%]	[‰]	[-]	[1/km]	[1/km]	[%]
TUA	West fl. end	F	2.1	87	0.69	42.6	44.0	3
TUC	East fl. end	G	2.0	66	0.84	33.6	28.8	-14
	Corner NW	H	2.5	49	0.62	31.1	30.9	-1

### Crushing of the confined concrete

Crushing of the confined concrete was observed for both TUC and TUD in the boundary element of the East flange end (Table 4.7). Limited crushing of the confined boundary element occurred also in the corners of TUC at  $\sim 2.5\%$  drift but strain values at this drift level are questionable (i.e., at position F and G of TUC compressed corners show positive strains) and cannot be compared to estimates.

Strain estimates by [MPP88] (Table 4.7 column six) multiplied by a factor of 1.3 to 1.6 as suggested by [PCK07] compare well with the average measured strains on the wall at the height where damage occurred, i.e.,  $h = 50 - 150$  mm (column five). However limit state curvatures determined from section analysis with these strain estimates significantly overestimate the experimentally determined base curvature (column nine).

For both cases, a concrete limit strain of  $\varepsilon_c = \sim -8\%$  instead of  $-24\%$  should be used in section analyses if the section analyses curvatures were to match the experimental base curvatures. This is in line with findings by [DBB09] who also observed that the measured wall strains where confined concrete crushing occurred were  $\sim 2.6$  times larger than the strain limits derived from section analysis for the same curvature as the experimental base curvature.

## Chapter 4. Experimentally derived quantities for the plastic hinge model

Based on these experimental findings it is recommended to use for section analysis a concrete limit strain equal to one third of the estimates obtained with [MPP88] equation for confined concrete crushing. This recommendation is highly empirical as it is based on very limited experimental data. In addition, the limit strain at the crushing of confined concrete will depend on concrete properties and confinement reinforcement properties and layout and hence proper validation requires extensive experimental data.

Alternatively, since confined concrete crushing is typically preceded by bar buckling, the ultimate limit state can be defined by the limit strain that characterizes the onset of bar buckling (see Table 4.5). Note, however, that the total strain limits for the onset of bar buckling yield only good predictions if the compressive strains are not larger than the tensile strains in which concrete crushing limit states should be used.

**Table 4.7:** Crushing of the confined concrete: experimentally determined LVDT strains ( $h = 50 - 150$  mm) at the limit state and comparison of experimentally determined base curvatures  $\phi_{b2}$  to section analysis curvatures  $\phi_{PSA}$ .

TU	Loca- tion	Pos.	Strains			Curvatures		Diff. [%]
			Drift [%]	$\epsilon_{LVDT}$ [‰]	$\epsilon_{c,[MPP88]}$ [‰]	$\phi_{b2}$ [1/km]	$\phi_{PSA}$ ( $\epsilon_{c,[MPP88]}$ ) [1/km]	
TUC	East fl. end	H	2.0	-34	-24	24.9	64.6	160
TUD	East fl. end	H	1.5	-30	-24	17.2	39.5	130

### Out-of-plane buckling of the wall boundary element

Local out-of-plane buckling of the boundary element was observed for TUC for the West flange end as described in Section 3. The out-of-plane buckling did not involve the entire height of the boundary element as a global buckling would (see Section 3.3.1.1). However, without a clear differentiation of these phenomena, estimates for maximum tensile strains triggering global out-of-plane buckling will be used for comparison with the experimentally measured strains.

Two different estimates by [PP93] and [CE99] were discussed in Section 2.2.3. The two estimates for the maximum tensile strain  $\epsilon_s$  were computed using the experimentally determined plastic hinge lengths (third column in Table 4.4). The two estimates yield similar values for the West flange end, i.e.,  $\epsilon_{s,Paul93} = 38\text{‰}$  and  $\epsilon_{s,Chai99} = 37\text{‰}$  but based on these estimates out-of-plane buckling should have occurred for the confined ends of both flanges already at 1.5% drift, instead of 2.5% drift. It was argued that the out-of-plane bending of the flange promoted the out-of-plane buckling behaviour of the flange end due to strain gradient through the thickness of the boundary element (Section 3). Intuitively, this should lead to out-of-plane buckling of the flange end at smaller top drifts than when the flange is only loaded in-plane (which is the load case considered in [PP93] and [CE99]). Therefore, the predictions for the tensile strain triggering the out-of-plane buckling of the flange ends seem rather conservative estimates.



## 4.7 Shear displacements

Shear displacements, typically used in plastic hinge analysis under the form of shear to flexural displacement ratios  $\Delta_s/\Delta_f$ , have been discussed in Section 2.2.2. In the following, the derivation of the experimental  $\Delta_s/\Delta_f$  ratios is discussed and the trends of these ratios over the ductility range examined. The experimental  $\Delta_s/\Delta_f$  ratios are compared with existing estimates.

### 4.7.1 Experimentally determined shear to flexural displacement ratios

#### 4.7.1.1 Experimental determination

For TUC and TUD, the shear displacements were experimentally determined in two different ways for the two types of conventional and optical measurements as explained in Section 4.2. Shear displacements were derived from the conventional measurement data (LVDTs) through the indirect method (i.e., top displacements minus flexural displacements). Shear displacements obtained from the optical measurement (LEDs) data were derived through the direct method (i.e., computing shear displacements from the change in length of diagonals of the rectangular LED-composed elements, and hence independently of the flexural displacements).

The experimentally determined values from the optical measurement system will be used in this section to assess the  $\Delta_s/\Delta_f$  ratios because this method is considered to be more accurate due to: (1) the relatively fine measurement grid as compared to the LVDT grid and (2) the good agreement between the sum of displacement components and the measured top displacement. The average error in the inelastic range between the sum of the deformation components and the top measured displacements for all loading positions is of 3.2% for the web, 0.8% for the West flange and 2.0% for the East flange with standard deviations of 7.9%, 3.8% and 6.3% respectively. Positions A and B were not accounted for in the measurements for the flanges and positions C and D were not accounted for in the measurements for the web.

For consistency, the shear displacements of TUA and TUB included in this section were also experimentally determined using the direct method. However, for TUA and TUB a conventional measurement system was used: string pots arranged diagonally and spanning rectangular panels over the outer faces of the flanges and the web. The procedure used for TUA and TUB is described in detail elsewhere [BDP08a]. The errors between the sum of displacement components and the measured top displacement were found to vary from approximately  $-20\%$  to  $+10\%$  with largest errors typically towards the elastic range [BDP08a].

#### 4.7.1.2 Variation of shear displacements with displacement ductility

The experimentally determined  $\Delta_s/\Delta_f$  ratios are shown in Figures 4.22 and 4.23 for all four test units, for the different wall sections and loading positions. As already observed by previous researchers [HRS04], [DBB09], [BDP11], for flexure controlled walls the  $\Delta_s/\Delta_f$  ratios are approximately constant in the inelastic range (i.e., for drifts larger than the nominal yield drift  $\delta_y$ ). The loading positions and the wall cardinal directions are repeated in Figure 4.21 for good readability of results.

## Chapter 4. Experimentally derived quantities for the plastic hinge model

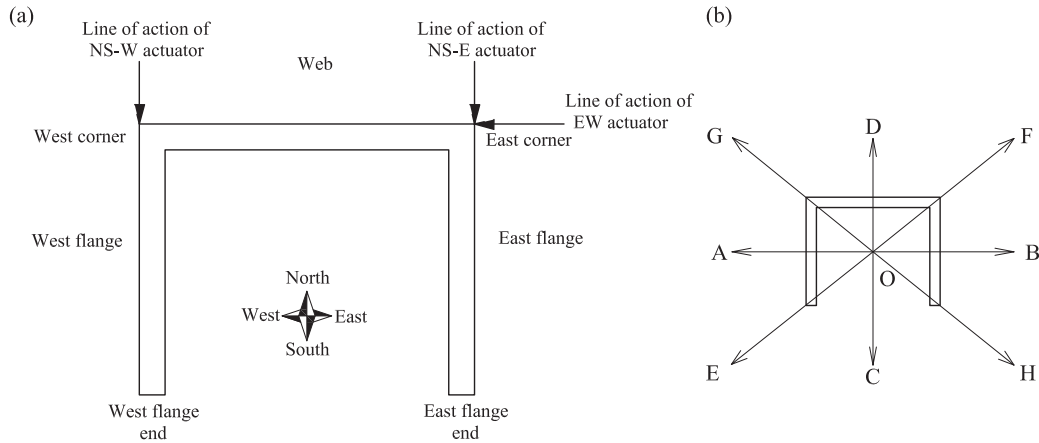


**Figure 4.21:** TUA, TUB, TUC and TUD: naming of the different wall parts and cardinal directions (a) and loading positions (b).

The  $\Delta_s/\Delta_f$  ratios depend strongly on the loading direction, with the largest contribution being when wall sections (flanges or web) are under net tension. This is the case for the web at positions A, B, E and H and for the West flange at position F and East flange at position G (Figures 4.22 a, b, e, f and 4.23 a, b, e, f). For example, for the West flange at position F of TUC and TUD (Figure 4.23e-f), the  $\Delta_s/\Delta_f$  ratios are as high as 1.00 (i.e., shear displacements equal to flexural displacements) and hence significantly higher than for typical rectangular slender walls. This is in line with experimental findings by [BDP08b] for U-shaped walls and [ZL14] for L-shaped and T-shaped walls.

At positions E and H, one obtains negative  $\Delta_s/\Delta_f$  ratios for the East and the West flange respectively (Figures 4.22e-f and 4.23 e-h). [BDP08b] first observed this trend in their tests and related this observation to the drop in the flange force (NSE force and NSW force, respectively) which reached its peak shortly after zero displacement and then decreased with increasing drifts.

Since the trend of the  $\Delta_s/\Delta_f$  ratios is constant over the inelastic phase, a single  $\Delta_s/\Delta_f$  ratio can be used to characterise the shear deformation. This value was determined for each test unit, for the different wall sections and each loading positions as the average of the  $\Delta_s/\Delta_f$  ratios at peak displacements larger than the yield displacement. The values are given in Tables 4.8 and 4.9.

### 4.7.2 Estimates for the shear displacements in the inelastic range

The empirical models by [HRS04] and [BDP11] presented in Section 2.2.2 are used here to predict the  $\Delta_s/\Delta_f$  ratios corresponding to the inelastic range for all four test units. For convenience the equations for both models are repeated here:

$$\frac{\Delta_s}{\Delta_f} = \alpha 0.35(1.6 - 0.2\theta_{max}) \frac{l_{wall}}{H} \quad (4.36a)$$

## 4.7. Shear displacements

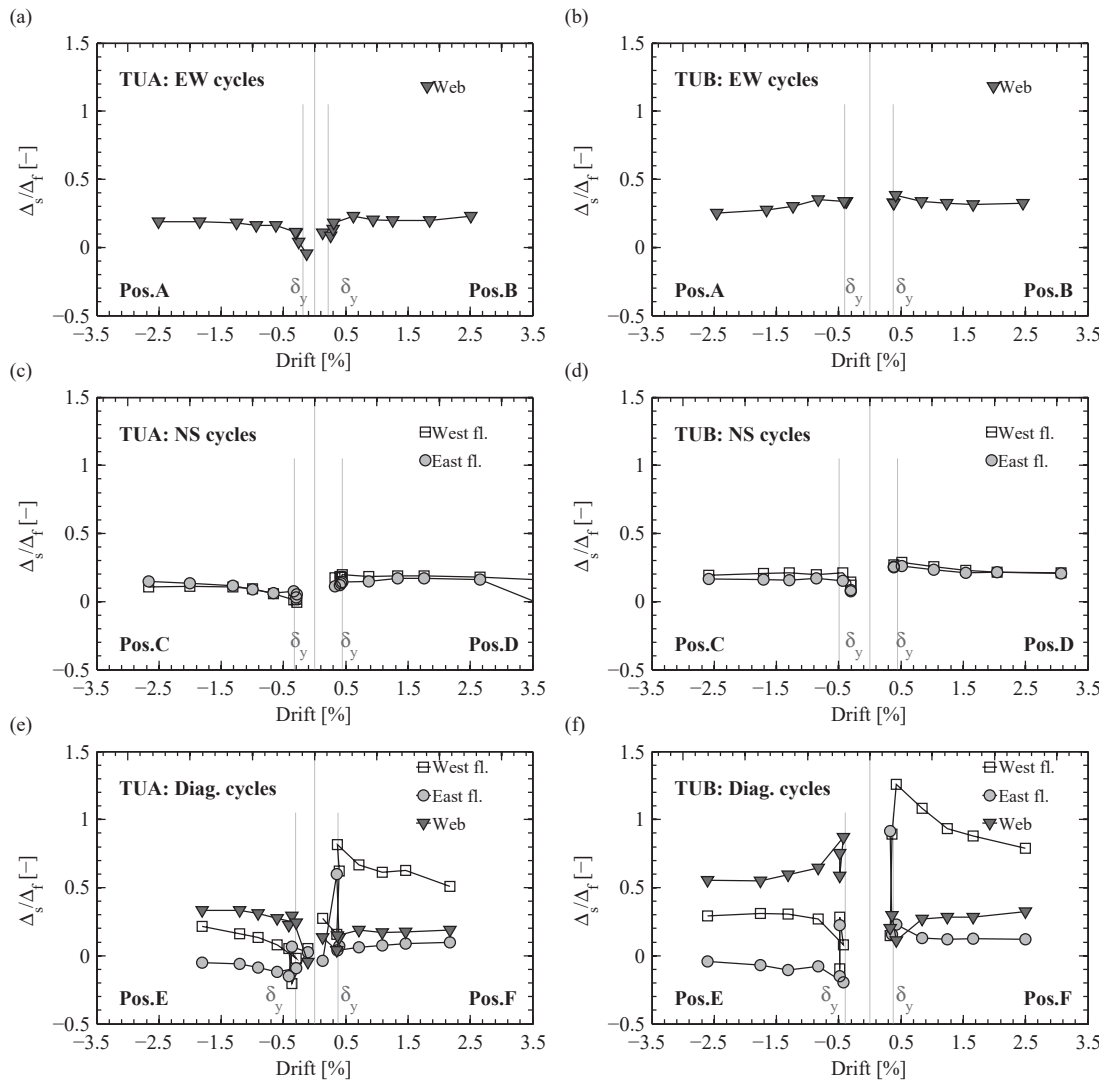


**Figure 4.22:** TUA and TUB: Experimentally determined shear to flexural displacement ratios

**Table 4.8:** TUA to TUB: experimentally determined average values of the  $\Delta_s/\Delta_f$  ratios in the inelastic phase

Pos.	TUA			TUB		
	West fl.	East fl.	Web	West fl.	East fl.	Web
A	-	-	0.12	-	-	0.31
B	-	-	0.17	-	-	0.33
C	0.06	0.08	-	0.18	0.14	-1.05
D	0.18	0.13	-	0.25	0.23	0.17
E	0.06	-0.05	0.25	0.21	-0.06	0.65
F	0.54	0.11	0.15	0.86	0.26	0.25

## Chapter 4. Experimentally derived quantities for the plastic hinge model

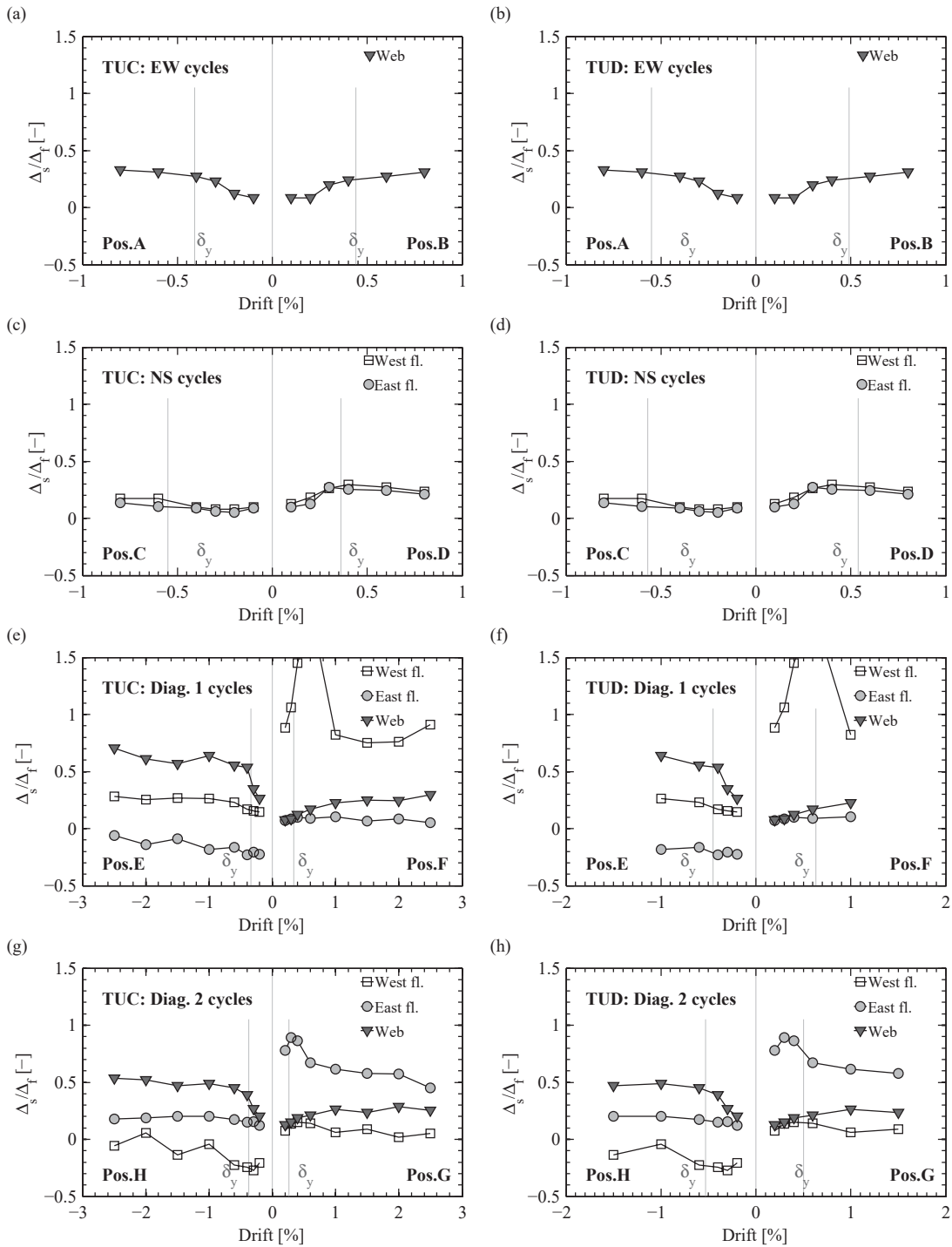


**Figure 4.23:** TUA and TUB: experimentally determined shear to flexural displacement ratios

## 4.7. Shear displacements

**Table 4.9:** TUC to TUD: experimentally determined average values of the  $\Delta_s/\Delta_f$  ratios in the inelastic phase

Pos.	TUC			TUD		
	West fl.	East fl.	Web	West fl.	East fl.	Web
A	-	-	0.25	-	-	0.33
B	-	-	0.25	-	-	0.26
C	0.16	0.16	-	0.12	0.16	-
D	0.26	0.21	-	0.31	0.26	-
E	0.15	-0.12	0.50	0.13	-0.13	0.60
F	1.11	0.11	0.21	1.22	0.15	0.18
H	-0.17	0.22	0.42	-0.17	0.19	0.37
G	0.15	0.69	0.22	0.26	1.18	0.26

$$1 \leq \alpha = \left( \frac{V}{V_n} + \frac{V}{V_{wc}} \right) \leq 2 \quad (4.36b)$$

where  $V_n$  is the diagonal tension capacity,  $V_{wc}$  is the web crushing capacity and  $\theta_{max}$  is the angle of the highest crack whose tip reaches the wall base.

$$\frac{\Delta_s}{\Delta_f} = 1.5 \frac{\epsilon_m}{\phi \tan \theta} \frac{1}{H} \quad (4.37)$$

where  $\phi$  is the wall curvature assumed constant over the plastic hinge,  $\theta$  is the crack angle at the top of the fan-like pattern where cracks begin to be parallel and 1.5 is an empirical correction factor.

For both models the crack angle  $\theta$  according to Equation 4.38 was used. This equation includes both the transversal  $\rho_h$  and the longitudinal reinforcement  $\rho_l$  contents to capture the variation of crack angles between the flange with distributed reinforcement and the one with concentrated reinforcement, while  $k_E$  is the ratio between the modulus of elasticity of steel and concrete  $k_E = E_s/E_c$  (see also Section 2.2.2).

$$\tan \theta = \sqrt[4]{\frac{\rho_h + k_E \rho_l \rho_h}{\rho_l + k_E \rho_l \rho_h}} \quad (4.38)$$

## Chapter 4. Experimentally derived quantities for the plastic hinge model

---

In the model by [HRS04], the correction factor  $\alpha$  (Equation 4.36b) was determined using as the shear demand  $V$ , the nominal shear force associated to the moment obtained from section analysis. The diagonal tension capacity  $V_n$  was determined using the modified UCSD model [PCK07], where a displacement ductility  $\mu_\Delta = 6$  was assumed in the computation of the concrete contribution  $V_c$ . The diagonal compression capacity was calculated according to [CEN04] (6.2.3). In the model by [BDP11], the mean axial strain over the wall sections  $\varepsilon_m$  and the curvature  $\phi$  corresponding to the plastic hinge, were derived from section analysis at nominal point.

The results obtained with the two models for all test units are compared to the experimentally determined  $\Delta_s/\Delta_f$  ratios in Figures 4.24 and 4.25. The model by [BDP11] shows a rather good match with the experimentally determined  $\Delta_s/\Delta_f$  ratios. The model by [HRS04] predicts for all test units and loading positions very similar  $\Delta_s/\Delta_f$  ratios. This is caused by the correction factor  $\alpha$  (Equation 4.36b), which varies very little as the ratio of the shear demand to shear capacity was close to 1 for both the diagonal tension and the diagonal compression capacities. Hence  $\alpha$  was in most cases slightly lower than 2 or equal to 2 if the estimated shear demand was higher than the design shear capacity.

When comparing the two approaches, [BDP11] yields better estimates than [HRS04] for medium  $\Delta_s/\Delta_f$  ratios as well as for the large  $\Delta_s/\Delta_f$  ratios. None of the two approaches captures the negative  $\Delta_s/\Delta_f$  ratios.

### 4.7.3 Estimates for the shear displacements at yield

The shear displacements at yield are of interest when estimating the wall yield displacement by predicting separately the flexural displacements and the shear displacements (Section 4.4.2). The experimental shear to flexural displacements ratios were taken as the  $\Delta_s/\Delta_f$  ratios at first yield, where the point of first yield was determined based on strains as discussed in Section 4.3.2.4. Estimates were computed using the [BDP11] model, since it resulted in good estimates for the inelastic  $\Delta_s/\Delta_f$  ratios. The comparison for all test units is shown in Figure 4.26.

The  $\Delta_s/\Delta_f$  ratios at yield are still relatively well captured with Equation 4.37, although the match is poorer than for the shear displacements in the inelastic range. The reasons for this observation are two-fold: (1) Equation 4.37 was calibrated for shear displacements in the inelastic range while the experimental  $\Delta_s/\Delta_f$  ratios at yield are slightly different than the experimental values in the inelastic range (see Figures 4.22 and 4.23) and (2)  $\Delta_s/\Delta_f$  ratios at yield are more sensitive to measurement errors, e.g. a error of 1-2 mm in the shear displacements can lead to errors of 10-20 % in the  $\Delta_s/\Delta_f$  ratios when top displacements are of below 10 mm. Despite these shortcomings, Equation 4.37 still provides reasonable estimates for the  $\Delta_s/\Delta_f$  ratios at yield and will be used for this purpose in Chapter 6.

## 4.7. Shear displacements

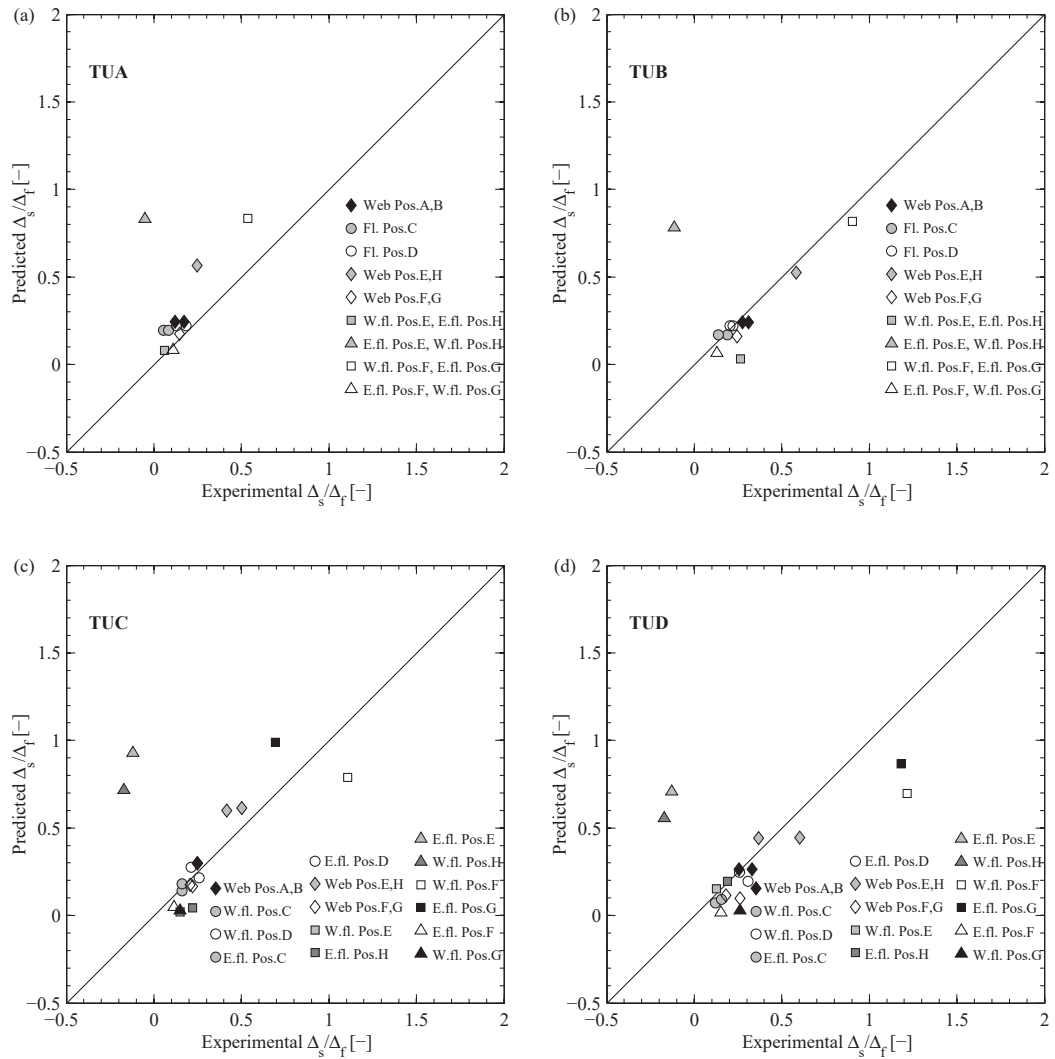


**Figure 4.24:** TUA, TUB, TUC and TUD: comparison of experimentally determined shear to flexural displacement ratios  $\Delta_s/\Delta_f$  in the inelastic phase with estimates based on the [BDP11] model.

## Chapter 4. Experimentally derived quantities for the plastic hinge model

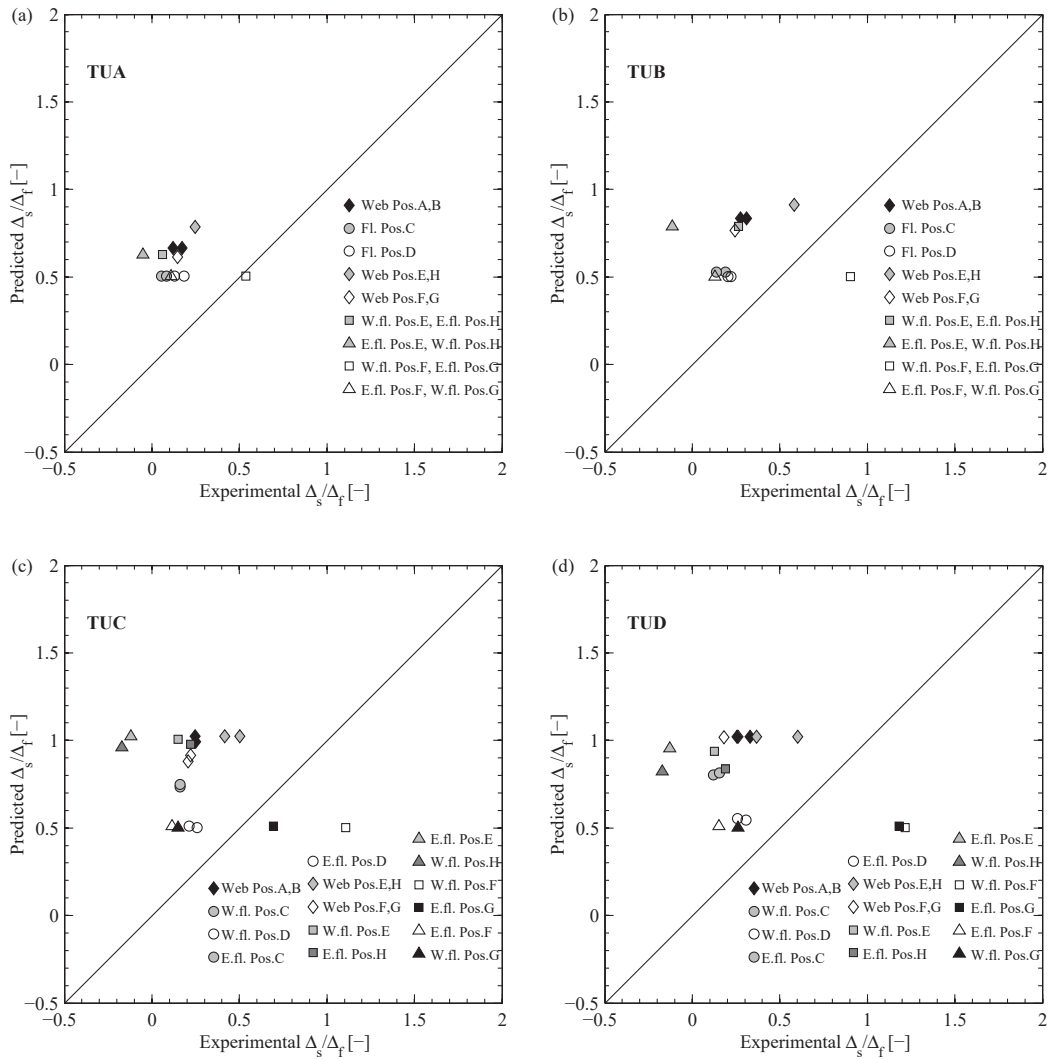


**Figure 4.25:** TUA, TUB, TUC and TUD: comparison of experimentally determined shear to flexural displacement ratios  $\Delta_s/\Delta_f$  in the inelastic phase with estimates based on the [HRS04] model.



## 4.7. Shear displacements

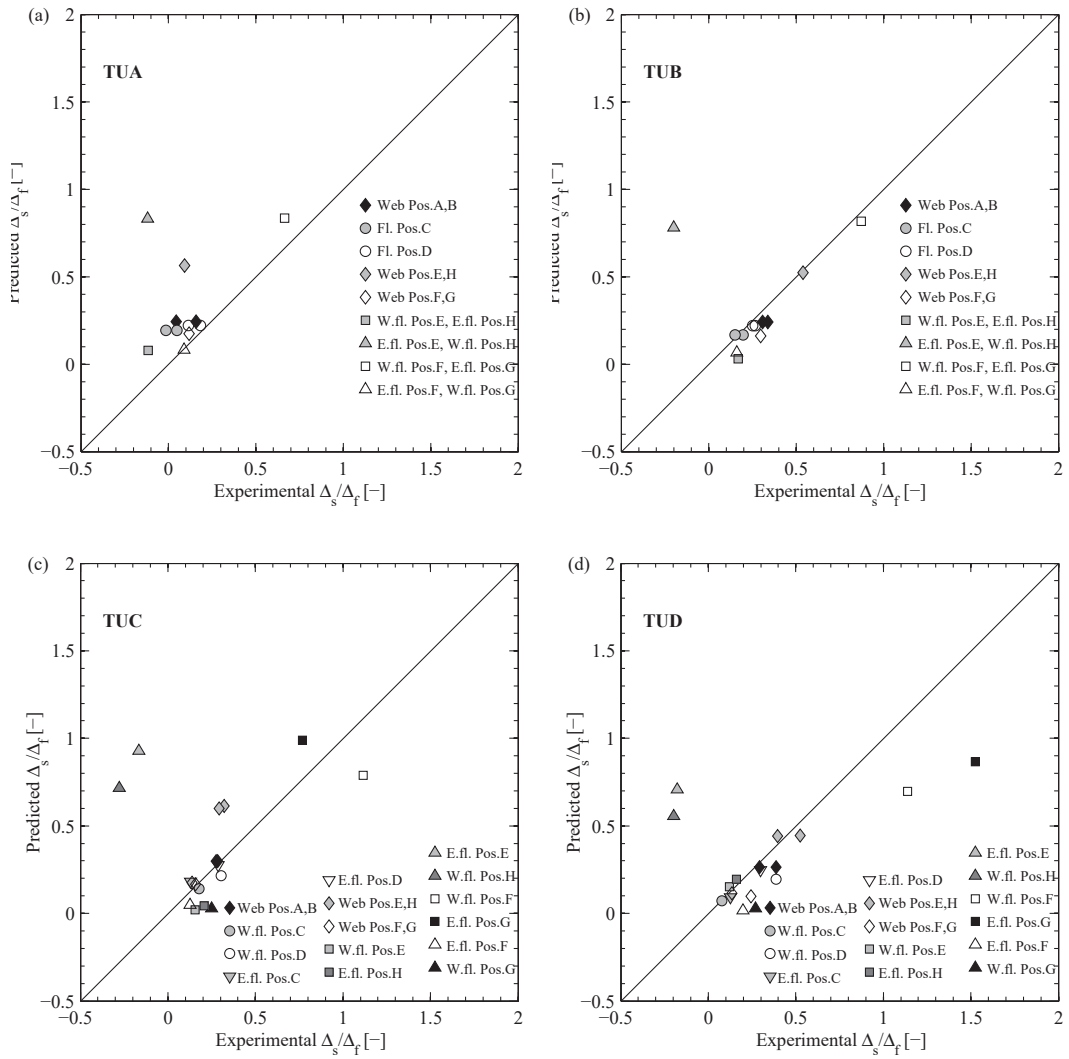


**Figure 4.26:** TUA, TUB, TUC and TUD: comparison of experimentally determined shear to flexural displacements ratios  $\Delta_s/\Delta_f$  at yield with estimates based on the [BDP11]

## 4.8 Effective stiffness of RC walls

The effective stiffness is an important quantity in the design of RC walls. Most estimates of the effective stiffness are expressed under the form of the ratio of the effective moment of inertia  $I_e$  to the gross moment of inertia of the section  $I_g$ , while assuming a constant wall stiffness over the height.

In order to compare with existing estimates, the experimentally derived effective stiffness  $K_{eff,exp}$  will be expressed under the form of a ratio of effective stiffness to the elastic flexural stiffness of a cantilever wall  $K_{th} = 3E_c I_g / H^3$ , where  $E_c$  is the concrete modulus of elasticity obtained from material tests and  $H$  is the height of the cantilever wall. The effective stiffness  $K_{eff,exp}$  was determined experimentally as the ratio between the first yield force  $F'_y$  and the first yield displacement  $\Delta'_y$ , both obtained from experimental measurements at the instant of first yield. The instant of first yield was determined for each loading position based on strain limits as discussed in Section 4.3. The estimates for the effective stiffness ratios have been reviewed in Section 2.2.4 and are briefly repeated below.

[PP92]: estimate which accounts for shear displacements and strain penetration for walls with aspect ratios lower than four

$$I_e = \left( \frac{100}{f_y} + \frac{N}{f_c A_g} \right) I_g \quad (4.39a)$$

$$I_w = \frac{I_e}{1.2 + F} \quad (4.39b)$$

$$F = \frac{30I_e}{H^2 l_{wall} t_{wall}} \quad (4.39c)$$

[FB00]: approach for slender walls, does not consider shear displacements but considers tension stiffening

$$I_e = 0.267 \left( 1 + 4.4 \frac{N}{f_c A_g} \right) \left( 0.62 + \frac{190}{f_y} \right) (0.76 + 0.005 f_c) I_g \quad (4.40)$$

[AIB07]: approach for high-rise slender walls, does not consider shear displacements, suggests lower bound and upper bound depending on the extent of cracking

$$I_e = \left( 0.6 + \frac{N}{f_c A_g} \right) I_g \leq I_g \quad (4.41a)$$

$$I_e = \left( 0.2 + 2.5 \frac{N}{f_c A_g} \right) \leq 0.71 I_g \quad (4.41b)$$

In addition, estimates based on the predicted yield displacements are included in the comparison, namely  $\Delta_{y,1L}$  and  $\Delta_{y,2L}$  estimates. In the computation of the estimates for the diagonal loading direction, the length of the wall was taken as  $l_{wall} = l_{diag}$  and the wall height as  $H = h_{NS}$ . The experimentally determined effective stiffness ratios  $K_{eff,exp}/K_{th}$  are compared with existing estimates in Figure 4.27.

Estimates by [AIB07] led to a lower bound of the effective stiffness ratio of approximately 0.26 to 0.56 (one constant value for each test unit) while the upper bound led to values of approximately 0.62 to 0.75 and hence these estimates were in all cases too high. Therefore they have been not been included in Figure 4.27 to improve the readability of the figure. As Figure 4.27 shows, the estimates by [PP92] led to values close to the experimental ones but do not capture the fact that effective stiffness vary with loading position. [FB00] estimates are too high and are also constant for all loading positions since they do not vary in any way with the loading position. Only estimates based on the yield displacements, i.e.,  $\Delta_{y,1L}$  and  $\Delta_{y,2L}$  vary for the different loading positions.

In most cases the effective stiffness ratio estimates based on the yield displacements are slightly overestimating the experimentally derived stiffness ratio but for TUD the difference is significant. While the yield displacements are well estimated (4.12), this difference is caused by the overestimation of the nominal moment by section analysis. The comparison between experimental and section analysis results is discussed in detail in Section 5.1.

In conclusion, for the test units analysed herein, several approaches can provide reasonable estimates of the effective stiffness ratio. Despite the somewhat large scatter, estimates based on the yield displacements typically capture the variation with the loading position, while the estimate by [PP92] provides a good average match of the values without however capturing the trend with the loading position. Another important point is that the test units included here all have slenderness ratios  $H/l_{wall}$  between 2.6 and 2.8 depending on the loading position, which is a rather limited slenderness range. Therefore the suitability of these estimates should be verified against a broader slenderness ratio range and especially for walls with large slenderness ratios since core walls are typically encountered in mid-to-high rise buildings. The effective stiffness ratios will be further investigated by means of parametric studies in Chapter 6.

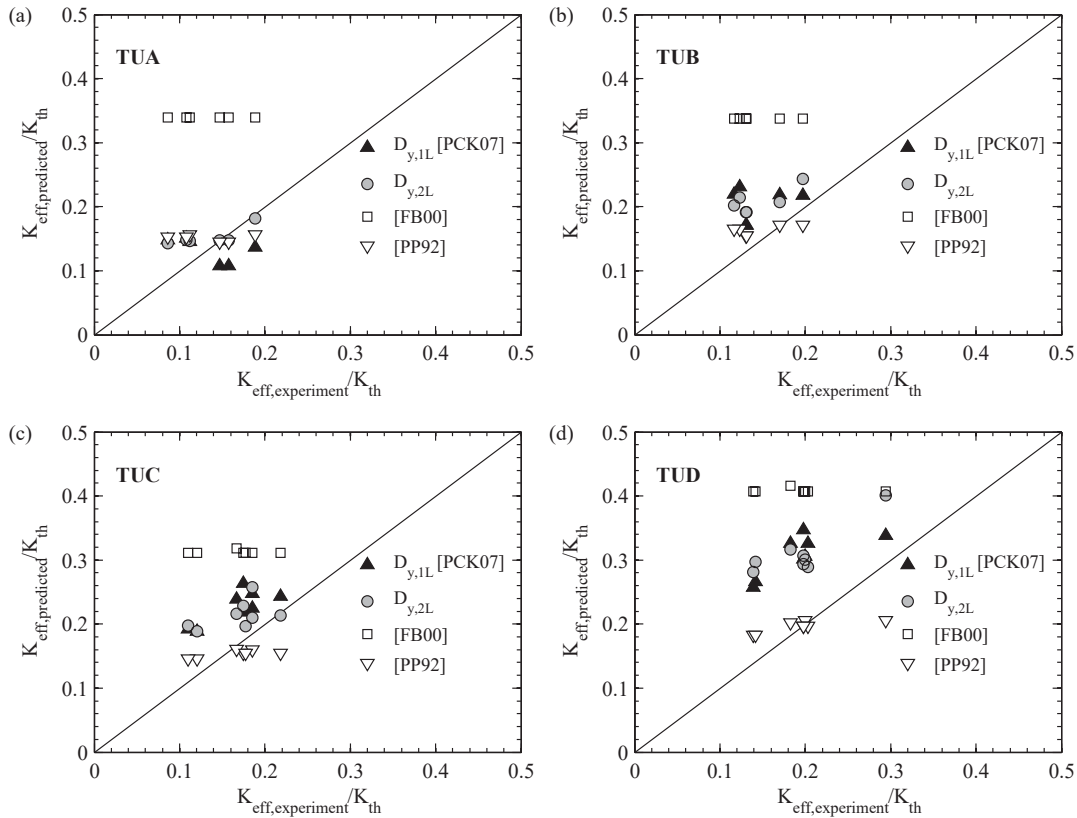


Figure 4.27: TUA, TUB, TUC and TUD: comparison of experimentally determined effective stiffness ratios  $K_{eff,exp}/K_{th}$  with estimates (a-b).

## 4.9 Conclusions

The objective of this chapter was to derive the experimental quantities required in plastic hinge models, from the quasi-static cyclic tests of four U-shaped walls and to compare these quantities with existing estimates. Different procedures for deriving the plastic hinge quantities were investigated so that the derived quantities are compatible with plane section analysis. It was found that despite the invalidity of the plane section assumption, section analysis curvatures can be used with limit strain estimates to determine the limit states of the wall, even at ultimate limit states.

The experimentally derived quantities will be used for the validation of two numerical finite element models at both local and global level in Chapter 5. In the following, the main conclusions from the comparison between the experimental PH quantities and existing estimates as well as the new proposed estimates and recommendations are summarised.

**Yield curvature and displacement** : The yield curvature, experimentally determined, was predicted relatively well by existing estimates for the principal loading directions ( $\sim 15\%$  difference). For the diagonal loading directions, estimates are not available in the literature but yield curvatures could be predicted well using section analysis.

The yield displacement was assessed in two ways: (1) by integrating the assumed linear curvature profile over the wall height at yield and (2) as the sum of the contributions of the flexural displacements due to wall deformation, flexural displacements due to strain penetration into the foundation and shear displacements. A new estimate for the flexural displacement due to wall deformation was proposed assuming a bi-linear curvature profile at yield, i.e., a partially cracked wall over the height. The match between the two different yield displacement estimates and the experimentally derived ones was moderately good, with none of the two approaches providing clearly superior estimates to the other one for the test units analysed herein.

However the approach for determining the yield displacement by accounting for the shear displacements and the partially cracked wall is expected to give relatively good estimates for a larger range of wall configurations as long as the shear displacements and the flexural displacements are well estimated. By comparison, the approach assuming a linear curvature profile is expected to lead to good estimates only as long as the shear displacements compensate for the extent of cracking along the wall height. For more slender walls, as it is the case for core walls in mid-to-high rise buildings, the shear displacements will be small and hence the latter approach is expected to overestimate the yield displacement. This aspect will be hence further examined in Chapter 6 when U-shaped walls with various geometries and slenderness ratios are analysed.

**Plastic hinge length** : The experimentally determined plastic hinge lengths were found yield the smallest values for the diagonal directions, in particular for loading with the corner web-flange in compression. Combined with the smallest curvatures under diagonal loading, this leads to lower displacement capacities for diagonal loading than for the principal loading directions. In addition, the experimental plastic hinge lengths were compared to state-of-the-art estimates for walls. All equations provided conservative estimates for the principal directions of loading. For the diagonal loading positions, especially for positions F and G (corner web-flange in compression), most equations overestimated the experimentally determined plastic hinge lengths or the degree of conservatism was significantly reduced when compared to the principal directions. Overestimating the plastic hinge lengths leads to unconservative displacement capacity estimates. For this reason, the plastic hinge lengths for the diagonal loading directions are further investigated in Chapter 6.

**Ultimate limit strains** : In order to obtain the displacement capacity of the wall, plastic hinge lengths are combined with ultimate curvatures derived from section analysis at the ultimate limit strains. Existing ultimate limit strain estimates for bar buckling, bar fracture and confined concrete crushing matched well the average measured strains on the wall at the location where damage occurred. However, when used in section analysis, the ultimate curvature was significantly overestimated if failure was controlled by the concrete strains, e.g., case of confined concrete crushing.

The following limit strains used with section analysis were found to predict well the experimentally determined ultimate curvatures:

- Bar buckling: total strain excursion  $\varepsilon_s - \varepsilon_c = 35\%$  [DBB09]
- Bar fracture after buckling: tensile steel strain  $\varepsilon_s = 0.5\varepsilon_{su}$  [PCK07]

## Chapter 4. Experimentally derived quantities for the plastic hinge model

---

- Confined concrete crushing: concrete compressive strain  $\varepsilon_c = 1/3\varepsilon_{c,[MPP88]}$

It is recommended to reduce the limit strain for confined concrete crushing to one third of the estimated value from [MPP88] equation. This recommendation is in line with previous findings for rectangular walls [DBB09] although it is based on limited experimental data. Alternatively, the strain corresponding to the bar buckling limit state which precedes confined concrete crushing can be used to determine the ultimate curvature, as long as tensile strains are controlling the behaviour at the damage location. For TUC also the strain limits related to the out-of-plane buckling of the boundary element [PP93], [CE99] were examined but found to be very conservative estimates.

**Shear displacements** : The shear displacements to flexural displacement ratios  $\Delta_s/\Delta_f$  were found to be constant over the inelastic ductility range, which was expected as the walls did not have a significant shear degrading mechanism. Over the elastic range,  $\Delta_s/\Delta_f$  ratios were either increasing towards the yield drift or constant depending on the loading position.  $\Delta_s/\Delta_f$  ratios in the inelastic range and at yield were captured fairly well with estimates by [BDP11] and a cracking angle accounting for the reinforcement contents in the wall.

**Effective stiffness** : In addition to the quantities required for the application of the plastic hinge model, effective stiffness estimates were assessed for all test units. Estimates by [PP92] for walls with aspect ratios lower than four were found to give the best results in terms of errors but they failed to capture the variation of the stiffness with the loading position. The variation was captured by predictions that are based on yield curvatures obtained from section analysis, despite a larger scatter in values due to discrepancies between the predicted and the experimentally measured moment at first yield. Estimates from models that do not account in a direct or indirect way for the shear displacements significantly overestimate the effective stiffness. Since the range of slenderness ratios of the test units included herein is rather limited ( $H/l_{wall}=2.6$  to  $2.8$ ), further studies including also more slender walls are required to assess the suitability of these stiffness estimates. The effective stiffness of U-shaped walls is further investigated in Chapter 6.

## 5. Validation of two numerical models for U-shaped walls

In the previous chapter, the experimental data from four quasi-static cyclic tests on U-shaped walls under bi-directional loading (TUA to TUD) was used to derive experimental quantities for the plastic hinge (PH) model. The experimental values were compared with existing estimates and research needs were identified. These research needs are to be addressed through parametric studies performed with suitable numerical models.

Hence, the objective of this section is to assess the suitability of two numerical models for capturing the seismic behaviour of reinforced concrete (RC) U-shaped walls by comparing the numerical results to experimentally derived quantities. The first model, plane section analysis, was chosen due to its simplicity and because it lies at the basis of plastic hinge analysis and most beam column formulations widely used in the design practice (Section 5.1). From section analysis one obtains the moment-curvature relationship of the section of the wall, hence information only about the wall flexural behaviour. The second model is a detailed shell element model aiming to capture the complete behaviour of U-shaped walls, i.e., flexural as well as shear and torsional behaviour (Section 5.2).

As the interest is to use these two numerical models to perform parametric studies and derive estimates for several plastic hinge quantities (Chapter 6), the two models are compared against the experimentally derived quantities as follows:

- Plane section analysis: in terms of moment capacity, yield curvature  $\phi_y$ .
- Shell element model: in terms of force capacity, yield curvature  $\phi_y$ , yield displacement  $\Delta_y$ , plastic hinge length  $L_{ph}$ , shear to flexural deformation ratios  $\Delta_s/\Delta_f$  and effective stiffness  $K_{eff}$ .

Following these comparisons, conclusions on the capabilities and drawbacks of the models are drawn in Section 5.3. Their suitability for parametric studies is also discussed in this last section.

## 5.1 Plane section analysis

In this section, plane section analysis (PSA) is used to predict the moment capacity and the yield curvature of RC core walls. These quantities are typically necessary in a plastic hinge analysis to predict the force-displacement response of the wall under horizontal loading. For this task, a model for the plane section analysis is set-up in Section 5.1.1. The numerical results obtained from this model are then compared to the experimentally derived results from four quasi-static cyclic tests in Section 5.1.2 and conclusions are presented in Section 5.1.3.

### 5.1.1 Model set-up

Monotonic plane section analyses of the four U-shaped sections of TUA, TUB, TUC and TUD were performed by means of a relatively simple numerical model using the “Opensees” software [MMG09]. A zero-length fibre element with approximately 200 concrete fibres and one fibre per reinforcement bar was used to model the sections (Figure 5.1a). For all sections, the concrete areas were grouped into different zones depending on the degree of confinement. The confined and unconfined concrete were model using the stress-strain relationship by [Pop73], i.e., Concrete04 material model in Opensees, while confinement properties were computed according to [MPP88] (Figure 5.1c). The reinforcement was modelled using an uni-axial Giuffre-Menegotto-Pinto steel material [FPB83], i.e., Steel02 material model in Opensees, with default parameters (Figure 5.1b).

Analyses were performed in displacement control. For the diagonal loading directions the loading was applied in a displacement controlled-mode so that the applied curvature vector had the same direction as one of the geometric diagonals of the section. Yield, nominal and ultimate strain limits were determined using recommendations by [PCK07] and discussed in the following.

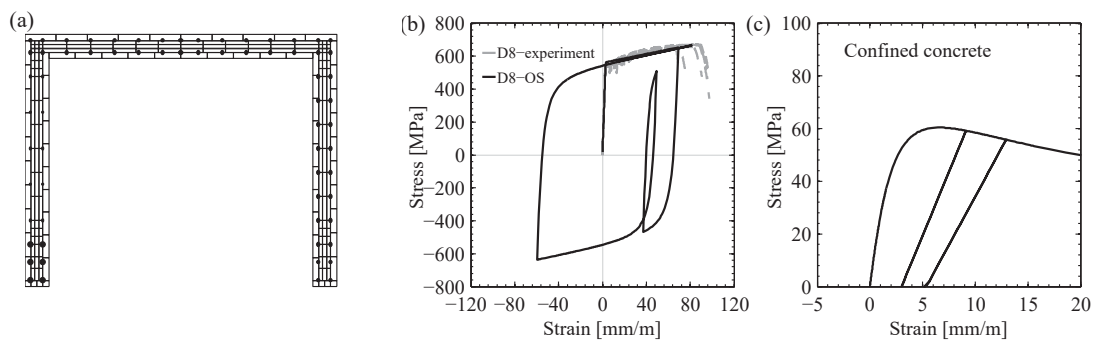


**Figure 5.1:** Section analysis model: subdivision of the section and examples of stress-strain relationships applied to reinforcement and concrete fibres



## 5.1.2 Model validation

### 5.1.2.1 Experimental determination of moment-curvature relationship

In order to compare the numerical results from a plane section analysis (PSA) to experimental data, the moment-curvature relationship must first be determined for all the directions in which loading was applied during the experiments. The directions (NS, EW and diagonal) and positions (A to G) along which displacements were applied at the top of the wall are shown in Figure 5.2b-c. When applying displacements along the geometric diagonals of the wall section, two diagonal loading directions are distinguished: loading direction between positions E and F (diagonal E-F) and loading direction between positions H and G (diagonal H-G).

The experimentally determined moment was computed from the actuator forces multiplied by the shear span corresponding to each direction, i.e.,  $h_{NS} = 2.95$  m for the NS cycles (positions C and D) and  $h_{EW} = 3.35$  m for the EW cycles (positions A and B). For loading along the diagonal directions, the moment was taken as equal to the SRSS moment of the NS and EW directions computed as in Equation 5.1. The SRSS value was multiplied by the sign of the NS force for plotting the hysteresis loops consistently, while  $M_{EW}$  and  $M_{NS}$  are the moments at the base of the wall for bending around the axis perpendicular to the web and parallel to the web respectively.

$$M_{SRSS} = \sqrt{(M_{EW}^2 + M_{NS}^2)} \cdot \text{sign}(F_{NS}) \quad (5.1)$$

The experimentally determined curvature was derived by extrapolating to the wall base the linear fit of the curvature profile over  $h = 50 - 850$  mm (Figure 5.2a). This height interval was the mean range over which the curvature profile was linear over the entire ductility range.

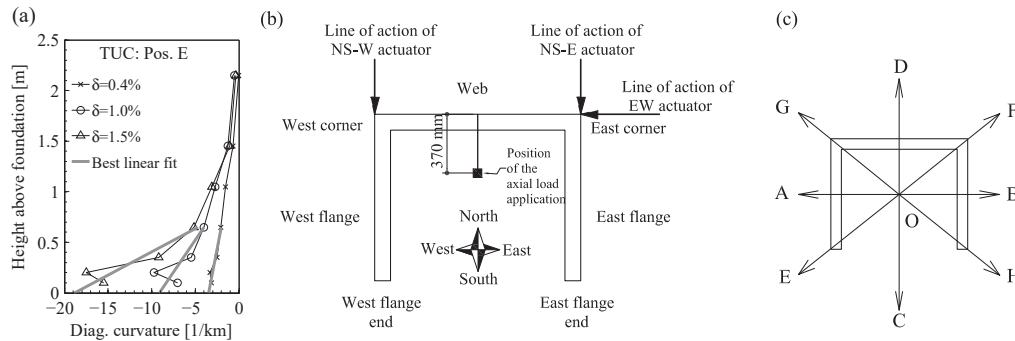


**Figure 5.2:** Example for the procedure of determining the experimental base curvature (a) and wall sections and directions along which displacements were applied at the top of the wall (b-c)

The experimentally derived moment-curvature relationship is compared to the PSA moment-curvature relationship in Figure 5.3 for TUA and TUB and in Figure 5.4 for TUC and TUD for all the loading directions. In the following sections, the differences between the experimentally determined moment-curvature relationship and PSA results will be discussed in terms of moment capacity, yield curvature and ultimate curvature as these are the quantities typically required from PSA when the plastic hinge model is applied.

## Chapter 5. Validation of two numerical models for U-shaped walls

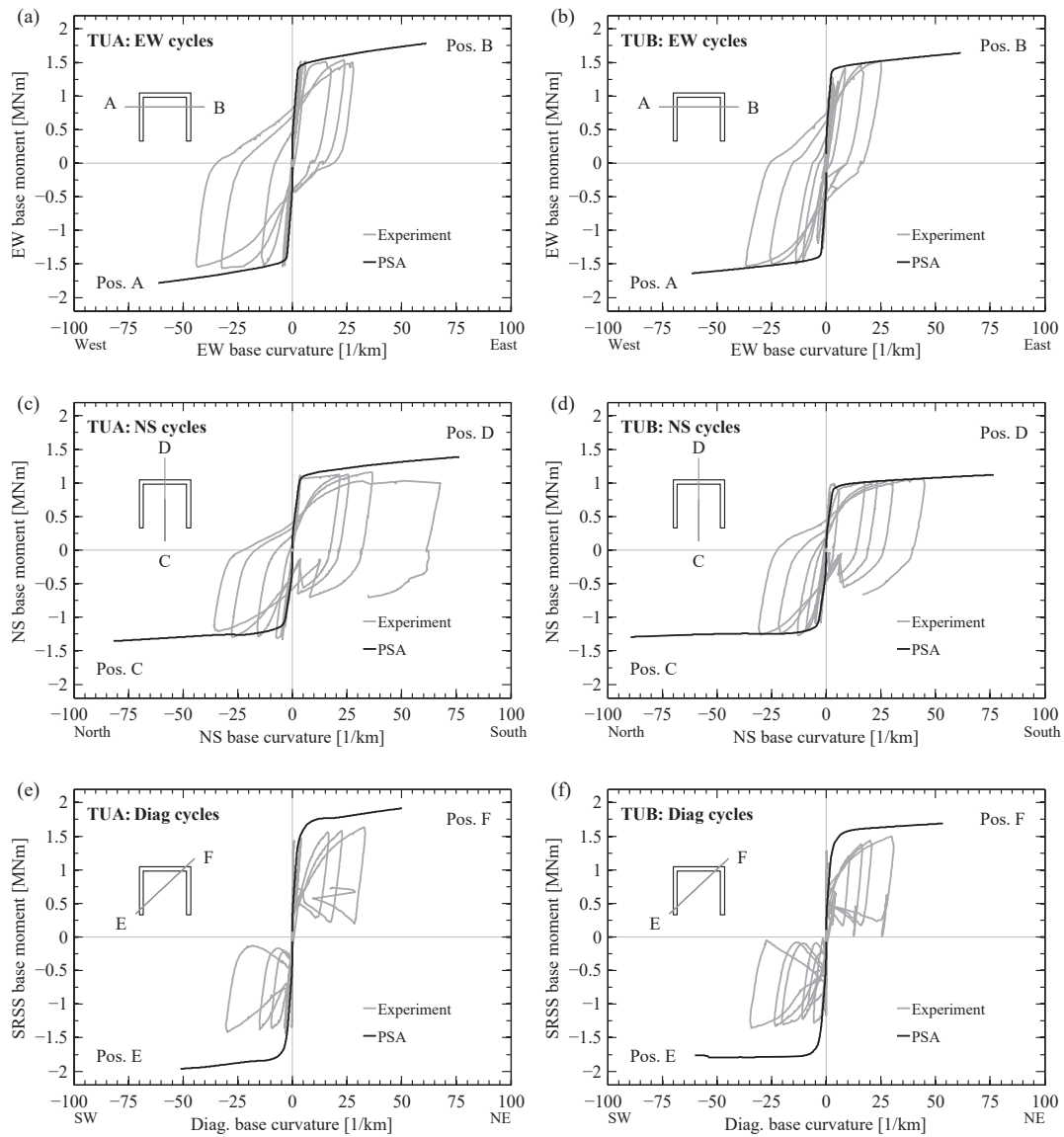


**Figure 5.3:** TUA and TUB: comparison of the experimentally derived moment-curvature relationship with section analysis results

## 5.1. Plane section analysis

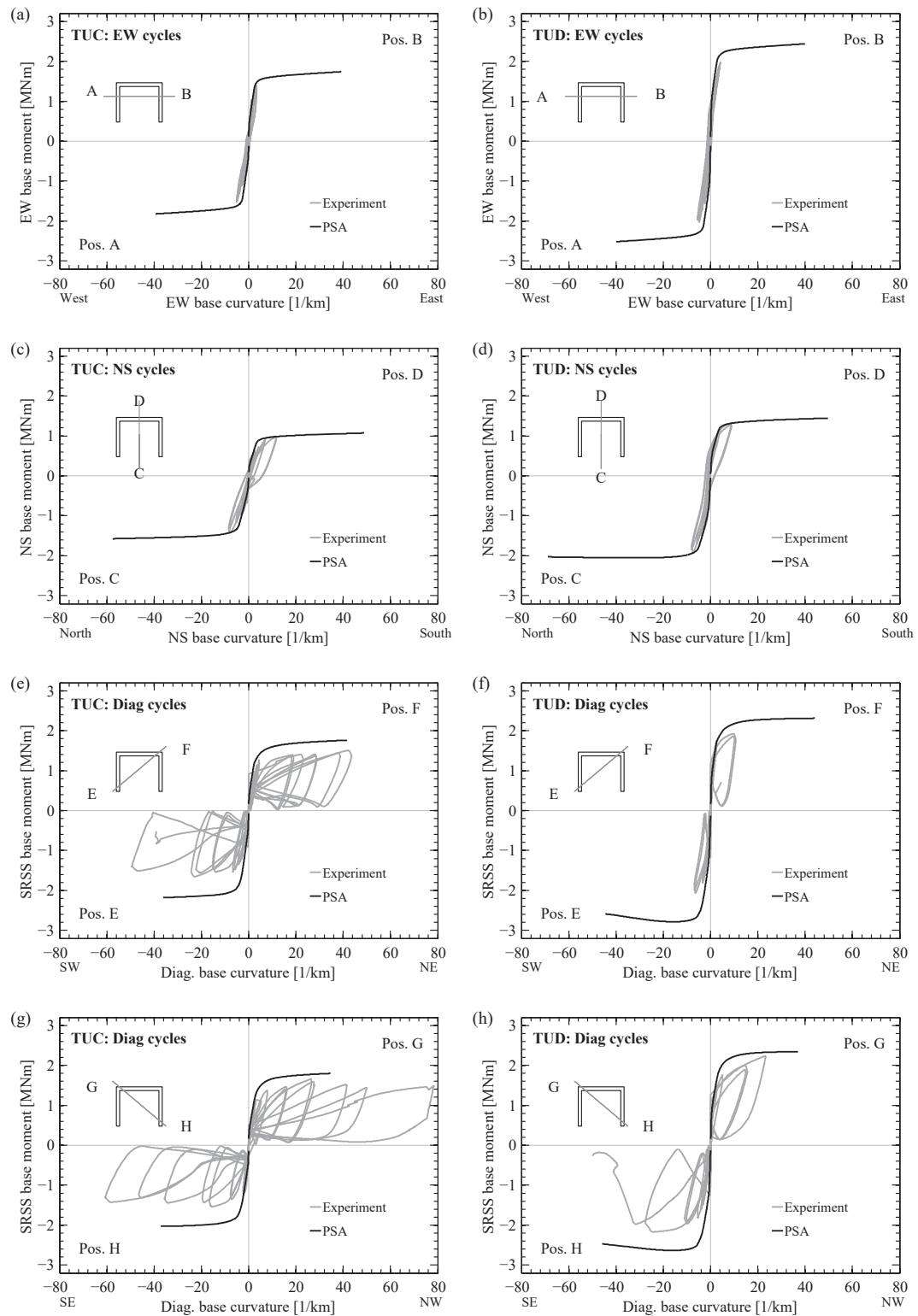


**Figure 5.4:** TUC and TUD: comparison of the experimentally derived moment-curvature relationship with section analysis results

### 5.1.2.2 Moment capacity

For TUA and TUB, the moment capacity is well predicted by the plane section analysis (PSA) for the principal loading directions, i.e., for the EW and the NS cycles (Figure 5.3a-b). For TUC and TUD, on the other hand, a different loading protocol was applied and loading in the principal directions was stopped just after the elastic phase. This is confirmed by the approximate linear shape of the experimentally determined moment-curvature hysteresis in the EW cycles of TUC and TUD (Figure 5.4a-b). Therefore the predicted moment capacity is slightly larger than the maximum moment reached for this loading direction. For the NS cycles, the hysteresis loops are slightly fatter than the EW direction indicating that the wall had passed the elastic phase for this direction. The match between the numerical and the experimental moment-curvature relationships up to where loading was stopped for the NS cycles, is very good for this loading direction. It can hence be concluded that plane section analysis provides a good estimate of the moment capacity of the U-shaped walls for the principal directions of loading, and this observation is in line with the previous remarks from [BDP08b].

For the diagonal loading directions however, section analysis overestimates the experimentally attained moment capacities by  $\sim 10$  to 30% depending on the test unit and loading position. This observation is valid for all four test units and all diagonal loading positions (Figures 5.3c and 5.4c-d).

For TUA and TUB, the difference between plane section analysis and experimental results can be partially attributed to the fact that the loading in the diagonal direction was applied after the wall had already been loaded in the principal directions, i.e., at this instant the wall had already softened. For TUC and TUD, this was no longer the case since in the inelastic range the cycles in the principal directions were omitted and the wall was loaded only in the diagonal directions. The cause for the overestimation of the moment capacity by section analysis for TUC and TUD was already discussed in the interpretation of the experimental results (Chapter 3).

It was concluded that under diagonal loading, the moment capacity is overestimated by plane section analysis due to the inability of this numerical model to capture the vertical strain distribution at the base of the wall. Two main differences were identified after comparing the assumed numerical vertical strain distribution to the experimentally determined vertical strain distribution at the base of the wall. Firstly, the flange width over which the tension reinforcement contributes effectively to the strength capacity of the wall is overestimated by section analysis and so is thus the moment capacity (Section 3.3.3.2 and Figure 5.5a-b). Secondly, the experimental strain distribution indicates the presence of an extra compression zone at the corner web-flange that is not captured by section analysis which accounts for this zone as being in tension (Section 3.3.3.2 and Figure 5.5a-b). Hence section analysis predicts that the reinforcement in this corner contributes in tension to the wall strength thus further increases the estimate of the moment capacity. Both phenomena are more important when loading with the flange end in compression, i.e., positions E and H, than for loading with corner web-flange in compression, i.e., positions F and G (Figure 5.4c-d and Section 3.3.3.2) which explains the larger moment overestimation at the former loading positions. These observations can be extrapolated also to TUA and TUB to explain part of the overestimation by section analysis of the attained experimental moment capacity (Figures 5.3c).

### 5.1.2.3 Moment capacity accounting for the effective flange width

As previously stated, part of the overestimation of the moment prediction under diagonal loading is due to overestimating the length of the flange in tension which contributes to the wall strength, i.e., shear lag effect. This effect can be taken into account in a plane section analysis by reducing the length of the flange in tension at these loading positions. Loading to position E (West flange end in compression) is first examined. A new wall section was set-up for TUC (Figure 5.5a) to account for the effective flange width. For position E, this effective flange width was taken as the length of the East flange for which the measured vertical strains reached the reinforcement yield strain at the nominal point (Figure 5.5b). The geometry of the new wall section is shown in Figure 5.6a.

The new moment-curvature results for position E are compared to the experimentally derived ones as well as to results from section analysis using the full wall section. Accounting for the effective flange width improves predictions of the SRSS moment (Figure 5.6g): the moment capacity is now 20% higher than the experimental moment capacity whereas the moment capacity of the full section was  $\sim 30\%$  higher. If the moment capacity in the two principal directions of the wall is examined (Figure 5.6c, e), the moment capacity in the direction of the web (EW moment computed about the direction of the flanges) is reduced as compared to the EW moment capacity of the full wall section. The moment in the direction of the flanges (NS moment computed about the direction of the web) is however increased as compared to the NS moment of the full wall section since the removed section contributed to the NS moment with opposite sign to this moment.

While for position E the new section approximates better the vertical strains in the East flange, the compression zone at the interface between West flange and web is still not captured. This is considered to contribute to the remaining discrepancies between the predicted moment capacity and the experimentally attained one when loading with the flange end in compression.

Loading to position F (corner between East flange and web in compression) is considered in the following. The experimentally determined vertical strain profile indicates compressive or low tensile strains in the corner between the web and the West flange whereas the PSA strain profile indicates large tensile strains in this region (Figure 5.5d-f). The discrepancy leads to an overestimation of the experimental moment for this loading position. To compensate for the fact that this compression zone is not captured by PSA, the concept of effective flange width is used also for loading to position F. In this case the length of the West flange is reduced to the effective flange width taken as previously for position E, i.e., 0.75 of the flange length. The reduced wall section is shown in Figure 5.6b.

## Chapter 5. Validation of two numerical models for U-shaped walls

The new moment-curvature results for position F indicate that using the effective flange width reduces the predicted SRSS moment capacity, which is now  $\sim 20\%$  lower than the experimentally obtained capacity (Figure 5.6g). The wall strength in the direction of the flanges (NS moment - Figure 5.6e) was already well predicted with the full wall section and only the strength in the direction of the web (EW moment - Figure 5.6c) was overestimated. With the reduced wall section, the moment capacity is reduced for both directions as compared to the full wall section and for both directions the predicted capacity is lower than the experimentally attained capacity. If a longer effective flange width would be used, the SRSS moment capacity could be well predicted but the errors associated with the NS and EW moment would increase. Therefore, even if the effective flange width is adjusted, monotonic plane section analyses will still not match the experimentally obtained moment capacity components in the two principal directions of the wall.

For completeness, the reduced wall section accounting for the effective flange width was used to predict the moment capacity also at positions H and G (East flange end in compression and corner web-West flange in compression, respectively). These moment predictions from the reduced wall section (Figure 5.6d,f and h) confirm the conclusions drawn from positions E and F, respectively. Further discrepancies in wall strength between monotonic plane section analyses and the experimentally attained value are due to the applied loading history of the experiments as discussed in Section 5.2.4.

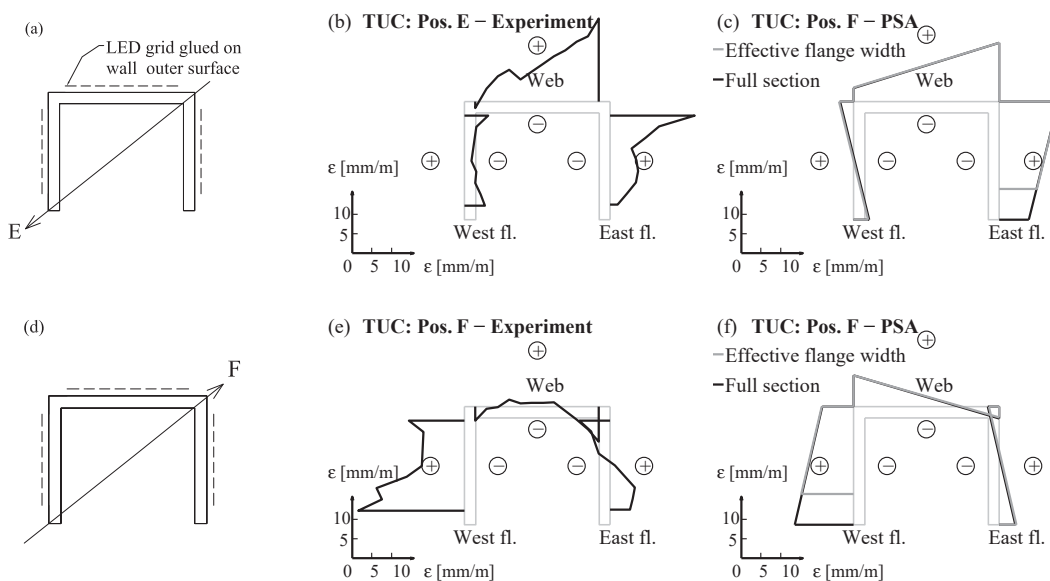


**Figure 5.5:** Vertical strains at the base of the wall under diagonal loading to position E: direction of the applied top displacement (a), experimentally determined vertical strains from LED measurements ( $h = 0 - 75$  mm) at nominal point (b) and vertical strains obtained from plane section analysis (PSA) at nominal point analysed using the full wall section or assuming an effective flange length (c).

## 5.1. Plane section analysis

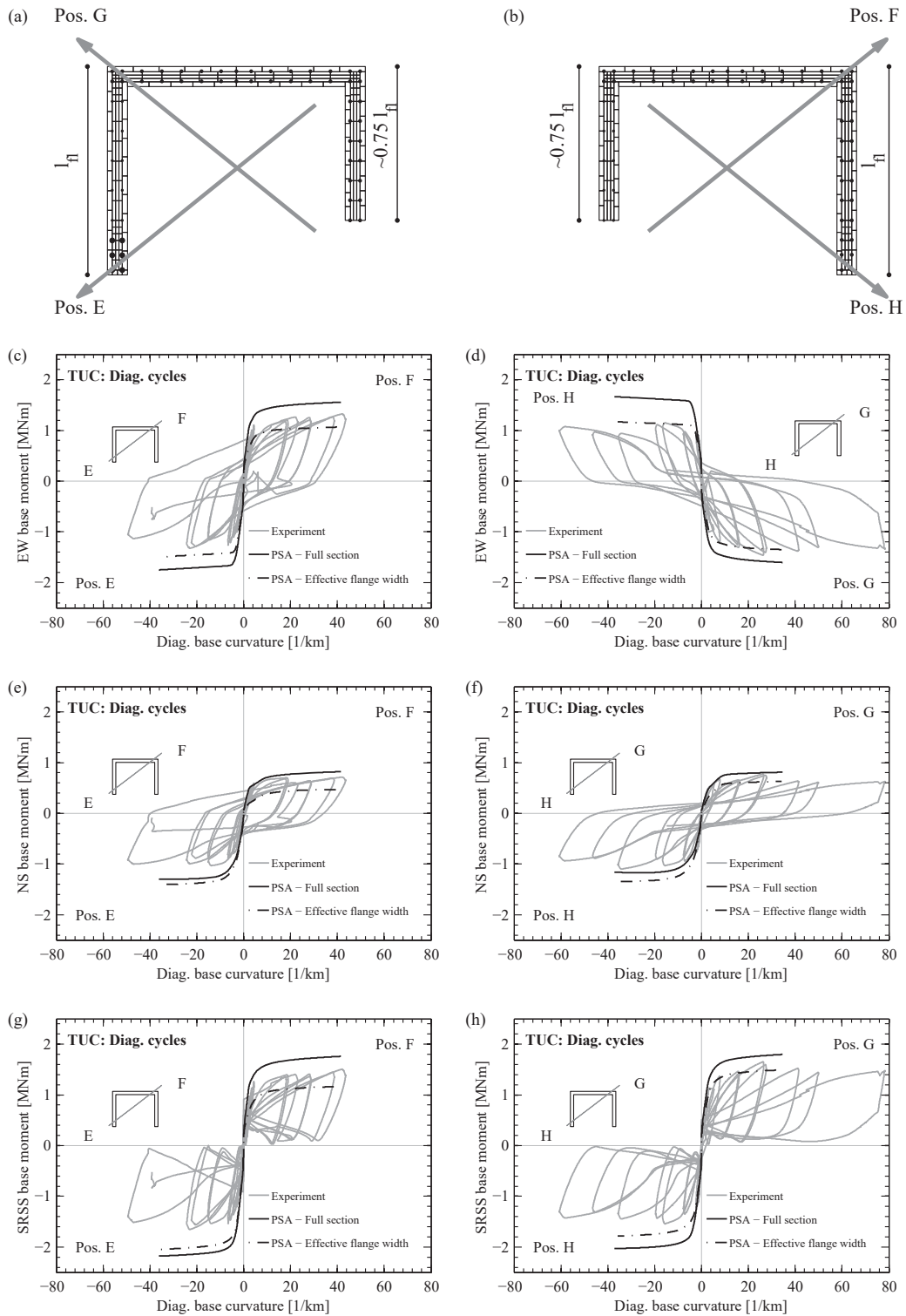


**Figure 5.6:** Comparison of moment-curvature relationships obtained from section analysis (PSA) with the experimentally derived ones when assuming an effective flange width for TUC: reduced wall section to account for the effective flange width at positions E and G (a), at positions H and F (b) and obtained moment-curvature relationships (c-h).

### 5.1.2.4 Yield curvature

The yield curvature marks the boundary between the elastic branch and the inelastic branch in an idealised moment-curvature response as previously discussed in Section 2.2.2 and 4.3. It is an important input parameter to many displacement-based design methods, which are frequently applied in the conceptual design phase.

The derivation of the yield curvature from the experimental data has been explained in detail in Section 4.3. In order to judge whether section analysis can capture the experimentally determined yield curvatures, each of the two quantities involved in deriving the yield curvature are assessed separately, namely the first yield curvature  $\phi'_y$  and the ratio between the nominal moment and the yield moment  $M_n/M_y$ . These two quantities are combined as in Equation 6.3 to give the nominal yield curvature.

$$\phi_y = \phi'_y \frac{M_n}{M_y} \quad (5.2)$$

**First yield curvature  $\phi'_y$**  The point of first yield was determined experimentally as the instant when the maximum tensile base strain first exceeded the reinforcement yield strain  $\epsilon_{sy}$  or the maximum absolute compressive strain first exceeded  $\epsilon_{cy} = 0.002$  [PCK07]. The base strain was computed as the extrapolation to the wall base of the best linear fit of the strain profile over the cracked height (see Section 4.3). The first yield curvature then corresponded to the linear fit of the curvature profile over the cracked height extrapolated to the wall base. These values are compared to the first yield curvature results from section analysis in Figure 5.7a where the first yield curvature from section analysis corresponds to the curvature at the instant when the most tensioned reinforcement fibre exceeds its yield strain  $\epsilon_{sy}$  or the most compressed concrete strain exceeds  $\epsilon_{cy}$ .

It is found that first yield curvatures obtained from section analysis (PSA) match rather well the experimentally derived ones. Except at position B of TUC, where the PSA value is  $\sim 26\%$  lower than the experimental value, for the other experimental values the match is within  $\sim 15\%$  error, and hence a good match. The mismatch at position B of TUC is most likely caused by errors in the experimental derivation of the first yield curvature, since the experimental first yield curvature for this case is significantly higher than for the other test units (with same geometry and similar reinforcement yield strength).

**$M_n/M_y$  ratio** For both experimental and numerical results, the yield moment  $M_y$  was determined as the moment corresponding to the point of first yield. Limit strains were also used to determine the nominal point, and hence the nominal moment.



The nominal moment capacity from section analysis was taken as the moment at the instant when the strain in the most tensioned reinforcement fibre first exceeded 0.015 or when the strain in the most compressed concrete fibre exceeded a compression strain of 0.004 whichever occurred first [PCK07]. The experimental nominal point was determined also by comparing the base strain with the same nominal strain limits listed above. The base strain determining the experimental nominal point was computed following a procedure similar to the one employed for determining the point of first yield. Assuming that the plastic strains are linearly distributed over the wall height for which  $\phi \geq \phi'_y$ , the strains were linearly fitted and the fit was extrapolated to the wall base. With this procedure, it was found that the nominal moment was not reached for loading to positions A, B, C and D of TUC and A, B and D of TUD. The experimentally and numerically determined results are compared in Figure 5.7b.

The nominal to yield moment  $M_n/M_y$  ratios are typically estimated less well by section analysis than the first yield curvature with differences up to  $\sim 17\%$ . However, overall the match between the experimental and the section analysis results of  $M_n/M_y$  ratios is still considered to be good.

**Yield curvature  $\phi_y$**  Having compared the quantities entering in the computation of the yield curvature, the experimental and the section analysis (PSA) results are finally compared in Figure 5.7c. The differences between the numerical (PSA) and the experimental yield curvature results stem from the differences in the first yield curvature  $\phi'_y$  and the nominal to yield moment ratios  $M_n/M_y$ . Overall, the errors from these two quantities either cancel out or accumulate resulting in differences between the numerical and the experimentally determined yield curvatures of  $\sim 20\%$  which can be considered as a satisfactory match given that the yield curvatures find their application in particular in the conceptual design phase.

## Chapter 5. Validation of two numerical models for U-shaped walls

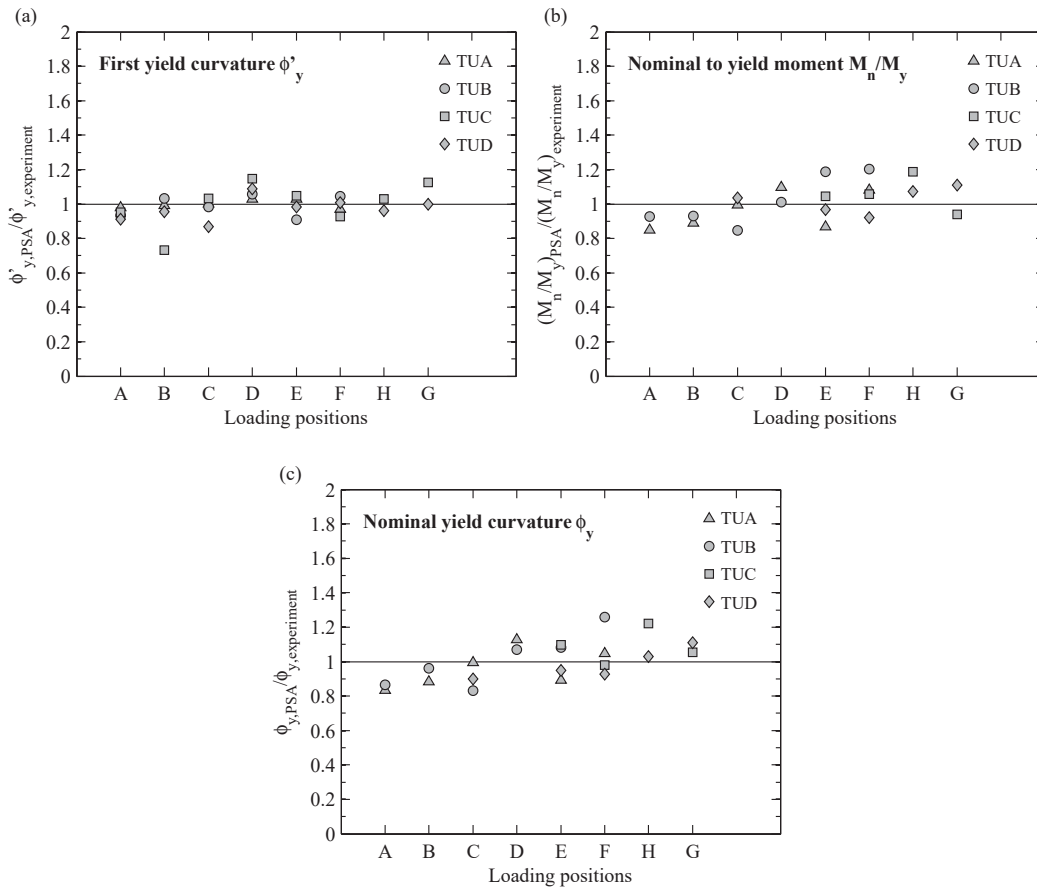


**Figure 5.7:** Comparison of experimentally derived first yield curvature  $\phi'_y$  (a), nominal to first yield moment ratio  $M_n/M_y$  (b) and nominal yield curvature  $\phi_y$  (c) with plane section analysis (PSA) results.

### 5.1.3 Summary of findings from plane section analysis

Quantities from the moment-curvature relationship required for the application of the plastic hinge model were experimentally derived and compared to numerical results from plane section analysis (PSA) in terms of moment capacity and yield curvature. The ultimate curvature was not discussed in this chapter as it was already compared to experimental data and conclusions were formulated in in Chapter 4. For the quantities investigated here, the following conclusions were drawn:

**Moment capacity** can be predicted with good accuracy by section analysis for the principal loading directions. For the diagonal loading directions however, PSA overestimated the experimentally determined moment capacities. The cause of this overestimation was identified to be the inability of PSA to capture the experimentally determined vertical strain distribution at the wall base. If the effective flange width is accounted for at position E (flange end in compression), the prediction of the moment capacity improves but it is still  $\sim 20\%$  higher than the experimental one. Further differences are assigned to the presence of a compression zone at the corner web-flange, which cannot be captured by a plane section hypothesis. Accounting for an effective flange width at position F (corner web-flange in compression) could lead to a good prediction of the overall SRSS moment but the moments in the two principal directions of the wall are still not captured. The discrepancy between the predicted moment capacity from monotonic section analyses and the experimentally attained moment capacity are further explained in Section 5.2.4.

**Yield curvature** can be predicted relatively well by section analysis within 20% difference from the experimentally determined yield curvatures. While the first yield curvature  $\phi'_y$  was predicted quite well, the nominal to yield moment ratios  $M_n/M_y$  were typically less well predicted but the match was still rather good ( $\sim 17\%$ ) resulting in an overall good prediction of  $\phi_y$ .

## 5.2 Shell element model

In addition to the plane section analysis previously discussed, a shell element model was also set-up to model the behaviour of U-shaped walls. A short description of the software used for this task is first given (Section 5.2.1), followed by a detailed presentation of the set-up of the shell element model (Section 5.2.2). Since one objective is to use the this model to perform parametric studies to derive plastic hinge quantities, the shell element model is then validated against the experimental data from four quasi-static tests (Section 5.2.3). Finally, the influence of the loading history on the numerical results is also discussed (Section 5.2.4).

### 5.2.1 VecTor4 software

The shell element model was set-up using VecTor4 (VT4) software [PV93], [Hry13]. VecTor4 (originally called APECS then RASP) is a nonlinear finite element analysis (NLFEA) software for modelling RC structures, developed at the University of Toronto [Hry13]. VecTor4 software was chosen because it specifically addresses reinforced concrete structures through state-of-the-art material models already implemented in the software. The software has the ability to model 3D reinforced concrete structures by means of multi-layered shell elements that can account for the out-of-plane behavior of the element including the transverse shear strains [PV93], [Hry13]. The VecTor4 software is currently under development and the version used for all the analyses within this report is version 4.10 (dated 14.06.2012). All the VecTor4 analyses performed for this report used only material models and finite elements already implemented in the software.

VecTor2 (VT2) [WV02] is another software developed at the University of Toronto for RC structures, part of the same suite programs as VecTor4. While VecTor2 addresses in-plane RC structures and is more widely used than VecTor4, the two programs share most of the material models. Therefore many of the material model references will be addressed through VecTor2 references throughout this section.

#### Shell element

VecTor4 uses a nine-node multi-layered shell element with five degrees of freedom (DOF) per node: three translations and two out-of-plane rotations. Eight nodes are located on the boundary of the shell element and one in the middle (Figure 5.8a). The displacement type shell element is based on the following assumptions: (1) plane sections prior to deformations remain plane after deformation but not necessarily normal to the element mid-surface (Mindlin theory [Min51]) and (2) stresses normal to the element mid-surface are negligible. Quadratic shape functions describe the displacement field of the element using nine Gauss integration points over the element (Figure 5.8b).

The shell element was provided with a layered approach to account for the variation of stresses and stiffness through the thickness of the shell (Figure 5.8c). In-plane strains are assumed constant over the thickness of one layer and vary linearly from one layer to another, i.e., over the thickness of the shell element. In the original shell element formulation by [OF84]), the out-of-plane shear strains followed a uniform strain distribution through the thickness of the element. However this distribution was modified in VecTor4 software to a parabolic one [Hry13], and this later distribution is used for the models described herein. The strain normal to the mid-surface of the shell elements is derived from enforcing the condition of zero out-of-plane normal stress. A complete description of the shell element used for the analyses and its implementation in VecTor4 software is beyond the scope of this report, and therefore for a complete description the reader is referred to [Hry13].

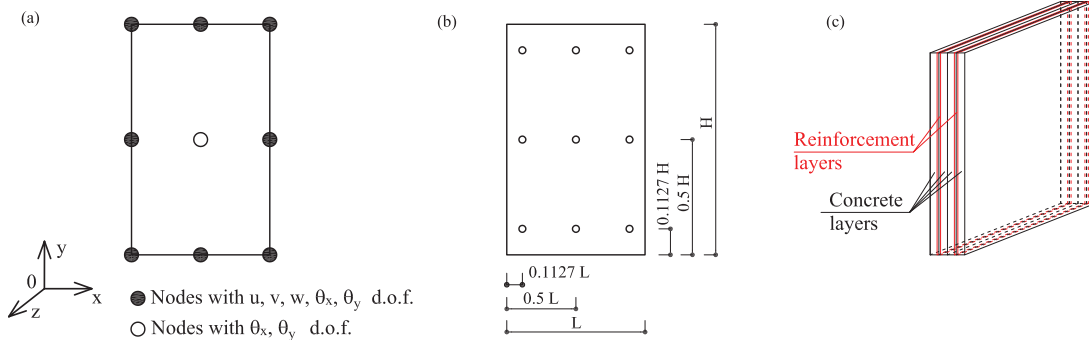


**Figure 5.8:** Characteristics of the shell element implemented in VecTor4: (a) element nodes and degrees of freedom (adapted after [PV93]); (b) location of the integration points; and (c) layered approach

### Material models

State-of-the-art material models are employed for the cracked reinforced concrete as the VecTor4 implements the Modified Compression Field Theory (MCFT) [VC86] and the Disturbed Stress Field Model (DSFM) [VL<sup>+</sup>01]. The MCFT is a generalized approach based on first principle mechanics that describes the behaviour of cracked RC elements under bi-axial loading. The cracked reinforced concrete is treated as an orthotropic material using a smeared rotating crack approach, i.e., cracks are considered as distributed over the element and can rotate following the changing direction of the principal concrete compressive stress. Average stresses and strains are used to write the equilibrium, compatibility and stress-strain relationships. A key feature of the MCFT is the examination of the local crack conditions with respect to the local stresses that can be transmitted across the crack.

The DSFM extends the formulations of the MCFT by including shear slip at the crack surface in the compatibility relationships. The restriction from the MCFT that the directions of the principal stresses and strains remain coincident is hence removed as well as the necessity of performing the crack slip check when examining the local crack conditions. For both MCFT and DSFM, the stress-strain relationship for the concrete accounts for the reduction of the compression strength and stiffness due to cracking and tensile strains in the transverse direction (compression softening). Concrete response after cracking accounts for the tensile stresses between cracks due to the bond between reinforcement and concrete (tension stiffening). Perfect bond is assumed between the in-plane reinforcement and the concrete. While some of the material options are discussed in more detail in the following section, for a complete overview of the material models and their software implementation, the reader is referred to [Hry13] and [WV02].

## 5.2.2 Model set-up

### 5.2.2.1 Reference model: geometry, mesh and material models

A 3D model for U-shaped core walls was set-up using the VecTor4 (VT4) software with the objective was to validate the model against the experimentally derived data from the four U-shaped walls: TUA, TUB, TUC and TUD (see Chapter 4). Figure 5.9 shows the model in elevation and cross-section for TUC. The geometry of the model is composed of two parts: the U-shaped wall from foundation to collar (height above foundation  $h = 0-2720$  mm) and of the collar connected to the wall (height above foundation  $h = 2720-3560$  mm), which enabled the application of the loads. The collar of the wall was modelled with an offset from the mid-surface of the wall so that the loading would be applied at the same position as in the experiments. The foundation of the test unit was not modelled but instead all nodes at the base of the wall were fully fixed (all DOFs restrained).

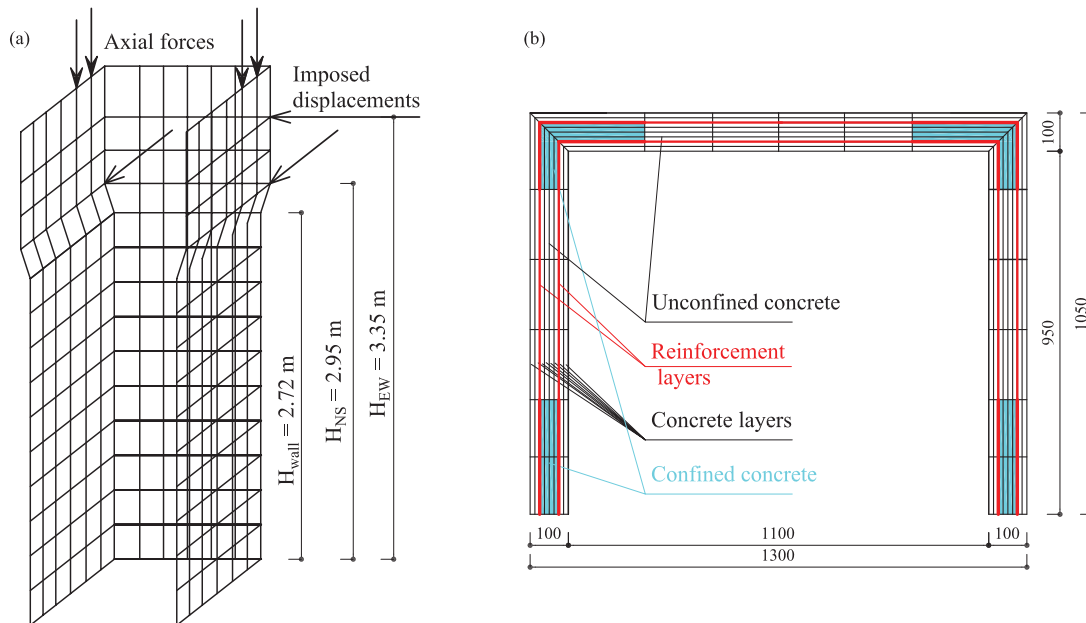


**Figure 5.9:** Mesh discretisation of the VT4 model for TUB, TUC and TUD: (a) elevation view of the wall mid-surface and (b) cross-section view with layer discretisation

A number of six distinct modelling "zones" were assigned to the model to account for the changes in geometry and material properties. Changes in reinforcement ratio, bar diameter, thickness of the wall or the presence of confining reinforcement, required new zones in the model. The final mesh was determined by the division of the wall into the distinct "zones", by the accuracy of the results when compared with the experimental ones and by the necessity to have a reasonable mesh density from the point of view of the convergence of results and computational time.

The final mesh of the wall was composed 18 x 10 approximately square shell elements: 18 elements over the cross-section (six elements over the length of each flange and the web) and 10 equal-height elements over the height of the wall(Figure 5.9b). The collar was also modelled with 18 elements over the cross-section and with four elements over the height. The wall thickness was discretised into eight equally thick concrete layers (Figure 5.9b). A mesh sensitivity study is presented in Section 5.2.2.2.

The in-plane reinforcement, both vertical and horizontal, was modelled as smeared reinforcement (Figure 5.9b). In total, four reinforcement layers were assigned per element (two vertical and two horizontal layers) with their position within the wall thickness corresponding to the actual location of the reinforcement bars. The different in-plane reinforcement percentages were accounted for by assigning different thicknesses to the reinforcement layers. The out-of-plane reinforcement (confinement reinforcement) was assigned as a property of the concrete in the confined zones which is accounted for in the material matrix and influences the computation of strains and stresses in the in-plane directions.

The behaviour models used for setting-up the U-shaped wall model were chosen based on the sensitivity study described in Section 5.2.2.3 as well as on recommendations by [Hry13] and [WV02]. These models chosen for the final model, that was validated and then used for the parametric study, are summarised below.

- Convergence Criteria : Displacements - Weighted
- Concrete Compression Base Curve : Hognestad parabola
- Compression Post-Peak : Modified Park-Kent
- Concrete Compression Softening : Vecchio 1992-A
- Concrete Tension Stiffening : Modified Bentz
- Concrete Tension Softening : Linear
- Concrete Tension Splitting : Not considered
- Concrete Confined Strength : Kupfer/Richart
- Concrete Dilatation : Fixed Poisson Ratio
- Concrete Cracking Criterion : Mohr-Coulomb(Stress)
- Concrete Crack Slip Check : Basic (DSFM/MCFT)
- Concrete Crack Width Check : Crack limit( $\text{agg}/2.5$ )
- Concrete Bond or Adhesion : Perfect bond
- Concrete Creep and Relaxation : Not considered
- Concrete Hysteresis : Nonlinear w/offsets
- Reinforcement Hysteresis : Bauschinger(Seckin)

## Chapter 5. Validation of two numerical models for U-shaped walls

---

- Reinforcement Dowel Action : Not considered
- Reinforcement Buckling : Not considered
- Element Strain Histories : Considered
- Element Slip Distortions : Not considered
- Geometric Nonlinearity : Not considered
- Crack Allocation Process : Uniform spacing

### 5.2.2.2 Mesh sensitivity

To determine the final mesh, sensitivity studies were performed varying the number of elements over the height, over the section or both. The number of layers over the thickness of the elements was also varied. For this task the model for TUB was analysed for monotonic loading in one of the principal directions (position B).

The influence of the element mesh size on the numerical results was assessed based on the comparison of the numerical results from the model with different meshes with the experimental data. The results were compared at the global level in terms of force-displacement curves and at the local level in terms of vertical strains at the most compressed and the most tensioned wall edges. For position B, investigated here, the most tensioned edge corresponds to the NW corner while the most compressed edge corresponds to the NE corner (see Figure 5.2b).

The mesh sensitivity was tested by changing the number of elements over the height of the wall between base and collar (collar not included), the number of elements over the wall section or by changing both number simultaneously. Dividing the section into several elements was somewhat limited by the different confined and unconfined concrete regions in the wall. Therefore the wall section could be divided into 15, 18 or 22 elements. Next, in order to test the influence of the element height on the numerical results, the wall was divided in five, ten or 20 equal elements over the height. And finally, reducing or increasing the element size simultaneously over the length and the height was taken into account by comparing three models: 15 elements/section and 5 elements/height (15S x 5H), 18 elements/section and 10 elements/height (18S x 10H) and 22 elements/section and 20 elements/height (22S x 20H). The global results (force-displacement curves) for all the meshes are compared with the experimental hysteresis in Figure 5.10. As the graphs indicate the variation of the force-displacement curves between the models with different meshes is rather small.



## 5.2. Shell element model

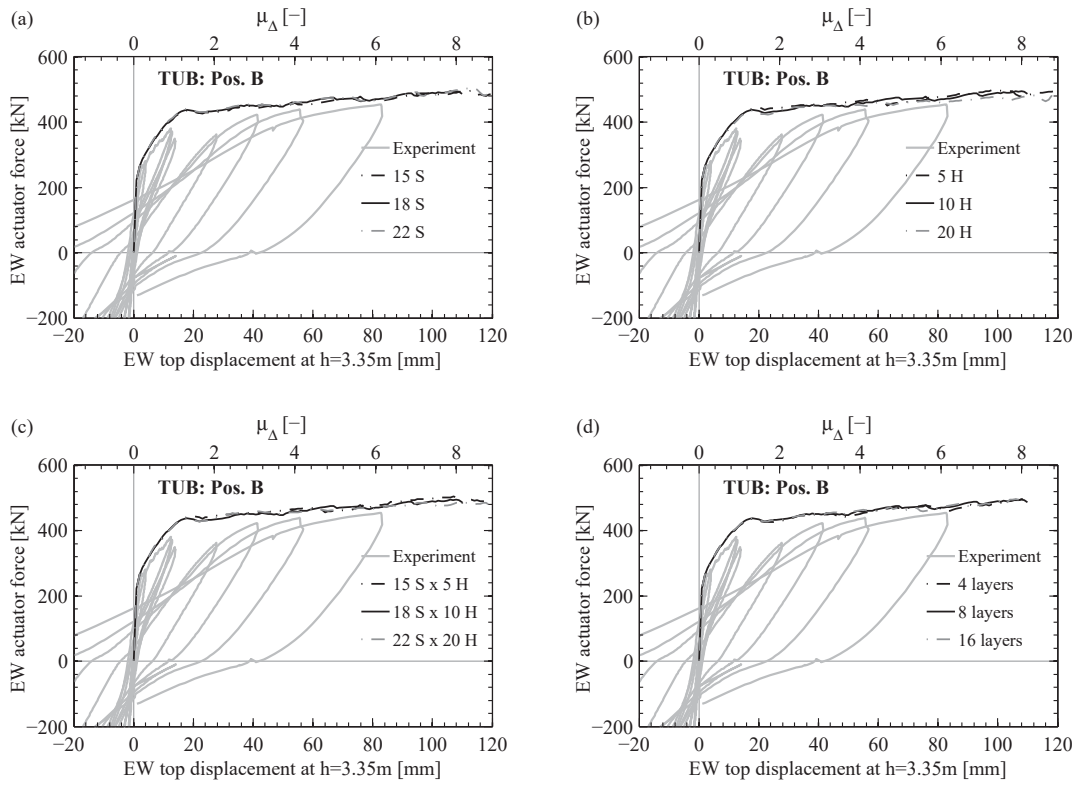


**Figure 5.10:** Mesh sensitivity: comparison of the experimental force-displacement curve with numerical results obtained from models by varying the element length (a), varying the element height (b) and varying the element length and height (c)

## Chapter 5. Validation of two numerical models for U-shaped walls

At the local level, the vertical strain profiles over the wall height at the most compressed (NE corner) and at the most tensioned (NW corner) wall edges are examined (Figure 5.11a). The experimental vertical strain profiles were determined as the average strains of the LVDT chains mounted at the outside edges of the wall as explained in Section 4.2 (Figure 5.11b). The numerical vertical strains were computed from the vertical displacements of nodes on the mid-surface of the wall model (Figure 5.11c). The experimental strains were corrected for the distance between the measurement device and the outer corners of the wall. The numerical strains were also corrected for the distance between the mid-surface and the outer corner of the wall. Both corrections were done assuming a linear vertical strain profile over the length of the flanges and the length of the web.

The experimental and the numerical results of models with different meshes are compared in Figures 5.12, 5.13 and 5.14. These local results are discussed by first comparing the numerical results from the final model with the experimental results, and secondly by comparing the numerical results from the different meshes between each other.

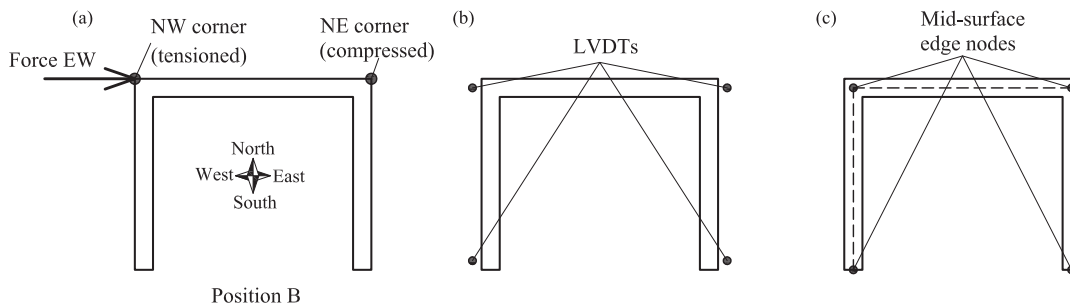


**Figure 5.11:** Location of the vertical strains at the wall outer corners (NE corner and NW corner) examined for local behaviour at position B (a). The vertical strains at the NW and NE corners were obtained by correcting the measured strains from LVDTs (b) and the numerical strains obtained at the wall mid-surface (c) by assuming a linear vertical strain profile along the length of the web and of the flanges.

In the tensile strain profile, at low displacement ductility ( $\mu_{\Delta} = 1$ ) the numerical vertical strains match rather well the experimental strain profile (Figure 5.12). The experimental strain at the base of the wall (over  $h = 0 - 50$  mm) is not plotted due to graph readability and because it mainly accounts for the strain penetration effect which is not modelled here. The experimental compressive strains at this displacement level are also matched relatively well by the numerical model. At a medium displacement ductility ( $\mu_{\Delta} = 3$ ), VecTor4 predicts an important concentration of tensile strains over the third element above the base which was not observed in the experiment (Figure 5.13b). However at high displacement ductility ( $\mu_{\Delta} = 4 - 6$ ) this concentration of numerical strains becomes less important and the numerical strain profile approaches the experimental strain profile (Figure 5.13c). The compressive strain profile is well captured by the model at low ductilities but not for medium and large ductilities, irrespective of the chosen mesh (Figure 5.12a, 5.13a and 5.14a).

The numerical strain profiles obtained with the different meshes show some differences especially at medium and large displacement ductilities (Figures 5.13b-c and 5.14b-c). Changing the number of elements over the wall height has the most important influence on the vertical strain results (Figures 5.13) while the number of elements over the section have a lesser influence (Figures 5.12). While the model is sensitive to mesh size for medium and height ductilities, at low ductilities the mesh influence is negligible (Figure 5.13a and 5.14a). The intermediate size mesh that gives the closest results to the experimental ones is chosen for the final model.

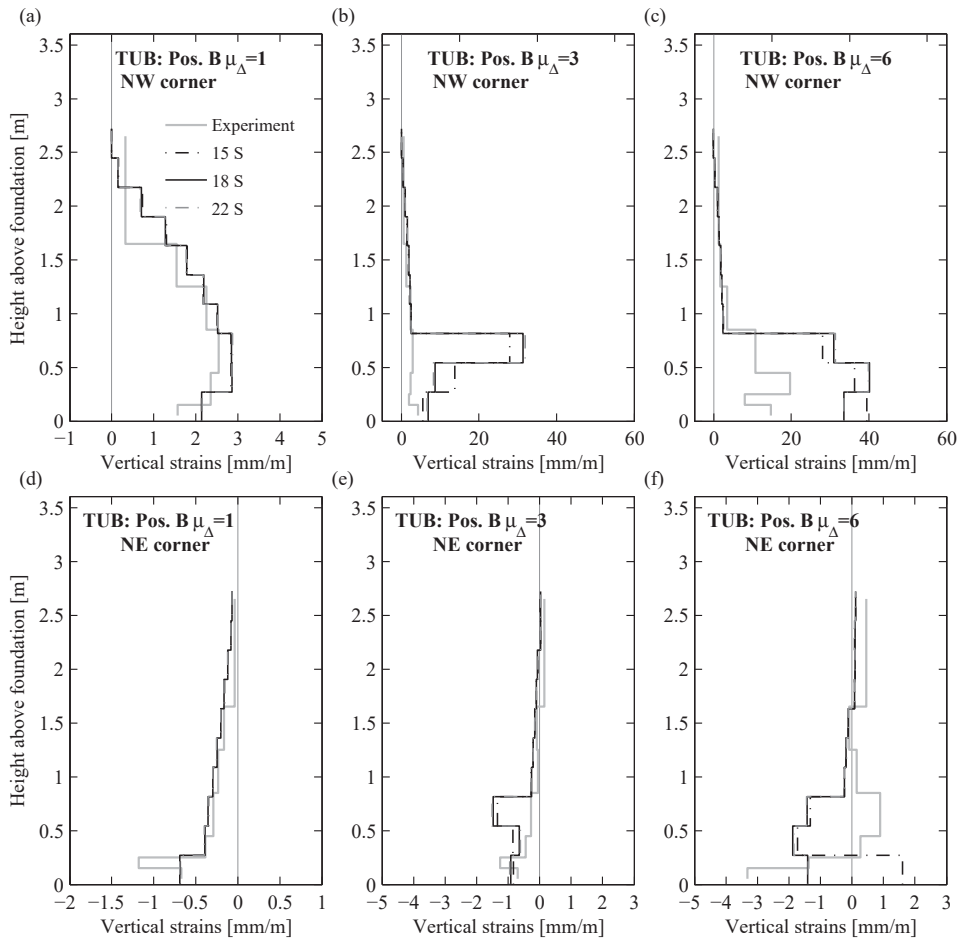


**Figure 5.12:** Mesh sensitivity: comparison of the experimental average vertical strains with numerical average vertical strains obtained from models by varying the numbers of elements per section. The results are compared for the wall edge with the maximum tensile strains (NE corner) (a-c) and for the edge with the minimum compressive strains (NW corner) (d-f) at position A and at three displacement ductility levels: at low ductility  $\mu_{\Delta} = 1$ , at medium ductility  $\mu_{\Delta} = 3$  and at a large ductility  $\mu_{\Delta} = 6$ .

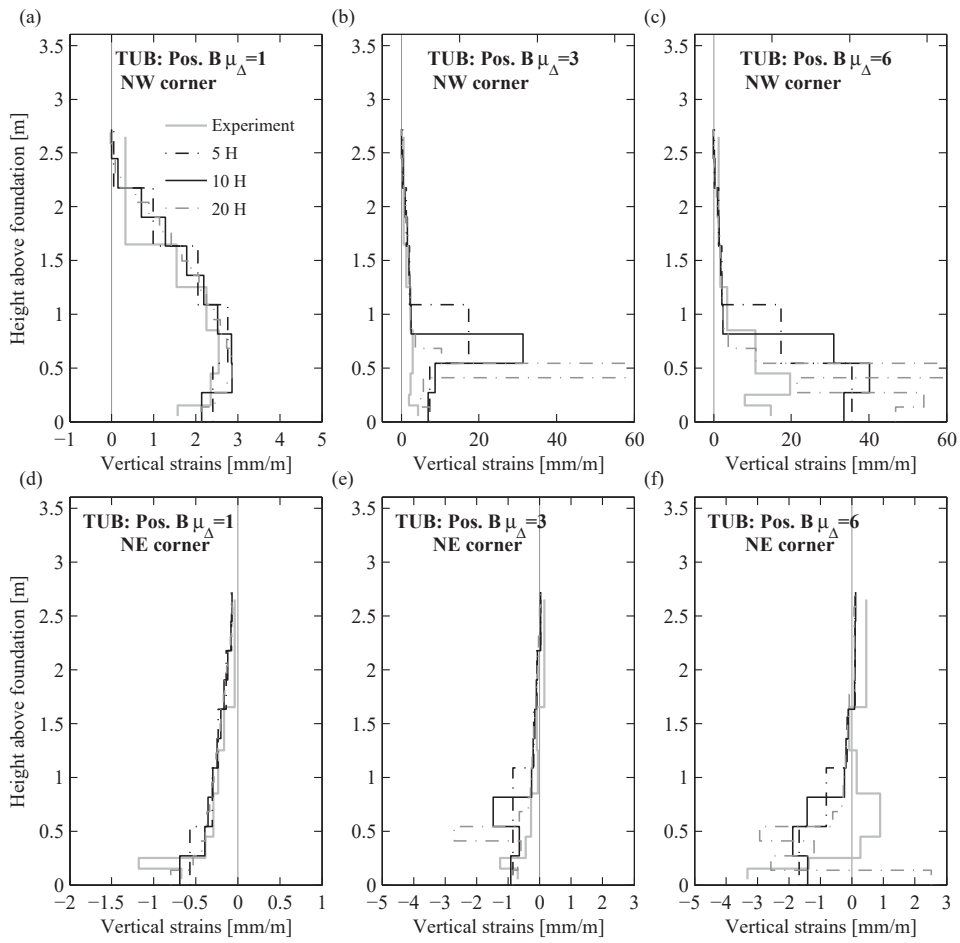


**Figure 5.13:** Mesh sensitivity: comparison of the experimentally derived average vertical strains with numerical average vertical strains obtained from models by varying the numbers of elements per height. The results are compared for the wall edge with the maximum tensile strains (NE corner) (a-c) and for the edge with the minimum compressive strains (NW corner) (d-f) at position A and at three displacement ductility levels: at low ductility  $\mu_{\Delta} = 1$ , at medium ductility  $\mu_{\Delta} = 3$  and at a large ductility  $\mu_{\Delta} = 6$ .

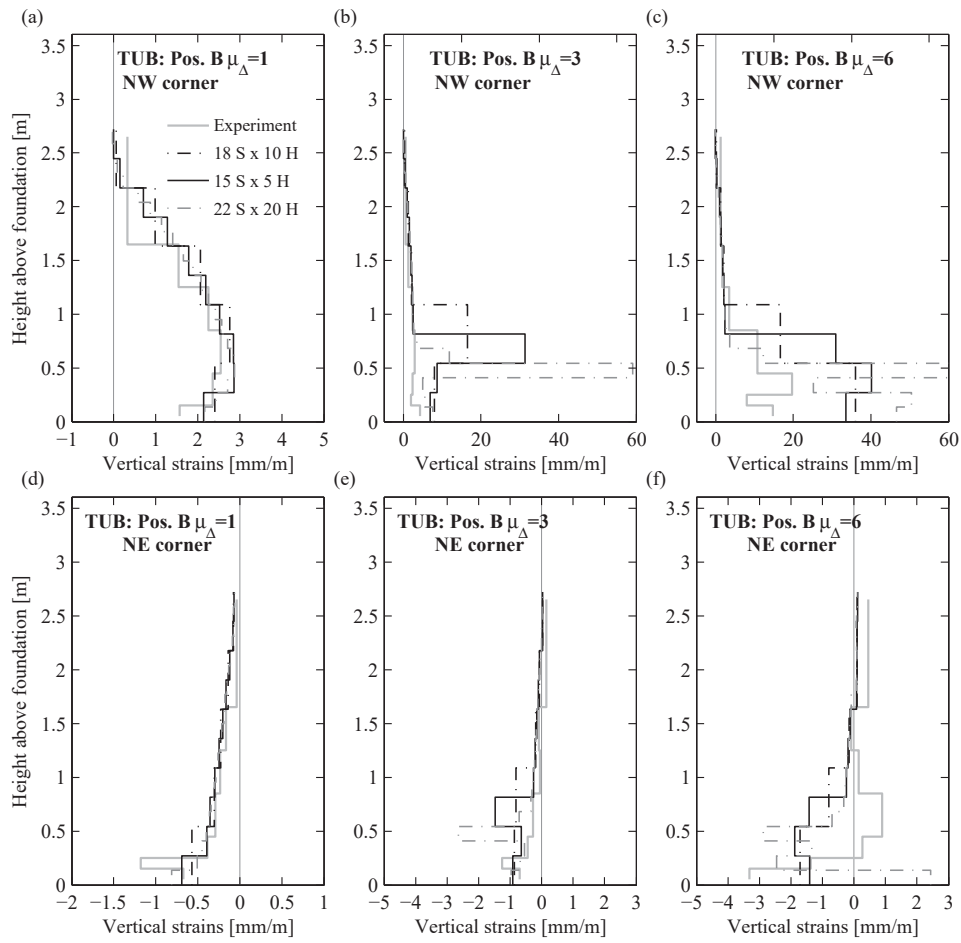


**Figure 5.14:** Mesh sensitivity: comparison of the experimentally derived average vertical strains with numerical average vertical strains obtained from models by varying the numbers of elements per section and per height. The results are compared for the wall edge with the maximum tensile strains (NE corner) (a-c) and for the edge with the minimum compressive strains (NW corner) (d-f) at position A and at three displacement ductility levels: at low ductility  $\mu_{\Delta} = 1$ , at medium ductility  $\mu_{\Delta} = 3$  and at a large ductility  $\mu_{\Delta} = 6$ .

**Number of layers over the wall thickness** The shell element can be subdivided into several layers over the thickness. For the final model, the elements were divided into eight layers through the wall thickness. To test the sensitivity of the results to the layer discretisation, a model with four and one with 16 layers through the thickness were considered. The force-displacements results are given in Figure 5.10d and indicate that the layer discretisation has little effect on the overall force-displacement curve. In terms of vertical strains, the layer discretisation influences the tensile strain results for medium and large ductilities (Figure 5.15): a large layer thickness reduces to some extent the strain concentration in the third element while a small layer thickness amplifies it. For tensile strains at low ductilities as well as for compression strains at all ductilities, the layer discretisation has very little influence on the local results.

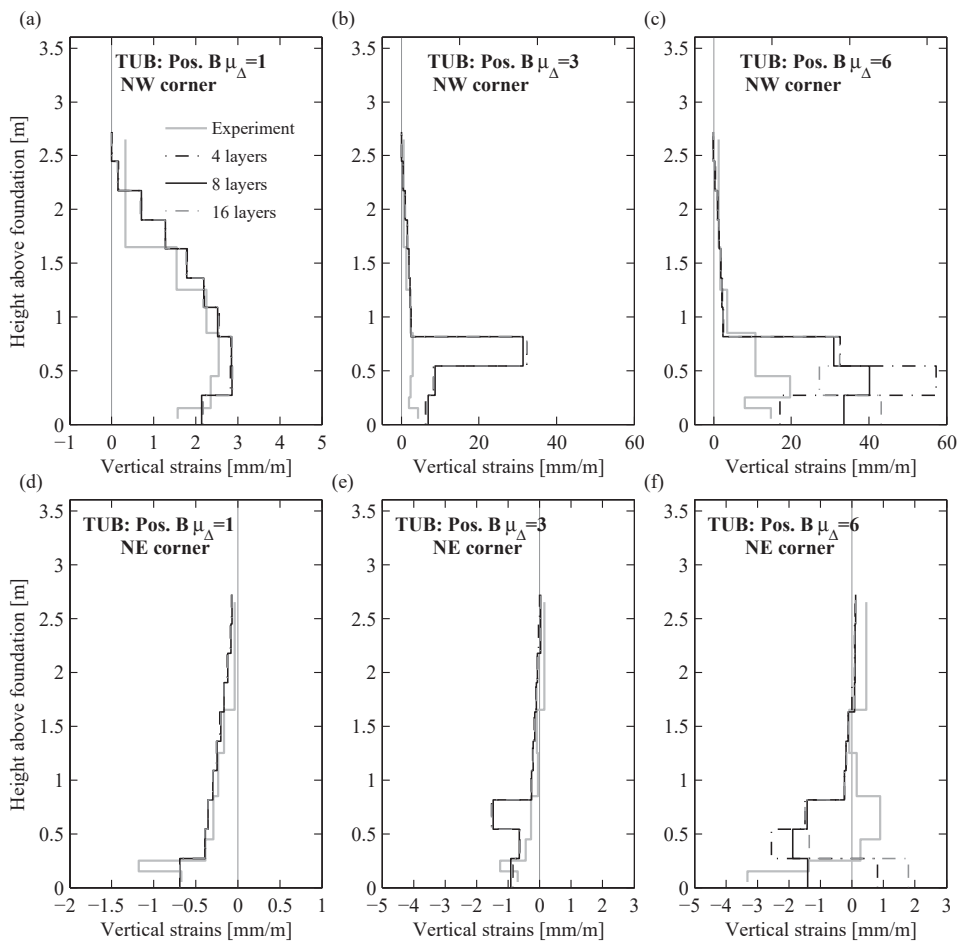


**Figure 5.15:** Mesh sensitivity: comparison of the experimentally derived average vertical strains with numerical average vertical strains obtained from models by varying the numbers of layers per thickness of element. The results are compared for the wall edge with the maximum tensile strains (NE corner) (a-c) and for the edge with the minimum compressive strains (NW corner) (d-f) at position A and at three displacement ductility levels: at low ductility  $\mu_{\Delta} = 1$ , at medium ductility  $\mu_{\Delta} = 3$  and at a large ductility  $\mu_{\Delta} = 6$ .

In conclusion, while the mesh sizing and layer discretisation does not influence the strength and stiffness of the wall, they do influence the magnitude of strains at medium and high ductilities and might hence influence the wall displacement capacity and failure mode.

5.2.2.3 Material models and analysis options: sensitivity studies

The series of VecTor programs are equipped with a wide choice of material models and options [WV02]. For VecTor4 the choice of material options is somewhat limited as compared for example with VecTor2 but still the user has wide range of choices. Performing sensitivity studies for all the material models using the full wall model of one of the tested U-shaped walls would be very time consuming. Therefore the following strategy was adopted: the material models are assessed using a one-element model with different boundary conditions and loading history, and based on these results only the most “promising” models are then evaluated using the full U-shaped wall model. When testing material models using the U-shaped model, comparison is made with the “reference model” which represents the final model used for the validation and parametric study and which is previously described in Section 5.2.2.1.

**Concrete compression pre-peak behaviour** Six models are available to describe the pre-peak behaviour of concrete. These models compute the principal compressive stress  $f_{c3}$  if the principal compressive strain  $\epsilon_{c3}$  is less than the peak strain  $\epsilon_p$ . While some models were derived for normal strength concrete, other have a steeper ascending branch in order to represent high strength concrete. The models were tested on a model with one single shell element without reinforcement applying the boundary conditions as shown in Figure 5.16a. An incremental displacement which compresses the element was applied at the top nodes of the element. The resulting stress-strain curves are given in Figure 5.16b and they are compared to the experimental stress-strain curve obtained from one concrete cylinder test corresponding to TUC at the day of testing. The linear pre-peak model was not represented in the graph as this model is not normally used.

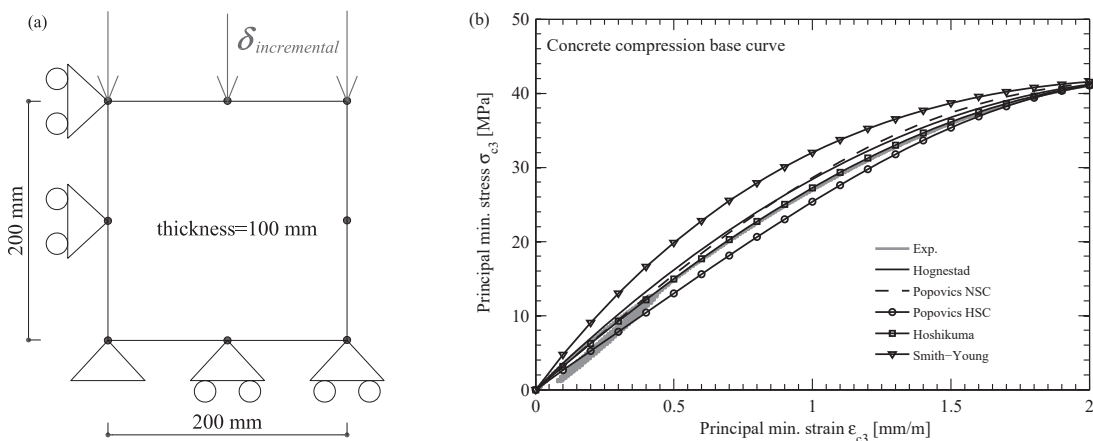
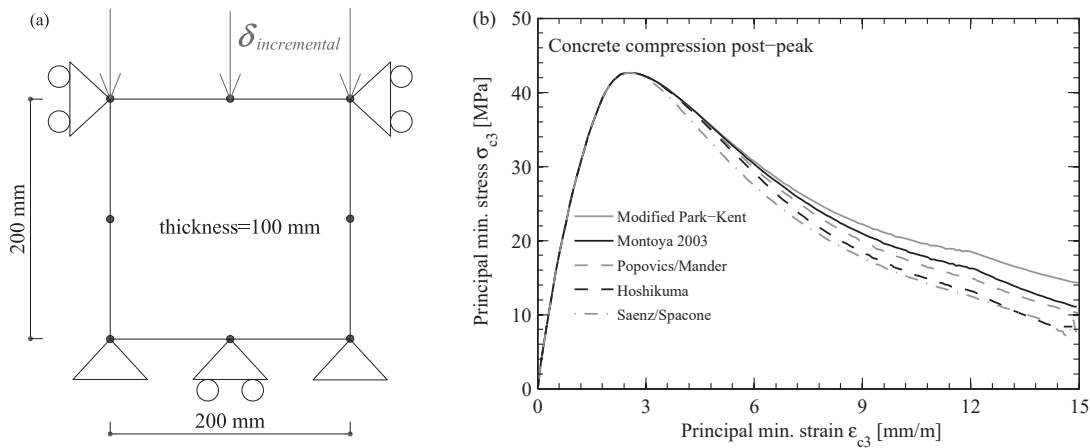


Figure 5.16: Behaviour of concrete in compression: concrete compression base curves

## Chapter 5. Validation of two numerical models for U-shaped walls

The comparison of the pre-peak models with the experimental stress-strain curve indicates that Hognestad, Hoshikuma and Popovics NSC all provide a rather good match. These three models will be investigated together with their corresponding post-peak curve on the full TUB model.

**Concrete compression post-peak behaviour** The compression post-peak models compute the principal compressive stress  $f_{c3}$  for principal compressive strains  $\epsilon_{c3}$  larger than the peak strain  $\epsilon_p$ . The peak stress and strain are determined by modifying the concrete cylinder strength and the corresponding strain to account for compression softening due to coexisting tensile strains and for strength enhancement due to confinement. Most of the post-peak models are formulated in the context of confined concrete and hence if the element is not confined all post-peak models yield the same stress-strain relationship (except for Saenz/Spacone). Hence the post-peak models are all assessed in the context of confined concrete for one element model with the boundary conditions as shown in Figure 5.17a. The element has no in-plane reinforcement and has a ratio of 0.75% of out-of-plane reinforcement, which is a typical confinement ratio for the test units investigated here. An incremental displacement which compresses the element was applied at the top nodes of the element. The Modified Park-Kent model which is also the recommended default model [WV02], provides the lowest degradation of the compressive stresses after peak as compared to the other models. Montoya2003 and Popovics/Mander have an intermediate behaviour while with Hoshikuma the degradation is faster. Saenz/Spacone model differentiates from all the other as the degradation initiates earlier in this model. The Modified Park-Kent, the Popovics/ Mander and the Hoshikuma models will be further investigated using the full TUB model.



**Figure 5.17:** Behaviour of concrete in compression: tested model with a single shell element (a) and VecTor4 post-peak models (b)



**Concrete compression softening** Compression softening refers to the reduction of the uni-axial concrete strength and strain (cylinder test strength and strain) due to coexisting transverse cracking and tensile straining. In VecTor4, the compression softening models are implemented by multiplying either both the uni-axial strength and strain or just the strength, with a reduction factor  $\beta_d$  in order to obtain the peak strength  $f_p$  and strain  $\epsilon_p$ . A one-element model is again considered with the boundary and loading conditions as shown in Figure 5.18a. An incremental displacement which compresses the element was applied at the top nodes of the element while a constant displacement was applied on one side of the element. The results given in Figure 5.18b show that the compression softening can vary significantly. Only Vecchio1992A, Vecchio1992C and Vecchio-Collins 1982 reduce both the strength and the strain while the others modify only the strength. However the Vecchio-Collins 1982 model does not recognize shear slip effects when these are included in the analyses and hence this model is also disregarded. As the remaining models: Vecchio1992A and Vecchio1992C provide similar results, Vecchio1992A is chosen for the final model.

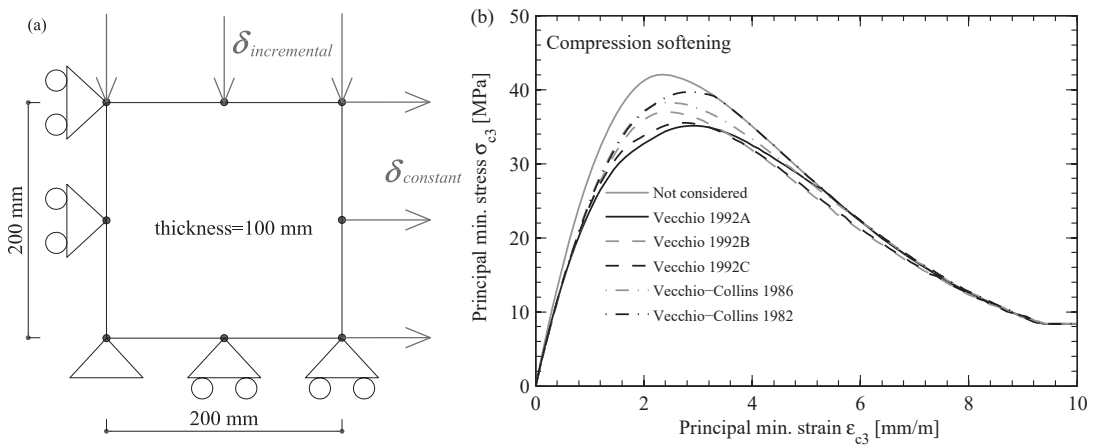


**Figure 5.18:** Behaviour of concrete in compression softening models: tested model with a single shell element (a) and VecTor4 models (b)

**Confined concrete strength** Confined concrete is implemented in VecTor4 by multiplying the uni-axial strength  $f_c$  and strain  $\epsilon_0$  (from cylinder test) with an amplifying factor  $\beta_l$  in order to obtain the peak strength  $f_p$  and strain  $\epsilon_p$ . Note that the computation of the peak strength and strain includes also the factor  $\beta_d$  which accounts for the compression softening effects (Equations 5.3 and 5.4). The different strength enhancement models are shown in Figure 5.19b as tested on a one-element model (Figure 5.19a).

The three confined concrete models provide rather different results: Selby model results in the most rapidly descending post-peak branch and lowest confined strength and strain, with Montoya/Ottosen the degradation after post-peak is very small while Kupfer/ Richart provides intermediate confinement strength and strain. The Kupfer/ Richart was chosen for the final model.

$$f_p = \beta_d \cdot \beta_l \cdot f_c \quad (5.3)$$

$$\varepsilon_p = \beta_d \cdot \beta_l \cdot \varepsilon_0 \quad (5.4)$$

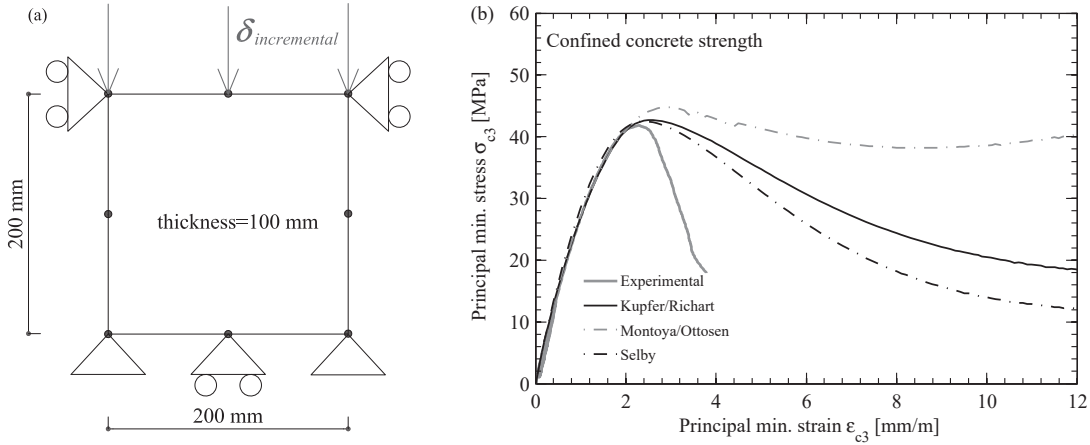


**Figure 5.19:** Behaviour of concrete in compression-confined concrete strength: tested model with a single shell element (a) and VecTor4 models (b)

**Lateral expansion model for concrete** The lateral expansion feature accounts for the lateral expansion of the concrete volume under increasing compressive strains. If the concrete is confined, this expansion results in passive confining pressures which can increase the strength and strain capacity of the concrete in compression. The lateral expansion is introduced in the software through the Poisson ratio, which relates the expansion of concrete in one principal direction orthogonal to the one in which compression the compression load is applied. The simplest model available considers a constant Poisson ratio, i.e., a Poisson ratio that is independent of the applied compressive strains. All the other models account for an increasing Poisson ratio with increasing compressive strains. The results for a one-element model are shown in Figure 5.20.

All models considering a variable Poisson ratio lead to an increase in the peak strength and strain with increasing compressive strain, which has been also observed in experimental tests [KHR69]. However their response is rather unstable. The fixed Poisson ratio shows the most numerically stable behaviour and despite not being the most realistic model, it is the preferred option for the final model due to its numerical stability.

**Concrete tension stiffening** Tension stiffening is a phenomenon specific to reinforced concrete in tension. When the reinforced concrete cracks, the stresses in the concrete in the direct vicinity of the cracks reduce to zero. However with increasing distance to the crack surface, tensile stresses in the concrete increase due to the bond between reinforcement and concrete. These stresses together with the reinforcement stresses give the stiffness of the reinforced concrete which is therefore larger than the stiffness of the reinforcement alone.

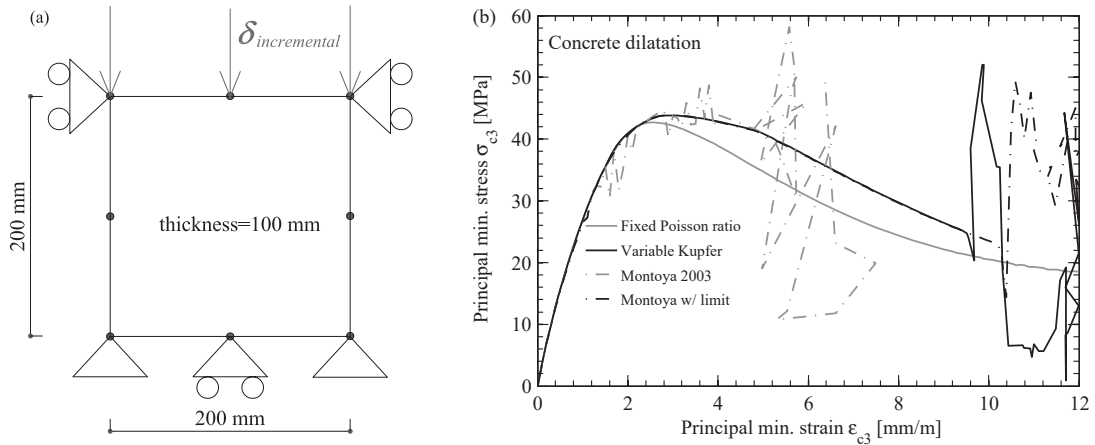


**Figure 5.20:** Behaviour of concrete in compression-lateral expansion models: tested model with a single shell element (a) and VecTor4 models (b)

The tension stiffening is implemented in the software by modifying the post-peak behaviour of concrete in tension. When tension stiffening is not considered, the concrete tensile stress drop immediately to zero stress after reaching the cracking stress  $f_{cr}$  (Figure 5.21b). Depending on the tension stiffening model used, the principal tensile stress in concrete  $f_{c1}$  after cracking can be written as a function of the cracking stress  $f_{cr}$  and the bond characteristics between reinforcement and concrete. The tension stiffening models provided in VecTor4 were tested on a one-element model, with 0.5% vertical reinforcement content. An incremental displacement that tensions the element was applied at the top nodes of the element (Figure 5.21a). Tension softening was not considered (see next section).

Except the Izumo, Maekawa et al. model, all the other tension stiffening models yield rather similar results (Figure 5.21b). The Modified Bentz model is chosen for the final model since it also accounts for the characteristics of the bond between reinforcement and concrete. Since tension stiffening affects the wall effective stiffness which is one of the quantities of interest in the model validation, the tension stiffening influence will be further assessed on the TUB wall model.

**Concrete tension softening** Tension softening is a phenomenon specific to plain concrete in tension: after cracking the concrete stresses do not decrease immediately to zero but the strength drop is gradual as the crack fracture process progresses. Tension softening is accounted for in VecTor4 by including a post-peak branch in the stress-strain behaviour of concrete. Note that also tension stiffening is included in the same manner, i.e. by including a post-peak descending branch. When both phenomena are considered, the post-peak principal concrete tensile stress is described by the maximum of the tensile stresses resulting from the two phenomena.

## Chapter 5. Validation of two numerical models for U-shaped walls

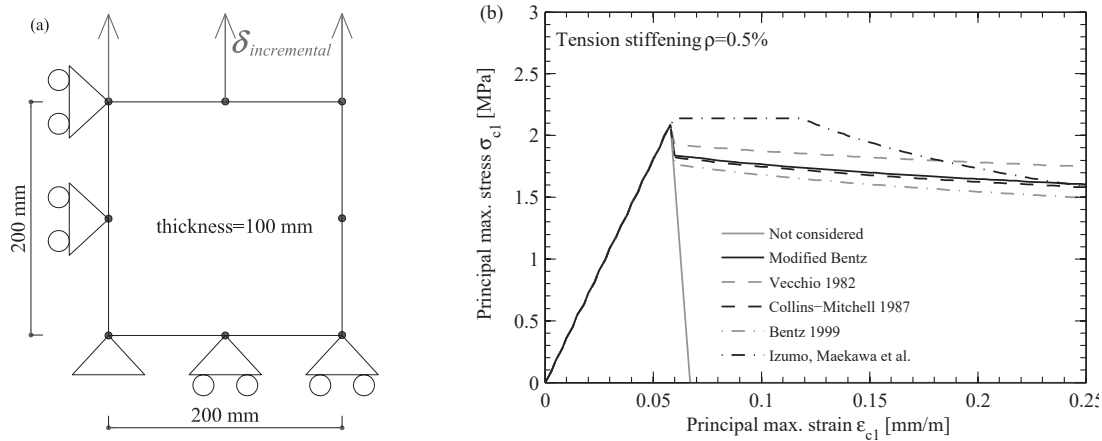


**Figure 5.21:** Behaviour of concrete in tension: tested model with a single shell element (a) and VecTor4 tension stiffening models (b)

A one-element model was again considered in order to assess the different tension softening models. Initially, tension stiffening was not considered, but in this way, all tension softening models yielded the same stress-strain relationship. Therefore the Modified Bentz was assigned as an option for tension stiffening, while the vertical reinforcement content was reduced to almost zero, thus reducing also the influence of considering the tension stiffening on the results.

The different tension softening models show various trends from a rapidly descending branch (Nonlinear Yamamoto) to a more slowly descending one (Nonlinear Hordijk). The linear model, which is the simplest model available, was chosen for the final wall model since more complex models were not considered necessary. As discussed in the following sections, the influence of tension softening on the results of the TUB wall model is negligible for the global results and rather small for the local results.

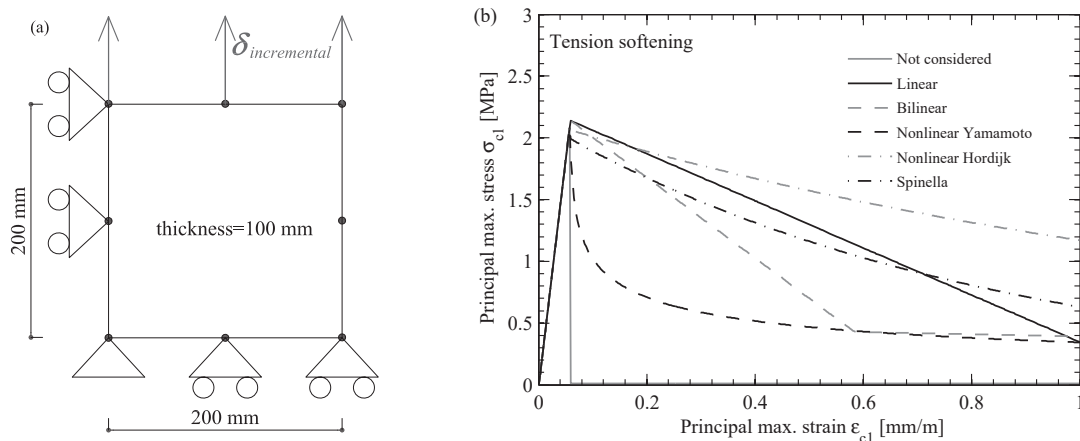


**Figure 5.22:** Behaviour of concrete in tension: tested model with a single shell element (a) and VecTor4 tension softening models (b)

**Concrete compression curve - TUB model** The different models were further examined by analysing the TUB model for the retained pre-peak and post-peak curves. The models are assessed in terms of global behaviour (force-displacement curve) and in terms of local behaviour (vertical strains profile over the wall height) by comparison to the experimentally determined results.

The force-displacement comparison, shown in Figure 5.23a indicates that the VecTor4 model matches rather well the experimental behaviour in terms of stiffness and strength. The overall differences between the models are very small.

When evaluating the vertical strain profiles (Figure 5.24), the differences between the models are still not significant especially at low ductilities while for medium and high ductility some trends can be observed. More precisely, the combination of Hognestad/ Park-Kent provides the best match with the experimental results. The Hoshikuma model gives rather similar results to Hognestad/ Park-Kent. Based on these observations the Hognestad/ Park-Kent combination is used to describe the concrete compression curve in the final model.

**MCFT vs. DSFM - TUB model** One material modelling option which was not evaluated on the one-element model is the choice between the Modified Compression Field Theory (MCFT) and the Disturbed Stress Field Model (DSFM). As previously stated, MCFT assumes that the principal stresses and strains are aligned. For DSFM this assumption is no longer valid and the principal stress rotation can lag behind the rotation of the principal strain [VL<sup>+</sup>01]. While MCFT requires examination of the local crack conditions (crack slip check) in order to address possible failure modes along the crack, the DSFM explicitly calculates the crack slip deformations and hence the crack slip check is no longer necessary.

From a practical point of view, DSFM was mainly developed to extend the application of MCFT to reinforced concrete structures that are very lightly or very heavily reinforced because for such extreme reinforcement ratios MCFT over- or under-predicted the shear stiffness and strength [VL<sup>+</sup>01]. The test units considered here have a reinforcement percentage around  $\sim 1\%$  which is hence considered a medium reinforcement content. It is therefore expected that MCFT and DSFM yield similar responses.

Indeed this is confirmed after comparing the two models at the global level (Figure 5.23b) and at the local level (Figure 5.25). Some more important variations can be observed only at the local level at high ductilities ( $\mu_{\Delta} = 6$ ) in the tensile strains (Figure 5.25c). Based on this comparison with the experimental results, the MCFT seems to be a more suitable choice. For this comparison the following complementary modelling options were used: crack slip check - Basic (DSFM/MCFT) option and for element slip distortions - Walraven.

## Chapter 5. Validation of two numerical models for U-shaped walls

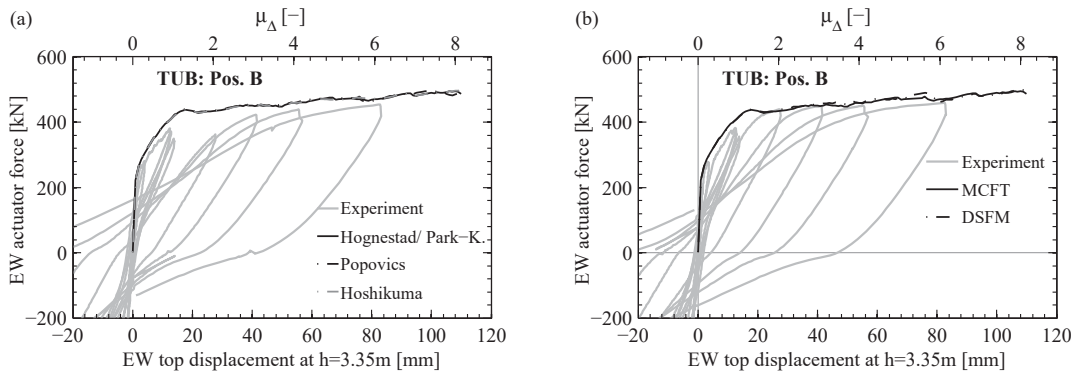


**Figure 5.23:** Sensitivity of the force-displacement curve to the compression pre-peak and post-peak models (a) and to the choice of analytical model (MCFT or DSFM) (b)

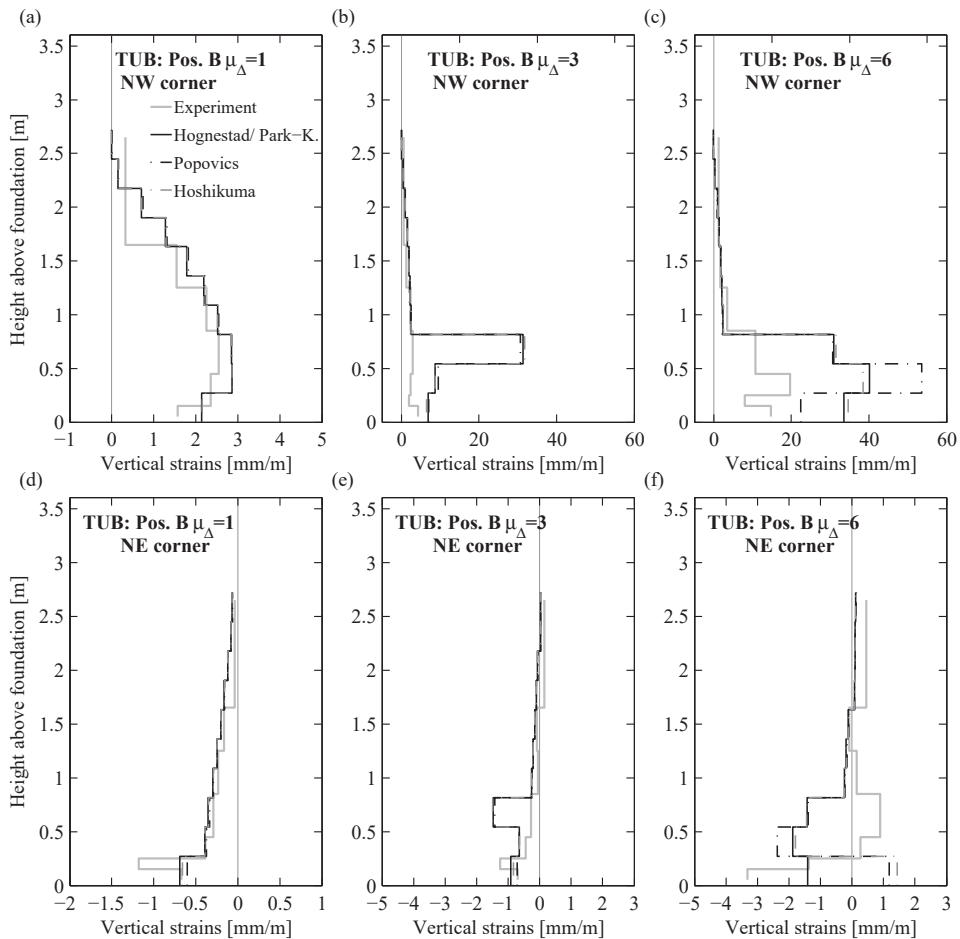


**Figure 5.24:** Sensitivity of the vertical strain profiles to the compression pre-peak and post-peak models

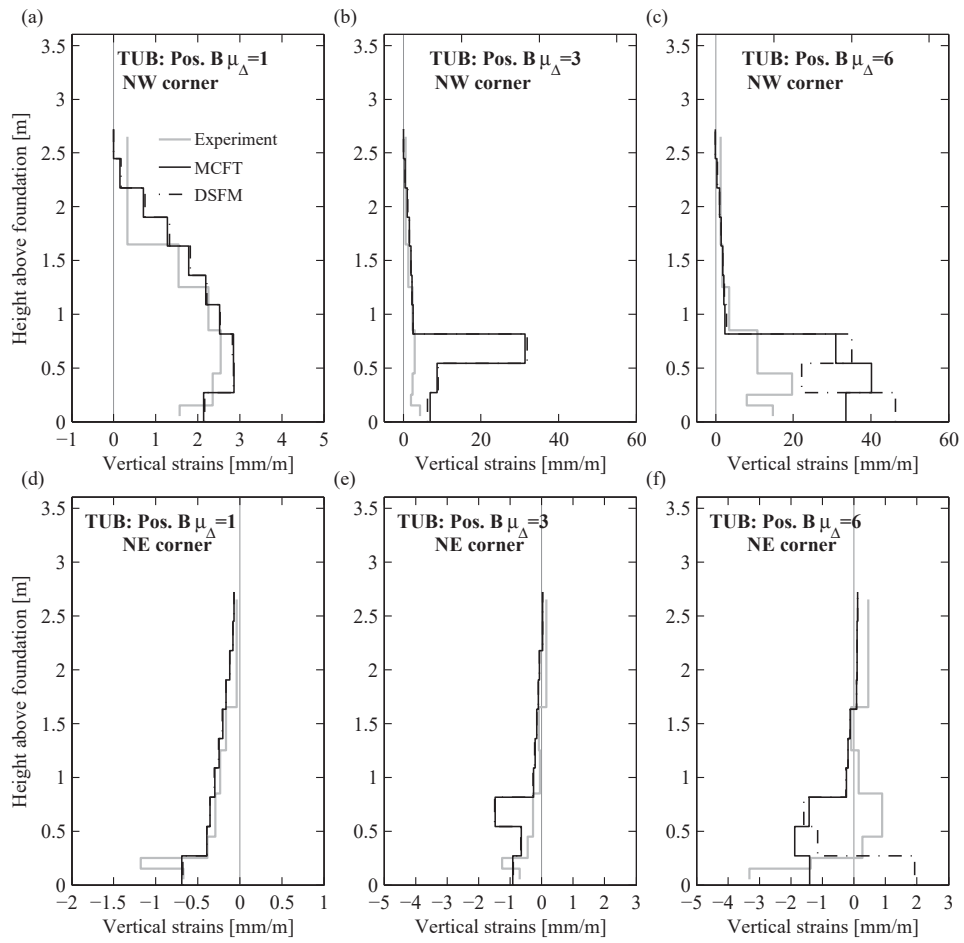


Figure 5.25: Sensitivity of the vertical strain profiles to the choice of analytical model (MCFT or DSFM)

**Tension stiffening and softening - TUB model** The post-peak behaviour of concrete in tension is expected to significantly influence the effective stiffness of the wall, i.e., the secant stiffness through the first yield point, which is one of the quantities of interest here. To verify this, results from the TUB model where tension stiffening is not considered were compared with the results from the reference model and with the experimentally derived quantities. The reference model which was described in Section 5.2.2.1 includes both tension stiffening (Modified Bentz) and tension softening (Linear). Note that, as previously mentioned VecTor4 does not consider tension softening when tension stiffening is neglected. Hence the results shown in Figure 5.26 consider that concrete tensile strength drops immediately to zero after cracking.

Neglecting tension stiffening and softening reduced significantly the initial wall stiffness when compared to the reference model. More importantly, this model has also a significantly lower stiffness than the experimental force-displacement curve.

When comparing the vertical strain profiles, the match between the reference model strains and the experimental ones is rather good at yield ( $\mu_{\Delta} = 1$ ). The model without tension stiffening and softening significantly overestimates the tensile strains in the upper part of the wall at yield, while underestimating the strains at the base. In contrast, at medium and high ductilities it is the latter model that predicts well the tensile strain distribution over the height of the wall, and the concentration of strains in the third element no longer occurs. This would indicate that the post-peak tension behaviour of concrete is responsible for the concentration of plastic strains in the third element above the base, which was observed in Section 5.2.2.2.

Figure 5.26 compares the force-displacement results when tension softening is not considered with results from the base model and experimental results. Not accounting for tension softening reduces slightly the elastic stiffness. However the largest differences with the final model and with the experimental results can be seen in the local results at yield. Without tension softening, the tensile strains in the upper part of the wall are overestimated at  $\mu_{\Delta} = 1$ . Without tension softening, the tensile strains at medium and large ductilities are now concentrated in the second element from the base, which is closer to the experimental observations.

In conclusion, not considering tension stiffening and softening underestimates significantly the elastic stiffness of the wall as well as it overestimates the tensile strains in the upper part of the wall at yield. Therefore it is necessary to consider these phenomena in the model if the elastic branch of the force-displacement curve is of interest, despite the shortcomings of these models related to numerical concentration of strains.

### 5.2.2.4 Material properties

The reinforcement stress-strain curves were fitted with the experimentally obtained curves of steel tests at the day of testing (Figure 5.29a). The steel properties introduced in the model correspond to those at day of testing, except the ultimate strain which was assigned a very large value.



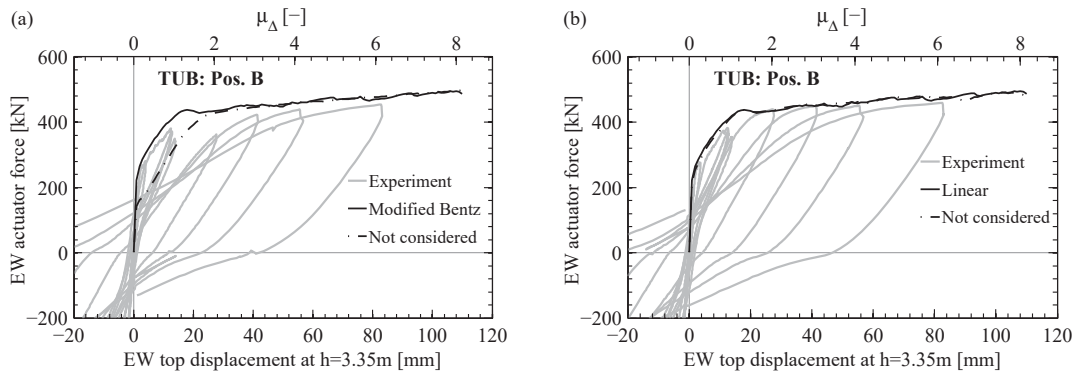


**Figure 5.26:** Sensitivity of the force-displacement curve to the choice of tension stiffening (a) and tension softening (b) models

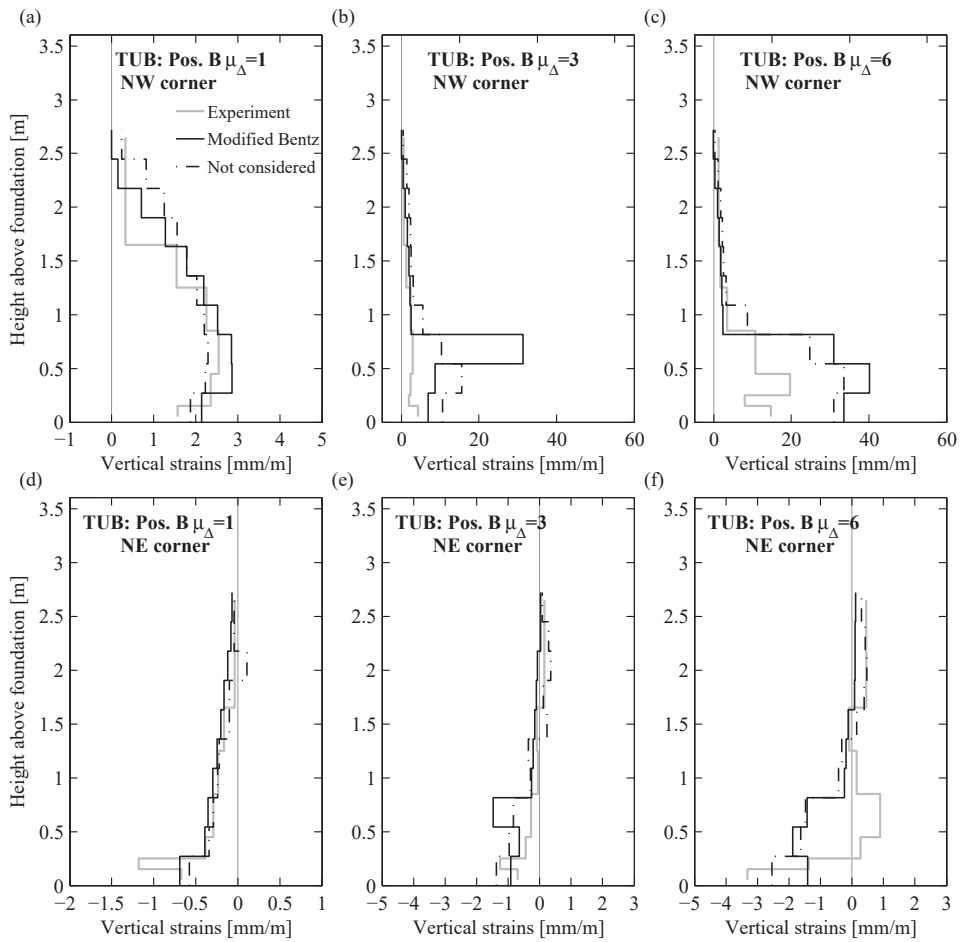


**Figure 5.27:** Sensitivity of the vertical strain profiles to the tension stiffening model

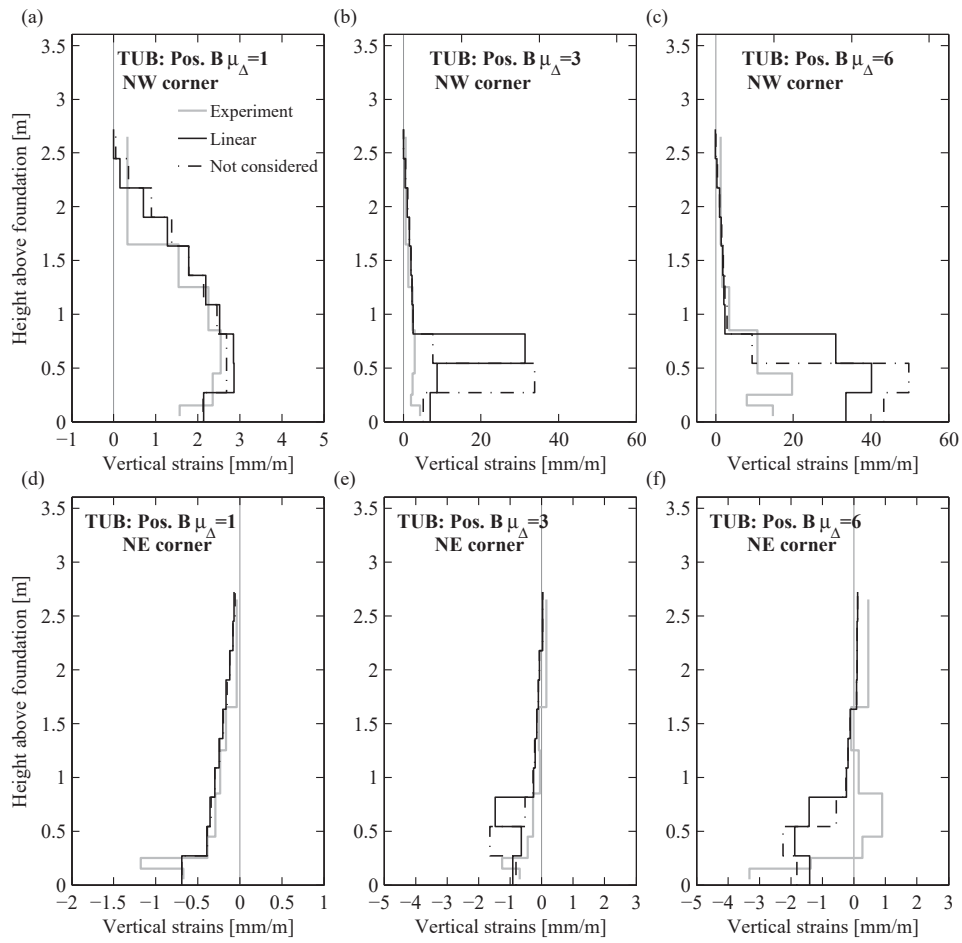
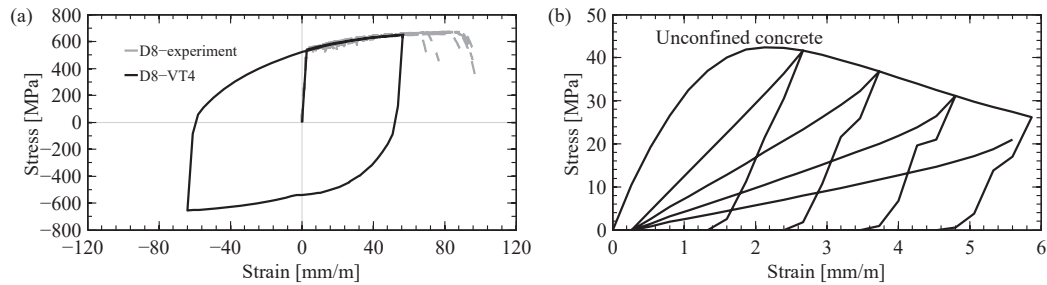


Figure 5.28: Sensitivity of the vertical strain profiles to the tension softening model

The concrete compressive strength  $f_c$  was taken from cylinder tests at the day of testing. The corresponding peak strain at maximum strength was set to the default VecTor4 value  $\epsilon_0 = 1.8 + 0.0075f_c$ . For the elastic modulus and the tensile strength, the default VecTor4 values were also assigned:  $E_c = 5500\sqrt{f_c}$  and  $f_t = 0.33\sqrt{f_c}$  correspondingly. As already discussed for the concrete compressive base curve the Hognestad model is used for the pre-peak and the Modified Park-Kent for the post-peak. To account for the cyclic behaviour, the concrete hysteresis is described by a nonlinear model with offsets (Figure 5.29).



**Figure 5.29:** Vector4 material models: (a) D8 and D12 reinforcement of TUC and TUD; and (b) unconfined concrete of TUC

**Concrete tensile strength** The extent of cracking over the height of the wall is one of the quantities of interest here. Since cracking depends significantly on the concrete tensile strength  $f_t$ , its influence on the results was verified by performing one analysis with half the default tensile strength. The default tensile strength is computed in VecTor4 as  $f_t = 0.33\sqrt{f_c}$ , where  $f_c$  is the uni-axial concrete compressive strength.

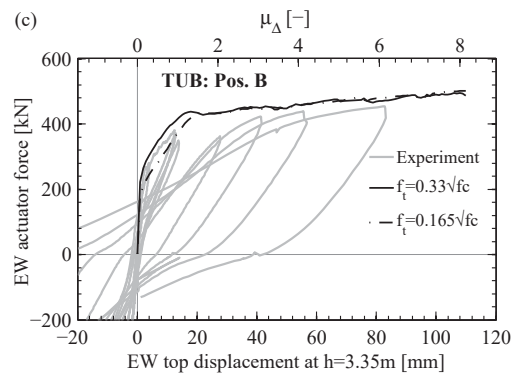


**Figure 5.30:** Sensitivity of the force-displacement curve to the value of the concrete tensile strength

Figure 5.30 indicates that the model with  $f_t$  leads to a reduced initial wall stiffness when compared to the reference model and also when compared to the experimental results. In terms of local behaviour, the tensile strains at yield are overestimated in the upper part of the wall at yield, indicating that using half the value of  $f_t$  will overestimate the extent of cracking over the wall height. At the same, the tensile strains towards the base of the wall, are underestimated when reducing  $f_t$ . At medium and high ductilities, reducing  $f_t$  has little influence on the tensile strain profile. Since capturing the extent of cracking at yield is essential, the default concrete tensile strength  $f_t = 0.33\sqrt{f_c}$  will be used in all the analyses.

## Chapter 5. Validation of two numerical models for U-shaped walls

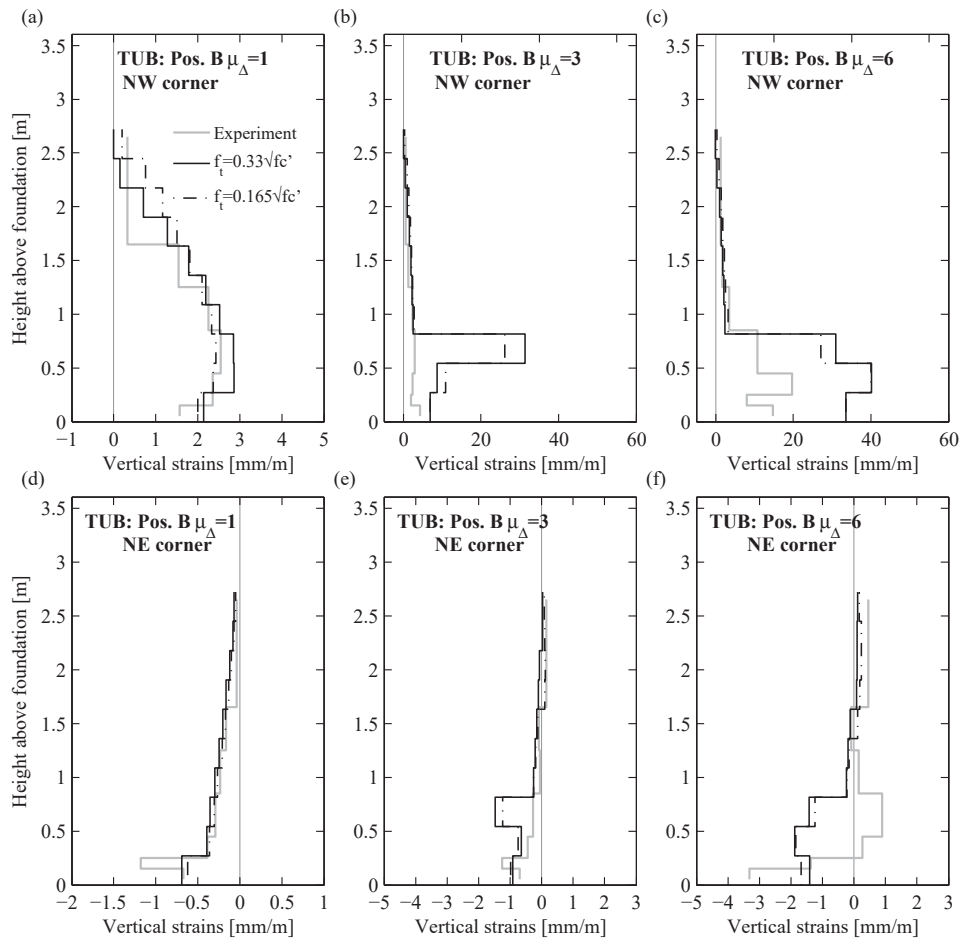


**Figure 5.31:** Sensitivity of the vertical strain profiles to the value of the concrete tensile strength

### 5.2.2.5 Load application and load history

The collar where all the loads were applied, was assigned a large tensile and compressive concrete strength to account for the pre-tensioning which was applied on the collar during the experiments. Four compressive forces representative for the axial load were applied vertically at the top of the collar with their resultant acting at the gravity centre of the wall U-shaped section (Figure 5.9). The three lateral loads were all applied by means of displacement increments for all analyses.

In all four tests which are used for the validation of the model, bi-directional loading histories were applied ([BDP08a] and Section 3). The same load histories were also applied to the VecTor4 models, except for TUA and TUB where the elastic cycles, as listed below, were applied in displacement control instead of force control as in the experiments.

The loading positions and directions are shown in Figure 5.2b-c. Three lateral loading directions: EW, NS and diagonal E-F, with two loading positions each were distinguished for TUA and TUB. For TUC and TUD, an additional loading direction is considered, i.e., diagonal H-G, due to the loading protocol and the asymmetry of the vertical reinforcement in the two wall flanges (Section 3). The loading history of all test units is summarised below:

- TUA and TUB
  - Elastic cycles: one cycle along EW, NS and diagonal E-F directions up 25%, 50%, 75% and 100% of the predicted force at first yield
  - Inelastic cycles: one cycle along EW, NS, diagonal E-F directions and one sweep cycle at each displacement ductility  $\mu_{\Delta} = 1, 2, 3, 4, 6$  (and 8 only for TUA)
- TUC and TUD
  - Elastic cycles: one cycle along diagonal E-F (Diag.1), diagonal H-G, NS and EW direction at drifts  $\delta = 0.1\%, 0.2\%, 0.3\%, 0.4\%$  and  $0.6\%$
  - Elastic cycles: two consecutive cycles per drift along NS followed by two cycles along EW direction at  $\delta = 0.8\%$
  - Inelastic cycles: two consecutive cycles per drift along diagonal E-F then two cycles along diagonal H-G  $\delta = 1.0\%$
  - Inelastic cycles: two consecutive cycles per drift along diagonal H-G then two cycles along diagonal E-F  $\delta = 1.5\%$
  - Inelastic cycles (only for TUC): continue alternating diagonals E-F and H-G at  $\delta = 2.0\%, 2.5\%$

### 5.2.3 Model validation

Once the model was set-up its validation is done against experimental results from the four quasi-static cyclic tests on U-shaped walls, namely TUA and TUB reported by [BDP08a] and TUC and TUD reported in Chapter 3. The VecTor4 models for the four walls differ with regard to concrete and steel properties, with regard to the imposed loading history both horizontal and vertical load as well as with regard to the vertical reinforcement contents. The mesh was kept the same for all models (Figure 5.9).

In the following, the numerical results from the VecTor4 analyses are discussed with respect to the experimentally derived values focusing on quantities involved in the plastic hinge model, since these quantities will also be of interest for the parametric studies. For consistency, the numerically determined quantities are derived using the same procedures that were used for the derivation of the experimental results (Section 4).

### 5.2.3.1 Force-displacement curves

The comparison between the experimental and the numerically obtained force-displacement hystereses is shown in Figures 5.32 to 5.34 with the force-displacement hystereses displayed for each loading direction and each test unit. The VecTor4 model captures very well the experimental force-displacement hysteresis in terms of strength, loading and reloading stiffness for all test units and loading directions.

### 5.2.3.2 Yield curvature

The yield curvature  $\phi_y$  is determined from the results of the shell element model following the same procedure as for the experimental results (Section 5.1.2.4). More precisely, the first yield is determined at the instant when the tensile strain at the base of the wall corresponding to the most tensioned flexural reinforcement bar reaches the reinforcement yield strain. The base strain was determined by extrapolating to the wall base a linear fit of the strains over the cracked height of the wall  $H_{cr}$ , where  $H_{cr}$  is computed as in Equation 5.5. In this equation,  $M_{cr}$  is the analytical cracking moment,  $M_y$  is the first yield moment from section analysis and  $H$  is the wall shear span depending on the loading direction.

$$H_{cr} = \max(l_{wall}; (1 - M_{cr}/M_y) \cdot H) \quad (5.5)$$

Once the first yield instant is determined, the first yield curvature  $\phi'_y$  is determined also by a best linear fit procedure and extrapolation to the base. The curvature profile at first yield is also fitted over  $H_{cr}$  and extrapolated to the wall base, thus giving the first yield curvature. Curvature profiles at first yield obtained from the analyses are shown for comparison with the experimentally derived profiles in Figures 5.35 and 5.36. The match between the experimentally and numerically determined curvatures profiles at first yield is overall rather good.

As Figure 5.37 indicates, the first yield curvatures obtained as explained above are slightly overestimated by the numerical model. This is the result of having the first yield instant being determined slightly later, i.e. for larger top displacements, in the numerical model due to larger size of the numerical load step increment as compared to the experimental load step. This will also lead to larger first yield moments and hence lower nominal to first yield moment ratios  $M_n/M_y$ . As will be discussed in the following, this difference is of little importance since the larger first yield curvatures  $\phi'_y$  and displacements  $\Delta'_y$ , combined with the lower nominal to first yield moment ratios  $M_n/M_y$  will lead to good predictions of the nominal yield curvature  $\phi_y$  and displacement  $\Delta_y$ , which are the quantities of interest.

## 5.2. Shell element model

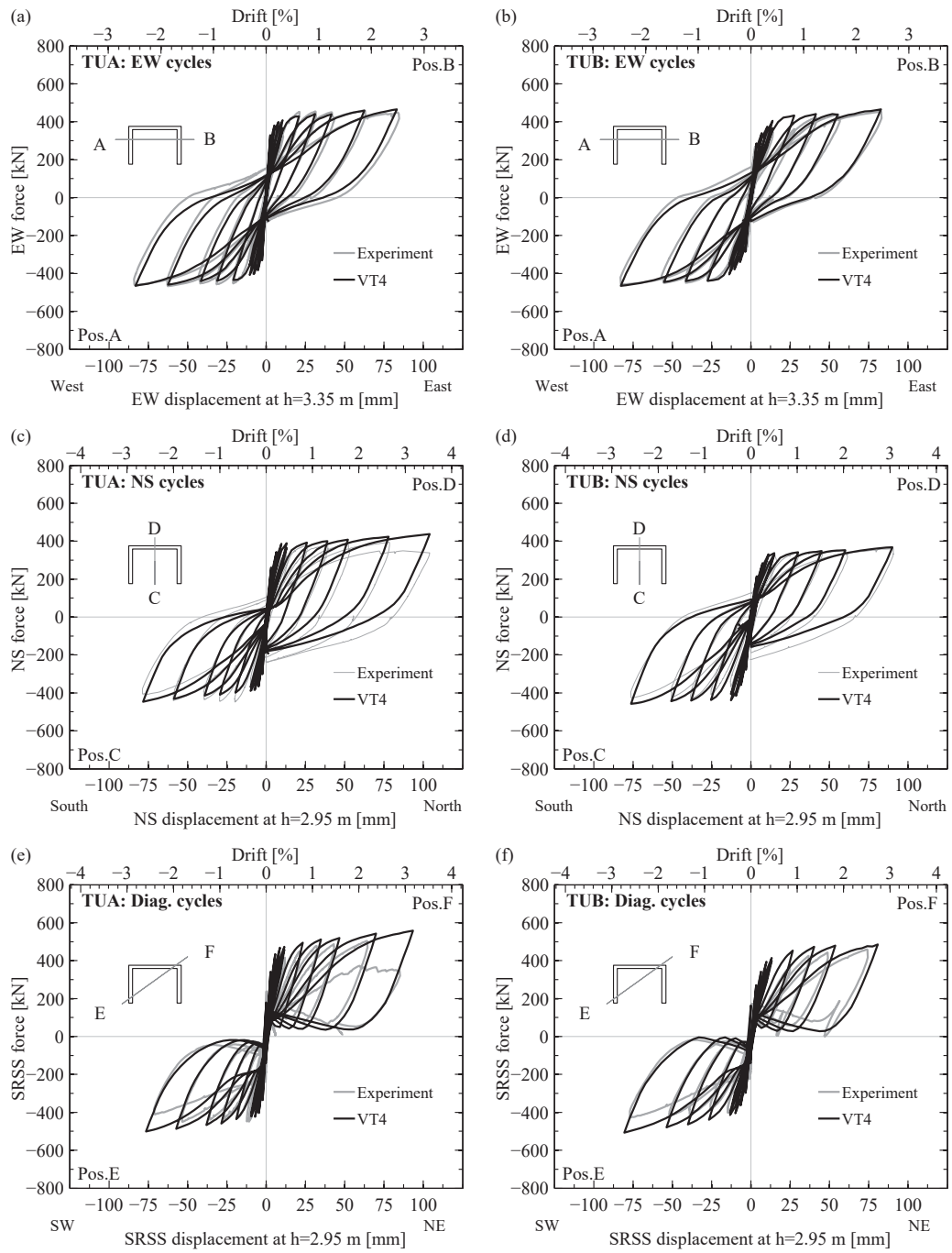


**Figure 5.32:** TUA and TUB: Comparison between the experimentally determined force-displacement hysteresses and full-cyclic VecTor4 (VT4) predictions

## Chapter 5. Validation of two numerical models for U-shaped walls

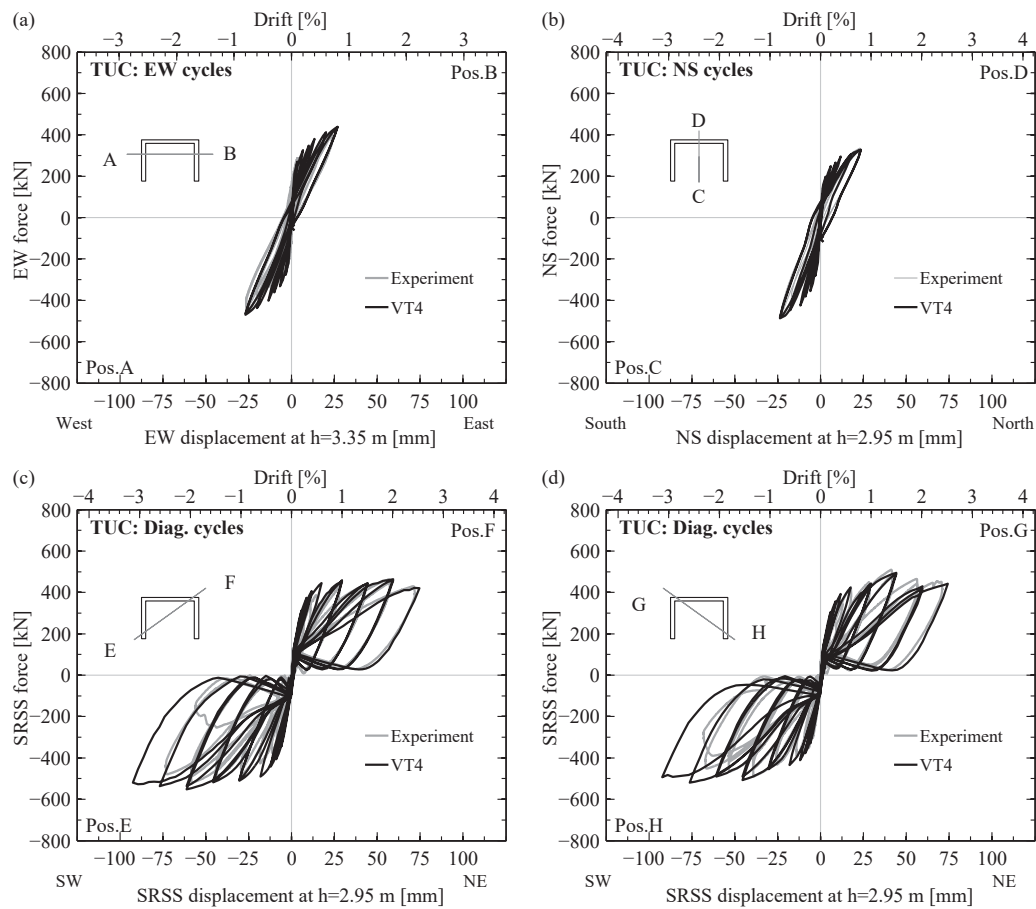


**Figure 5.33:** TUC: Comparison between the experimentally determined force-displacement hysteretic behavior and full-cyclic VecTor4 (VT4) predictions



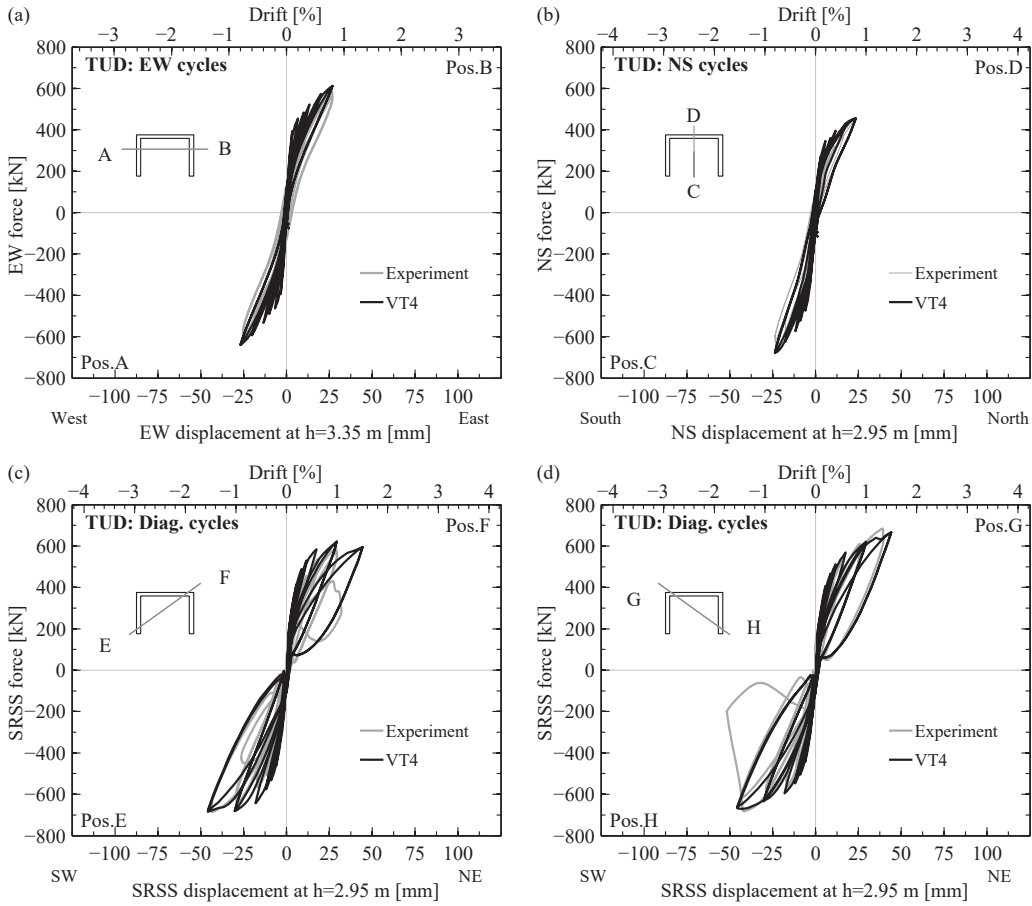


Figure 5.34: TUD: Comparison between the experimentally determined force-displacement hysteresses and full-cyclic VecTor4 (VT4) predictions

Chapter 5. Validation of two numerical models for U-shaped walls

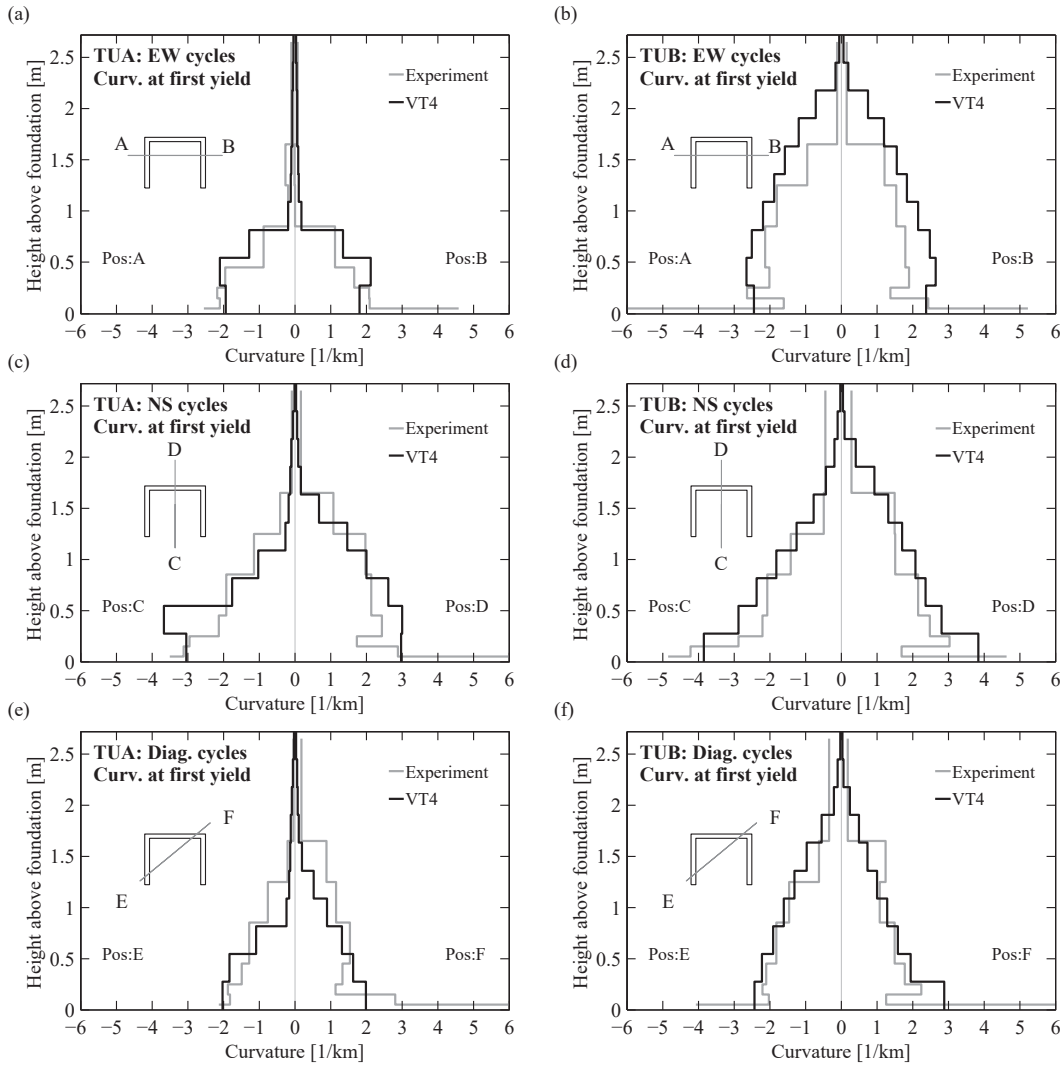
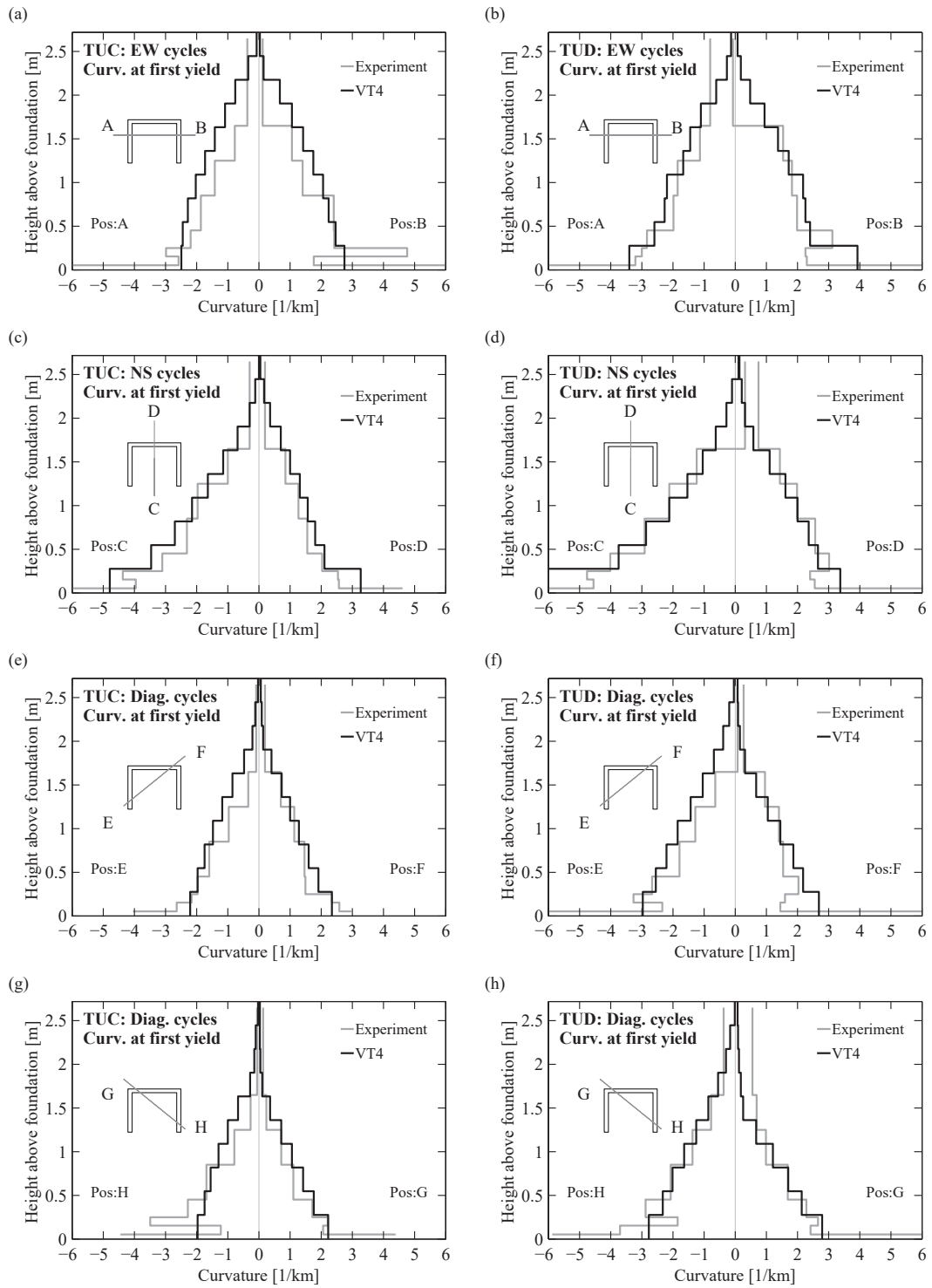


Figure 5.35: TUA and TUB: comparison of experimentally determined curvatures profiles at first yield with VT4 results



**Figure 5.36:** TUC and TUD: comparison of experimentally determined curvatures profiles at first yield with VT4 results

Next, in order to obtain the nominal yield curvature  $\phi_y$ , the yield and the nominal moment need to be determined. The yield moment is defined as the moment when the base strain corresponds to the yield strain limits and the nominal moment as the moment when the nominal strain limits are reached. The same procedure was used for deriving the nominal moment from the experimental data (Section 5.1.2.4). The nominal limit strains are  $\varepsilon_s = 0.015$  or  $\varepsilon_c = -0.004$  whichever occurs first. The base strain is obtained by extrapolating to the wall base the best linear fit of the strain profiles over the height of inelastic strains. A linear variation of the inelastic strains is hence assumed.

A comparison of the numerically and experimentally obtained  $M_n/M_y$  ratios is shown in Figure 5.37b. As discussed, the predictions of the nominal moment to first yield moment  $M_n/M_y$  ratio are slightly lower than the experimentally derived  $M_n/M_y$  ratios, within  $\sim 20 - 30\%$  (Figure 5.37b) due to the higher numerical yield moments  $M_y$  (Figure 5.39a).

Finally, the nominal yield curvature will be obtained by multiplying the first yield curvature  $\phi'_y$  with the  $M_n/M_y$  ratio. The discrepancies between the numerically and the experimentally determined nominal yield curvatures stem from the differences in two multiplied quantities which tend to cancel out (Figure 5.37c) since the  $\phi'_y$  is slightly overestimated while  $M_n/M_y$  is slightly underestimated. Overall, the shell element model captures relatively well the experimentally derived nominal yield curvatures: within  $\sim 20\%$  difference if the positions E and F of TUA are not considered.

Note that for TUA, the experimental data for the elastic cycles to 25% and 50% of the yield force was missing (Figure 5.32) as the top displacements were too small to be recorded by the measurement instruments. The experimental first yield instant was determined during the first recorded cycle (loading up to 75% of the yield force) but the first yield instant might have already been reached in the missing cycles. Hence the experimentally determined wall response of TUA in the elastic range is most likely softer than the actual wall behaviour especially for positions cycled last at this ductility, i.e., positions E and F but also positions C and D. For these loading cases of TUA, empty markers are used in the figures.

### 5.2.3.3 Yield displacement

The yield displacement can be directly obtained from the VecTor4 model as the displacement at the first yield instant  $\Delta'_y$  multiplied by the  $M_n/M_y$  ratio. The numerically determined first yield displacement is shown in Figure 5.37c for comparison with the experimentally determined values while the nominal yield displacement  $\Delta_y$  is given in Figure 5.37d. Again if the values for TUA at the missing data positions are not considered, the match for the  $\Delta_y$  is fairly good, within  $\sim 20 - 30\%$  difference.

The first yield and the nominal points from experimental and numerical results are shown on the force-displacement curves in one example in Figure 5.38. Despite predicting larger first yield displacements  $\Delta'_y$  and hence also larger first yield moments  $M_y$ , VecTor4 underestimates the  $M_n/M_y$  ratio and hence the nominal yield displacement  $\Delta_y = \Delta'_y \cdot M_n/M_y$  is well predicted.

## 5.2. Shell element model

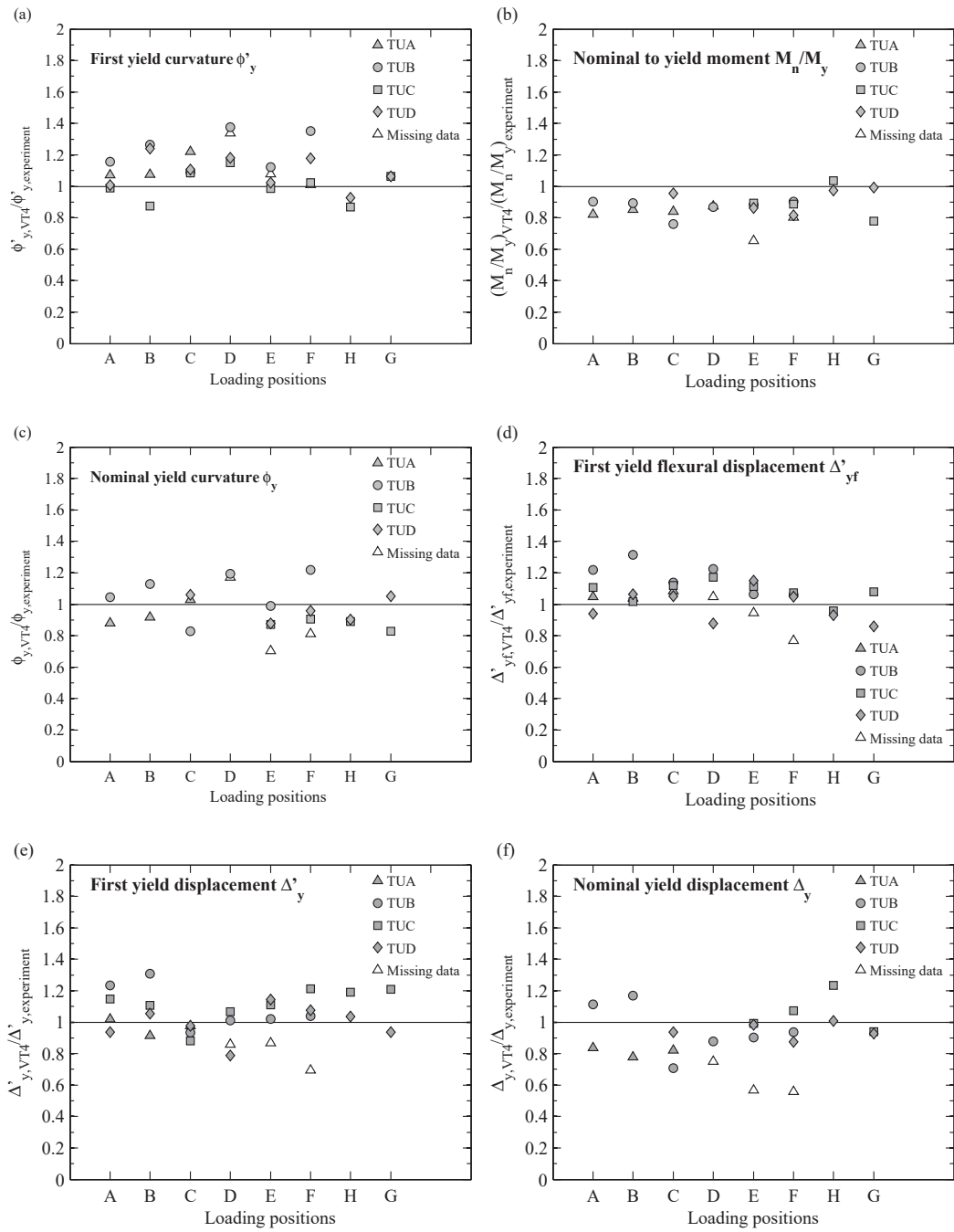


**Figure 5.37:** Comparison between the experimentally determined quantities and the VecTor4 derived quantities at yield: first yield curvature (a), nominal to yield moment ratio (b), nominal yield curvature(c), first yield flexural displacement(d), first yield displacement (e) and nominal yield displacement (f)

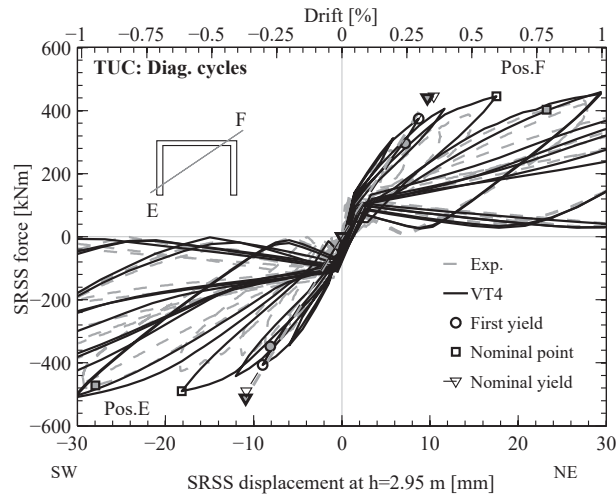


Figure 5.38: TUC: comparison of experimentally determined curvatures profiles at first yield with VT4 results

5.2.3.4 Effective stiffness

The effective stiffness of the U-shaped wall under the different loading direction was evaluated from the experimental results in Section 4.8 as the force at first yield divided by the displacement at first yield. The numerical values of the effective stiffness are also determined in this manner. As discussed, while the first yield displacements are typically slightly overestimated (Figure 5.37d), so are the first yield moments (Figure 5.39). Hence the overall match of the effective stiffness ratios  $K_{eff}/K_{th}$  (i.e., effective stiffness divided by the elastic stiffness of the gross section) is relatively good, again after removing the points corresponding to the missing cycles of TUA.

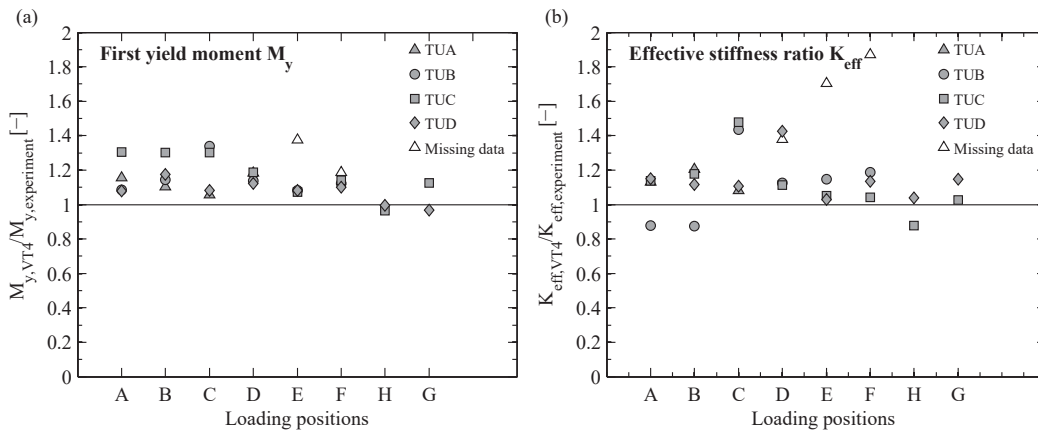
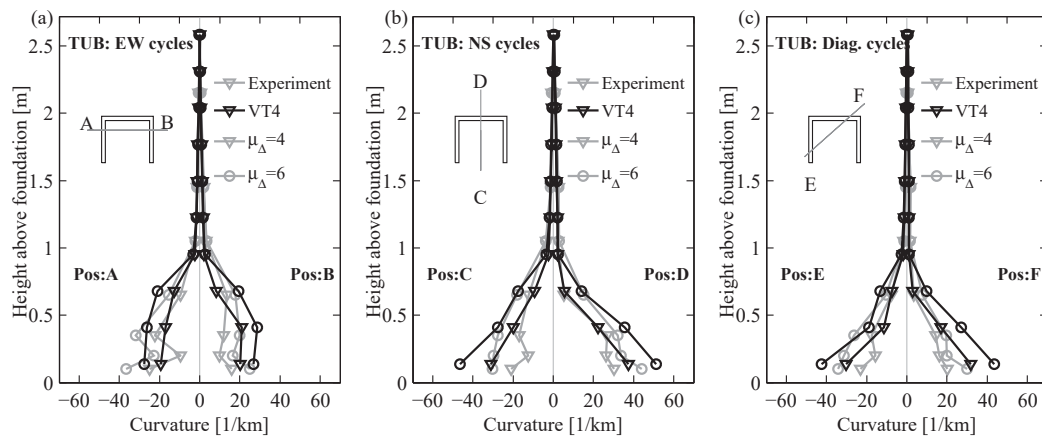


Figure 5.39: Comparison between the experimentally determined quantities and the VecTor4 derived quantities: first yield moment (a) and effective stiffness ratio(b)

## 5.2.3.5 Plastic hinge length

In Section 4.5, the experimentally determined plastic hinge length was evaluated in two ways in order to compare with estimates: (1) by back-calculating the  $L_{ph}$  value from the top plastic flexural displacement and (2) by taking  $L_{ph}$  as half the height of the plastic zone  $L_{pz}$ . For both approaches, the match between the  $L_{ph}$  experimental and numerical values will depend on how well the numerical model captures the experimental curvature distribution over the wall height in the inelastic range. The curvature profiles, experimentally and numerically determined, are hence compared for one of the test units, TUB, in Figure 5.40 for the different loading positions and displacement ductilities. The match between the experimental and the numerical determined curvature profiles is rather good and hence also the match between the plastic hinge values derived from the curvature profile is rather good and match the experimentally observed constant trends of the plastic hinge lengths over the ductility range (Figures 5.41 and 5.42).

If average values over the inelastic range ( $\delta \geq \delta_y$ ) of the plastic hinge length computed as half the height of the plastic zone  $L_{ph} = L_{pz}/2$  are compared to the numerically determined values (Figure 5.43), the match is relatively good. The experimental  $L_{ph}$  average values are captured by the VecTor4 model within an error of  $\sim 20\%$  with numerical values typically underestimating the experimental values. For TUD, the differences between experimental and numerical  $L_{ph}$  values are larger than for the other test units. However the experimental  $L_{ph}$  values of TUD are less reliable since only one or two  $L_{ph}$  values are available to compute the average  $L_{ph}$  at these loading positions and they correspond to low displacement ductilities ( $\mu_\Delta = 2 - 3$ ) which are more sensitive to measurement errors.



**Figure 5.40:** TUB: comparison between the experimentally determined curvature profiles and the curvature profiles from the VecTor4 model at displacement ductilities  $\mu_\Delta = 4$  and 6.

## Chapter 5. Validation of two numerical models for U-shaped walls

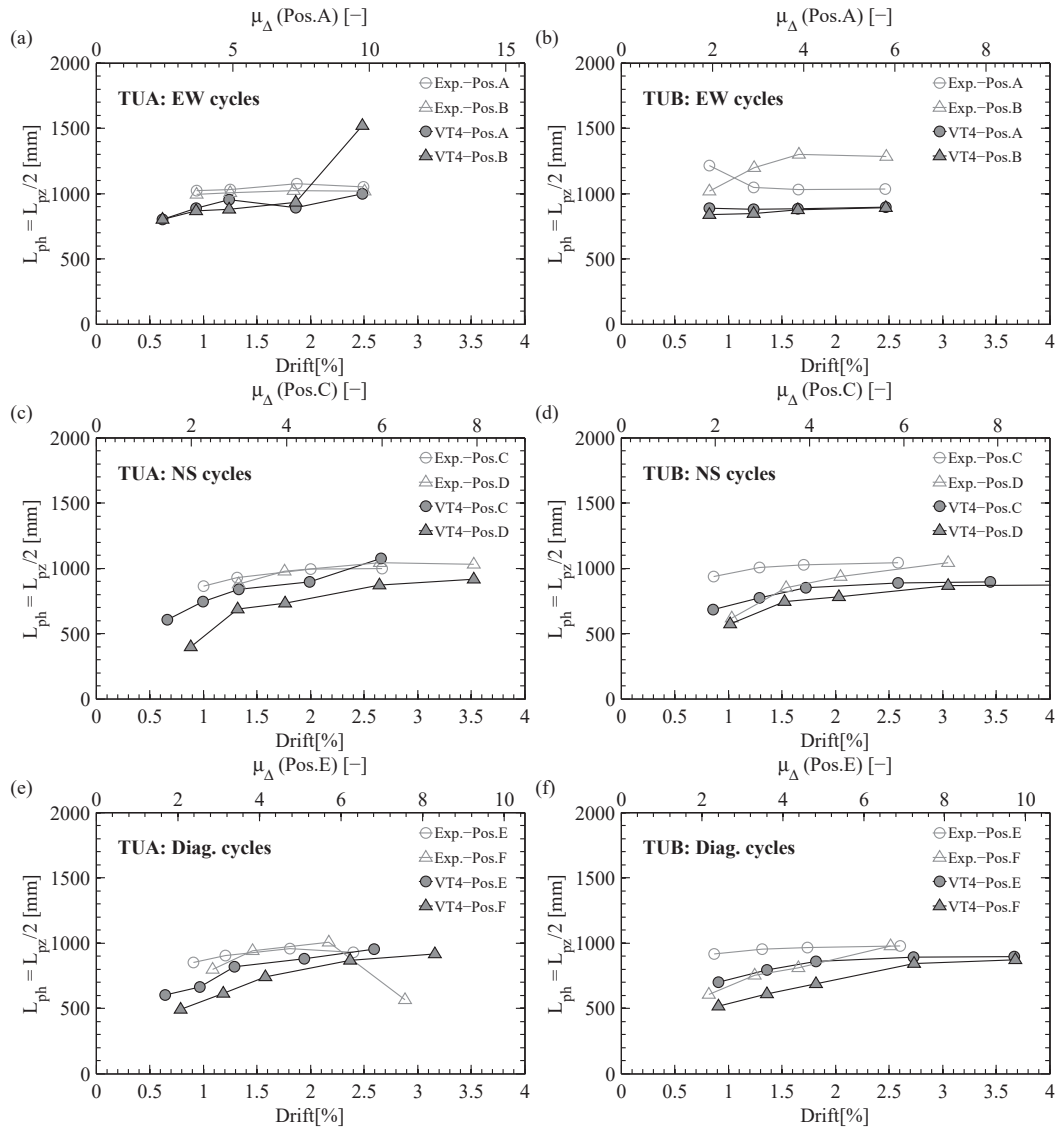


**Figure 5.41:** TUA and TUB: Comparison of experimentally determined plastic hinge lengths  $L_{ph}$  (Exp.) with numerically determined  $L_{ph}$  from VecTor4 (VT4) analyses. Plastic hinge lengths  $L_{ph}$  were computed assuming the centre of rotation at the middle of the plastic hinge length.



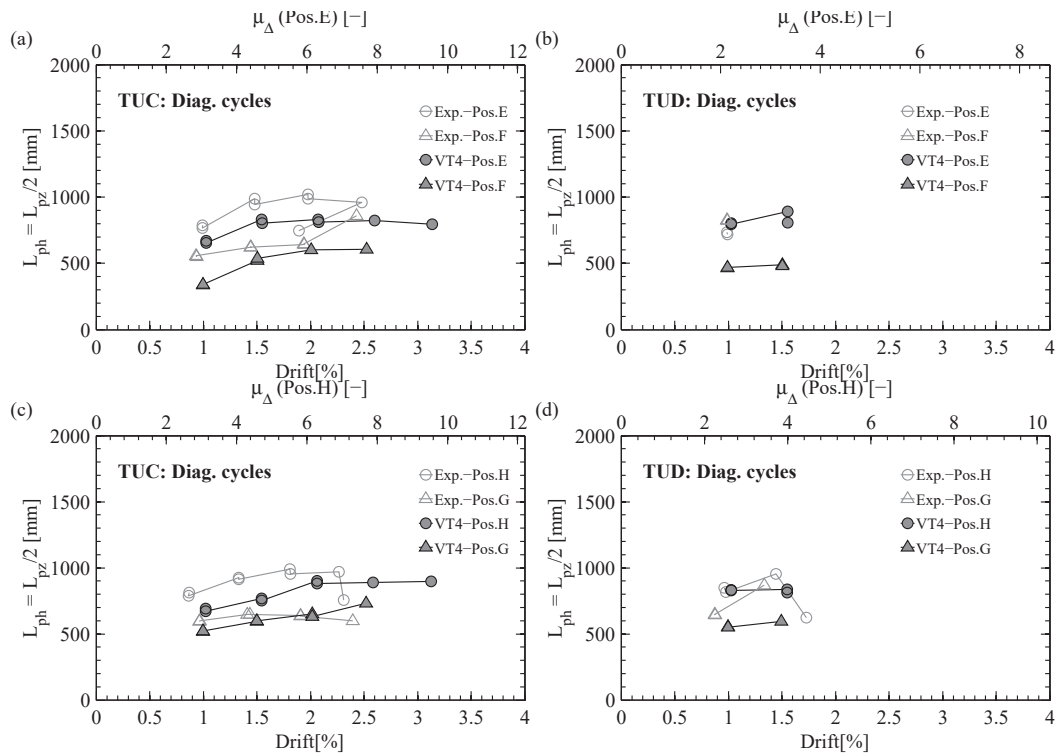


**Figure 5.42:** TUC and TUD: Comparison of experimentally determined plastic hinge lengths  $L_{ph}$  (Exp.) with numerically determined  $L_{ph}$  from VecTor4 (VT4) analyses. Plastic hinge lengths  $L_{ph}$  were computed assuming the centre of rotation at the middle of the plastic hinge length.

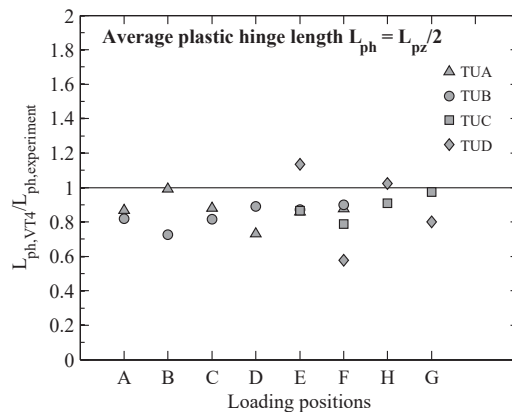


**Figure 5.43:** TUA to TUD: comparison of experimentally determined average plastic hinge lengths  $L_{ph}$  (Exp.) with numerically determined  $L_{ph}$  from VecTor4 (VT4) analyses. Plastic hinge lengths values at peak drifts larger than twice the yield drift ( $\delta \leq 2\delta_y$ ) were averaged.

5.2.3.6 Ratio of shear to flexural displacements

The experimentally derived shear to flexural displacements ratios  $\Delta_s/\Delta_f$  have been determined and discussed in Section 4.7. The numerical  $\Delta_s/\Delta_f$  ratios were computed from the displacements of the nodes located at the four vertical edges of the wall (Figure 5.9). Average curvatures were computed over the height of one-element row ( $h = 272$  mm) and they were integrated over the shear span of the wall ( $h = 0 - H$ ) to obtain the flexural displacements. The shear deformations were derived over one row of elements (extending horizontally over one wall section: web or flanges) from the change in the length of the diagonals over this row of elements as in Section 4.7.

The experimentally determined  $\Delta_s/\Delta_f$  ratios are compared to the numerical ratios in Figures 5.45 and 5.46 for the values over the ductility range and in Figure 5.47 for average values over the inelastic range. For the naming of the different wall sections (flanges and web) as well as for the loading positions and directions, the reader is referred to Figure 5.44.

Despite overestimating the large  $\Delta_s/\Delta_f$  ratios (e.g., Web at position E or H) the model captures relatively well the experimental  $\Delta_s/\Delta_f$  ratios. The model also captures the negative  $\Delta_s/\Delta_f$  ratios of the flange in tension at positions E or H (Figure 5.47).

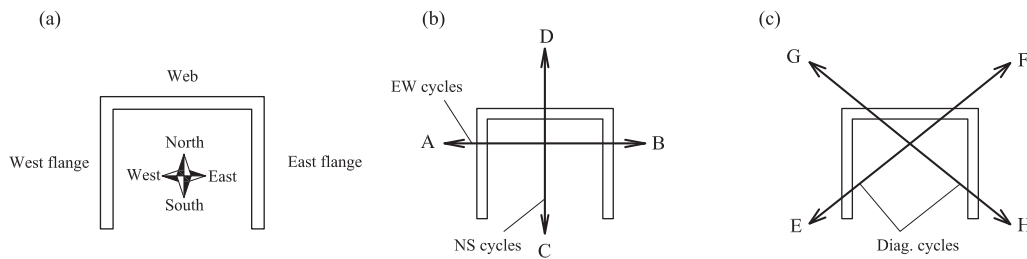


**Figure 5.44:** Cardinal points for the wall (a) and loading cycles and positions for the principal directions (b) and for the diagonal directions (c)

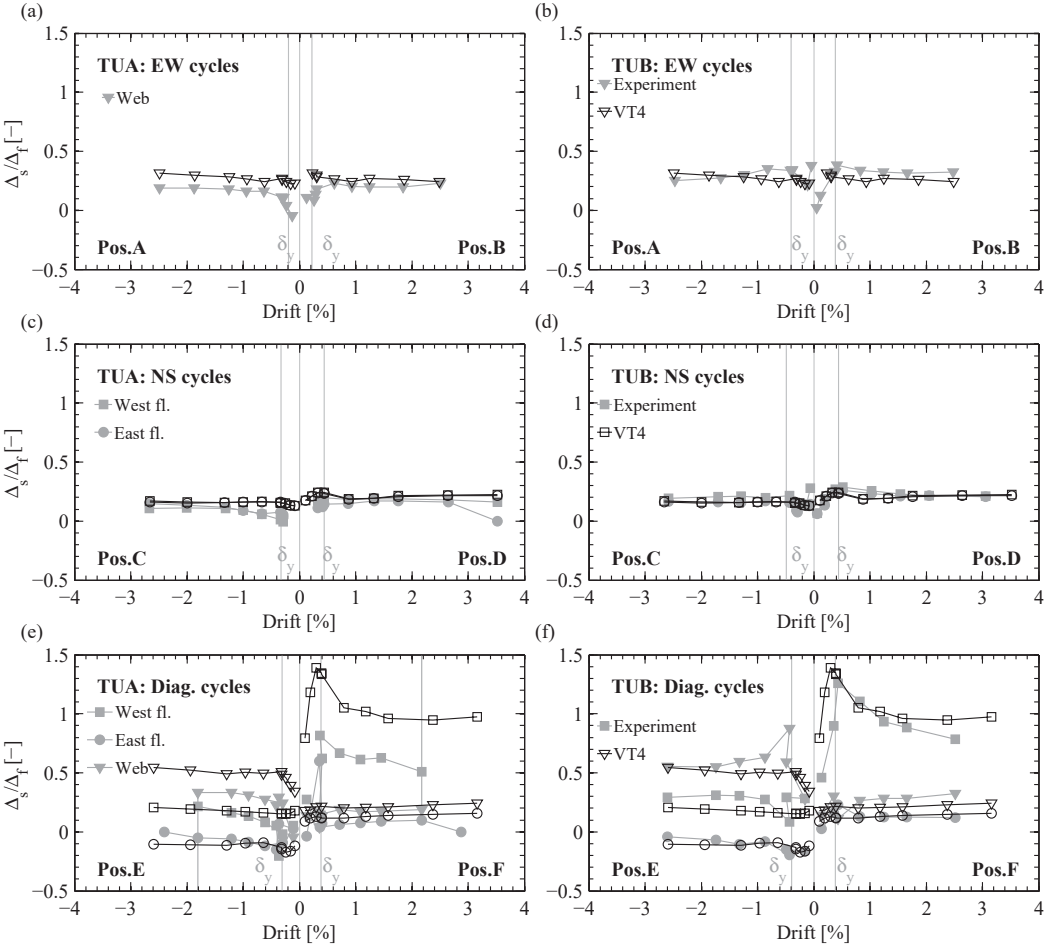
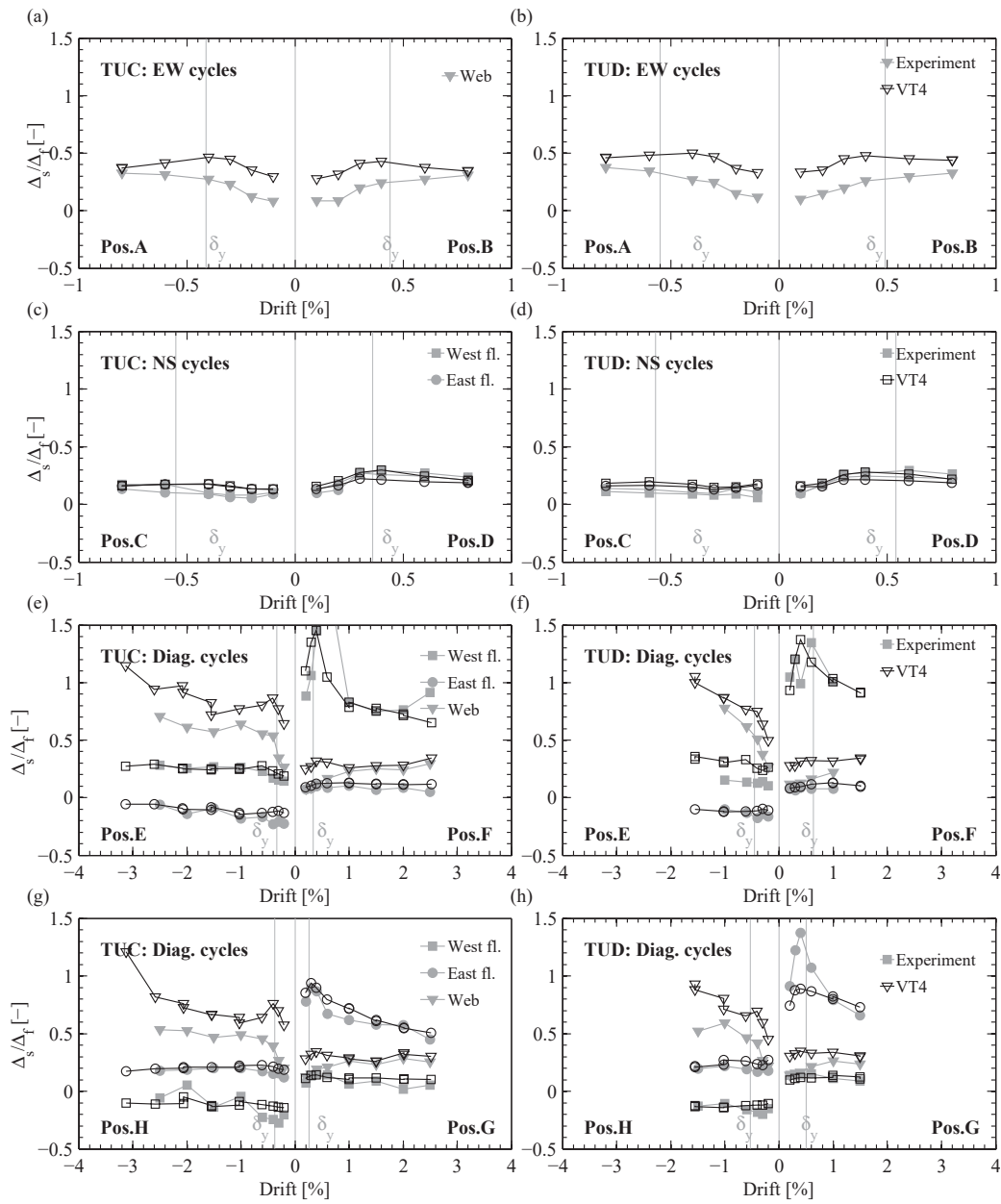
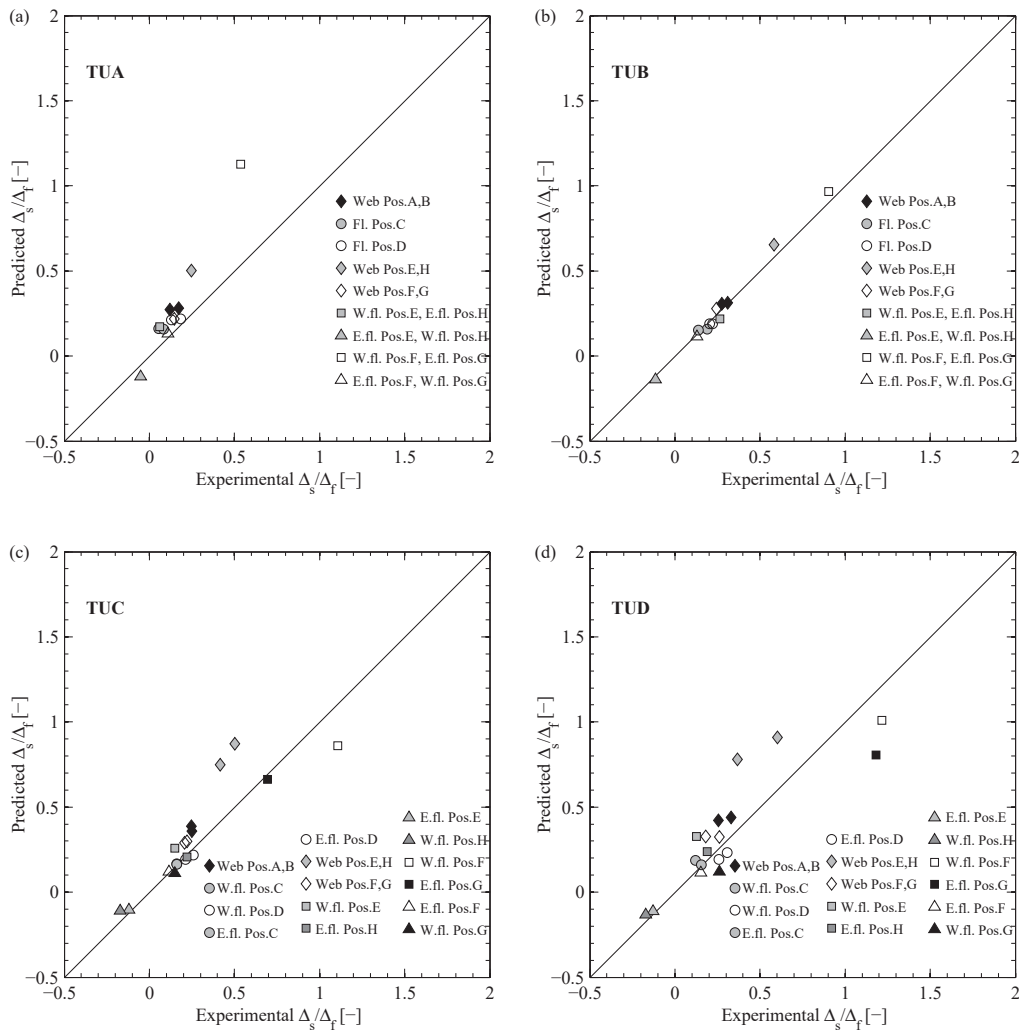


Figure 5.45: TUA and TUB: comparison of experimentally determined shear to flexural displacement ratios  $\Delta_s/\Delta_f$  with numerically  $\Delta_s/\Delta_f$  from VecTor4 (VT4) analyses



**Figure 5.46:** TUC and TUD: comparison of experimentally determined shear to flexural displacement ratios  $\Delta_s/\Delta_f$  with numerically  $\Delta_s/\Delta_f$  from VecTor4 (VT4) analyses



**Figure 5.47:** TUA to TUD: Comparison between the experimentally determined shear to flexural deformation average ratio  $\Delta_s/\Delta_f$  with numerically  $\Delta_s/\Delta_f$  from VecTor4 (VT4) analyses

## 5.2.4 Influence of the loading history

### 5.2.4.1 Introduction

The shell element model presented in Section 5.2.2 was validated against experimental data in Section 5.2.3. For this validation, the model was subjected to the same loading history as in the experiments, i.e., a multi-directional cyclic loading (see Section 5.2.2.5). However, it is intended to use this shell element model for parametric studies. Given the large number of analyses to be performed, cyclic analyses would be too computationally expensive. Therefore, it is envisaged to perform the parametric studies as monotonic analyses. However, before doing so, one must check whether the loading history influences the numerical results of interest namely the wall strength, the yield curvature and displacement, the effective stiffness and the plastic hinge length.

## Chapter 5. Validation of two numerical models for U-shaped walls

---

The monotonic analyses included in this section were performed using the same shell element models of TUA, TUB, TUC and TUD as the ones used for the cyclic analyses presented in Section 5.2.2. Monotonic analyses to each of the individual loading positions were carried out, i.e., to positions A to G (Figure 5.2b).

### 5.2.4.2 Wall strength

The force-displacement curves obtained with the shell element model under multi-directional cyclic loading and under monotonic loading are compared in Figures 5.48, 5.49 and 5.50. For the principal loading directions, the force capacity obtained under cyclic loading is similar to the one obtained under monotonic loading. However, for the diagonal loading directions the force capacity obtained from the monotonic analyses is up to 20% higher than in the cyclic analyses depending on the loading position. The cause of these differences is investigated in the following.

The loading history applied in the experiments and in the cyclic analyses of the shell element model differs from a monotonic loading in two regards. Firstly, the loading is cyclic and secondly, it is multi-directional, i.e., loading is applied in several directions successively: e.g., for TUC two complete reverse cycles are applied in the direction of the E-F diagonal followed by two reverse cycles applied in the diagonal H-G, all at the same ductility level (Figure 5.51a). In order to understand what effect each of the two characteristics has on the wall strength, a uni-directional but cyclic analysis in the diagonal direction E-F is performed (Figure 5.51b).

A comparison of the three analyses for the TUC model (monotonic, cyclic uni-directional and cyclic multi-directional) is presented in Figure 5.52 for the diagonal direction E-F. While under monotonic and cyclic uni-directional loading the wall model reaches similar force capacities, for the cyclic multi-directional loading, the force capacity is smaller than the one obtained from the other two analyses. These results indicate that:

- Monotonic analysis will predict rather well the wall strength in the diagonal directions under cyclic loading if the wall is loaded uni-directionally.
- The difference in strength between cyclic unidirectional and cyclic multi-directional is mainly caused by the cyclic loading history of the bars which undergo loading beyond yield and partial unloading when the wall is pushed to the different directions. In addition, the shear deformations are more significant in the multi-directional loading history than for the monotonic analyses (see Section 5.2.4.5 and hence they exacerbate shear lag effects which further increase the difference in strength between the different loading histories.

### 5.2.4.3 Yield curvature, yield displacement and effective stiffness

Yield curvature, yield displacement and effective stiffness ratios were derived from the numerical results of the monotonic analyses using the same procedures as for the cyclic analyses (see Section 5.2.3.2, 5.2.3.3 and 5.2.3.4). These numerical values are compared in Figures 5.53 and 5.55 to the experimentally derived quantities (for derivation see Chapter 4).

## 5.2. Shell element model

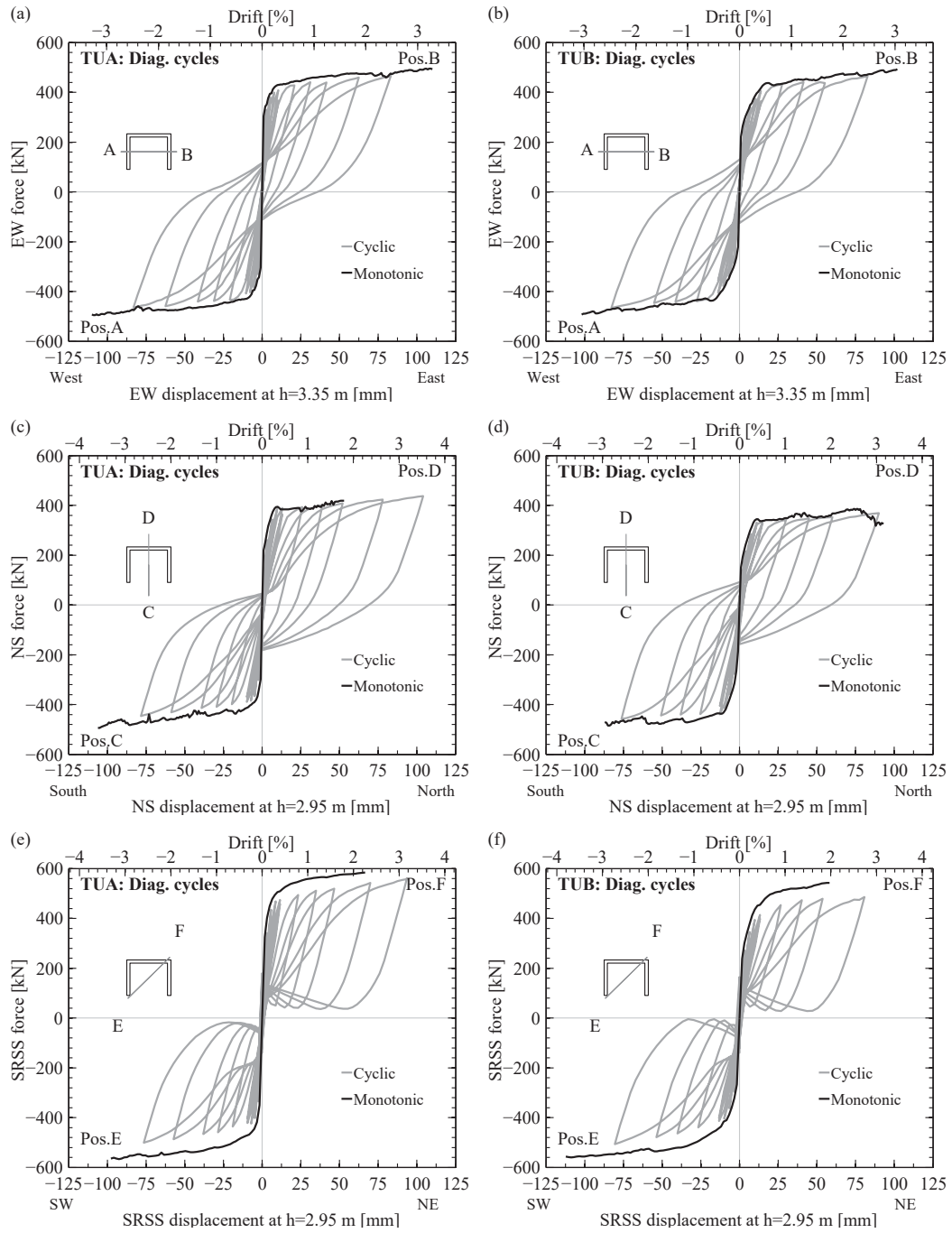


**Figure 5.48:** TUA and TUB: Comparison between the numerically obtained force-displacement hysteresses from VecTor4(VT4) under full-cyclic loading history (Cyclic) and monotonic loading (Monotonic)

Chapter 5. Validation of two numerical models for U-shaped walls

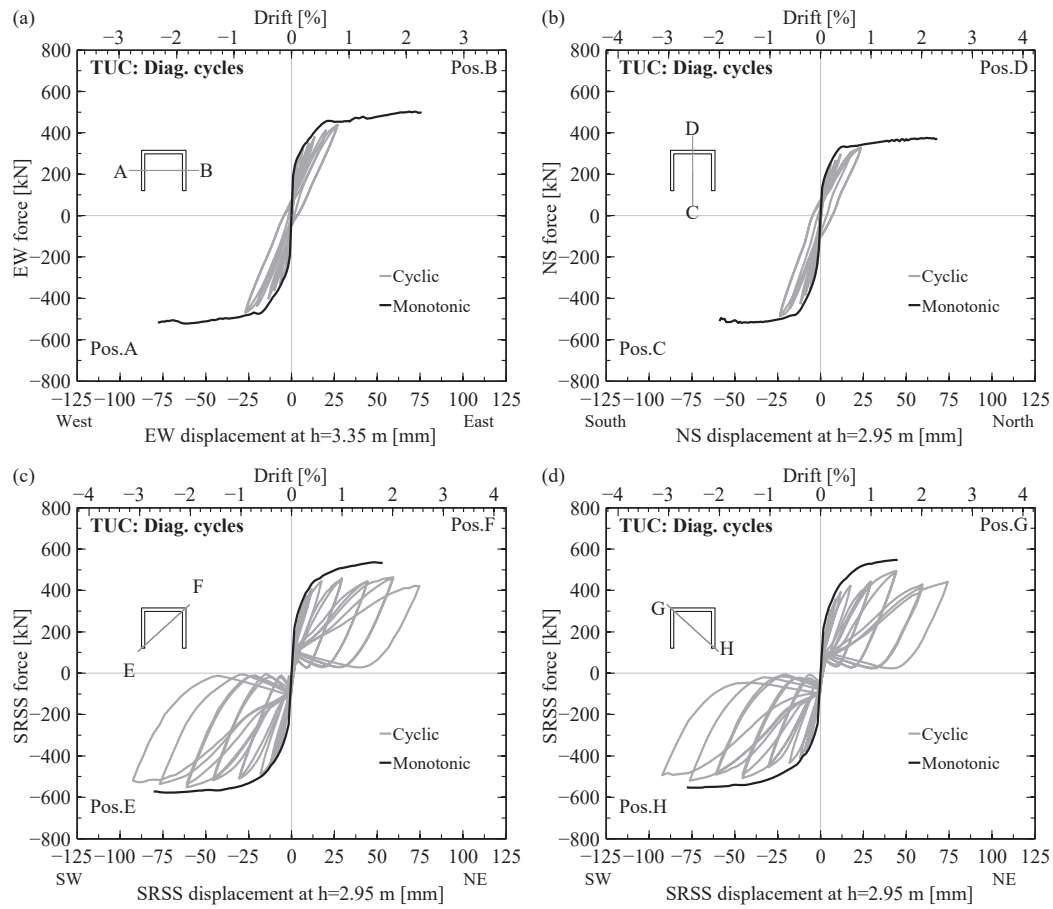


**Figure 5.49:** TUC: Comparison between the numerically obtained force-displacement hysteresses from VecTor4(VT4) under full-cyclic loading history (Cyclic) and monotonic loading (Monotonic)



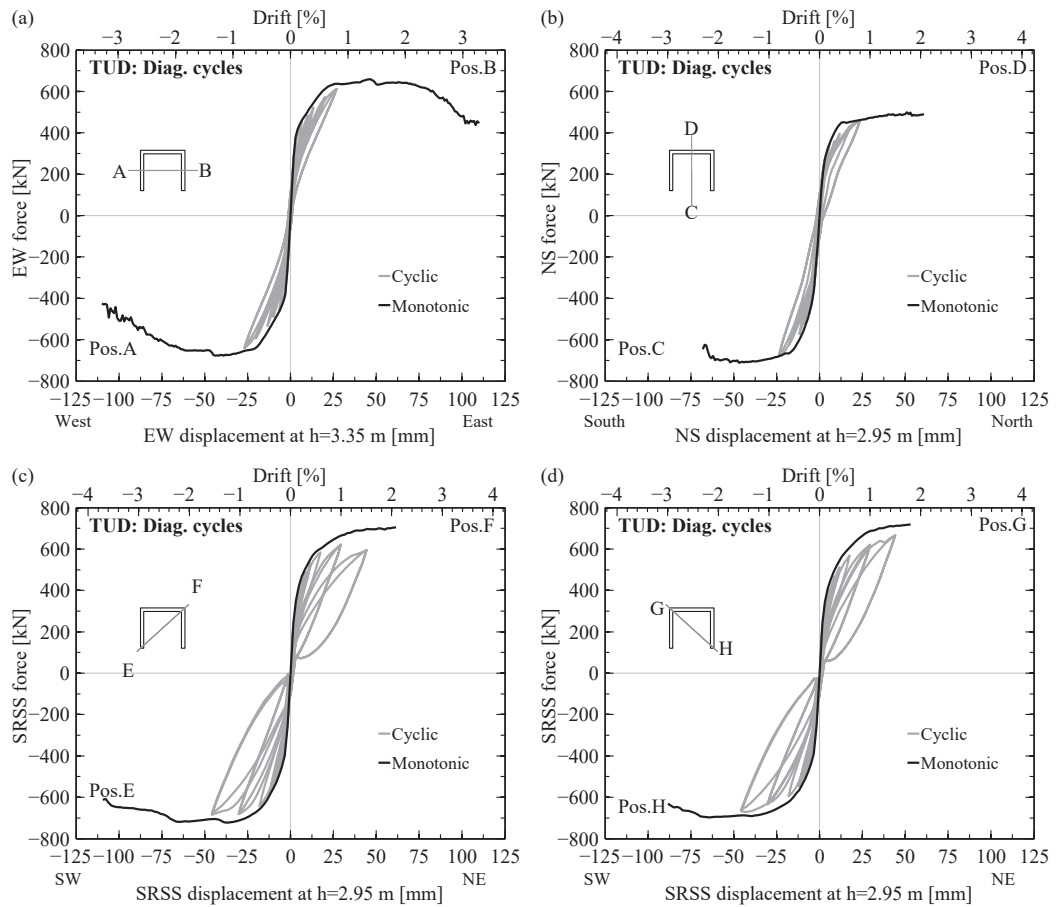


**Figure 5.50:** TUD: Comparison between the numerically obtained force-displacement hysteresses from VecTor4(VT4) under full-cyclic loading history (Cyclic) and monotonic loading (Monotonic)

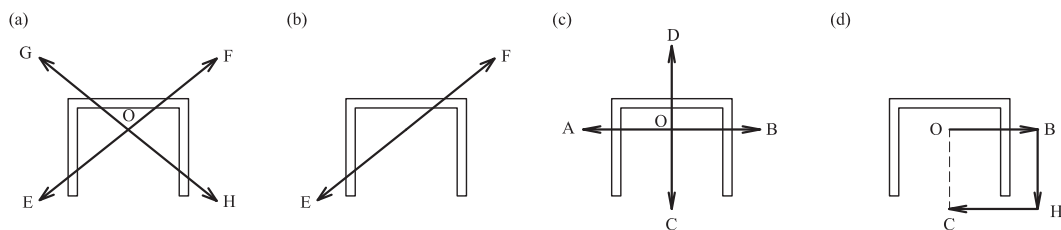


**Figure 5.51:** Loading patterns for U-shaped walls: (a) diagonal criss-cross as applied in the inelastic cycles of TUC and TUD, (b) diagonal uni-directional, (c) principal directions criss-cross and (d) principal direction with orthogonal pre-displacement

## Chapter 5. Validation of two numerical models for U-shaped walls

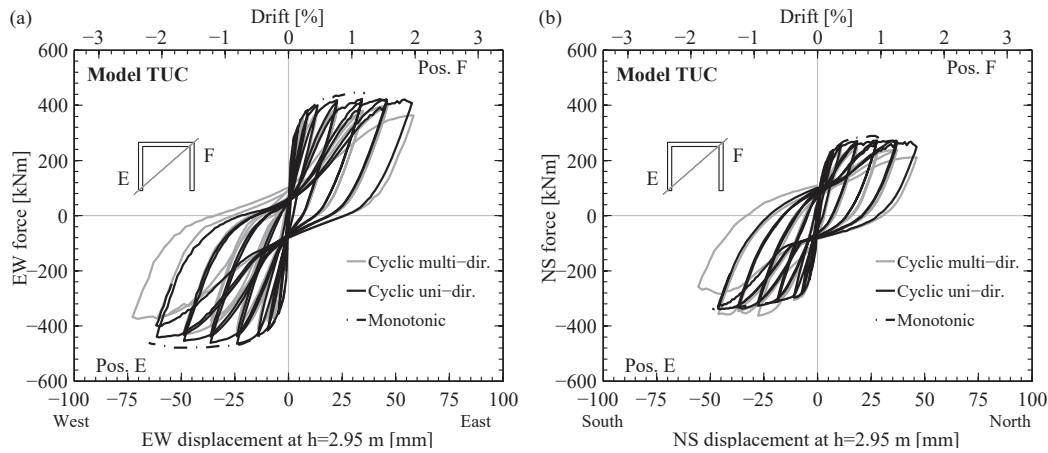


**Figure 5.52:** Shell element model for TUC: influence of the loading history on the force-displacement hysteresis

Grey markers are used for values that are obtained for the direction that is cycled first at a new drift level and white markers for directions that are cycled second, third or fourth (e.g., for TUA and TUB, loading to a new displacement ductility was first applied in the EW direction (parallel to the web), the second cycle was applied in NS direction (parallel to the flanges) and the third cycle in diagonal direction). The different plotting styles are used to separate between the effects of cyclic loading and the effects of multi-directional loading, which was found to significantly soften the wall when compared to a uni-directional cyclic loading (Figure 5.52).

The flexural response of the wall at yield, i.e., yield curvature  $\phi_y$  and flexural first yield displacement  $\Delta'_{y,f}$ , are captured by the monotonic analyses with the same precision as by the cyclic analyses, irrespective of the loading direction that was cycled first at a new drift level (Figure 5.53c-d). However, the first yield displacement  $\Delta'_y$ , composed of the flexural and the shear displacement at first yield ( $\Delta'_y = \Delta'_{y,f} + \Delta'_{y,s}$ ), is captured by the monotonic analyses with a lower precision than by the cyclic analyses ( $\sim -40/+40\%$ ). Since the flexural first yield displacement  $\Delta'_{y,f}$  is well captured (Figure 5.53e), the difference between the  $\Delta'_y$  values from cyclic and monotonic analyses must stem from the shear response of the wall at first yield  $\Delta'_{y,s}$ . Indeed, the shear displacements at first yield  $\Delta'_{y,s}$  are typically smaller for the monotonic analyses than for the cyclic analyses (Figure 5.54).

If the effects of the multi-directional loading are removed by considering only the loading positions from the first cycle at a new drift level (i.e., positions A and B for TUA and TUB, and positions E and F for TUC and TUD), the monotonic analyses predict the experimentally determined first yield displacement  $\Delta'_y$  with a similar precision as the cyclic analyses ( $\sim -15/+25\%$ ). The monotonic analyses predict the experimentally determined nominal yield displacement  $\Delta_y$  (Figure 5.53f) with an error of  $\sim -30/+20\%$ , which is also similar to the precision of the cyclic analyses results.

Since the shear displacements at first yield are mostly underestimated by the monotonic analyses, the effective stiffness  $K_{eff}$  is hence expected to be overestimated. Indeed,  $K_{eff}$  is predicted with similar precision by the monotonic and cyclic analyses for directions that are cycled first at the same displacement ductility level. For directions that are cycled second, third or fourth at a new drift level, the monotonic analyses overestimate  $K_{eff}$  by up to  $\sim 80\%$  (Figure 5.55b).

### 5.2.4.4 Plastic hinge length

The experimental curvature profiles are compared with curvature profiles obtained numerically from the monotonic analyses for different loading positions and displacement ductilities of TUB (Figure 5.56). The match is rather good although at positions C, D and F, the monotonic curvatures tend to concentrate at the wall base. As a result, for these positions the height over which inelastic curvatures concentrate tends to reduce especially for lower displacement ductilities (e.g., position D in Figure 5.57).

$L_{ph}$  predictions computed as half the height of the plastic zone  $L_{pz}$  from the monotonic analyses are compared to the experimentally determined  $L_{ph}$  values in order to assess the error when predicting  $L_{ph}$  values from the monotonic analyses. First,  $L_{ph}$  values averaged over the inelastic range are compared. The experimentally determined  $L_{ph}$  values at peak displacements of the cycles larger than displacement ductility  $\mu_{\Delta} = 2$  were averaged since these values showed a constant trend with the displacement. The numerically determined  $L_{ph}$  values were also averaged over same displacement interval. Figure 5.58a shows that the precision of predicting  $L_{ph}$  average from monotonic analyses is rather poor, as experimental values are underestimated by up to 60%.

Unlike the  $L_{ph}$  values determined from the experimental data and from the cyclic analyses, which follow a rather constant trend over the ductility range (Figure 5.41 and 5.42), the  $L_{ph}$  values from monotonic analyses tend to slightly increase with increasing top displacement for most loading positions. Hence, it seems more suitable to compare the  $L_{ph}$  value at ultimate displacement instead of an average over the ductility range. By doing so, the predictions of the  $L_{ph}$  using the monotonic analyses are now  $\sim 0 - 30\%$  lower than the experimental quantities (Figure 5.58b). Note that for this comparison, the numerical ultimate displacement was determined as the displacement corresponding to the instant when the base curvature reaches the ultimate curvature determined from section analysis.

### 5.2.4.5 Ratio of shear to flexural displacements under monotonic loading

To assess the influence of the loading history on the shear displacements, the numerically determined  $\Delta_s/\Delta_f$  ratios from cyclic and monotonic analyses are compared between each other. This comparison is preferred to comparing experimental ratios and ratios from monotonic analyses since differences are clearer and more detailed data is available.

Numerically determined shear to flexural displacement ratios  $\Delta_s/\Delta_f$  derived as in Section 5.2.3.6 were averaged for peak top displacements in the inelastic range ( $\mu_{\Delta} \geq 1$ ). For both cyclic and monotonic analyses the average  $\Delta_s/\Delta_f$  ratios were computed for the same top displacements.

## Chapter 5. Validation of two numerical models for U-shaped walls

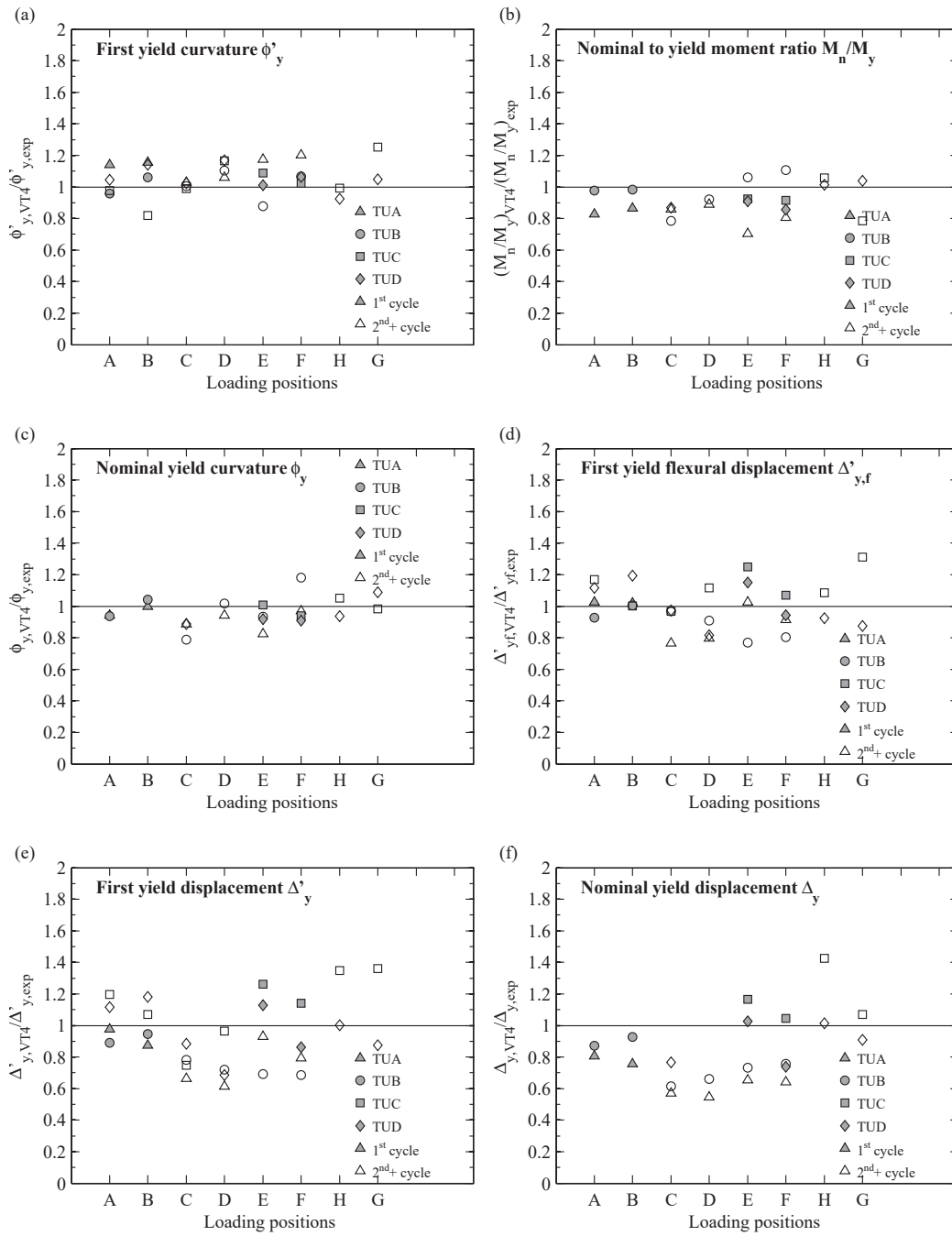


**Figure 5.53:** Comparison between the experimentally determined quantities and the VecTor4 derived quantities at yield from monotonic analyses: first yield curvature (a), nominal to yield moment ratio (b), nominal yield curvature(c), first yield flexural displacement(d), first yield displacement (e) and nominal yield displacement (f)

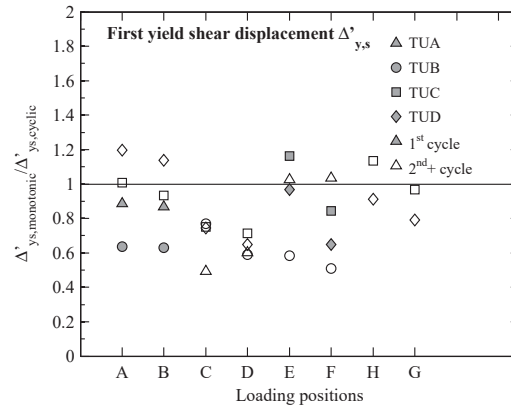


Figure 5.54: Numerical first yield shear displacements: comparison between results from monotonic and cyclic multi-directional analyses

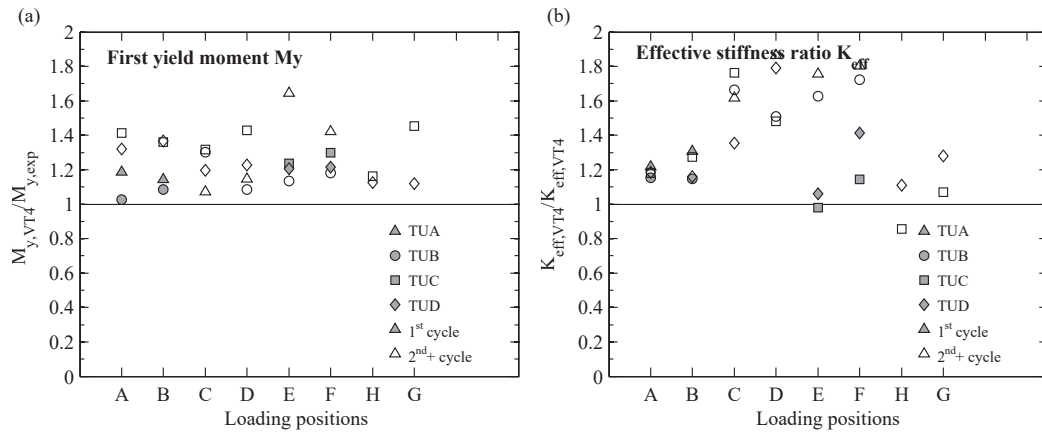
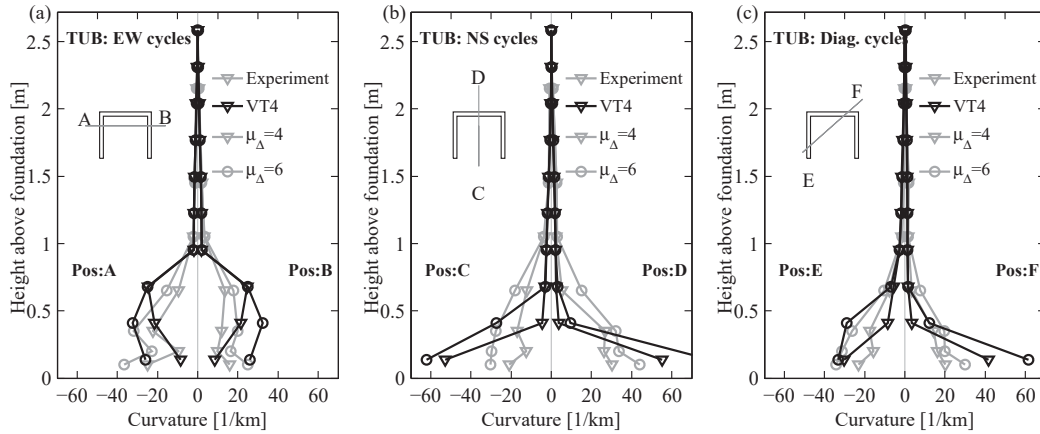
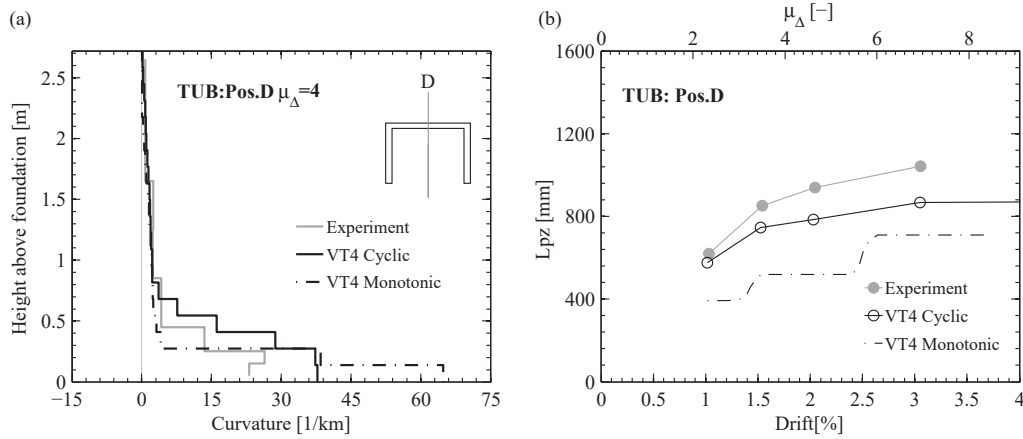


Figure 5.55: Comparison between the experimentally determined quantities and the VecTor4 derived quantities from monotonic analyses: first yield moment (a) and effective stiffness ratio(b)

## Chapter 5. Validation of two numerical models for U-shaped walls



**Figure 5.56:** TUB: comparison between the experimentally determined curvature profiles and the curvature profiles from the VecTor4 model at displacement ductilities  $\mu_{\Delta} = 4$  and 6.



**Figure 5.57:** TUB, loading position D (flange ends in tension, web in compression): (a) comparison between experimental, cyclic analyses and monotonic analyses in terms of curvature profiles in the inelastic range and (b) the height of the plastic zone  $L_{pz}$ .

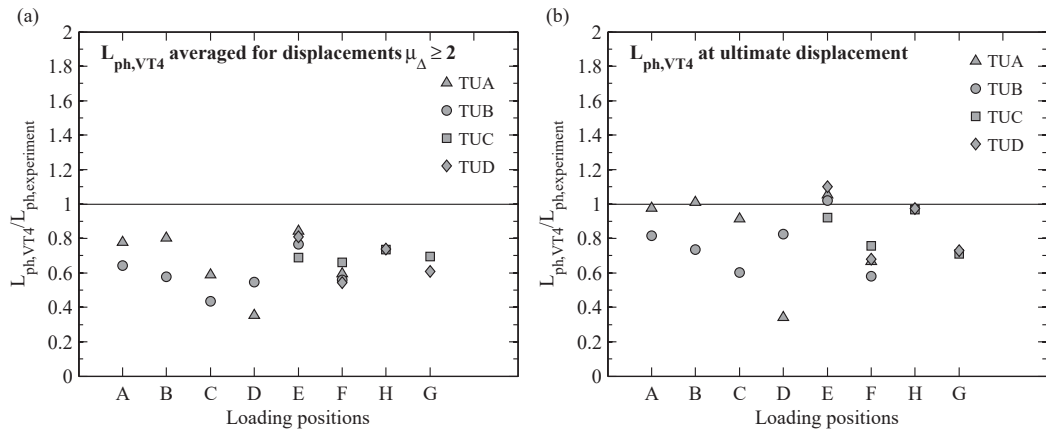


**Figure 5.58:** Plastic hinge length: comparison of the experimentally determined  $L_{ph,experiment}$  average value over the inelastic range (i.e., average of values at peak displacements for which  $\mu_{\delta} \geq 2$ ) with the numerically determined  $L_{ph,VT4}$  average value from the monotonic analyses results (a) and with the numerical  $L_{ph,VT4}$  value at ultimate displacement (b).

Figure 5.59 shows that the  $\Delta_s/\Delta_f$  ratios obtained from the monotonic analyses are up to by up to  $\sim 40\%$  lower than the ratios obtained from the cyclic analyses. The largest percentage differences are obtained for positions C and D (Figure 5.59a) but in absolute values the differences are actually small, i.e., below  $\sim 0.05$  (Figure 5.59b). The largest absolute differences are seen for the  $\Delta_s/\Delta_f$  ratio at positions F and G ( $\sim 0.1 - 0.15$ ). At these loading positions, larger crack widths in the unconfined concrete of the flange in tension and of the web are obtained from the cyclic analyses as compared to the monotonic ones (Figure 5.60). At positions E and H, the  $\Delta_s/\Delta_f$  ratios from monotonic loading are similar or even slightly higher than those from cyclic loading. This can be explained by the larger shear forces that are attained for monotonic loading (Figures 5.48, 5.49 and 5.50).

If the  $\Delta_s/\Delta_f$  ratio is considered as an indicator of the wall shear stiffness it can be concluded that cyclic loading reduces the shear stiffness of the wall. At the same top displacement, crack widths in the concrete from the cyclic analyses are larger than those from monotonic ones, thus shear transfer through aggregate interlock, is reduced and shear flexibility is increased.

## Chapter 5. Validation of two numerical models for U-shaped walls

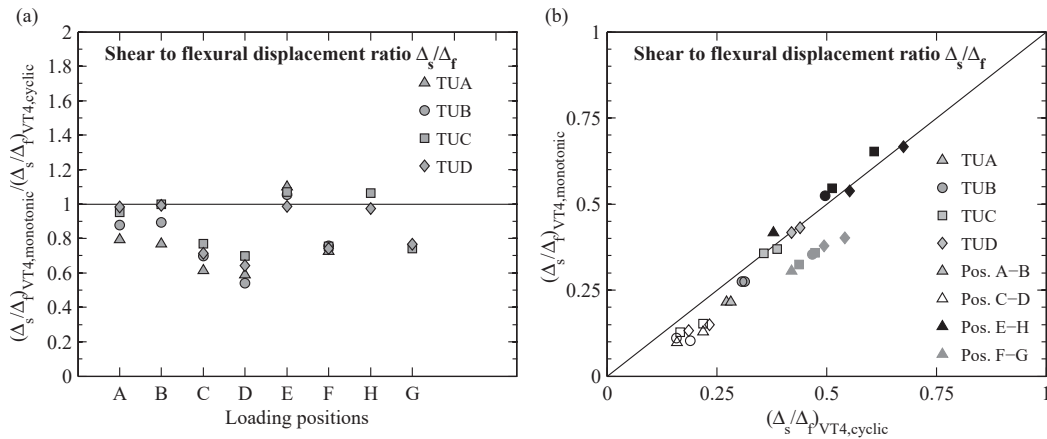


**Figure 5.59:** TUA to TUD: numerically determined shear to flexural displacement ratios  $\Delta_s/\Delta_f$  - comparison between cyclic and monotonic analysis results averaged for the same top displacements in the inelastic range: (a) comparison of percentage difference and (b) comparison of actual values.

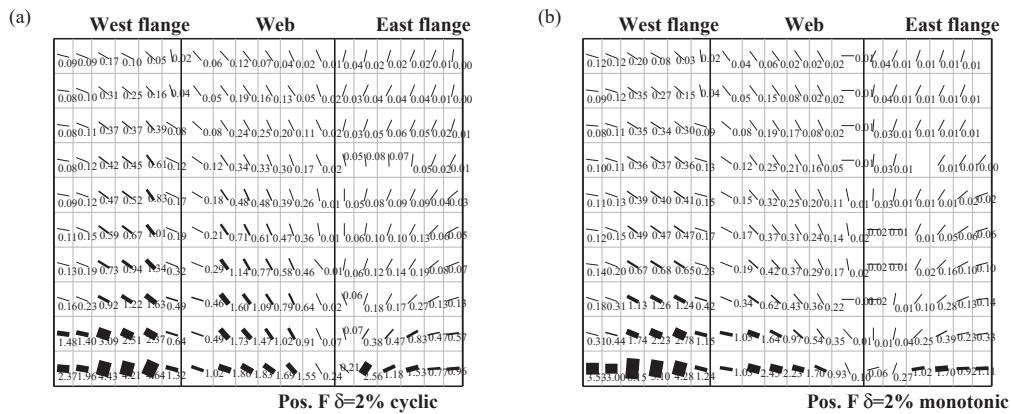


**Figure 5.60:** TUC: numerically determined cracks widths and orientation at 2% drift at position F (Web-East flange corner in compression) in the central concrete layer (layer 5 with its centre located at 6.25 cm from the outer face of the wall) and central integration point (GP 5): (a) from cyclic analyses (b) from monotonic analyses. 2D view of the U-shaped wall, unfolded from the inner side. The numbers given inside each element indicate the crack widths.



### 5.3 Conclusions

In this chapter two numerical models were compared to experimental data from quasi-static cyclic tests on four U-shaped walls (TUA, TUB, TUC and TUD). The two numerical models were: (1) a simple and widely used plane section analysis; and (2) a detailed shell element model. As the objective is to use these two numerical models for parametric studies to derive plastic hinge quantities for U-shaped walls, the results from both models were evaluated with respect to several quantities. The influence of the loading history on the results of the shell element model was also investigated in this section. This was done by comparing results from the cyclic analyses subjected to the full cyclic loading history, with cycles imposed in several directions successively at the same displacement level, as applied in the experiments, and results from monotonic analyses of the same models. The conclusions are summarised in the following.

**Wall strength** : The moment capacity was well captured for the principal loading directions by both section analysis and the shell element model. Only the shell element model was able to capture the experimentally determined wall strength reached under diagonal loading while monotonic section analysis lead to a significant overestimation of the wall strength for this direction. Section analysis predictions of the overall moment under diagonal loading were improved if the wall section was reduced to account for the effective flange width but predictions of strength components in the principal directions were not. Further discrepancies between monotonic plane section analyses and the experimentally attained moment originated in the experimentally applied loading history.

The maximum attainable wall strength was found to depend on the applied loading history. Monotonic analyses using the shell element model can be used to predict the wall strength under uni-directional cyclic loading. However, care should be taken when complex multi-directional loading histories are involved. For these cases, accounting for the cyclic loading history of the reinforcement bars and for shear lag effects is critical in predicting accurately the wall strength.

**Yield curvature  $\phi_y$**  : The section analysis and the shell model captured the yield curvature relatively well. Both models can therefore be used to derive  $\phi_y$  with an accuracy of  $\pm 20\%$ , irrespective of the applied loading history.

**Yield displacement  $\Delta_y$  and effective stiffness  $K_{eff}$**  : For these two quantities the shell element model resulted in fairly good estimates of the experimental results ( $\sim 20 - 30\%$  difference for  $\Delta_y$  and slightly higher for  $K_{eff}$ ). As both quantities are typically used in a conceptual design phase, these errors are acceptable.

While the flexural response at first yield (yield curvature  $\phi_y$  and first yield flexural displacement  $\Delta'_y$ ) was not influenced by the loading history, the shear response was. Under monotonic loading, shear deformations at first yield were typically lower than under cyclic loading leading to smaller yield displacements  $\Delta_y$  and higher effective stiffness  $K_{eff}$  than in the cyclic analyses. However, if only the direction that was cycled first at a new displacement level is considered (i.e., a loading history equivalent to a uni-directional cyclic loading), the softening effect of the full loading history is filtered-out and results from monotonic analyses lead to predictions of  $\Delta_y$  and  $K_{eff}$  as good as those from the analyses with the full loading history.

## Chapter 5. Validation of two numerical models for U-shaped walls

---

**Plastic hinge length  $L_{ph}$**  : The  $L_{ph}$  values were slightly underestimated by the model by up to 30%. The  $L_{ph}$  values determined from the monotonic analyses were typically smaller than those from cyclic analysis due to numerical concentration of curvatures at the wall base in the monotonic analyses. Despite this discrepancy, if the  $L_{ph}$  value at ultimate displacement is considered, the match with the experimental  $L_{ph}$  values improves and the error is similar to the one from the cyclic analyses. Hence,  $L_{ph}$  values derived from the numerical analyses can be used to predict a slightly conservative value of the experimental  $L_{ph}$  values, which is suitable for design purposes. Moreover, irrespective of this underestimation, a parametric study using monotonic analyses is still expected to provide indications on the main quantities influencing the  $L_{ph}$  values specific to U-shaped walls.

**Ratio of shear to flexural displacements  $\Delta_s/\Delta_f$**  : The shell element model predicted very well the  $\Delta_s/\Delta_f$  ratios of all test units in the inelastic range, including the negative ratio of one of the flanges under diagonal loading.  $\Delta_s/\Delta_f$  ratios derived from the monotonic analyses were found to be lower than those derived from cyclic analyses, indicating a lower shear stiffness of the wall under the full cyclic loading than under monotonic loading which contributes to the observed softening response of the wall under the full cyclic loading.

Having evaluated the discrepancies between the numerical and experimental results, as well as the influence of the loading history it is concluded that the two numerical models that were investigated here can be used under monotonic loading for parametric studies for U-shaped walls. Section analysis will be used to derive yield curvature estimates while the shell element model will be used to derive estimates for the yield displacement, the effective stiffness and the plastic hinge lengths with the precision as discussed above (Chapter 6). These values, to be obtained from the monotonic analyses, were shown to be representative for a reversed cyclic loading applied in only one direction of the wall section. Such a loading history seems more reasonable for design purposes than the loading history applied in the experiments used for the validation of the models, where loading was applied in several different directions successively, leading to considerable softening of the wall and reduction of the wall strength.

# 6. Yield and ultimate displacement of U-shaped walls

## 6.1 Introduction

The objective of this section is to derive several quantities that characterise the displacement response of U-shaped RC walls under seismic loading. More specifically, yield curvature, yield displacement, effective stiffness ratio and plastic hinge lengths are investigated for U-shaped cantilever walls subjected to horizontal displacements in different directions. To this purpose, a parametric study is conducted by means of the two numerical models that have been validated in Chapter 5, i.e., a plane section analysis model and a shell element model.

Existing estimates for the yield curvature  $\phi_y$  of U-shaped wall sections are compared against the analyses results and new values that account also for the angle of the loading direction are proposed. The new analytical expression of the yield displacement  $\Delta_{y,2L}$ , accounting for the extent of cracking over the wall height, presented in Section 4.4 is validated against the analyses results of the shell element model. The effective stiffness  $K_{eff}$  derived with the new yield displacement expression is compared with the numerical results and modifications are proposed to the existing effective stiffness estimates, which account for the cracked height. Finally, plastic hinge lengths are derived from the results of the shell element model, compared to existing estimates and new equations that consider also the average shear stress ratio are proposed.

## 6.2 Design of the parametric study

This section describes the wall geometries chosen for the parametric study as well as their design. The main parameters that are varied within the study are discussed and the numerical models used for the analyses are briefly presented.

### 6.2.1 Design of the U-shaped RC walls

#### 6.2.1.1 General design considerations and parameters of the study

Typically, RC core walls are used as the main lateral force resisting structural elements in mid-to-high-rise buildings. Therefore, the U-shaped walls designed for this study are representative for this type of buildings. Since buildings with RC core walls are very popular in the seismic areas in the U.S., the American Standard ACI318-11 [ACI11] provides some design indications and requirements that specifically address RC core walls. For this reason the design of the walls in this study follows the American Standard ACI318-11 design code considering the typical mid-to-high-rise RC core wall dimensions and reinforcement detailing encountered in the U.S. design practice [MG<sup>+</sup>12], [SML03], [SM08], [LL<sup>+</sup>13], [Bru09] and [Fie15] - email communication.

Three wall sections with different web to flange length ratios  $l_{web}/l_{fl}$  were considered for the design. The variation of the  $l_{web}/l_{fl}$  ratio was achieved through variation of the web length. These three wall sections were designed with the longitudinal reinforcement uniformly distributed along the section. Another set of three walls with the same overall dimensions as the first three was detailed with the longitudinal reinforcement concentrated in the confined boundary elements. All six wall sections had the same total longitudinal reinforcement ratio of  $\sim \rho_{tot} = 0.95\%$ . The obtained wall sections are shown in Figure 6.2.

For each of the six wall sections, the wall shear span  $H$  was varied by changing the number of stories: 10, 15 and 20 stories. The storey height was taken as  $h_{storey} = 3.3$  m. Based on a linear lateral static force distribution compatible with the first eigen mode, the resulting shear span was approximately equal to  $0.7H_{wall}$ . These shear spans led to values of shear span to web length ratios of  $H/l_{web} = 2.56$  to  $10.26$ , hence rather slender walls. The wall thickness was the same for all models and was equal to  $t_{wall} = 450$  mm. The values of the varying parameters of the wall models are summarised in the following.

- web to flange length ratio  $l_{web}/l_{fl}$ : 1.25, 1.875 and 2.5 by varying the web length  $l_{web}$  from 4.5 m to 9.0 m
- axial load ratio  $n = N/(f_c A_g)$ : 0.02, 0.06 and 0.10
- shear span  $H$ : 23.10 m, 34.65 m and 46.20 m which represent walls with a number of stories  $N_{stories}$  equal to: 10, 15 and 20 stories
- vertical reinforcement layout: vertical reinforcement uniformly distributed over the section or mainly concentrated at the wall boundary elements

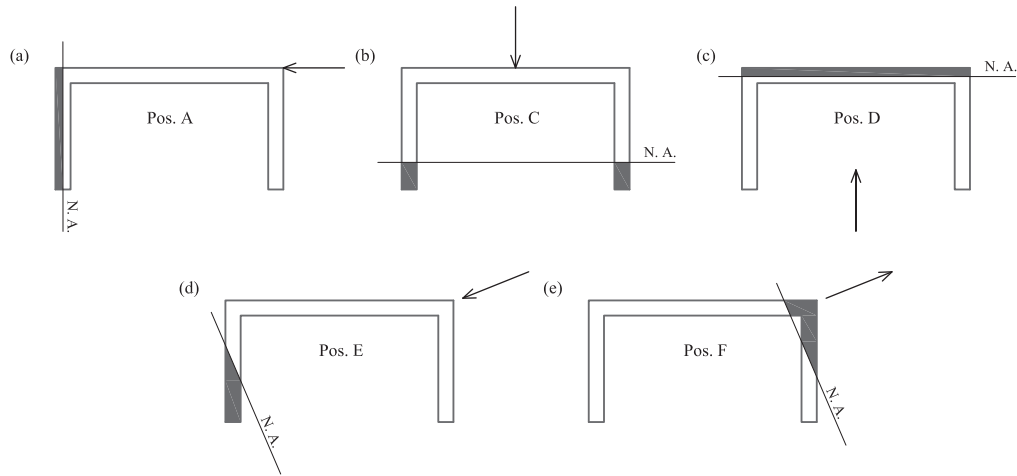


**Figure 6.1:** Loading directions considered for the design. Bending along the web direction: position A (a); bending along the flange direction with the flange ends in compression: position C (b); bending along the flanges direction with the web in compression: position D (c) and bending along the geometric wall diagonal with the flange end in compression: position E (d) or with the corner web-flange in compression: position F (e).

The wall flexural capacity was computed from section analyses for five loading cases (Figure 6.1): bending in the web direction (position A), bending in the flange direction with the flange ends in compression (position C), bending in the flanges direction with the web in compression (position D) and bending in the direction of the geometric wall diagonal with the flange end in compression (position E) or with the corner web-flange in compression (position F). According to ACI318-11 (21.9.5.2), the wall section considered for the flexural strength calculation should be reduced to account for the effective flange width, which extends “from the face of the web a distance equal to the smaller of one-half the distance to an adjacent wall web and 25 percent of the total wall height”. For all the wall sections analysed here, this results in having the effective flange width equal to the entire length of the flange or of the web, depending on the loading direction.

The expected values of the material properties were used for both concrete and reinforcement [AAS09] and they are summarised in Table 6.1. The higher mode effects, which can amplify the wall shear demand, were taken into account in a simplified manner through the dynamic amplification factor  $\omega$  as recommended by [SEA08]. For buildings with more than six stories [SEA08] suggests a value of  $\omega$  given by Equation 6.1, which is based on research by [PP93]. In this equation,  $N_{stories}$  is the number of stories and need not be taken larger than 15. Therefore for more than 15 stories,  $\omega = 1.8$ .

$$\omega = 1.3 + \frac{N_{stories}}{30} \quad (6.1)$$

## Chapter 6. Yield and ultimate displacement of U-shaped walls

**Table 6.1:** Expected material properties used for the wall models in the parametric study

Reinforcement					Concrete		
Bar diam.	$f_y$	$f_u$	$E_s$	$\epsilon_{su}$	$f_c$	$E_c$	$\epsilon_c$
[mm]	[MPa]	[Mpa]	[GPa]	[%]	[MPa]	[MPa]	[%]
14-30	470	625	200	100	45	31.6	2.00

The shear reinforcement was computed for the following determining load cases: shear reinforcement in the web was determined from bending in the direction of the web while the one in the flanges was determined under bending along the diagonal direction with one flange end in compression. At this loading position the shear demand on the flange is the largest as the majority of the shear force in the direction of the flanges is taken by the flange in compression ([RF01], [BDP08b] and Section 3.3.1).

The wall satisfies the shear stress limit imposed by ACI318-11 [ACI11] (21.9.4.4) for the vertical wall segments, i.e., web or flange: the shear strength shall be lower than  $0.83A_{cv}\sqrt{f_c}$  for any individual vertical wall segment or lower than  $0.66A_{cv}\sqrt{f_c}$  for all vertical wall segments resisting a common force.

### 6.2.1.2 Design procedure steps

This section outlines the step by step procedure that was followed when designing the U-shaped walls that were analysed within the parametric study. The wall section dimensions and vertical reinforcement content were initially assumed based on typical values and detailing encountered in U.S. seismic design practice.

1. Perform section analysis of the wall section to determine the moment capacity for each loading position and compute the corresponding shear force demand  $V_{nec}$  for each shear span.
2. Multiply the shear force demand with the dynamic amplification factor to account for the higher mode effects:  $V_{nec}^* = V_{nec}\omega$
3. Dimension shear reinforcement of the web for the largest shear demand  $V_{nec}^*$  in the direction of the web, of the five analysed loading positions. Do the same for the flanges. The necessary shear reinforcement content is back-calculated from Equation 6.2 which defines the shear strength of special structural walls according to ACI318-11 (21.9.4.1.), and where  $A_{cv}$  is the gross area of the flanges or of the web,  $\alpha_c$  is a coefficient accounting for the slenderness of the of the wall (equal 0.17 for  $H/l_{wall} \geq 2.0$ ),  $f_c$  is the concrete compressive strength,  $f_y$  is the yield strength of the shear reinforcement and  $\rho_h$  is the shear reinforcement content.

$$V_{nec}^* = A_{cv}(\alpha_c\sqrt{f_c} + \rho_h f_y) \quad (6.2)$$

4. Compute the shear force capacity  $V_{design}$  for the web and for the flanges obtained with Equation 6.2 for the proposed shear reinforcement contents.

5. Check if:

- $V_{design,flanges} \leq 0.66A_{cv}\sqrt{f_c}$  when both flanges are resisting a common lateral force (position C) and where  $A_{cv}$  is the gross area of both flanges;
- $V_{design,flange} \leq 0.83A_{cw}\sqrt{f_c}$  when only one flange resists the entire shear force in the direction of the flanges (position E) and where  $A_{cw}$  is the gross area of one flange;
- $V_{design,web} \leq 0.83A_{cw}\sqrt{f_c}$  (position A) where  $A_{cw}$  is the gross area of the web;

If these conditions are not met, increase the wall thickness and restart design procedure from 1, else end design procedure.

### 6.2.1.3 Confinement lengths

ACI318-11 suggests the use of plane section analysis to determine the compression depths  $c$  on the wall section. Since the application of plane section analysis is questionable (see Section 3.3.3.2), these depths were determined from the shell element model.

The compression depths  $c$  on the flange ends were determined from loading in the diagonal direction with one flange in compression. At the corner into the web and into the flange these depth were determined from loading with the corner in compression (position F). The minimum confinement lengths were taken as the largest of  $c - 0.1l_{wall}$  and  $c/2$  [ACI11] 21.9.6.4.

ACI318-11 (21.9.6.4) requires that the confined boundary elements include the effective flange width in compression. For the wall sections analysed here, this would mean that the entire wall section needs to be confined since the effective flange width is approximately equal to the length of the web or of the flanges. While indeed the shell element model results indicated that almost the entire flange requires confinement when the axial load is the largest, confining also the entire web seems overly conservative and based on the shell element model results not necessary. The resulting confinement is shown for all the wall sections in Figure 6.2. The same confinement reinforcement percentage was used for all wall sections.

## 6.2.2 Numerical models

### 6.2.2.1 Plane section analysis

A fibre section model was set-up for section analyses using the Opensees software [MMG09] and validated against experimental data in Section 5.1. The same model is adapted for the walls in the parametric study herein and used to derive values of the nominal yield curvature  $\phi_y$ . The mesh for the wall sections with the largest web length, with both concentrated and distributed vertical reinforcement layout, is shown in Figure 6.3. As in the validation models, loading is applied in displacement control by imposing curvature increments in the direction of the web, in the direction of the flange or in the direction of the geometric diagonal of the walls. The axial load was applied at the gravity centre of the section.

## Chapter 6. Yield and ultimate displacement of U-shaped walls

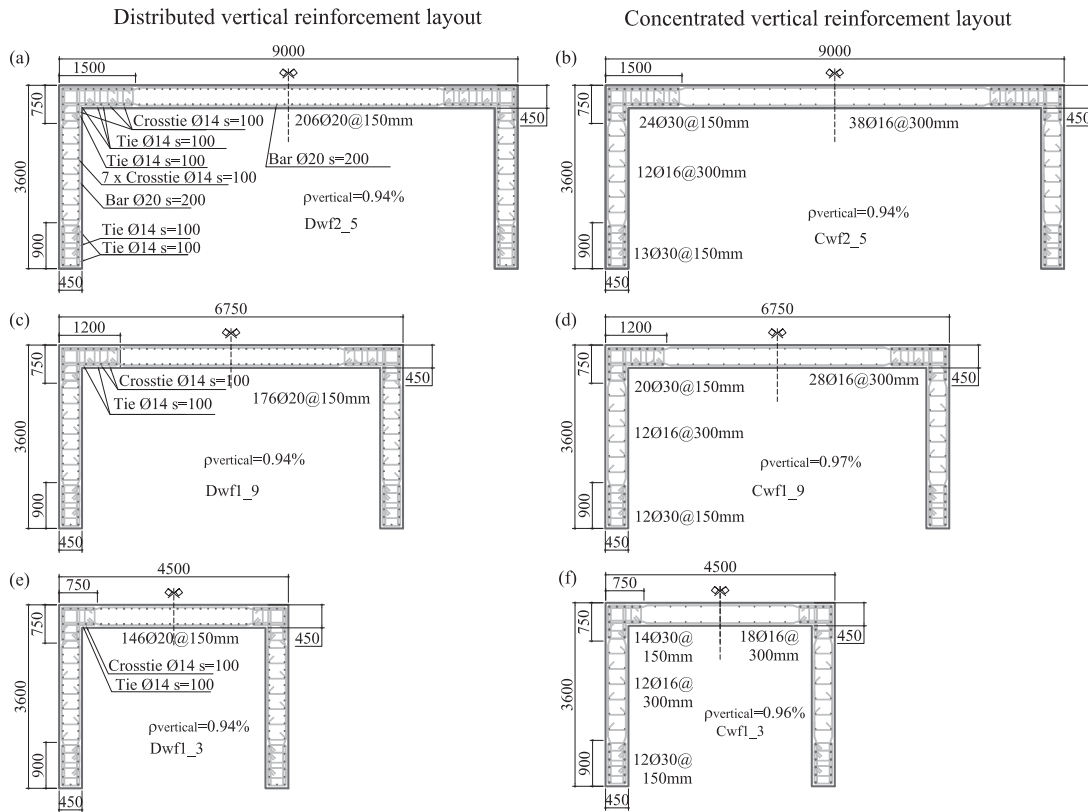


**Figure 6.2:** Cross-sections of the U-shaped walls designed to be analysed in the parametric study. All dimensions are in mm.

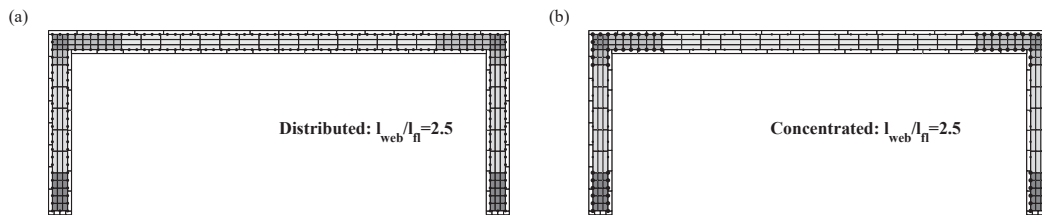


**Figure 6.3:** Openses fibre models of the U-shaped wall sections with  $l_{web}/l_{fl}=2.5$ : Dwfl2.5 (distributed reinforcement layout) (a) and Cwfl2.5 (concentrated reinforcement layout) (b)



### 6.2.2.2 Shell element model

A shell element model using VecTor4 (VT4) software [PV93], [Hry13] was validated against experimental data from U-shaped wall tests in Chapter 5. The validated model was then adapted to match the geometry and properties of the U-shaped walls that are analysed within this parametric study.

The walls were analysed as cantilever walls subjected to a horizontal displacement at their top. The walls were modelled up to the height of the shear span, which was taken equal for both principal loading directions, i.e., horizontal displacement was applied in the direction of the flanges and of the web at the same height  $H$  (Figure 6.4). The axial load was equally distributed over the height of the wall and applied at each storey height. At each storey, the axial loads were applied at four nodes of the wall section so that the resultant force acted at the gravity centre of the section.

The first three stories of the wall were modelled using a refined mesh in order to have a detailed representation of strains and curvatures over the zone where plastic deformations are expected. Above the first three stories the mesh size is increased as shown in Figure 6.4. Due to limitations on the maximum number of elements, the wall models corresponding to  $N_{stories} = 20$  and web to flange length ratios  $l_{web}/l_{fl} = 1.875$  and  $2.5$  had a refined mesh over the first two stories only. Only the walls with one reinforcement layout (distributed) were considered for the shell element model resulting in 135 analyses. All the principal loading directions were considered for the analyses, and in addition, analyses for loading along the wall geometric diagonal (position E and F) were performed. The reasons for this choice are two-fold: (1) loading along the geometric diagonal instead of a fixed skew angle, like for example  $45^\circ$ , captures also the influence of the bending angle (Figure 6.8), since the angle of bending of the geometric diagonal changes with  $l_{web}/l_{fl}$  and (2) loading along the diagonal directions leads to the lowest ultimate curvature of all loading positions, since the wall length is the longest, and hence possibly also to the lowest displacement capacity.

## 6.3 Yield curvature

The yield curvature  $\phi_y$  is an important design quantity marking the border between the “elastic” and the “plastic” branches of the bi-linear idealisation of the moment-curvature response. In this section, the yield curvature  $\phi_y$  is evaluated from both plane section and shell element model analyses. Results are compared with existing estimates and new parameters influencing the value of the yield curvature are identified. Finally, new estimates for yield curvatures when loading the U-shaped wall section under any bending angle  $\alpha$  are proposed in Section 6.3.3.

## Chapter 6. Yield and ultimate displacement of U-shaped walls

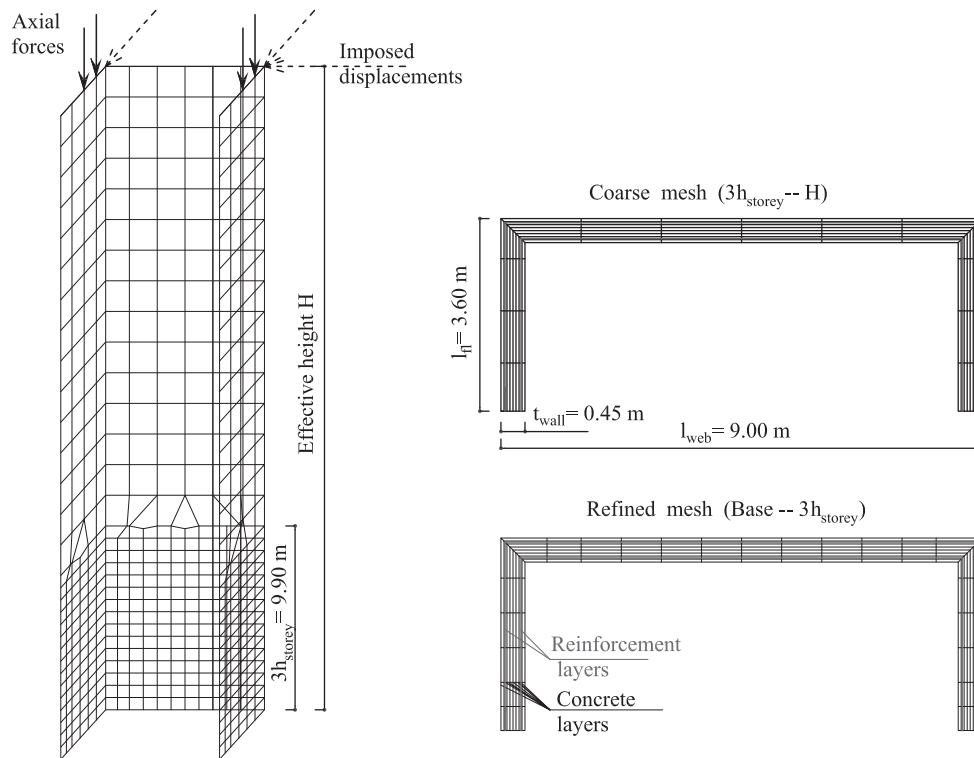


**Figure 6.4:** VecTor4 model in elevation and sections for the  $D_{wf}2.5$  wall configuration (i.e., distributed reinforcement and web to flange length ratio  $l_{\text{web}}/l_{\text{fl}}=2.5$ ) with  $N_{\text{stories}}=15$

### 6.3.1 Results from plane section analysis

The yield curvature was computed as in Equation 6.3. The first yield curvature  $\phi'_y$  from section analysis corresponds to the curvature at the instant when the most tensioned reinforcement fibre exceeds its yield strain  $\varepsilon_{sy}$  or the strain in the most compressed concrete fibre exceeds  $\varepsilon_{cy} = -0.002$  whichever occurs first. In an analogous manner, the nominal point is reached when the reinforcement tensile strain first attains 0.015 or a concrete compressive strain attains 0.004 whichever occurs first [PCK07].

$$\phi_y = \phi'_y \frac{M_n}{M_y} \quad (6.3)$$

For a more meaningful evaluation of the results, the dimensionless yield curvature  $K_y$  will be used in this section, defined as in Equation 6.4, where  $\phi_y$  is the nominal yield curvature,  $\varepsilon_{sy}$  is the yield strain of the most tensioned reinforcement bar and  $l_{wall}$  is the wall length in the direction of loading. The dimensionless yield curvatures  $K_y$  are obtained using a wall length equal to the length of the web  $l_{web}$  for bending in the web direction (Position A) and to the length of the flanges  $l_{fl}$  for bending in the flange direction (Position C and D). For loading in directions other than the principal directions, the wall length is taken as the distance perpendicular to the neutral axis, between the most tensioned and the most compressed fibre. This means that for loading along the diagonal of the wall, the wall length is equal to the geometric diagonal, i.e.,  $l_{diag} = \sqrt{l_{web}^2 + l_{fl}^2}$ .

Except for the principal loading directions, the other bending directions investigated were: (1) bending along the geometric diagonal of the section with one flange end in compression (Position E) or with the corner web-flange in compression (Position F) as well as (2) loading at a 45 ° angle with respect to the principal loading directions, with one flange end in compression (Position E45) or with the corner web-flange in compression (Position F45). For clarity, the loading positions are shown in Figure 6.5a.

$$K_y = \phi_y \frac{l_{wall}}{\varepsilon_{sy}} \quad (6.4)$$

The results for the dimensionless yield curvatures  $K_y$  are shown for different loading positions of the U-shaped wall section in Figures 6.5 and 6.6. Figure 6.5 shows the variation of  $K_y$  with the axial load ratio. For the practical values of axial load ratio (i.e., 0.02 to 0.10), the dimensionless yield curvatures remain rather constant.

The influence of the web to flange ratio  $l_{web}/l_{fl}$  is also not very significant (Figure 6.6), except at Positions E and F (Figure 6.6e, f) where  $K_y$  increases with increasing  $l_{web}/l_{fl}$ . Unlike for the positions E45 and F45 where the bending angle remains constant irrespective of  $l_{web}/l_{fl}$ , at positions E and F the bending angle varies since loading is done along the geometrical diagonal which also changes with  $l_{web}/l_{fl}$ . Therefore  $K_y$  varies significantly with the bending angle, illustrated as angle  $\alpha$  in Figure 6.8.

## Chapter 6. Yield and ultimate displacement of U-shaped walls

---

As expected, distributed reinforcement layouts lead to larger dimensionless yield curvatures  $K_y$  than concentrated reinforcement layouts due to increased compression depths at yield. Values of  $K_y$  for walls with distributed reinforcement layout are  $\sim 2 - 10\%$  larger than for the concentrated layout case depending on the loading position. The difference in yield curvatures for distributed and concentrated reinforcement layouts are similar to those reported for T-shaped walls [SS<sup>+</sup>13] and somewhat smaller than those reported for planar walls [PCK07].

### 6.3.2 Comparison with existing estimates

After having established the main trends of the dimensionless yield curvature  $K_y$  with the varied parameters,  $K_y$  values obtained from section analyses are compared with existing estimates in this section. As already discussed in Section 2.2.2,  $K_y$  estimates have not been specifically derived for U-shaped walls but values from other flanged wall sections can be adapted to U-shaped walls. For convenience, these adaptations are briefly enumerated below:

- Curvature applied parallel to the web of the U-section (Position A) - consider values from I-shaped walls loaded parallel to their web ([Pau02], [PCK07])
- Curvature applied parallel to the flanges of the U-section with the flange ends in compression and the web in tension (Position C) - consider values from I-shaped walls loaded perpendicular to the web of the I-section [Pau02], [PCK07] or T-shaped walls loaded with the flange of the T-section in tension and the web toe in compression [SS<sup>+</sup>13]
- Curvature applied parallel to the flanges of the U-section with the flange ends in tension and web in compression (Position D) - consider values from T-shaped walls loaded with flange of the T-section in compression and the web toe in tension [SS<sup>+</sup>13], [Pau02] and [PCK07]

The  $K_y$  values are shown in Figure 6.7 for the principal loading directions, together with their corresponding estimates, for both the distributed and the concentrated reinforcement layout. For all the principal loading positions, existing estimates for  $K_y$  values match rather well the section analysis results. At position A, the estimates by [PCK07] seem to be provide a match with numerical results than those by [Pau02] (Figure 6.7a, b). For positions C and D, estimates by [SS<sup>+</sup>13] result in a slightly better overall match than the other estimates while also accounting for the small variation due to the web to flange length ratio  $l_{web}/l_{fl}$  (Figure 6.7c, f). In conclusion, the dimensionless yield curvature for the principal loading direction of the U-shaped walls can be determined with sufficient accuracy using existing estimates adapted from other types of flanged walls. This finding is in line with previous observations from Section 4.3 as well as by [BDP08b].

As already mentioned, no estimates are currently available for other loading directions than the principal ones. This issue is addressed in the following section.

### 6.3. Yield curvature

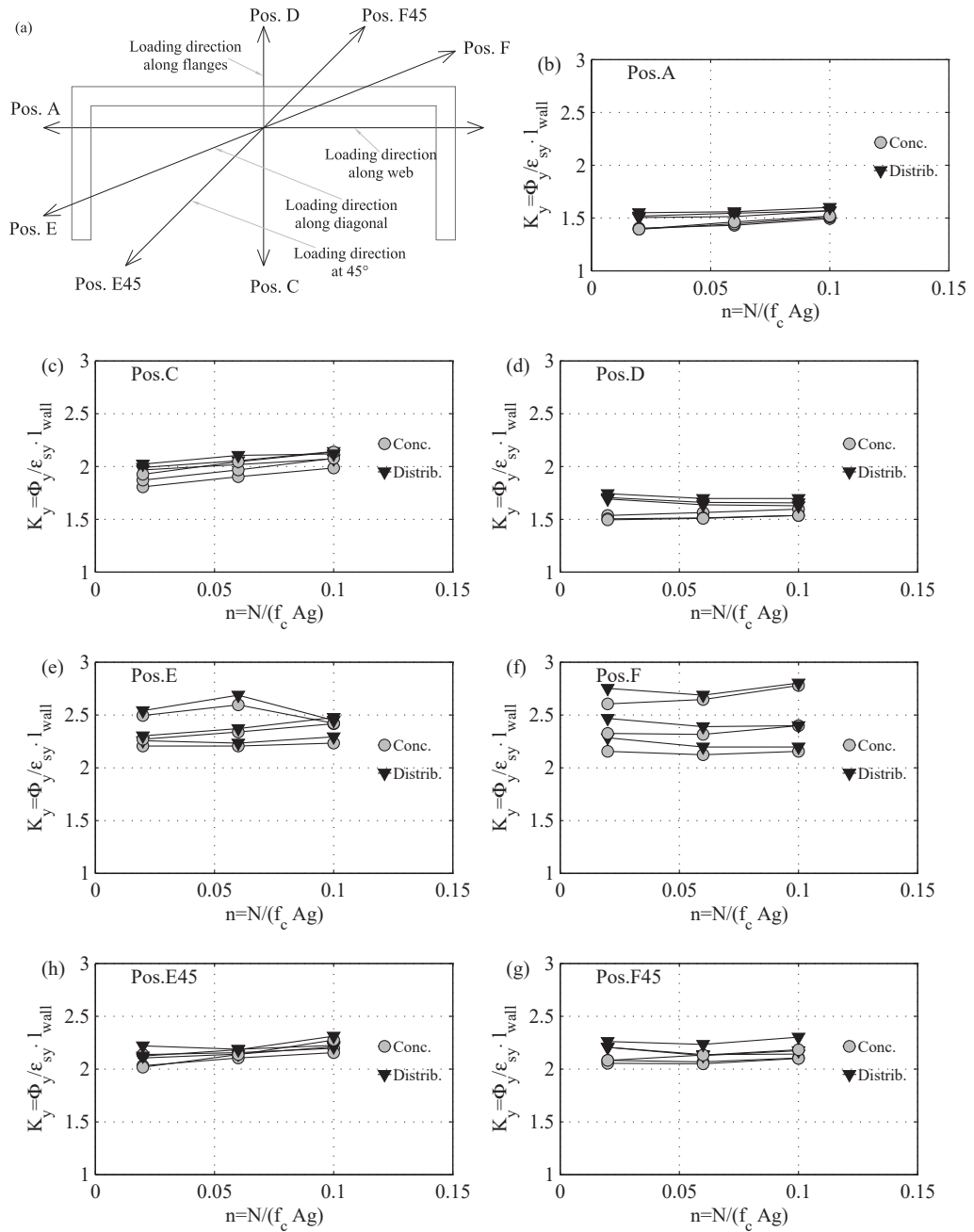


**Figure 6.5:** Dimensionless yield curvature  $K_y$  from plane section analyses: influence of the axial load ratio. Loading directions (a) and  $K_y$  results for the different loading positions (c-f)

## Chapter 6. Yield and ultimate displacement of U-shaped walls

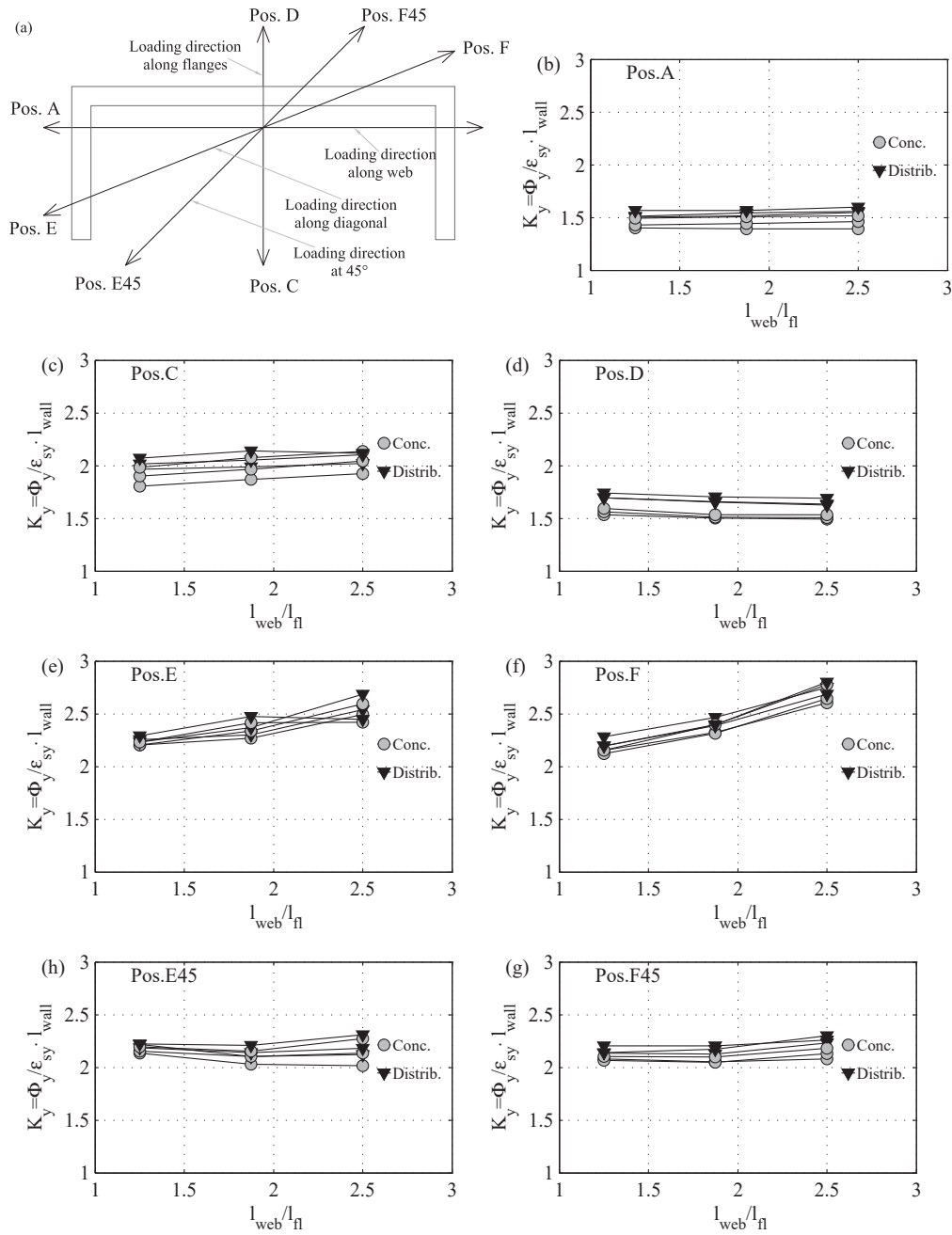


**Figure 6.6:** Dimensionless yield curvature  $K_y$  from plane section analyses: influence of the web to flange ratio. Loading directions (a) and  $K_y$  results for the different loading positions (c-f)

### 6.3. Yield curvature

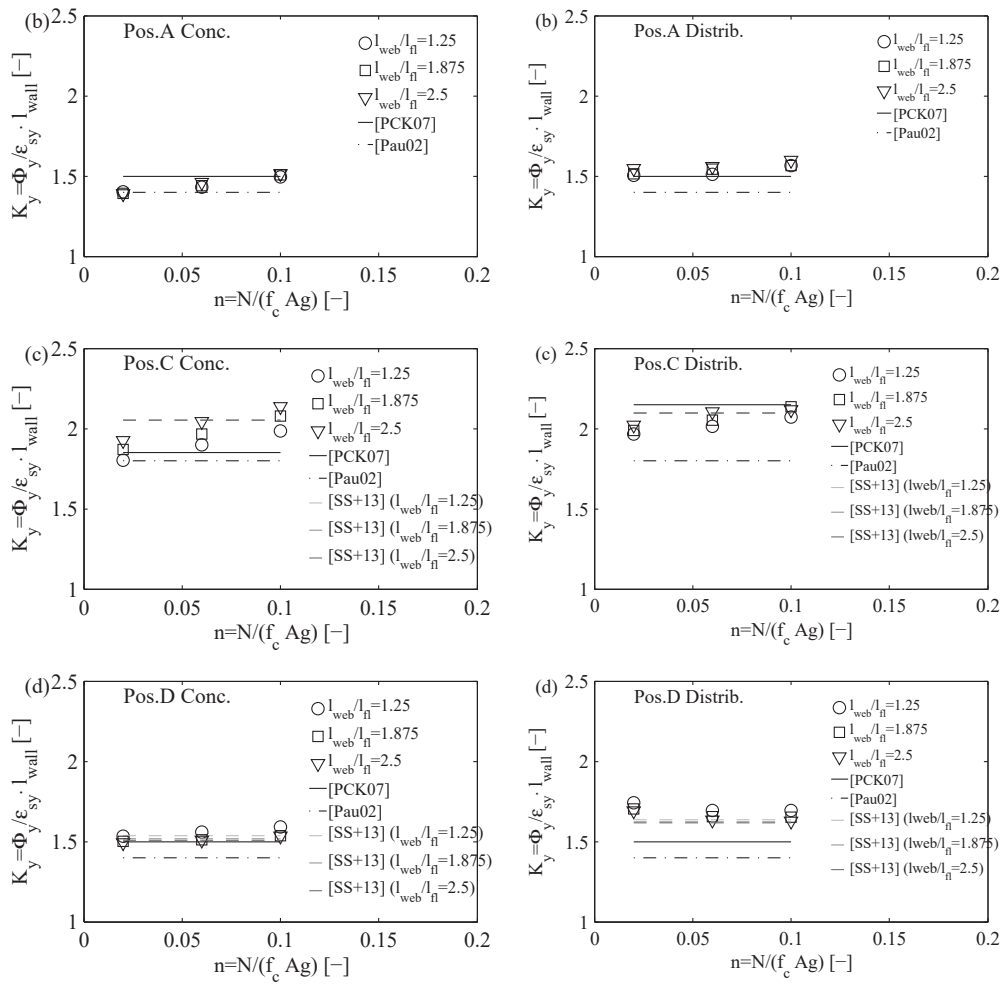


**Figure 6.7:** Dimensionless yield curvature  $K_y$  from plane section analyses: comparison with existing estimates for the orthogonal loading directions

## Chapter 6. Yield and ultimate displacement of U-shaped walls

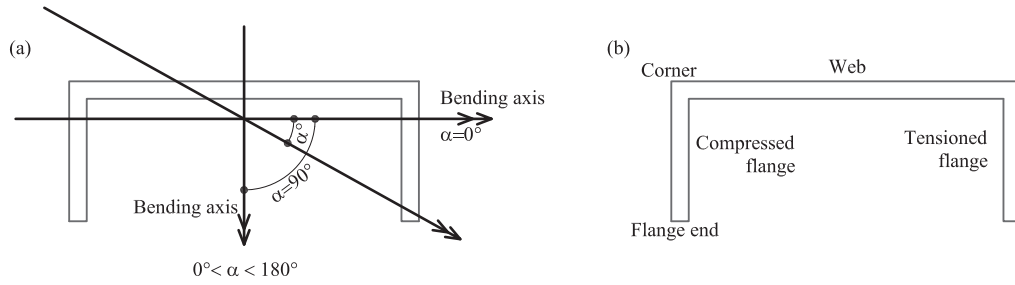


**Figure 6.8:** Bending axis when performing the sweep analysis by varying the angle  $\alpha$  of the bending axis with respect to the horizontal axis ( $\alpha = 0^\circ$ ):  $0^\circ \leq \alpha \leq 180^\circ$  (a). During the sweep, one flange of the wall is mainly compressed, the other flange is mainly tensioned (b) while the web is mainly tensioned for  $\alpha < 90^\circ$  and partially compressed for  $\alpha > 90^\circ$ .

### 6.3.3 New estimates for yield curvature for any loading direction

Sweep analyses, with a bending angle  $\alpha$  (Figure 6.8) incremented in steps of  $9^\circ$  were performed for all the wall configurations. The dimensionless nominal yield curvatures  $K_y$  for the distributed and the concentrated reinforcement layout cases are plotted in Figure 6.9. The two graphs clearly show the influence of the loading angle as well as a less significant influence of the web to flange length ratio  $l_{web}/l_{fl}$ .

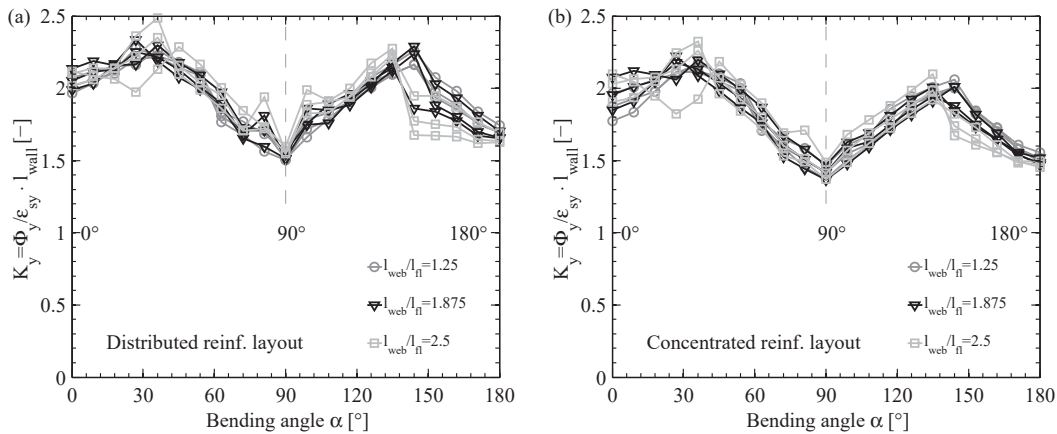


**Figure 6.9:** Dimensionless yield curvature  $K_y$  from plane section analyses: results from sweep analyses



The nominal and the yield moment  $M_n$  and  $M_y$  used in the computation of  $K_y = \phi'_y \frac{M_n l_{wall}}{M_y \epsilon_{sy}}$  were taken as the SRSS moment at nominal and at first yield for most directions. However, for loading directions at angles close to the principal loading directions, the curvature decomposed along of the principal directions, e.g.,  $\phi_{web}$  in Figure 6.12c, was considerably smaller than the yield curvature in the loading direction of interest (e.g.  $\phi'_y$  in Figure 6.12c). In such a case, using the SRSS moments to compute  $M_n/M_y$  does not seem reasonable as the large  $M_n/M_y$  ratio from the SRSS moment is associated to the web direction where the curvature is small, whereas the bending occurs mostly in the flange direction. Hence, for this case, the  $M_n/M_y$  was computed from the moment at yield and nominal in the direction of the flanges. The  $M_n/M_y$  ratio was similarly computed for all cases where the curvature at first yield in one of the principal directions was considerably smaller than the first yield curvature in the loading direction, i.e., arbitrarily taken as smaller than half of the yield curvature.

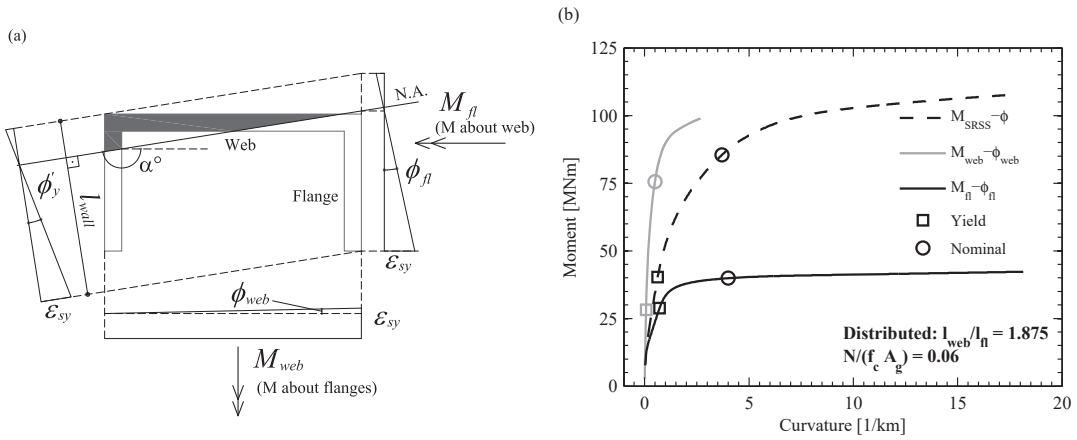


**Figure 6.10:** Nominal to yield moment ratio for loading directions close to the principal directions of the sections: (a) plane section deformation and (b) moment-curvature relationships for the loading case from (a)

### 6.3.3.1 Derivation of yield curvature estimates for any loading direction

Figure 6.11 shows the bending of a U-shaped wall section in the direction of the geometric diagonal of the wall (i.e., curvature applied in the diagonal direction). At the instant of first yield, i.e., when the reinforcement yield strain  $\epsilon_{sy}$  is reached in the most tensioned fibre, the diagonal curvature reaches the first yield curvature  $\phi_{diag} = \phi'_y$ . The following geometrical relations can hence be written as shown in Figure 6.11 :

$$\phi_{web} = \frac{\epsilon_2 - \epsilon_1}{l_{web}} \tag{6.5a}$$

$$\phi_{fl} = \frac{\epsilon_1 + \epsilon_3}{l_{fl}} \tag{6.5b}$$

$$\phi_{diag} = \frac{\epsilon_2 + \epsilon_3}{l_{wall}} \tag{6.5c}$$

## Chapter 6. Yield and ultimate displacement of U-shaped walls

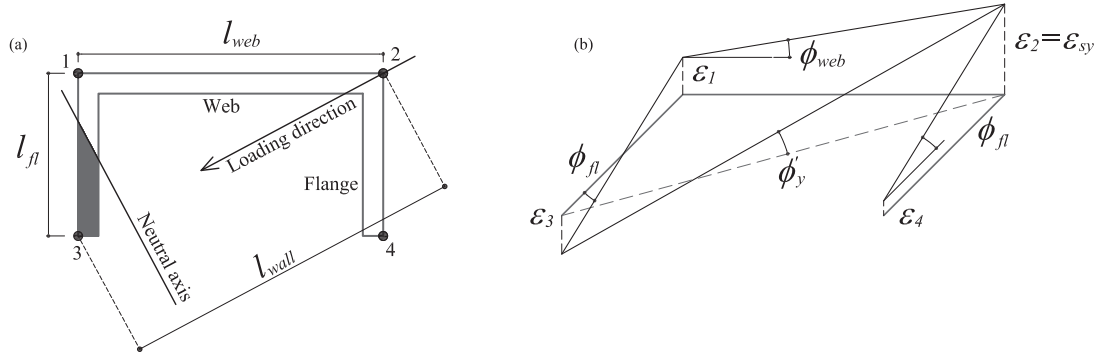


**Figure 6.11:** First yield curvature when loading in the direction of the geometric diagonal of the wall (curvature applied in the diagonal direction): (a) section dimensions and loading direction and (b) plane section deformation under the applied loading

If  $\varepsilon_2$  and  $\varepsilon_3$  are taken from Equations 6.5a and 6.5b, respectively and introduced in Equation 6.5c, one obtains that the diagonal curvature  $\phi_{diag}$  is equal to:

$$\phi_{diag} = \frac{\phi_{web}l_{web} + \phi_{fl}l_{fl}}{l_{wall}} \quad (6.6)$$

In Figure 6.11, the diagonal loading direction was chosen for easy geometrical representation, but the derived Equation 6.6 is valid for any loading direction. The loading direction is accounted for by defining the wall length as the length perpendicular to the neutral axis between the most compressed and the most tensioned fibre of the section (see Figure 6.12c) depends on the loading direction (bending angle  $\alpha$ ) and the web to flange ratio  $l_{web}/l_{fl}$  ( $l_{wall} = \sqrt{l_{web}^2 + l_{fl}^2} \sin(\alpha + \text{atan}(l_{fl}/l_{web}))$ ). Hence, the first yield curvature for any loading direction can be written as in Equation 6.7.

$$\phi'_y = \frac{\phi_{web}l_{web} + \phi_{fl}l_{fl}}{\sqrt{l_{web}^2 + l_{fl}^2} \sin(\alpha + \text{atan}(l_{fl}/l_{web}))} \quad (6.7)$$

Note that the curvatures  $\phi_{web}$  and  $\phi_{fl}$  (Figure 6.11) are not equal to the first yield curvatures for loading in the direction of the web  $\phi'_{y,web}$  or in the direction the flanges  $\phi'_{y,fl}$ , but they are smaller as shown in Figure 6.12a-c. If the relation between  $\phi_{web}$  for an arbitrary loading direction and  $\phi'_{y,web}$ , and also between  $\phi_{fl}$  and  $\phi'_{y,fl}$  would be known, then one could write the first yield curvature for any loading direction as a function of the first yield curvatures for loading in the principal wall directions. Therefore, Equation 6.7 is rewritten as:

$$\phi'_y = \phi'_{y,web} \frac{l_{tens,web}^y}{\varepsilon_{sy}} \frac{\varepsilon_{sy}}{l_{tens,web}} \frac{l_{web}}{l_{wall}} + \phi'_{y,fl} \frac{l_{tens,fl}^y}{\varepsilon_{sy}} \frac{\varepsilon_{sy}}{l_{tens,fl}} \frac{l_{fl}}{l_{wall}} \quad (6.8a)$$

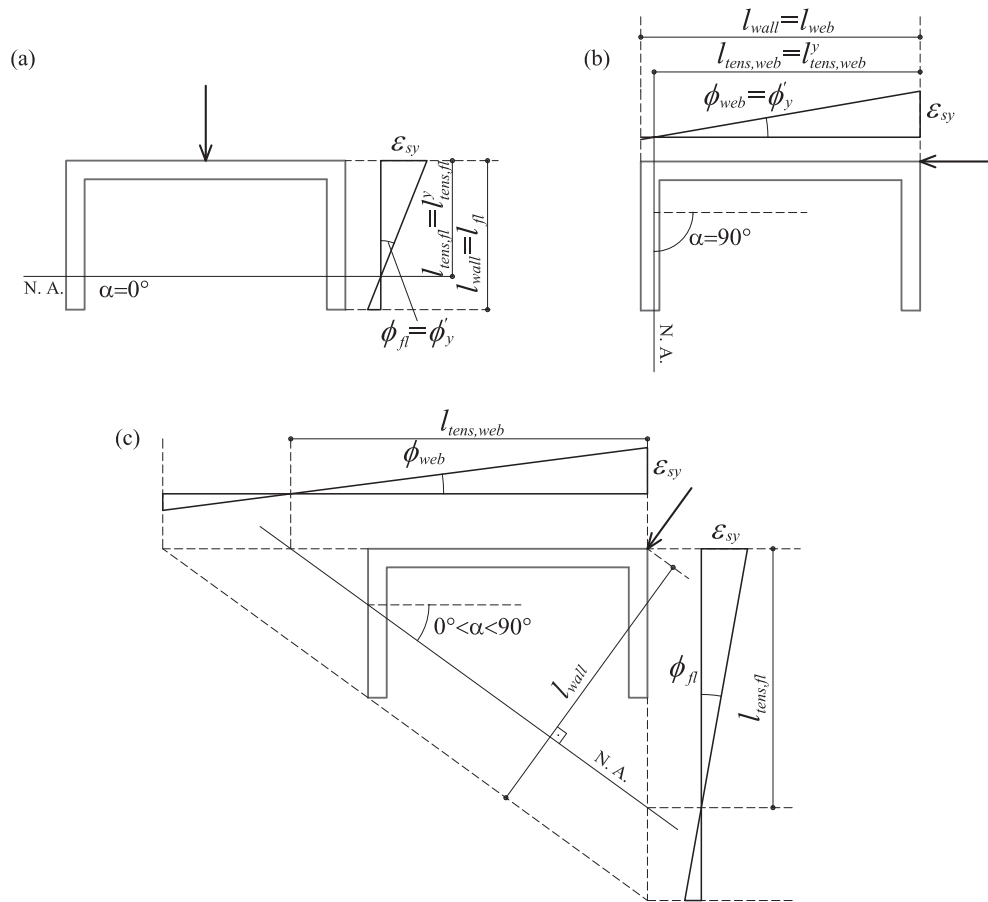


**Figure 6.12:** Section deformation at first yield for different loading directions: (a) curvature applied in the direction of the flanges with the flange ends in compression ( $\alpha = 0^\circ$ ), (b) curvature applied in the direction of the web ( $\alpha = 90^\circ$ ) and (c) curvature applied in an arbitrary direction ( $0^\circ < \alpha < 90^\circ$ )

## Chapter 6. Yield and ultimate displacement of U-shaped walls

$$\phi'_y = \phi'_{y,web} \frac{l_{tens,web}^y}{l_{tens,web}} \frac{l_{web}}{l_{wall}} + \phi'_{y,fl} \frac{l_{tens,fl}^y}{l_{tens,fl}} \frac{l_{fl}}{l_{wall}} \quad (6.8b)$$

Next, it is convenient to pass on the right side of Equation 6.8b from first yield curvatures  $\phi'_y$  to nominal yield curvatures  $\phi_y$ . Therefore, if we write the nominal yield curvature for loading in the direction of the flanges (Figure 6.12a) as  $\phi_{y,fl} = \phi'_{y,fl} M_{n,fl} / M_{y,fl}$  and similarly for the curvature when loading in the direction of the web (Figure 6.12b)  $\phi_{y,web} = \phi'_{y,web} M_{n,web} / M_{y,web}$  Equation 6.8b can be rewritten as Equation 6.9.

$$\phi'_y = \phi_{y,web} \frac{M_{y,web}}{M_{n,web}} \frac{l_{tens,web}^y}{l_{tens,web}} \frac{l_{web}}{l_{wall}} + \phi_{y,fl} \frac{M_{y,fl}}{M_{n,fl}} \frac{l_{tens,fl}^y}{l_{tens,fl}} \frac{l_{fl}}{l_{wall}} \quad (6.9)$$

Since the sought quantity is the nominal yield curvature, the entire equation is multiplied by the ratio of nominal to yield moment  $M_n(\alpha) / M_y(\alpha)$  corresponding to the bending angle  $\alpha$  (Equation 6.10a). Since  $M_n(\alpha) / M_y(\alpha)$  can be roughly approximated as constant when the angle  $\alpha$  varies (Figure 6.13a), Equation 6.10a is simplified to Equation 6.10b. Then, in order to pass to dimensionless yield curvatures  $K_y$ , the equation is further multiplied by the wall length  $l_{wall}$  and divided by the reinforcement yield strain  $\epsilon_{sy}$  resulting in Equation 6.10c and 6.10d.

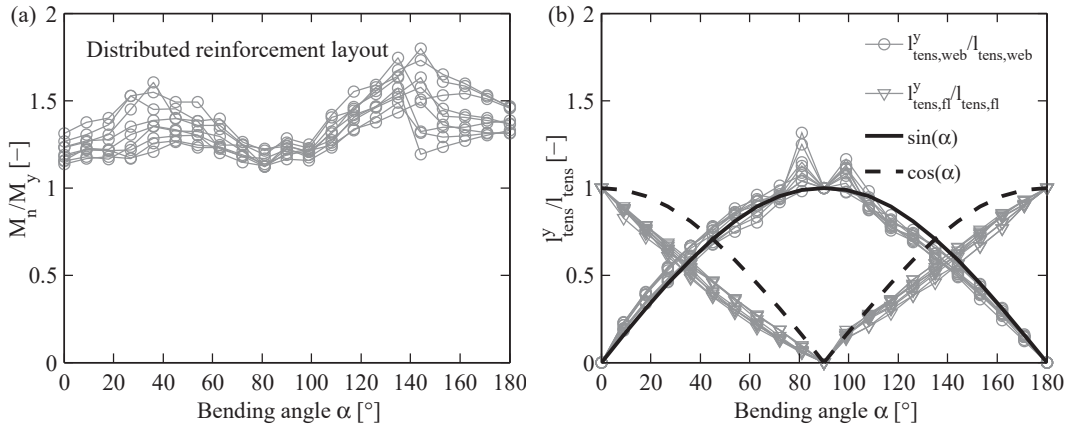


**Figure 6.13:** Variation of the ratio of nominal to yield moment (a) and of the tensioned wall length (b) with the bending angle  $\alpha$ .

$$\phi'_y \frac{M_n(\alpha)}{M_y(\alpha)} = \phi_{y,web} \frac{M_{y,web}}{M_{n,web}} \frac{M_n(\alpha)}{M_y(\alpha)} \frac{l_{tens,web}^y}{l_{tens,web}} \frac{l_{web}}{l_{wall}} + \phi_{y,fl} \frac{M_{y,fl}}{M_{n,fl}} \frac{M_n(\alpha)}{M_y(\alpha)} \frac{l_{tens,fl}^y}{l_{tens,fl}} \frac{l_{fl}}{l_{wall}} \quad (6.10a)$$

$$\phi'_y \frac{M_n(\alpha)}{M_y(\alpha)} = \phi_{y,web} \frac{l_{tens,web}^y}{l_{tens,web}} \frac{l_{web}}{l_{wall}} + \phi_{y,fl} \frac{l_{tens,fl}^y}{l_{tens,fl}} \frac{l_{fl}}{l_{wall}} \quad (6.10b)$$

$$\phi'_y \frac{l_{wall}}{\epsilon_{sy}} = \left( \phi_{y,web} \frac{l_{tens,web}^y}{l_{tens,web}} \frac{l_{web}}{\epsilon_{sy}} + \phi_{y,fl} \frac{l_{tens,fl}^y}{l_{tens,fl}} \frac{l_{fl}}{\epsilon_{sy}} \right) \quad (6.10c)$$

### 6.3. Yield curvature

$$K_y = K_{y,web} \frac{l_{tens,web}^y}{l_{tens,web}} + K_{y,fl} \frac{l_{tens,fl}^y}{l_{tens,fl}} \quad (6.10d)$$

The dimensionless yield curvature  $K_y$  is hence a function of the dimensionless yield curvatures for the principal loading directions of the wall.  $K_y$  varies with the wall lengths that are under tension for the different loading angles  $l_{tens,web}$  and  $l_{tens,fl}$ . Figure 6.13b shows, the variation of these two quantities with the bending angle. For practical purposes, the variation of  $l_{tens,web}^y/l_{tens,web}$  and of  $l_{tens,fl}^y/l_{tens,fl}$  with the bending angle  $\alpha$  can be approximated by  $\sin(\alpha)$  and  $\cos(\alpha)$ . Hence if these values are introduced in Equation 6.10d, the dimensionless yield curvature can be estimated as in Equation 6.11.

Estimates from Equation 6.11 match well the dimensionless yield curvature from section analyses (Figure 6.14). For the distributed reinforcement layout the mean of all the ratios between the estimated and the section analysis yield curvature ( $K_y/K_{y,PSA}$ ) was of 1.08 with a coefficient of variation  $COV = 8.2\%$  while for the concentrated reinforcement layout this mean was of 1.14 and  $COV = 7.2\%$ . Note that this precision can be improved if the variation of the ratio of nominal to yield moment  $M_n/M_y$  with the bending angle is considered. In Equation 6.11, it was assumed that  $M_n/M_y$  is constant irrespective of the bending angle.

$$K_y = K_{y,web} \cos(\alpha) + K_{y,fl} \sin(\alpha) \quad (6.11)$$

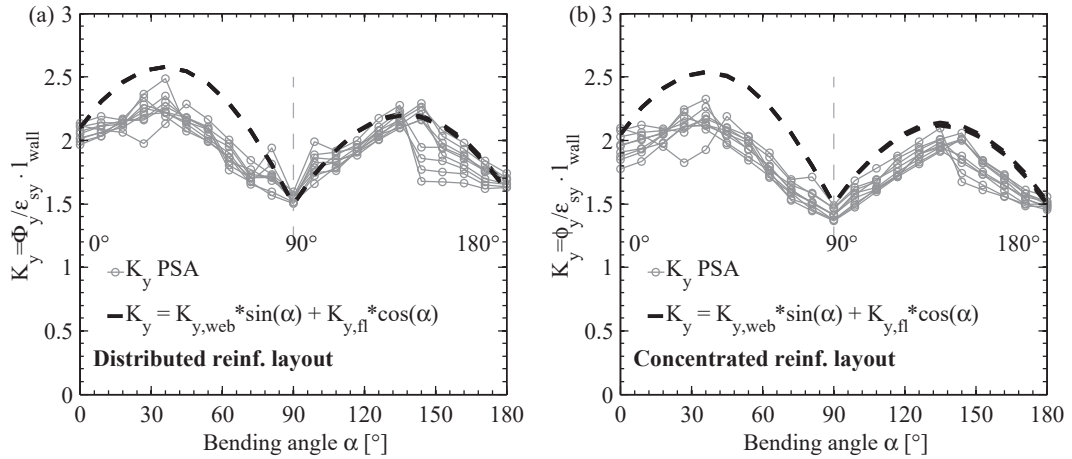


**Figure 6.14:** Comparison between dimensionless yield curvatures ( $K_y = \phi_y l_{wall} / \epsilon_{sy}$ ) obtained from section analyses and estimates for the case of (a) distributed reinforcement layout and (b) concentrated reinforcement layout.

### 6.3.4 Comparison of section analysis and shell element model results

Most of the existing studies on the yield curvature have been based on moment-curvature analyses (plane section assumption) [PK98], [Pau02], [SS<sup>+</sup>13], [PCK07] as it is also the case for the previous section. In this section, yield curvatures derived from plane section analyses are compared with results from shell element model analyses.

The dimensionless yield curvature  $K_y$  was computed from analyses of the shell element model according to the procedure used in the model validation (Section 5.2.3). Briefly, the first yield was determined in the shell element model as the instant when the base curvature reaches the first yield curvature determined from section analyses  $\phi'_y$ , while the nominal moment corresponded to reaching a base tensile strain of 0.015 or base compression strain of -0.004 whichever occurred first. The base curvature at first yield and the base strain at nominal point were determined by extrapolating to the wall base the linear fit of the curvatures and correspondingly of the strains, over the cracked height of the wall at first yield  $H_{cr}$  (Section 6.4) and over the height of the plastic zone at nominal, respectively.

The two sets of  $K_y$  values are compared in Figure 6.15 with respect to the web to flange ratio  $l_{web}/l_{fl}$ , and implicitly with the bending angle for the diagonal loading directions. Figures 6.15a, b indicate a rather good match between the  $K_y$  values obtained from the two different types of analyses.

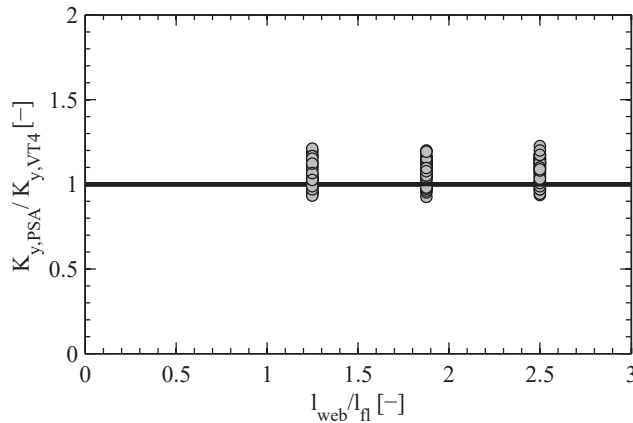


**Figure 6.15:** Comparison of dimensionless yield curvature  $K_y$  obtained from plane section analyses (PSA) and from shell element model analyses (VT4).

## 6.4 Yield displacement

Once estimates of the yield curvature are available, it is possible to compute the yield displacement of the wall. In this section, estimates of the yield displacement are computed according to the procedure outlined in Section 5.2.3 which was verified against the experimental data. These estimates are then compared with values of the yield displacement obtained from the shell element model parametric analyses (Section 6.2.2.2), model which was also verified against the experimental data.

The procedure for estimating the yield displacement is briefly repeated here for convenience (Equations 6.12 to 6.14). The yield displacement is computed as the sum of the displacement components: flexural displacement due to wall deformation assuming a wall that is cracked over part of the height and shear displacements. The flexural displacement due to strain penetration into the foundation is not considered here since it was not accounted for in the shell element model.

The shear displacement at yield were accounted for through the shear to flexural displacement ratio  $\Delta_s/\Delta_f$  estimate. This estimate follows the Equation 4.37, except the correction factor has been reduced from 1.5 to 1.0 to account for the reduced shear displacements under monotonic loading (see Section 5.2.4).

$$D_{y,2L} = K_y \frac{\epsilon_{sy}}{l_{wall}} k_{cr} \frac{H^2}{3} \left(1 + \frac{\Delta_s}{\Delta_f}\right) \quad (6.12)$$

where  $H$  is the wall shear span,  $k_{cr}$  is a factor accounting for the partially cracked wall over the height assuming a bi-linear curvature profile at yield (see Section 4.4 and Equation 6.13) and  $\Delta_s/\Delta_f$  is the shear to flexural displacement ratio (Equation 6.14 [BDP11]).

$$k = \beta + 0.5(1 - \beta) \left(3 \frac{H_{cr}}{H} - \left(\frac{H_{cr}}{H}\right)^2\right) \quad (6.13)$$

where  $\beta$  is the ratio of cracked to uncracked flexural wall stiffness ( $EI_{cr}/EI_g$ ) and  $H_{cr}$  is the height up to which the wall is cracked at first yield.

$$\frac{\Delta_s}{\Delta_f} = 1.0 \frac{\epsilon_m}{\phi \tan \theta} \frac{1}{H} \quad (6.14)$$

where  $\phi$  is the constant curvature in the plastic hinge,  $\theta$  is the crack angle at the top of the fan-like pattern where cracks begin to be parallel.

The yield displacements from the shell element model are obtained as the displacement at first yield times the nominal to yield moment ratio  $M_n/M_y$ . The comparison between the analysis results and the estimated yield displacements is shown in Figure 6.16 for all wall configurations and heights and all loading directions. Additionally, yield displacements estimated under the assumption of a fully cracked wall at yield (linear curvature profile) [PCK07] are added to the plots for comparison. The assumption of a fully cracked wall is intended to implicitly account for the strain penetration at yield and partially for the shear deformations [PCK07]. In order compare equivalent quantities, the displacement due to strain penetration was subtracted from the estimate assuming a linear curvature profile at yield (Equation 6.15)..

$$D_{y,1L} = K_y \frac{\epsilon_{sy}}{l_{wall}} \left(\frac{H^2}{3} - L_{sp}H\right) \quad (6.15)$$

## Chapter 6. Yield and ultimate displacement of U-shaped walls

---

As expected, the  $\Delta_{y,1L}$  estimate provides in all cases, yield displacements that are larger than the  $\Delta_{y,2L}$  estimates. For rather slender walls, i.e.,  $H/l_{wall} \geq 4$  the yield displacement predictions  $\Delta_{y,1L}$  overestimate the yield displacements obtained from the analyses  $\Delta_{y,num}$  for all loading positions with up to 50%. For these walls, the  $\Delta_{y,2L}$  estimate matches rather well the yield displacements obtained from the analyses.

For walls with slenderness  $2.6 \leq H/l_{wall} \leq 4$ ,  $\Delta_{y,1L}$  and  $\Delta_{y,2L}$  predictions typically underestimate the analyses results  $\Delta_{y,num}$ . For these walls: (1) shear displacements are larger than for more slender walls ( $H/l_{wall} \geq 4$ ), and (2) tension shift effects due to shear cracking are more important and increase the cracked height. The two phenomena lead to large yield displacements  $\Delta_{y,num}$  for these walls.

The  $\Delta_{y,1L}$  estimates compensate for the contribution of the shear deformations to the total displacement through the linear curvature profile. If shear displacements are significant (i.e.,  $2.6 < H/l_{wall} < 4$ ) the estimate matches well or underestimates the  $\Delta_{y,num}$  values. When shear displacements are small (i.e.,  $H/l_{wall} \geq 4$ ),  $\Delta_{y,1L}$  overestimates the  $\Delta_{y,num}$  values (Figure 6.16).

Since  $\Delta_{y,2L}$  accounts specifically for the shear deformations while  $\Delta_{y,1L}$  partially compensates for them with the possibility to add them in case of walls with important shear deformations [PCK07], the two estimates are also compared without the shear deformations of  $\Delta_{y,2L}$  (Figure 6.17). The superiority of the  $\Delta_{y,2L}$  estimate becomes even more evident. Without the shear deformations  $\Delta_{y,2L}$  are slightly low at positions A and E for very slender walls and significantly lower for walls with  $2.6 < H/l_{wall} < 4$  for these positions. For this latter category of walls, further discrepancies between  $\Delta_{y,2L}$  and  $\Delta_{y,num}$  stem from the prediction of the cracked height. For walls with low slenderness ratio, the cracked height is influenced by diagonal cracking that leads to larger cracked heights due to tension shift (Figure 6.18). The tension shift was considered in simplified manner in the prediction of the cracked height (see Section 4.3.2.3).



## 6.4. Yield displacement

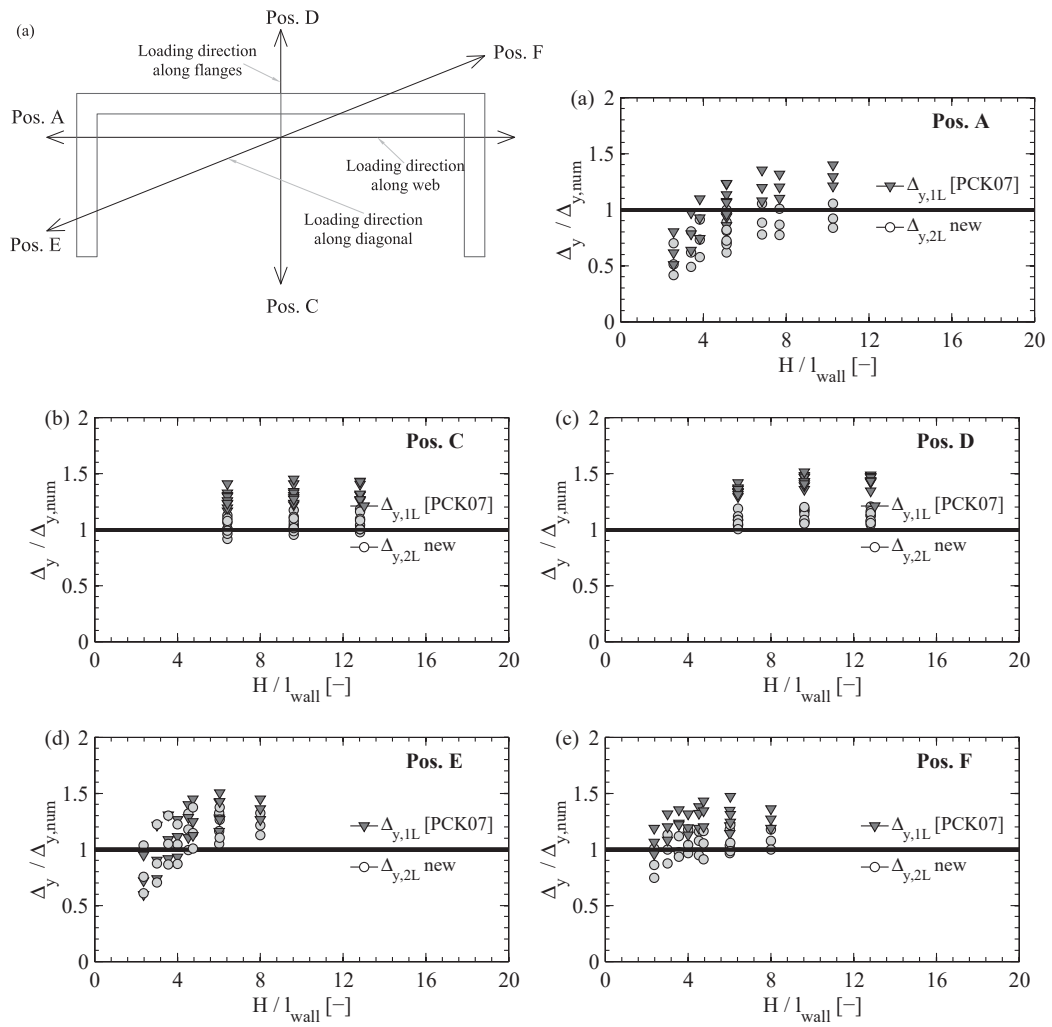


**Figure 6.16:** Comparison of yield displacement estimates  $\Delta_{y,1L}$  and  $\Delta_{y,2L}$  with numerical results from the shell element model  $\Delta_{y,num}$  for the different loading positions (a-f).

## Chapter 6. Yield and ultimate displacement of U-shaped walls

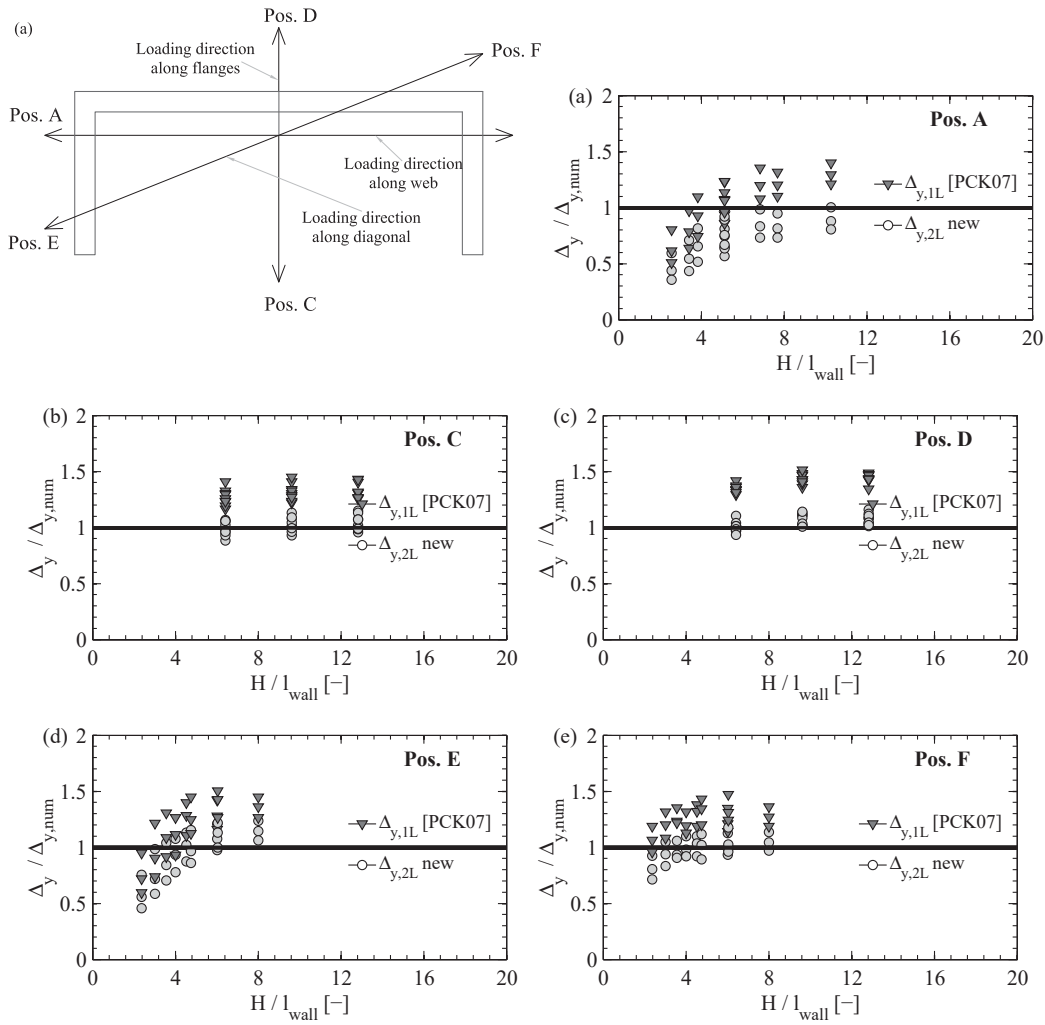


**Figure 6.17:** Comparison of yield displacement estimates  $\Delta_{y,1L}$  and  $\Delta_{y,2L}$  without shear displacements, with numerical results from the shell element model  $\Delta_{y,num}$  for the different loading positions (a-f).

## 6.4. Yield displacement

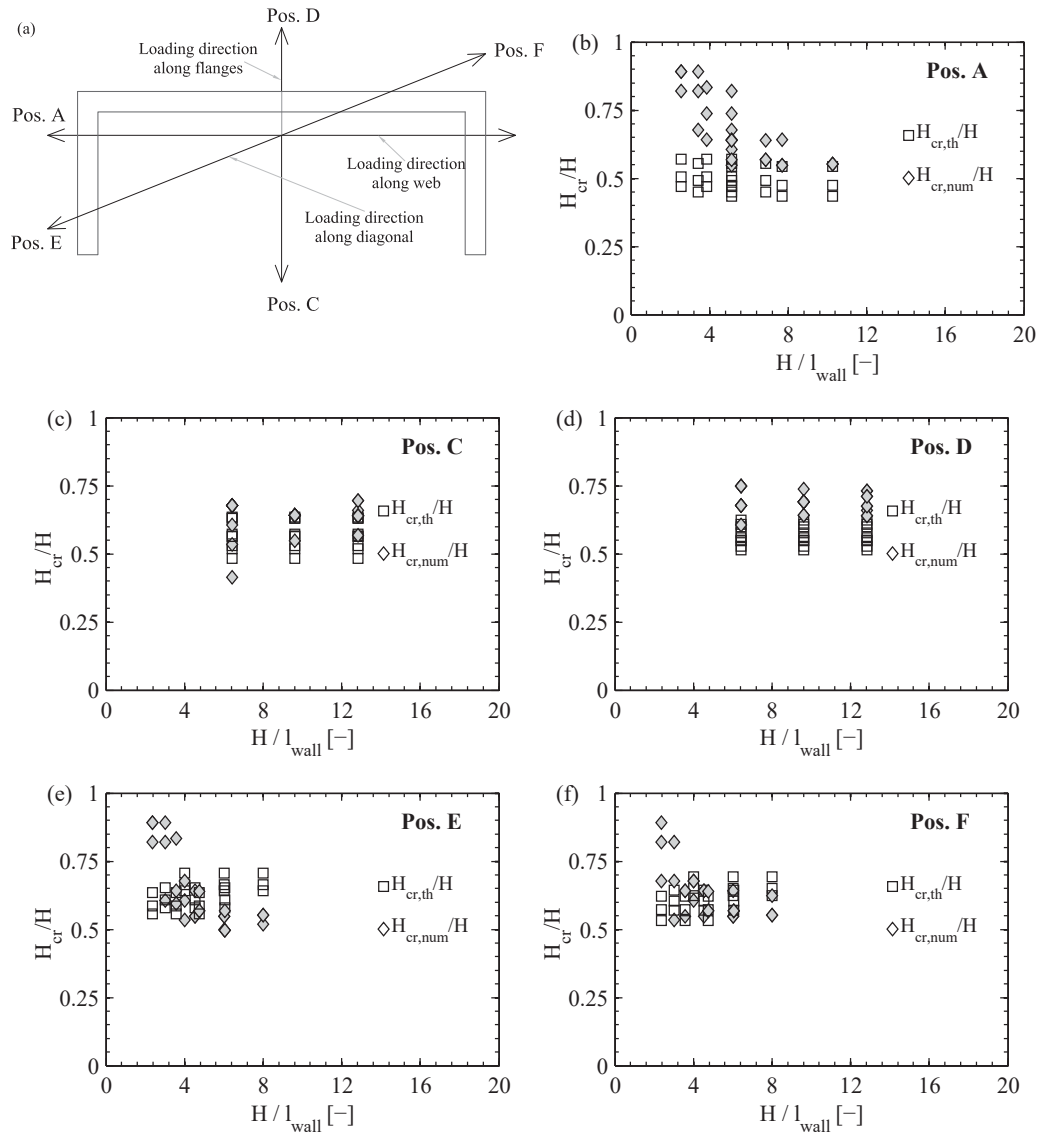


**Figure 6.18:** Comparison of cracked height predictions with cracked height obtained from the numerical model as the height over which the maximum vertical strain at the edges of the wall are larger than the cracking strain.

## 6.5 Effective stiffness ratio

In this section,  $K_{eff,num}$  values obtained from the shell element model analyses are compared to estimates based on gross sectional stiffness and estimates based on yield displacement predictions. The effective stiffness of the walls was computed as outlined in Section 5.2.3.4 as the nominal force divided by the nominal yield displacement. This is equivalent to computing  $K_{eff}$  as the first yield force divided by the first yield displacement. The effective stiffness ratio was then computed as the effective stiffness  $K_{eff}$  divided by the elastic flexural stiffness of a cantilever wall  $K_{th} = 3E_c I_g / H^3$ , where  $E_c$  is the concrete elastic modulus and  $I_g$  is the moment of inertia of the uncracked U-shaped section depending on the loading direction.

### 6.5.1 Comparison with existing estimates

Effective stiffness ratio estimates by [FB00], [PP92] and [PCK07] are included in this comparison against the parametric study results. In addition, the stiffness ratios based on the predicted yield displacements  $\Delta_{y,2L}$  and  $\Delta_{y,1L}$  are included in the comparison.

The effective stiffness ratios that are based on gross sectional stiffness were summarised in Section 4 and are briefly repeated here for convenience. The effective stiffness ratio by [FB00] (Equation 6.16) were derived by accounting for a partially cracked wall over the height at yield as well as for the tension stiffening effect, but did not consider the shear deformations or the strain penetration into the foundation. In addition the axial force was considered constant over the height of the wall. Estimates by [PP92] (Equation 6.17a) accounted for strain penetration and for walls with an aspect ratio  $H/l_{wall}$  lower than 4 also for shear deformations. Finally, [PCK07] recommends to evaluate the effective stiffness as the secant flexural stiffness at yield (Equation 6.18). Note that estimates based on Equation 6.18 are very similar to estimates based on the yield displacement  $\Delta_{y,1L}$  and for this reason only the latter estimates are included in the comparison.

$$I_e/I_g = 0.267(1 + 4.4 \frac{N}{f_c A_g})(0.62 + \frac{190}{f_y})(0.76 + 0.005 f_c) \quad (6.16)$$

where  $N/(f_c A_g)$  is the axial load ratio,  $f_y$  is the reinforcement yield strength and  $f_c$  is the concrete compression strength.

$$I_e/I_g = (\frac{100}{f_y} + \frac{N}{f_c A_g}); H/l_{wall} \geq 4 \quad (6.17a)$$

$$I_w/I_g = I_e/I_g \frac{1}{1.2 + F}; H/l_{wall} < 4 \quad (6.17b)$$

where  $F = 30I_e/(H^2 t_{wall} l_{wall})$ .

$$I_e/I_g = \frac{M_n}{\phi_y E_c I_g} \quad (6.18)$$

When computing the effective stiffness ratios based on the predicted yield displacements the nominal moment was obtained from section analyses. The yield displacement  $D_{y,2L}$  is based on a bilinear curvature distribution over the height of the wall; the kink of this distribution is at the cracked height. When evaluating  $D_{y,2L}$  the cracked height was taken from the numerical model instead of the predicted value, in order to capture the errors related to the employed concept for determining the effective stiffness and to not propagate errors in the prediction of the cracked height prediction, which was already discussed in the previous section. The the effective stiffness ratio  $K_{eff,num}/K_{th}$  that are obtained from the shell element model of are compared to the different estimates in Figures 6.19 to 6.22.

While estimates by [PP92] provide on average the best match with the numerical results, only the estimates which account for the cracked height completely capture the variation of the stiffness with the wall slenderness ratio (Figures 6.19 and 6.22). The equation by [PP92] partially captures this trend by accounting for the wall geometry for slenderness ratios  $H/l_{wall} < 4$ .

The yield displacement prediction based on the linear curvature profile at yield  $\Delta_{y,1L}$  did not capture the variation of the yield displacement with the  $H/l_{wall}$  (Section 6.4). Therefore stiffness estimates based on  $\Delta_{y,1L}$  do not capture this variation either (Figure 6.21).

The equation by [FB00] generally overestimates the numerical effective stiffness ratios. In the derivation of this equation the cracked height due to the moment gradient was accounted for but its increase due to tension shift effects was not. In addition, shear deformations were not considered or accounted for in any way. Therefore this equation results in a stiffer response.

### 6.5.2 Trends of effective stiffness with the different loading positions

The variation of the effective stiffness ratio  $K_{eff}/K_{th}$  determined from the shell element model is discussed in this section with respect to axial load ratio, slenderness ratio  $H/l_{wall}$  and web to flange ratio  $l_{web}/l_{fl}$ . For all the loading positions, increasing the axial load ratio increases the compression zone of the wall and hence also the stiffness of the wall (Figure 6.23).

For low wall slenderness ratios  $H/l_{wall} \leq 4$  the effective stiffness is proportional to the ratio  $H/l_{wall}$ . For these walls, the shear deformations and the effects of diagonal cracking on the cracking height increase with decreasing slenderness ratios and the effective stiffness reduces. For more slender walls ( $H/l_{wall} > 4$ ), the effective stiffness does not varies with the slenderness ratio (e.g., positions C and D in Figure 6.24d,e).

Increasing the web to flange ratio  $l_{web}/l_{fl}$  by increasing the length of the web, results in reduced effective stiffness due to reduction of the slenderness ratio. At position C, increasing the web length increases the compression depth on the flange ends while at position D it leads to smaller compression depth on the web. Hence for the former effective stiffness is increased while for the latter it is decreased.

### 6.5.3 Modified equation for effective stiffness ratio

From the above observations and the comparison of the effective stiffness ratios that were obtained from the analyses of nonlinear shell element models with estimates reported in the literature, one finds that the height over which the wall cracks at yield plays an important role in the prediction of the effective stiffness.

Since the existing estimates by [PP92] (Equation 6.17a) provided on average a rather good match with the shell element model results, this estimate is modified in this section to account for the effects of cracked height on the effective stiffness ratio.

The equation by [PP92] was derived as the flexural stiffness of the wall and a assumed constant flexural stiffness over the wall height, i.e., linear curvature profile over the height. Hence in order to introduce the cracked height in this equation, one can relate the two curvature profile assumptions: linear curvature profile and bi-linear curvature profile accounting for the cracked height. The connection can be done through the factor  $k$  (Equation 6.19) which related the flexural displacements computed with the two assumptions (see Section 6.4).

$$k = \beta + 0.5(1 - \beta)\left(3\frac{H_{cr}}{H} - \left(\frac{H_{cr}}{H}\right)^2\right) \quad (6.19)$$

By assuming that the gross sectional stiffness  $I_g$  reduces by half when cracking occurs, then  $\beta = EI_{cr}/EI_g$  is equal to 0.5. By further neglecting the squared term of  $H_{cr}/H$  in Equation 6.19, the  $k$  factor simplifies to  $k = 0.5 + 0.75H_{cr}/H$  and can be introduced into Equation 6.17a. Since  $k$  is proportional to the yield displacement, it will be inversely proportional to the stiffness. Equation 6.17a then becomes:

$$(I_e/I_g)_{mod2} = \left(\frac{100}{f_y} + \frac{N}{f_c A_g}\right) \frac{1}{0.5 + 0.75\frac{H_{cr}}{H}}; H/l_{wall} \geq 4 \quad (6.20a)$$

$$(I_w/I_g)_{mod2} = I_e/I_g \frac{1}{1.2 + F} \frac{1}{0.5 + 0.75\frac{H_{cr}}{H}}; H/l_{wall} < 4 \quad (6.20b)$$

The resulting effective stiffness ratios are plotted against the results from the shell element model in Figure 6.26. Indeed, introducing the cracked height in the stiffness estimate equation by [PP92] the match with the numerical results is improved, especially at positions A, E, C and F since the cracked height is dependent on the axial force. For position D, the improvement is less because the cracked height at this position is rather independent of wall geometry.

## 6.5. Effective stiffness ratio

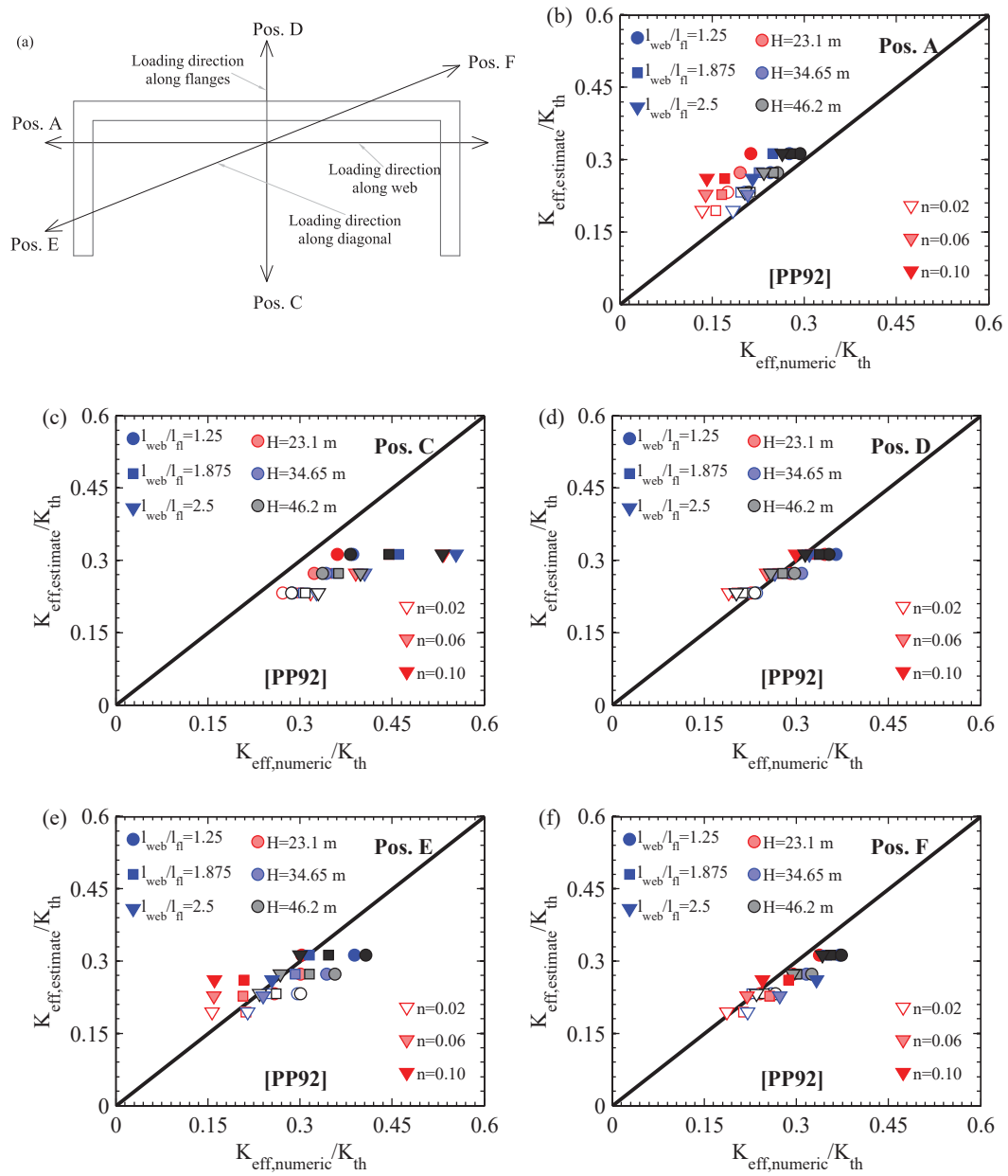


**Figure 6.19:** Comparison of effective stiffness estimates from [PP92] with shell element model results for different loading positions (a-f)

## Chapter 6. Yield and ultimate displacement of U-shaped walls

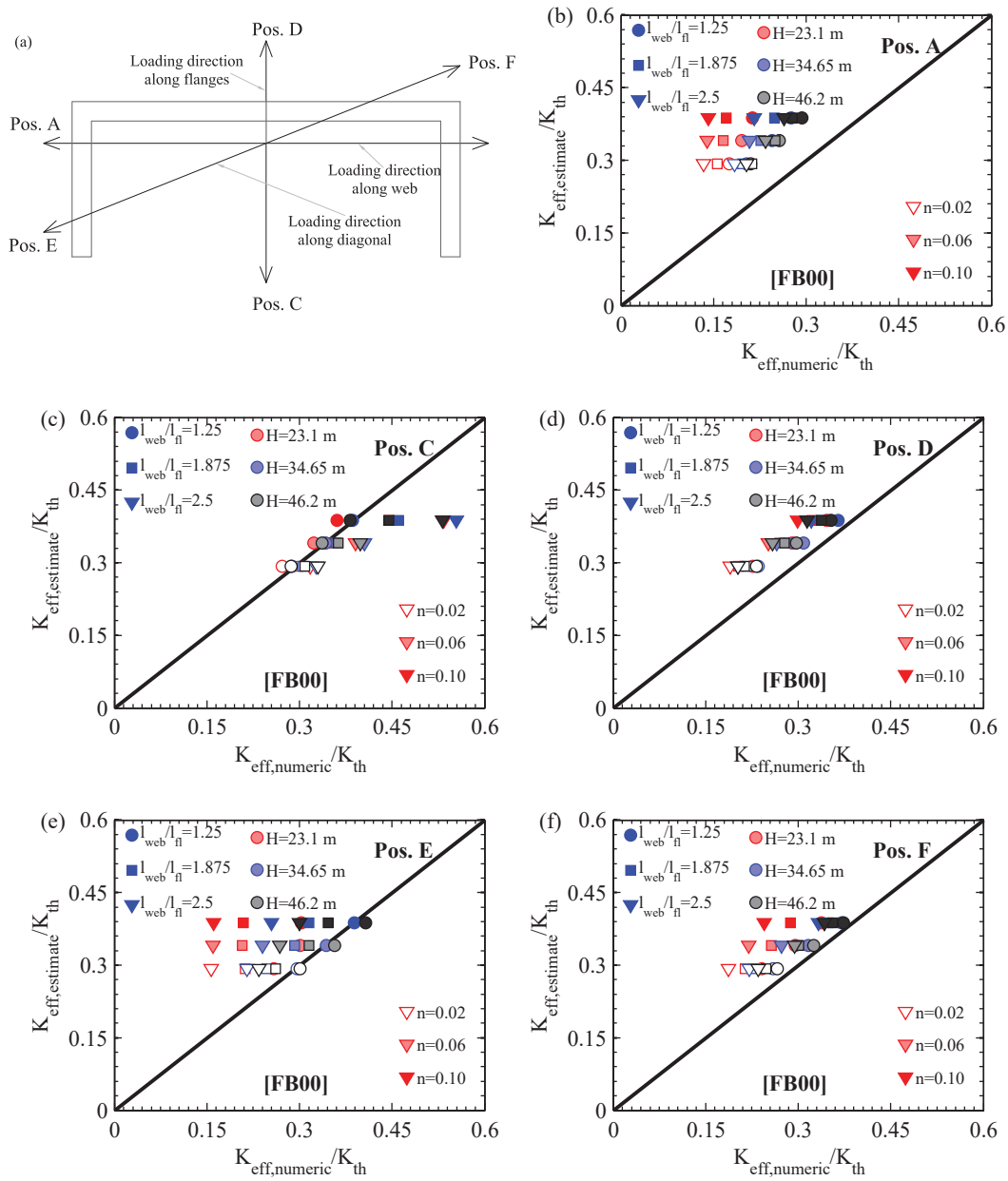


**Figure 6.20:** Comparison of effective stiffness estimates from [FB00] with shell element model results for different loading positions (a-f)



## 6.5. Effective stiffness ratio

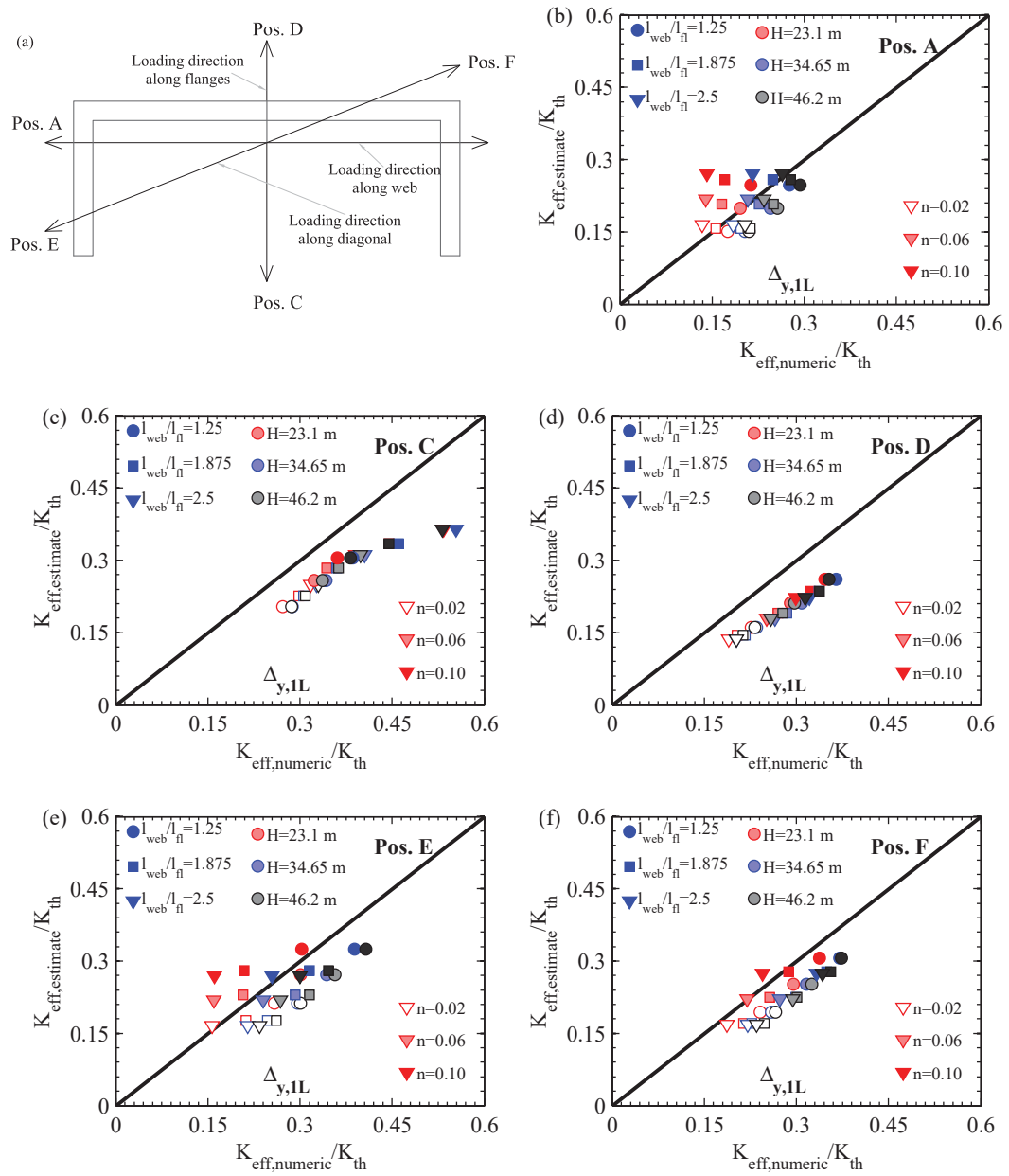


**Figure 6.21:** Comparison of effective stiffness estimates based on yield displacement predictions  $\Delta_{y,1L}$  with shell element model results for different loading positions (a-f)

## Chapter 6. Yield and ultimate displacement of U-shaped walls

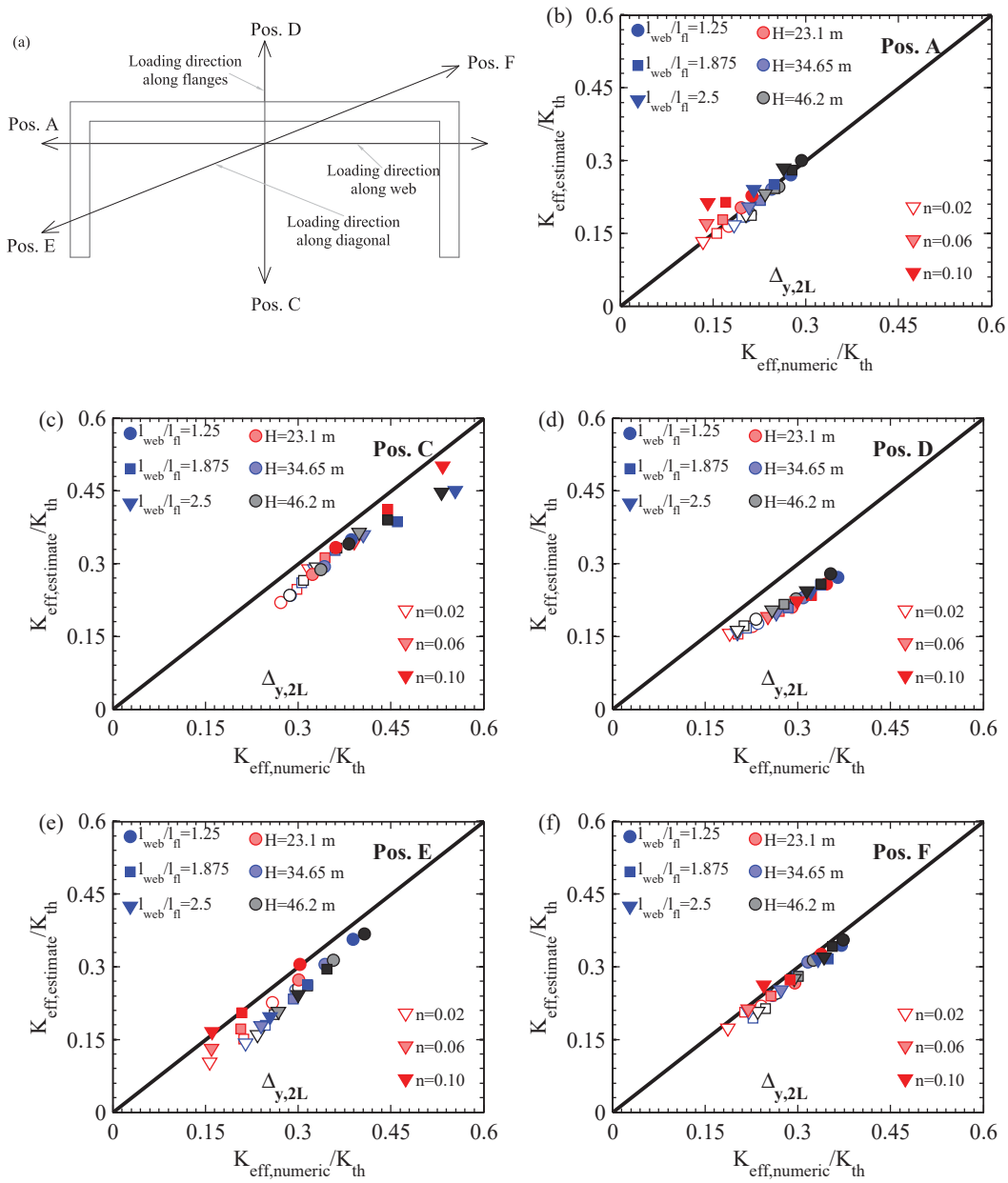


**Figure 6.22:** Comparison of effective stiffness estimates based on yield displacement predictions  $\Delta_{y,2L}$  with shell element model results for different loading positions (a-f)

## 6.5. Effective stiffness ratio

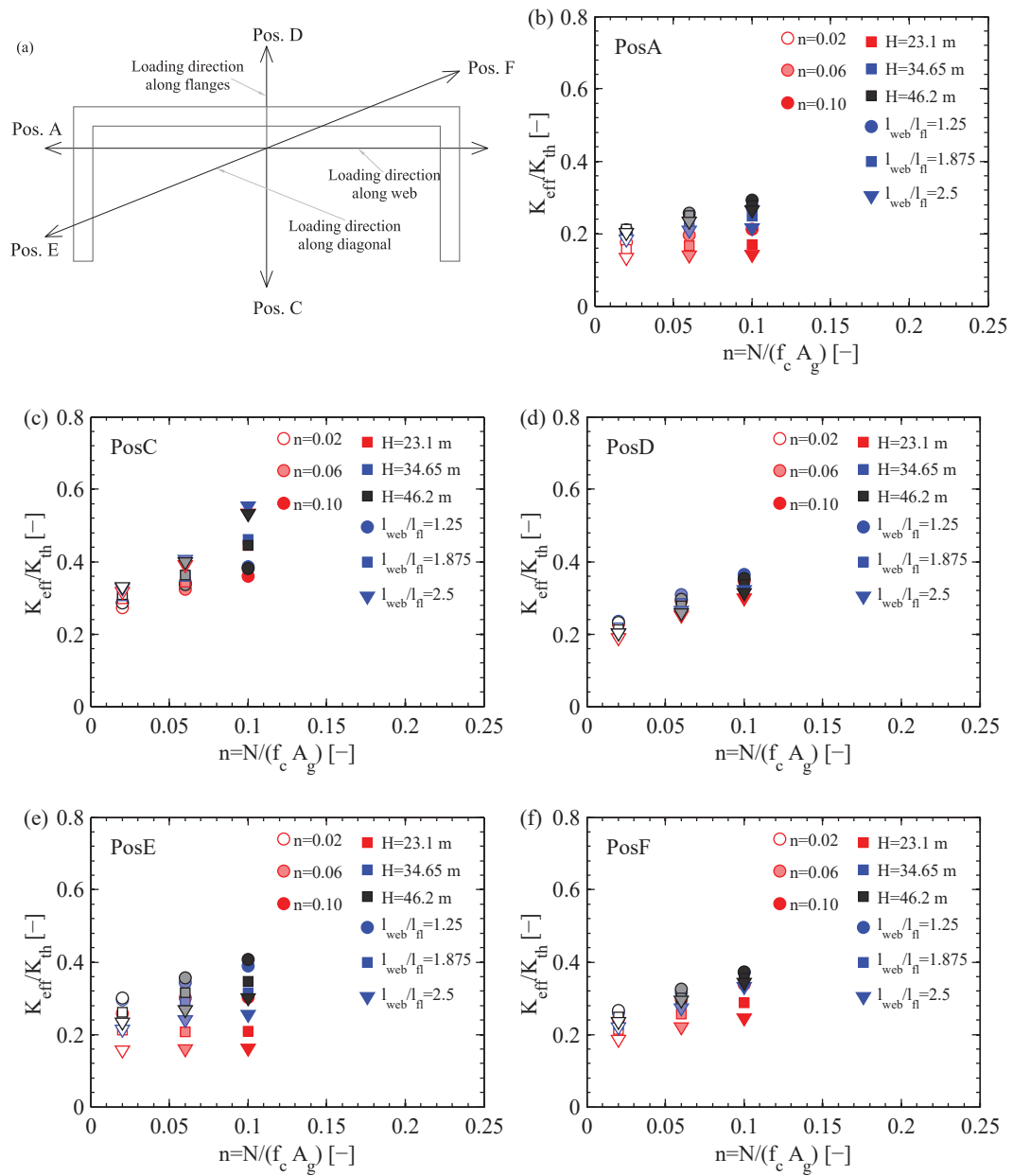


**Figure 6.23:** Trends of the effective stiffness ratios obtained from the shell element model results  $K_{eff,num}/K_{th}$  with the axial load ratio  $n = N/(f_c A_g)$  for the different loading positions.

## Chapter 6. Yield and ultimate displacement of U-shaped walls

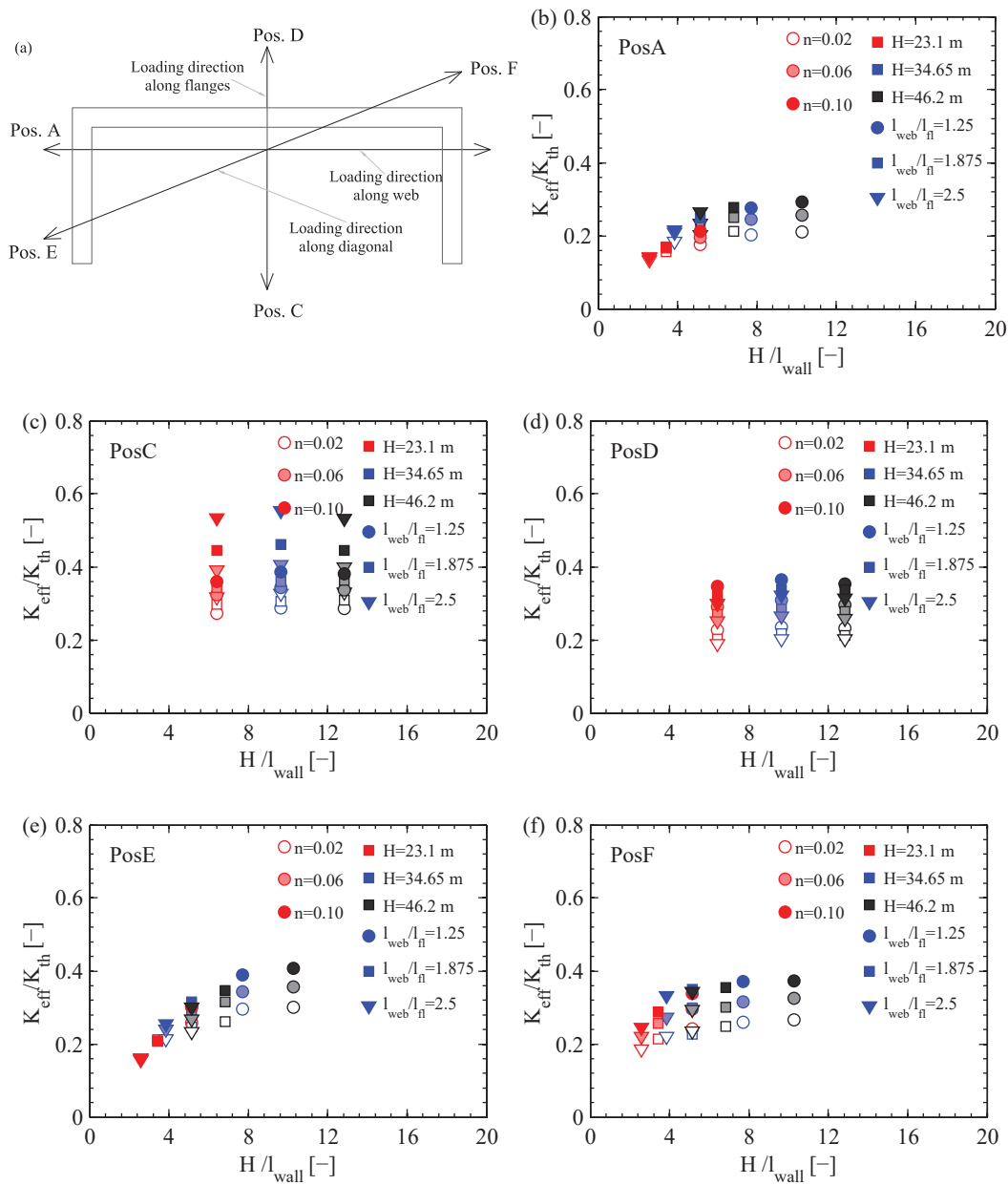


**Figure 6.24:** Trends of effective stiffness ratios obtained from the shell element model results  $K_{eff,num}/K_{th}$  with the wall slenderness  $H/l_{wall}$  for the different loading positions.

## 6.5. Effective stiffness ratio

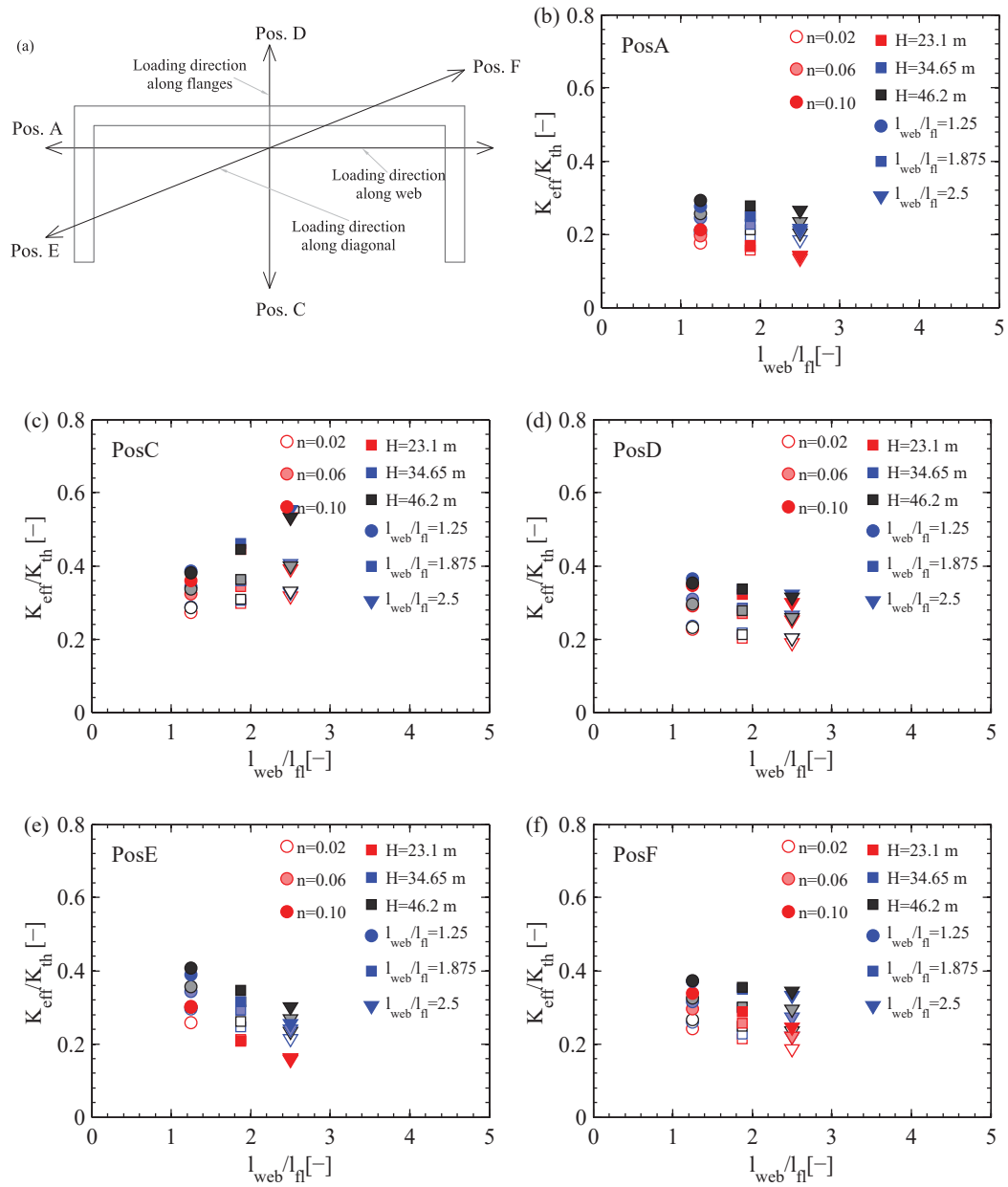


**Figure 6.25:** Trends of effective stiffness ratios obtained from the shell element model results  $K_{eff,num}/K_{th}$  with the web to flange ratio  $l_{web}/l_{fl}$  for the different loading positions.

## Chapter 6. Yield and ultimate displacement of U-shaped walls

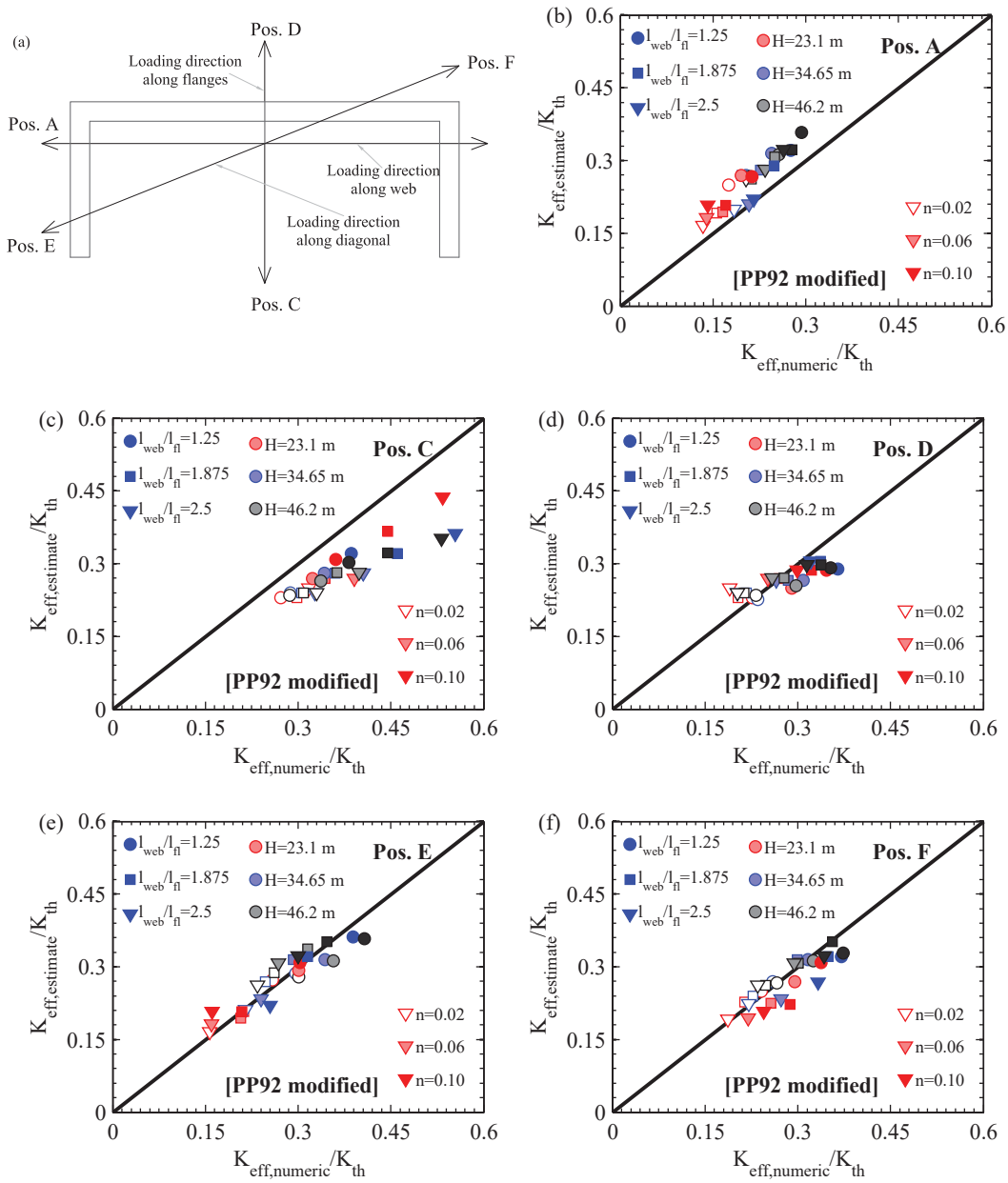


**Figure 6.26:** Comparison of effective stiffness ratios estimates with shell element mode results: [PP92] estimate modified to account for the cracked height (Equation 6.20a)

## 6.6 Plastic hinge lengths

This section presents the derivation of a new equation for the plastic hinge length based on the results of the parametric study. First, the curvature profiles over the height of the wall are examined for the inelastic displacement range. Then, the displacement capacity of the analysed walls is determined and its variation with the different loading positions is discussed. Displacement predictions using existing estimates of the plastic hinge length are compared to the numerical displacement capacity. Finally, the determination of the numerical plastic hinge length is presented and a new prediction equation for plastic hinge length proposed.

Note that throughout the section, the contribution of the strain penetration to the plastic hinge length was not considered since it was not accounted for in the shell element model. Strain penetration can be considered separately and the flexural displacement due to strain penetration can be added to the final value of the ultimate displacement capacity as for example in [GF<sup>+</sup>15].

### 6.6.1 Inelastic curvature profiles

Examples of curvature profiles over the wall height when the wall responds in the inelastic range are presented in Figure 6.27. The figure shows the profiles for one wall configuration that was analysed within the parametric study for different drift levels, axial load ratios and loading positions. The axial load is distributed over the height of the wall and applied at each storey level. The change in axial force at a storey leads also to a change in moment capacity. As a result, one observes a concentration of curvatures just above the storey levels where the ratio of moment demand to moment capacity is smallest. The curvature profile contains therefore spikes just above the storey level.

In experimental tests or numerical simulations where the axial load is constant over the height of the wall, the height of the plastic zone  $L_{pz}$  is evaluated as the maximum wall height over which curvatures exceed yield curvatures. For the walls analysed here where the axial force variation over the height of the wall is modelled by applying axial forces at each storey level, the resulting spiky curvature profile will lead to rather large  $L_{pz}$  values and more importantly, it disrupts the linearity of the inelastic curvature profiles over  $L_{pz}$ . Therefore, for this study the height of the plastic zone is determined as 2/3 of the maximum height over which curvatures exceed yield curvatures.

### 6.6.2 Displacement capacity

The displacement capacity of the walls in the parametric study was determined based on the ultimate curvature obtained from section analysis  $\phi_{u,PSA}$ . For the shell element model, the ultimate displacement was reached when the base curvature  $\phi_{b2}$  attained the  $\phi_{u,PSA}$  value.

## Chapter 6. Yield and ultimate displacement of U-shaped walls

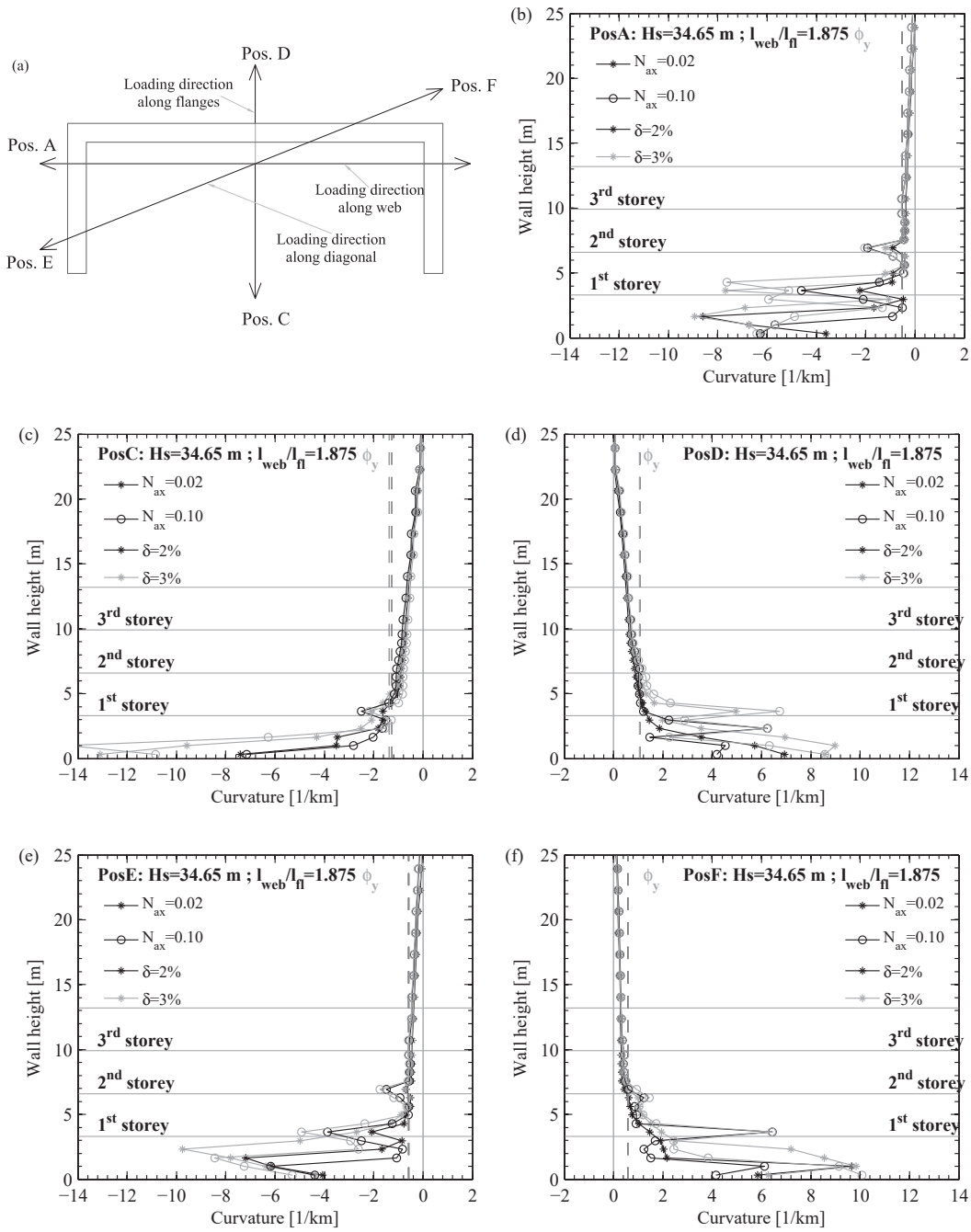


**Figure 6.27:** Curvature profiles at drifts of  $\delta = 2\%$  and  $\delta = 3\%$  for two axial load levels and for all loading positions (a-f). Results are shown for the wall model with web to flange ratio  $l_{web}/l_{fl} = 1.875$  and shear span of  $H = 34.65$  m.



The ultimate curvature from section analysis was determined as the curvature corresponding to reaching one of the two ultimate limit states, whichever occurred first: (1) bar fracture after buckling or (2) confined concrete crushing. The bar fracture limit state was considered reached when the maximum tensile strain in the reinforcement bar exceeded  $0.5\varepsilon_{su}$ . The confined concrete crushing limit state was reached when the minimum compressive strain exceeded one third of the strain estimate by [MPP88]. These values were established based on comparison with experimental results and section analysis in Section 4.6. In the shell element model, the curvature at the base of the wall  $\phi_{b2}$  was determined from the rotation above the height of  $L_{pz}$  assuming a linear curvature profile over this height.

The obtained displacement capacities are shown in terms of ultimate drift for the different loading positions and wall configurations in Figure 6.28. Several observations can be made from this figure:

- The smallest drift capacity of all the investigated loading positions often corresponds to one of the two diagonal loading positions: either with one flange end in compression (compression failure) either with the flange end in tension (tension failure). When the axial load ratio is the highest ( $n = 0.1$ ), the smallest drift capacity can correspond to position C (e.g., case of wall with  $H = 23.1$  m and  $l_{web}/l_{fl} = 2.5$ ). The latter is caused by the deep compression zones, in particular for large web to flange length ratios.
- For tension controlled failures (round markers) the drift capacity increases with increasing axial load ratio which is partially related to the higher spread of plastic deformations (see Section 6.6.1).
- For compression controlled failures (triangle markers) the drift capacity decreases with increasing axial load ratio. In addition, when the axial load ratio increases, the failure mode migrates from tension failure to compression failure for loading positions with one or both flange ends in compression. The axial load ratio should hence be limited in order to ensure sufficient drift capacity for these loading positions.

The plastic flexural displacements at ultimate  $\Delta_{p,f}$  are determined from the shell element model by integration of curvature profiles minus the predicted yield flexural displacement  $\Delta_{y,2L}/(1 + \Delta_s/\Delta_f)$ . The plastic hinge length estimates are combined with the plastic curvatures obtained from section analyses as the ultimate curvature minus the nominal yield curvature  $\phi_p = \phi_{u,PSA} - \phi_{y,PSA}$  to predict the plastic displacement at ultimate limit state. For each estimate, the centre of rotation of the plastic hinge needs to be considered accordingly to the derivation of the estimate: centre of rotation at the base of the wall [PCK07], centre of rotation at the centre of the plastic hinge length [Kaz13] and centre of rotation at one third  $L_{pz}$  from base [BA11]. Only the estimates by [BA11] are compared here and hence only the equation for this case is given, but conclusions in this section apply to all other estimates discussed above. The following estimates of the plastic displacements at ultimate were hence used:

$$D_{p,[BA11]} = L_{ph,[BA11]} \phi_p \left( H - \frac{2}{3} L_{ph,[BA11]} \right) \quad (6.21)$$

## Chapter 6. Yield and ultimate displacement of U-shaped walls

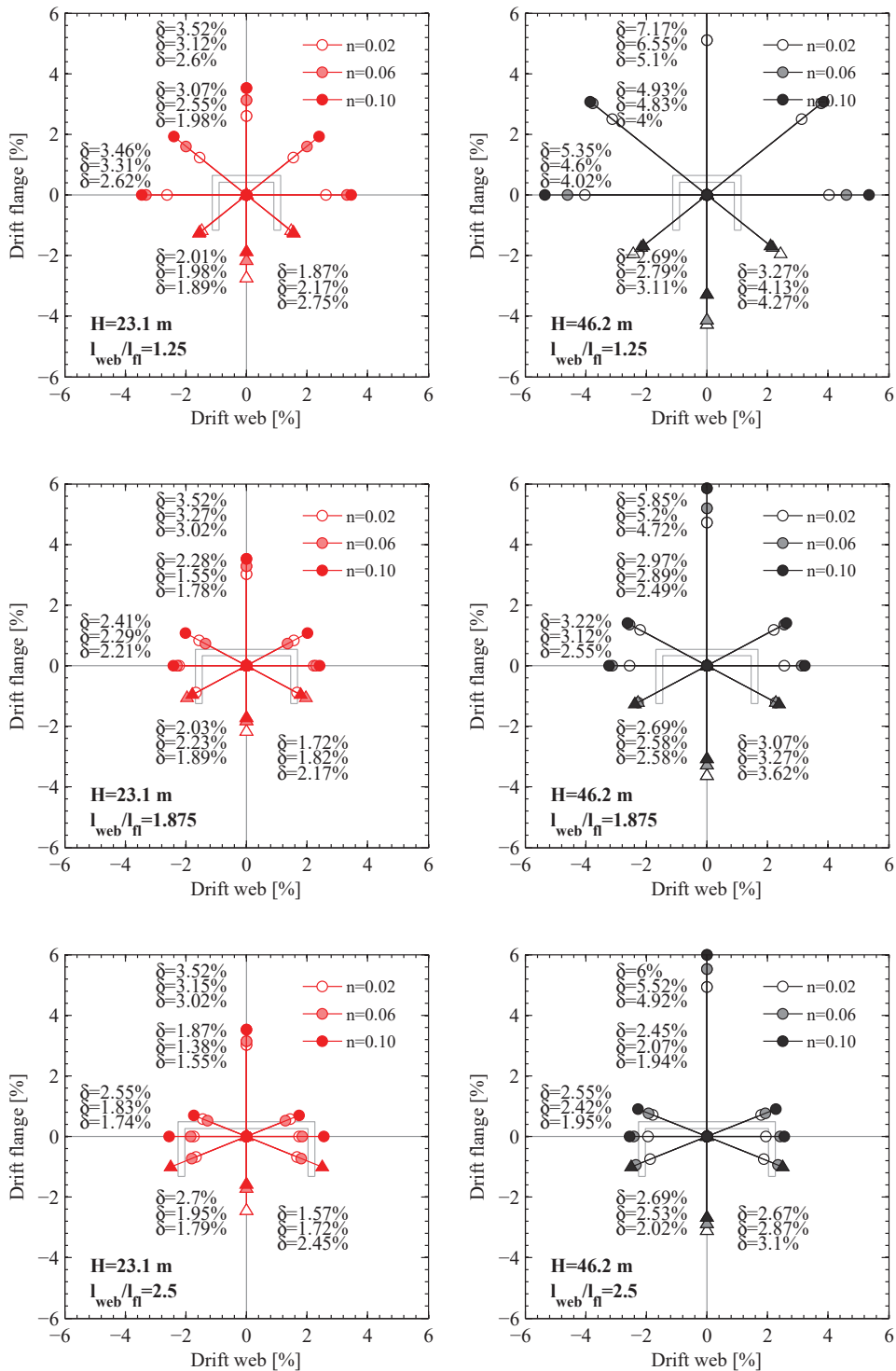


**Figure 6.28:** Ultimate drift capacities of the different wall configurations accounting for tension failure due to bar fracture (round marker) and for compression failure due to confined concrete crushing (triangle marker). The axial load ratio  $n$  is indicated by the full, half-full or empty markers. The ultimate drift values  $\delta$ , three for each loading position correspond to axial load ratios: the value placed down to  $n=0.02$  while the placed upper of the three to  $n=0.1$ .

In the estimates, the wall length was taken as equal to the web length at positions A, E and F and equal to the flange length at positions C and D. The shear stress  $\tau$  plotted in Figure 6.32 was computed at positions A, E and F as the average shear stress on the web while at C and D as the average shear stress on the flanges. Shear demands were obtained from the section analysis moments

The comparison between the estimates for the plastic flexural displacement and numerical results is done for each loading position with respect to the wall length (Figure 6.30), shear span (Figure 6.29), axial load ratio (Figure 6.31) and shear stress demand (Figure 6.32). From these comparisons the following observations can be made:

- The plastic displacement is typically underestimated for most loading positions, which is in line with the purpose of the  $L_{ph}$  estimate by [BA11] that are intended as a lower bound. At position F, the plastic displacement is however significantly overestimated especially for walls with low axial load ratio and long webs. The overestimation of the plastic hinge length at position F was also observed when comparing the equations by [BA11] with the experimental data (Section 4.5.3).
- The trend of the plastic hinge length with the axial load ratio is not well captured by the estimates by [BA11]. Increasing axial load results in more pronounced inelastic curvature spikes at the storey levels and hence larger plastic zone heights  $L_{pz}$ . [BA11] had found that increased axial load reduces the spread of inelastic curvatures over the wall height. The difference between the two cases lies in the application of the axial loads: distributed at each storey level in the study presented herein and concentrated at the top of the wall in the study by [BA11].
- The variation of the plastic displacement with the shear stress demand is also not well captured (Figure 6.32). [BA11] argued that for planar walls, it is not necessary to account for the shear stress demand in the expression of  $L_{ph}$  as long as the shear span and the wall length are accounted for. However for non-planar walls, varying wall dimensions other than  $l_{wall}$  or  $H$  can modify the shear stress demand, which in turn affects the tension shift effects due to diagonal cracking and hence the plastic hinge length. For example, at position C, increasing the length of the web  $l_{web}$  increases the shear stress demand on the flanges while the wall length does not modify. Hence the increase in shear stress is not accounted for in the expression of  $L_{ph}$ . Overall  $L_{ph}$  values corresponding to large shear stresses are underestimated while the values corresponding to low shear stresses are overestimated.

## Chapter 6. Yield and ultimate displacement of U-shaped walls

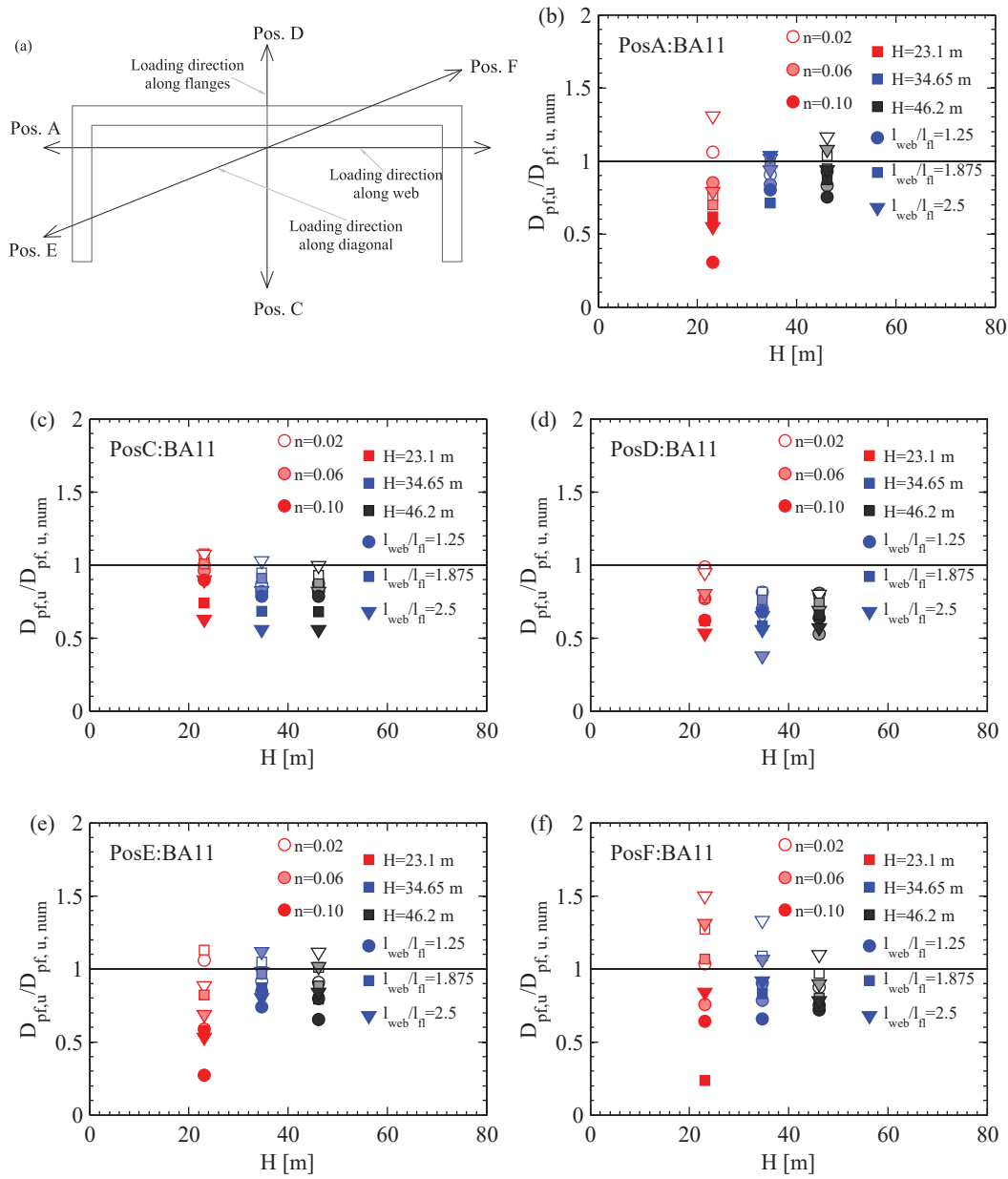


**Figure 6.29:** Comparison between the numerically determined plastic displacement at ultimate limit state and the predicted displacements using plastic hinge length estimates by [BA11] with respect to the wall shear span  $H_s$ .

## 6.6. Plastic hinge lengths

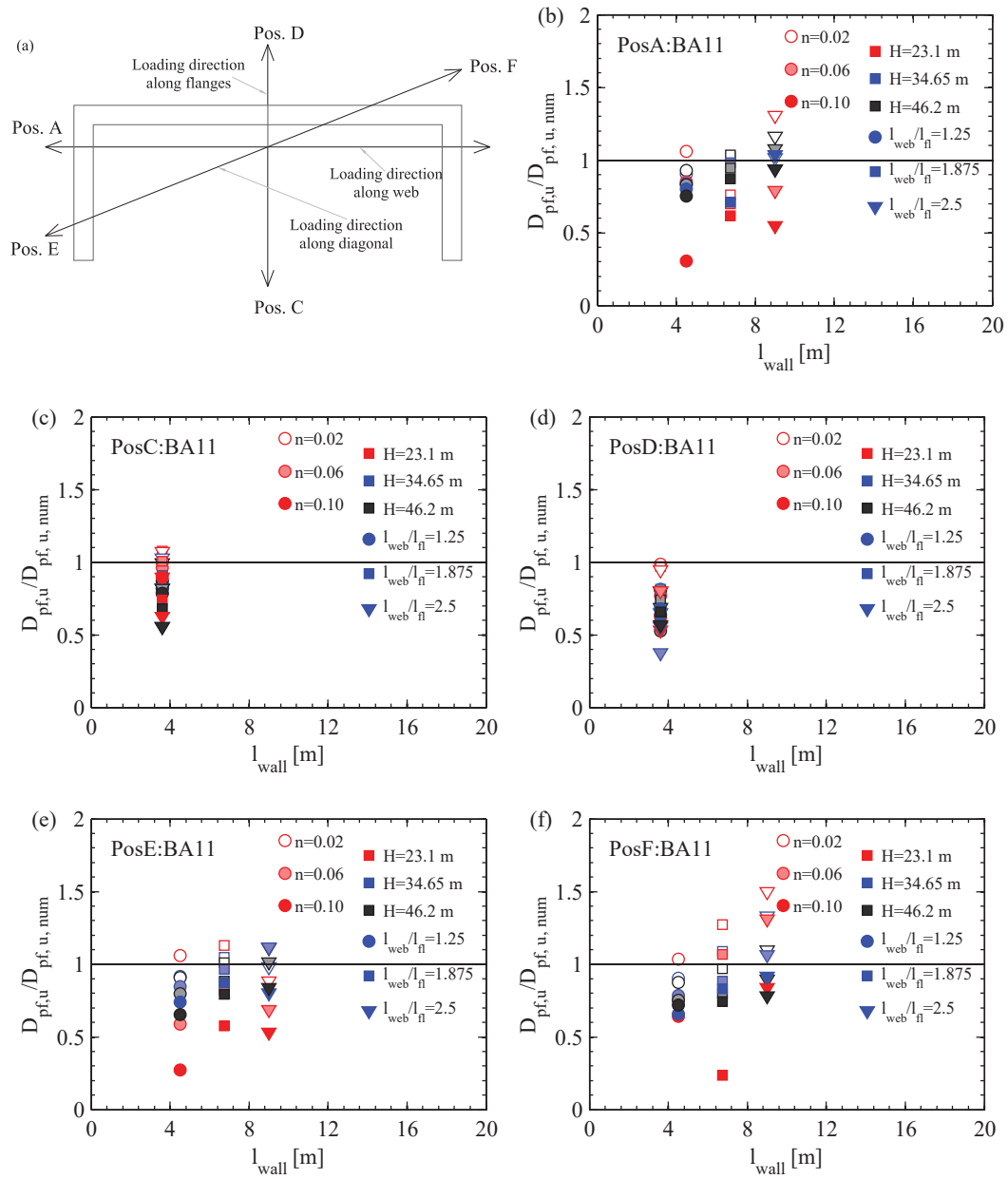


**Figure 6.30:** Comparison between the numerically determined plastic displacement at ultimate limit state and the predicted displacements using plastic hinge length estimates by [BA11] with respect to the wall length  $l_{wall}$ .

## Chapter 6. Yield and ultimate displacement of U-shaped walls

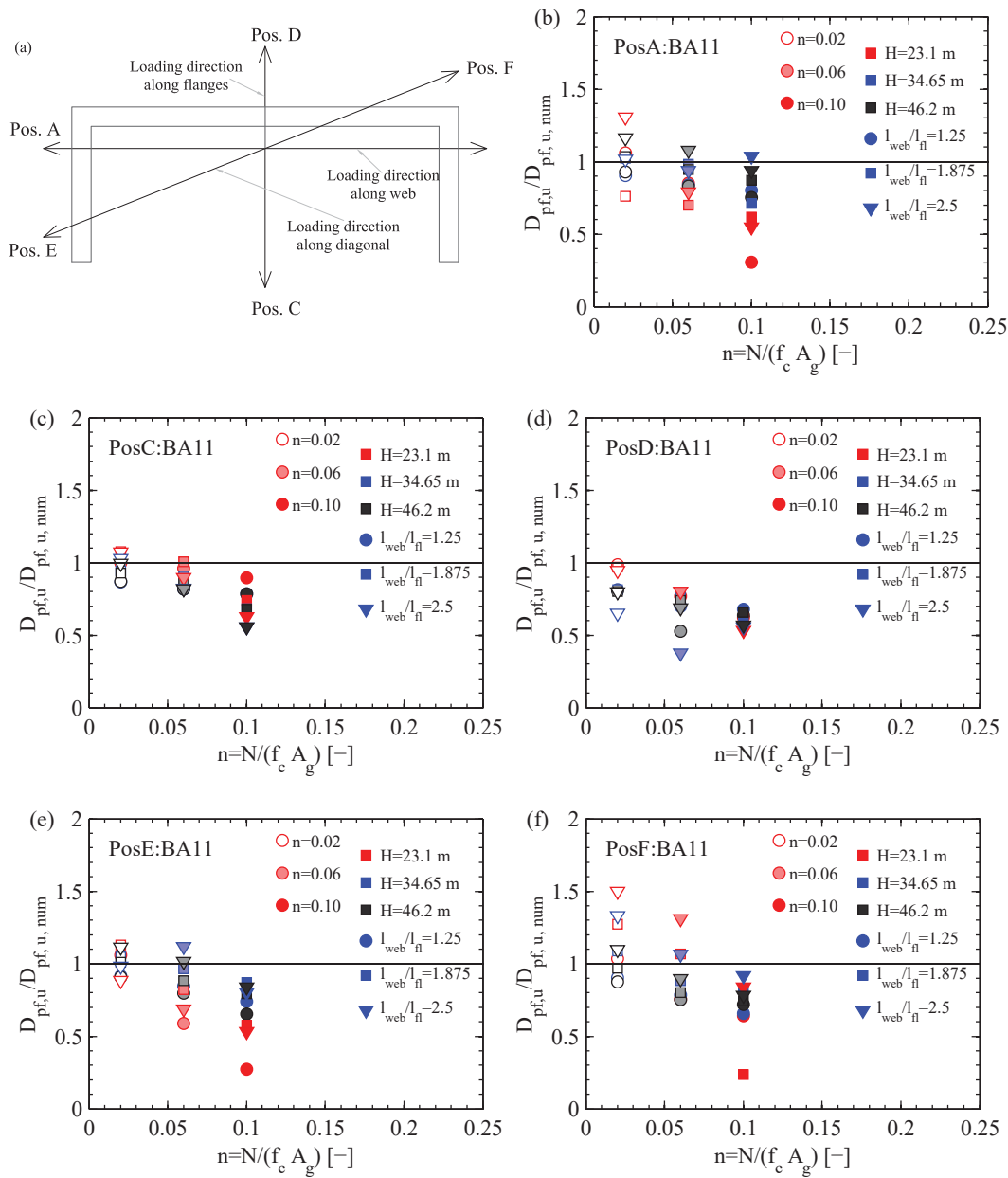


**Figure 6.31:** Comparison between the numerically determined plastic displacement at ultimate limit state and the predicted displacements using plastic hinge length estimates by [BA11] with respect to the axial load ratio  $n = N / (f_c A_g)$ .

## 6.6. Plastic hinge lengths

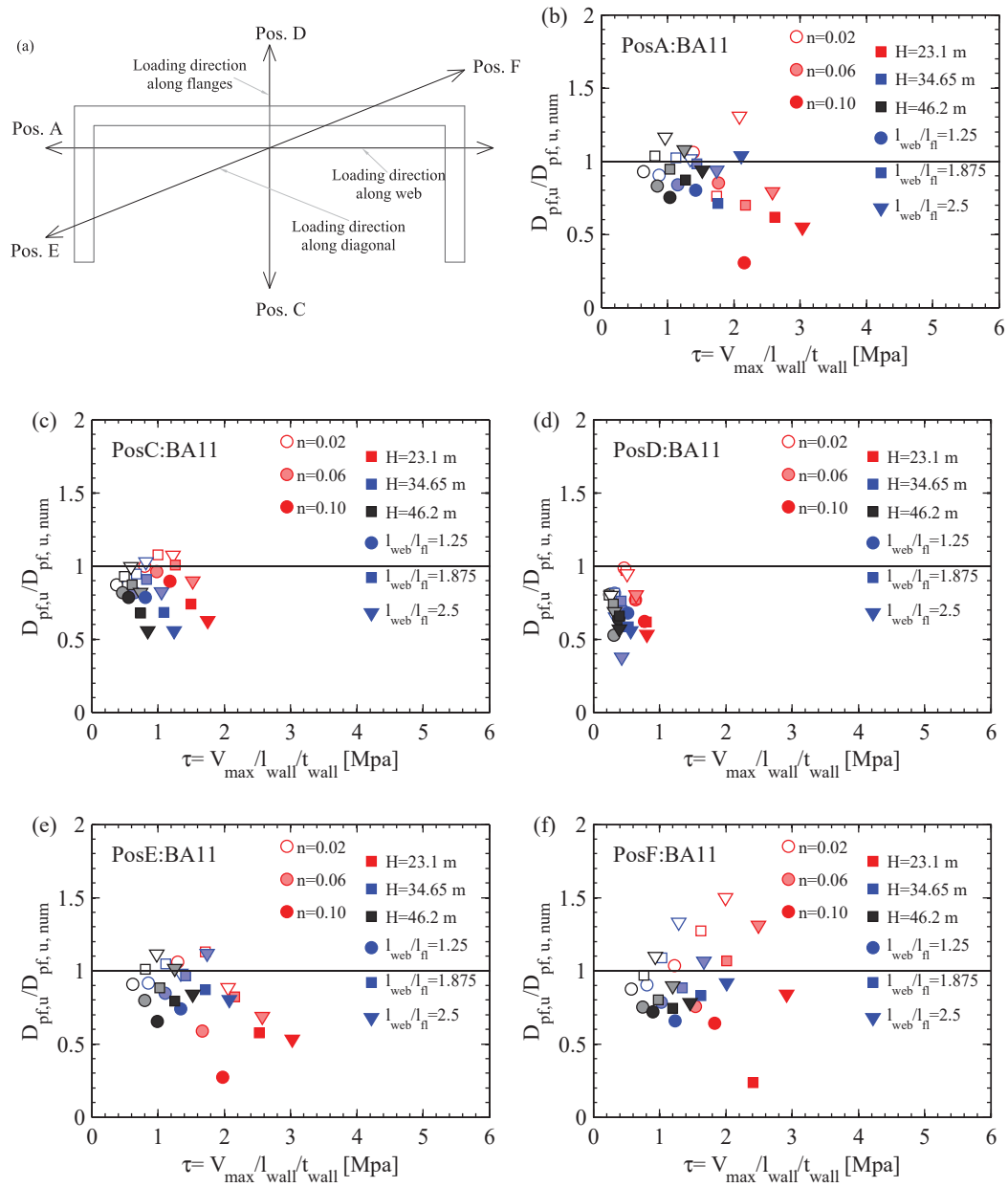


**Figure 6.32:** Comparison between the numerically determined plastic displacement at ultimate limit state and the predicted displacements using plastic hinge length estimates by [BA11] with respect to the shear stress demand  $\tau$ .

### 6.6.3 Plastic hinge length

Based on the observations from the comparison of the plastic displacements with the estimates, results from the shell element model are used in this section to propose new estimates for the plastic hinge length  $L_{ph}$ . The plastic hinge length was derived from the shell element model by back-calculating its value from the numerical ultimate displacement (Equation 6.23). In this equation, it is assumed that the center of rotation of the plastic hinge is located at  $2/3L_{ph}$  from the wall base.

$$L_{ph} = 1.5H - \sqrt{2.25H^2 - \frac{6\Delta_p}{\phi_p}} \quad (6.22)$$

#### 6.6.3.1 Trends with wall length, shear span, axial load ratio and shear stress

The trends of the obtained  $L_{ph}$  values with respect to shear span, wall length, axial load ratio and shear stress are shown in Figures 6.33 to 6.36 for the different loading positions. The main observations from these figures are summarised in the following:

- Plastic hinge length increases with the wall shear span due to moment gradient and with the wall length due to tension shift effects caused by the diagonal cracking. These trends are confirmed by the Figures 6.33 and 6.32. The wall length corresponding to positions C and D is the length of the flanges  $l_{fl}$  which was not varied during the parametric study.
- Increasing the axial load ratio increases the plastic hinge length due the development of inelastic curvature spikes at the storey level for the larger axial load ratios as previously discussed.
- Plastic hinge length increases with increasing shear stress demand as it contributes to the tension shift effects. Walls with large shear spans  $H$  have high slenderness ratios  $H/l_{wall}$  and hence low shear stress demands but can have large plastic hinge lengths due to the shear span contribution (see Figure 6.36). As already mentioned, the shear stress demand should be accounted for in the expression of the plastic hinge length since for non-planar walls, modifications of different wall dimensions other than  $l_{wall}$  and  $H$  can modify the shear stress demand and hence the plastic hinge length due to the tension shift effects caused by diagonal cracking (e.g., position C in Figure 6.36c).

#### 6.6.3.2 New estimates for plastic hinge lengths

The  $L_{ph}$  values obtained from the shell element model are used in this section to derive new estimates for plastic hinge lengths of U-shaped walls. The objective is to obtain a general expression for all the loading positions. The variation of the plastic hinge length with the loading position is to be accounted for through the wall length and the shear stress demand.



## 6.6. Plastic hinge lengths

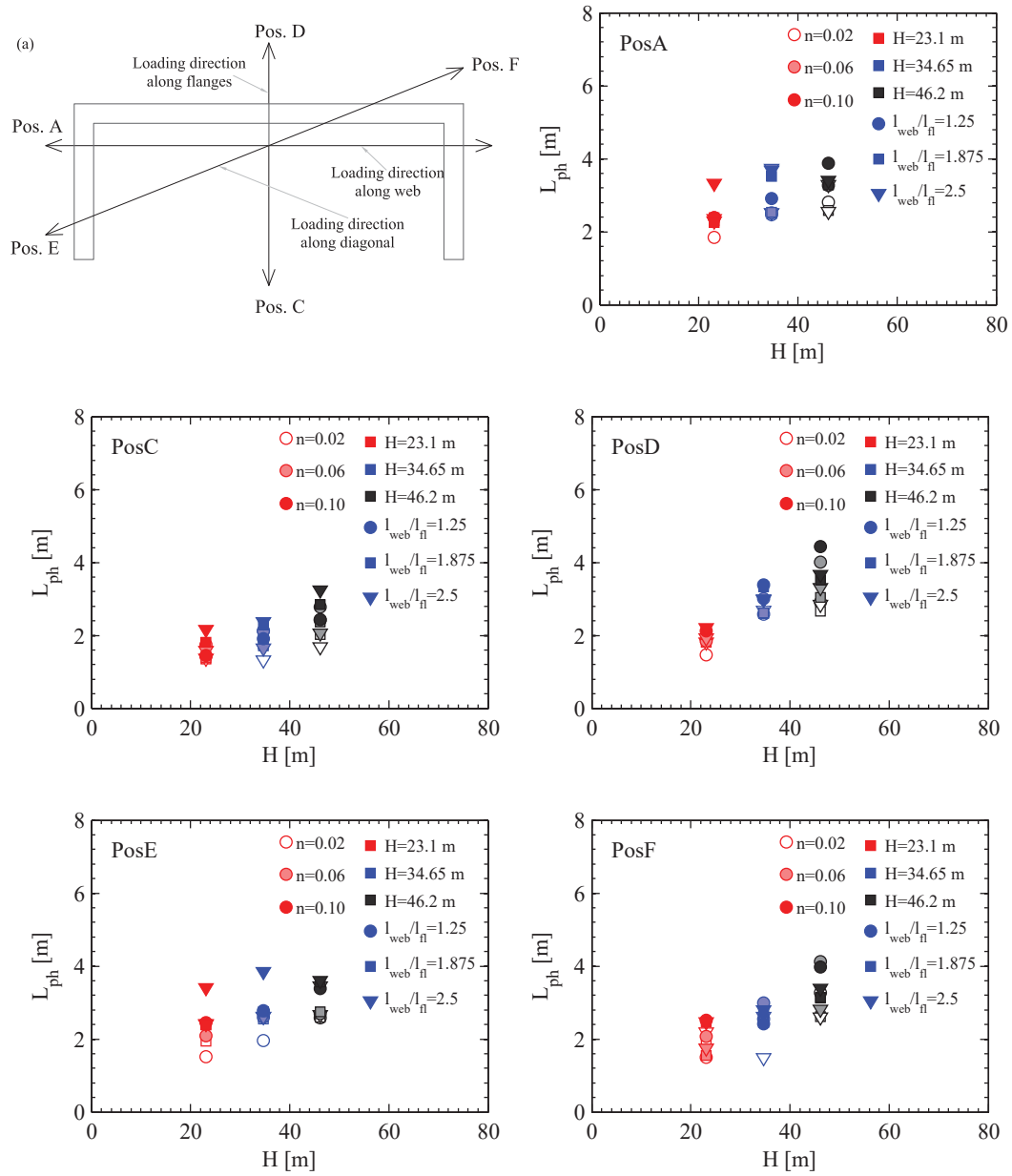


**Figure 6.33:** Trends of the plastic hinge length values determined from the shell element model with respect to the shear span  $H_s$ .

## Chapter 6. Yield and ultimate displacement of U-shaped walls

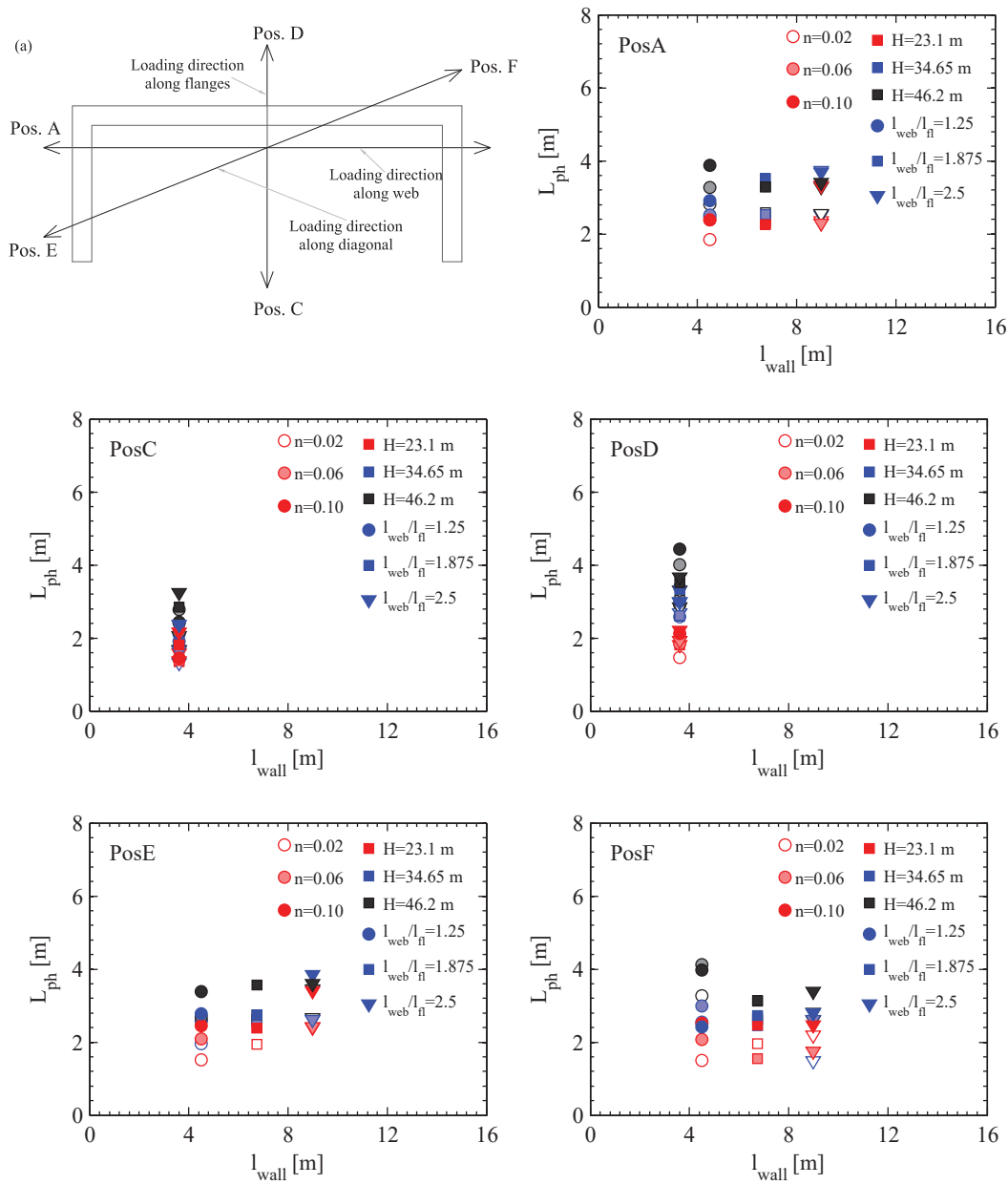


**Figure 6.34:** Trends of the plastic hinge length values determined from the shell element model with respect to the shear stress demand  $l_{wall}$ .

## 6.6. Plastic hinge lengths

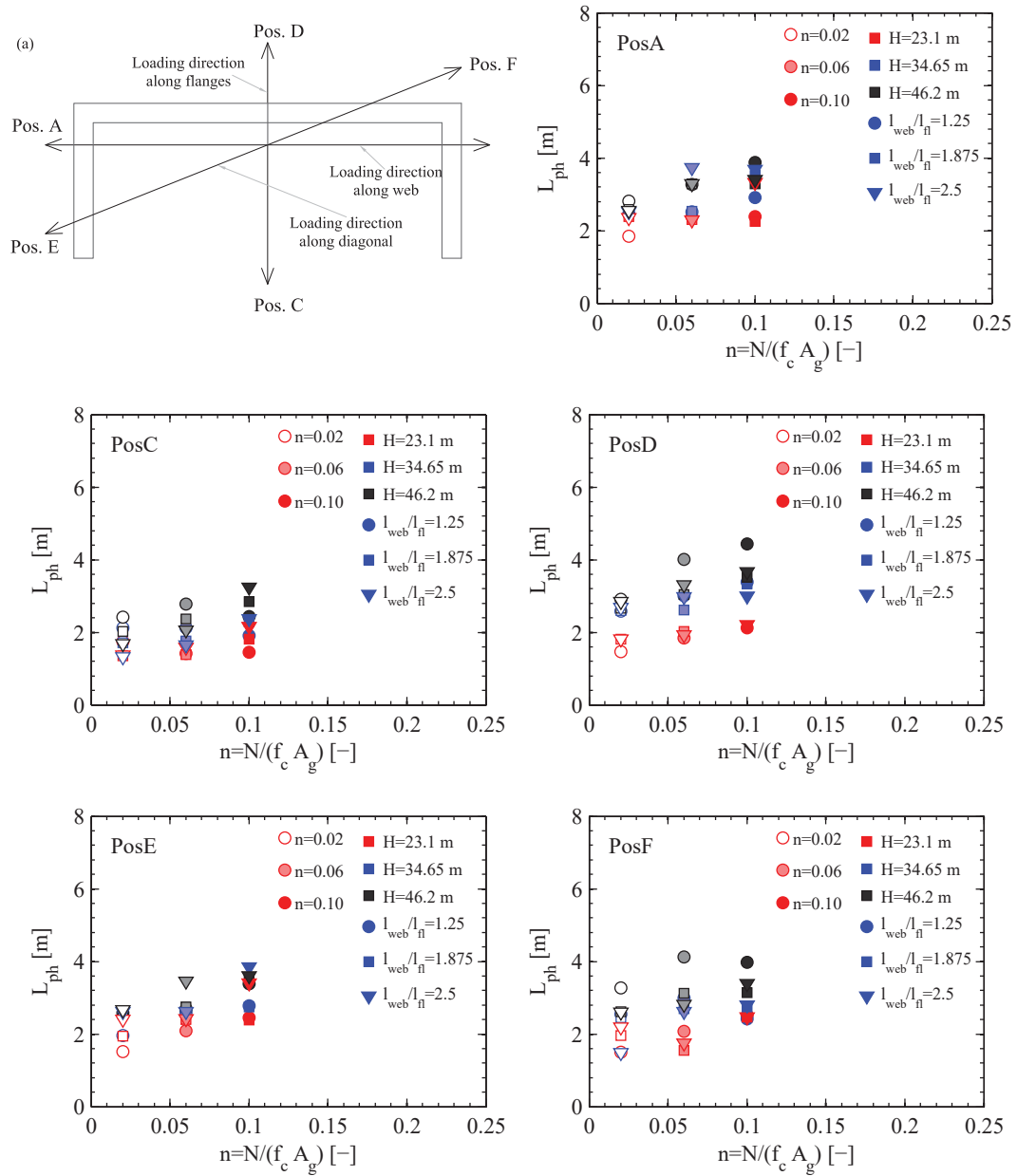


**Figure 6.35:** Trends of the plastic hinge length values determined from the shell element model with respect to the axial load ratio  $n = N/(f_c A_g)$ .

## Chapter 6. Yield and ultimate displacement of U-shaped walls

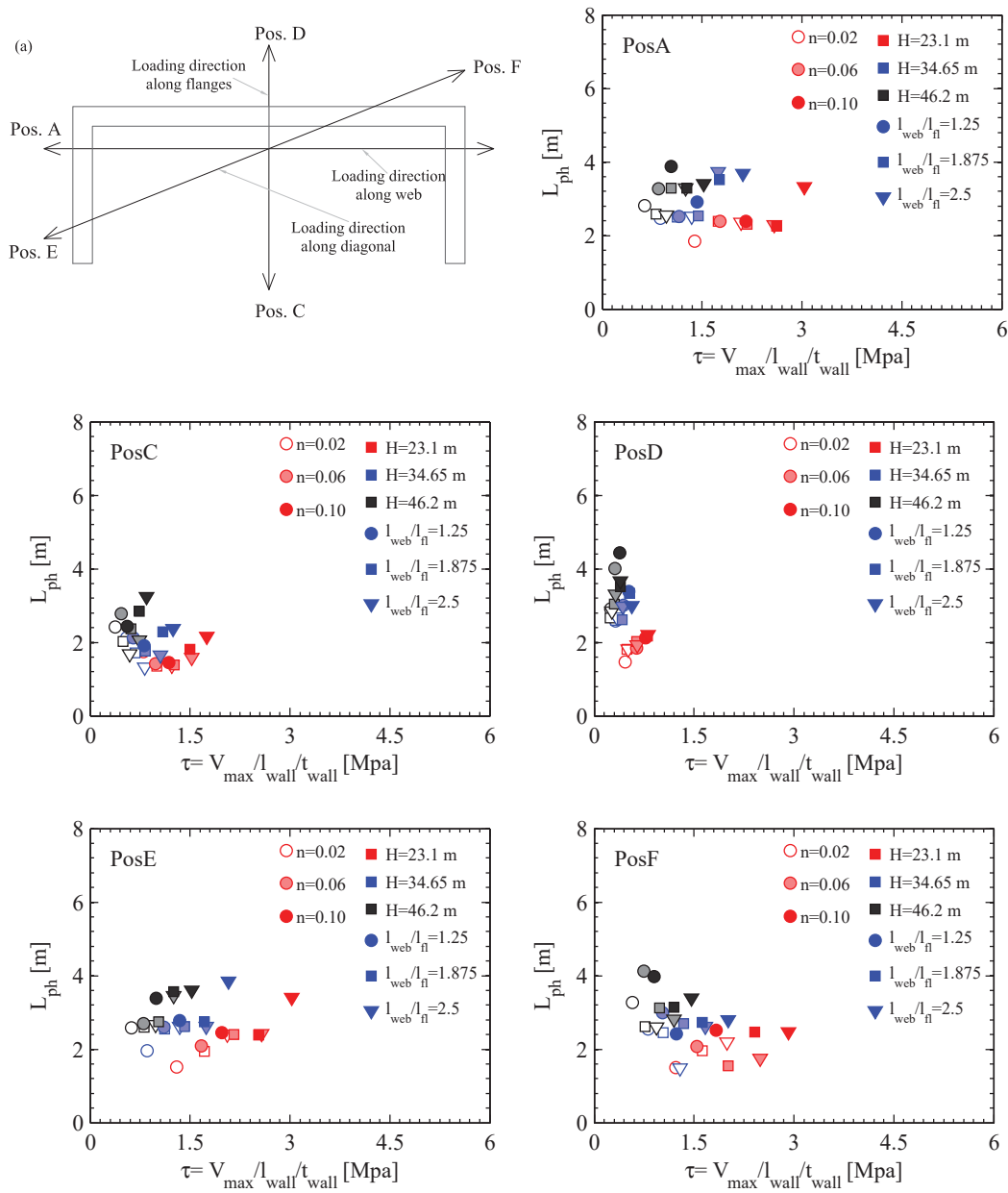


**Figure 6.36:** Trends of the plastic hinge length values determined from the shell element model with respect to the shear stress demand  $\tau$ .

In the following, in order to evaluate the importance of the different variables in predicting the plastic hinge length, these variables are introduced consecutively in the general expression of the plastic hinge length which is fitted to the  $L_{ph}$  values from the numerical model. The data fitting was performed using a nonlinear least square solver as implemented in Matlab [Mat13] software (@lsqnonlin function) which minimises the sum of squares of the residuals.

The general form of the equation that is first considered is  $L_{ph} = a_1H + a_2l_{wall}$  is the simplest plastic hinge equation for walls, accounting only for the shear span and the wall length. The obtained coefficients of the data fitting, the mean of the ratio between predicted and numerical  $L_{ph}$  value and the coefficient of variation are given in Figure 6.37a. This figure shows that the equation does not capture at least one trend, as predicted values display rather constant value bands for the same shear span value.

Next, the average shear stress is added into the general form of the equation under the form of a ratio of demand to capacity, i.e., of shear stress demand on the wall to the shear stress at diagonal cracking (taken as  $0.17\sqrt{f_c}$  [ACI11] with the coefficient of 0.17 included in the coefficient of  $l_{wall}$ ).

Considering the influence of the average shear stress, improves the fit of the equation with the numerical data (Figure 6.37b), except for the slender walls (large shear span - black markers) where shear stresses are small and hence do not influence the tension shift effects due to diagonal cracking. If in addition to the average shear stress, the axial load ratio is included in the general equation, the trends are now well captured (Figure 6.37c). The final form of the proposed  $L_{ph}$  estimate is given in Equation 6.23. The final mean error of the predicted to numerical  $L_{ph}$  value is 0.98 and a coefficient of variation of  $COV = 18\%$  is obtained.

$$L_{ph} = (0.05H + 0.05l_{wall} \frac{\tau}{0.17\sqrt{f_c}})(1 + 4n) \quad (6.23)$$

In the above equation, at position A and E, the wall length was taken as the length of the web and the shear stress  $\tau$  as the average shear stress corresponding to the web and determined using section analysis. At positions C and D, the length of the flanges and the shear stress on the flanges was considered, with the shear force in the direction of the flanges equally distributed between the flanges.

Initially at position F, the same wall length and average shear stress as for positions A and E were considered. However, after examining the strain profiles for these loading position (Figure 6.38) as discussed in the following, it was decided to take the wall length and the average shear stress on the section as the mean between the web and the flange, i.e.,  $l_{wall} = (l_{web} + l_{fl})/2$  and  $\tau = (\tau_{web} + \tau_{fl})/2$ . It was observed that the tensile strains that control the curvature profile for this loading position (SW corner in Figure 6.38) and hence the plastic hinge length are influenced by both the web and the flange characteristics. Considering  $l_{wall} = l_{web}$  would best describe the tensile strain distribution at the NW corner (Figure 6.38c) while considering  $l_{wall} = l_{fl}$  would not account in any way for the influence of the web which carries a significantly larger shear force than the flanges at this loading position. It was assumed that at position F, the entire shear force in the direction of the flanges is carried by one flange only.

## Chapter 6. Yield and ultimate displacement of U-shaped walls

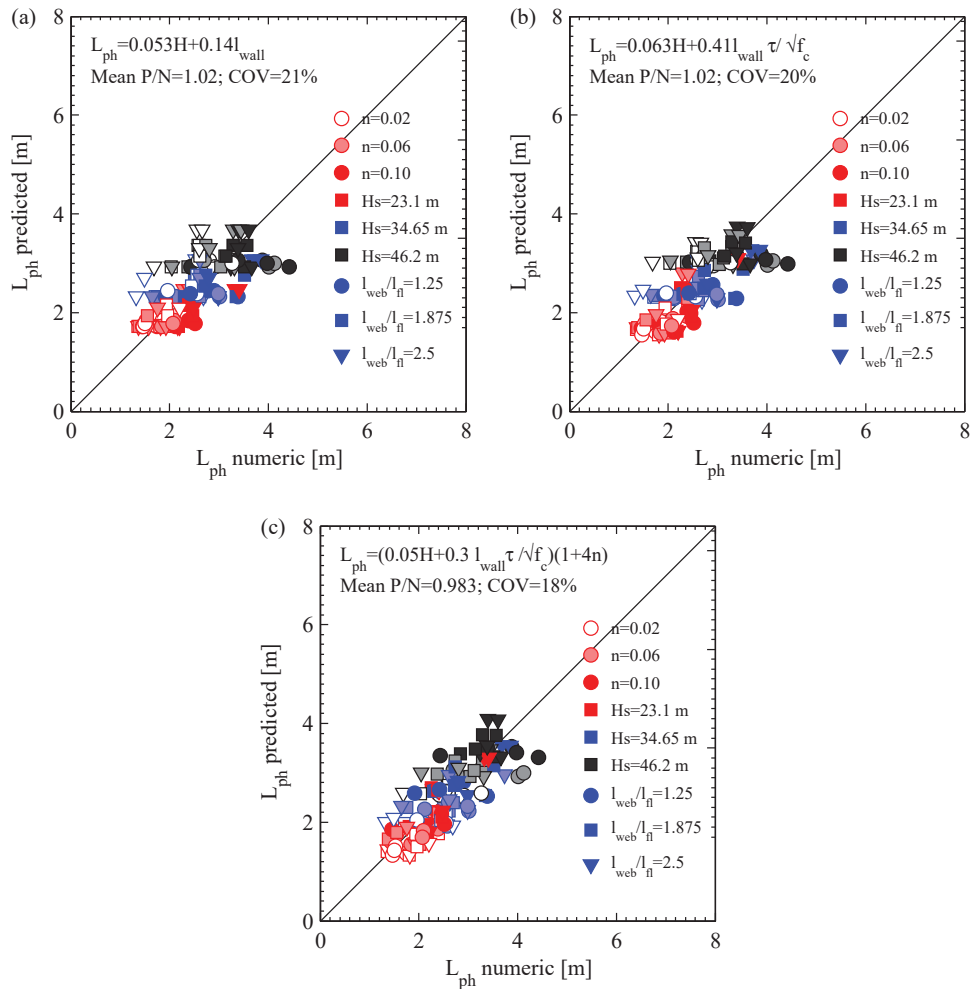


**Figure 6.37:** Fitting of the  $L_{ph}$  values with different equations accounting for: wall length  $l_{wall}$  and shear span  $H_s$  (a) and shear stress  $\tau$  (b) and axial load ratio  $n$  (c).

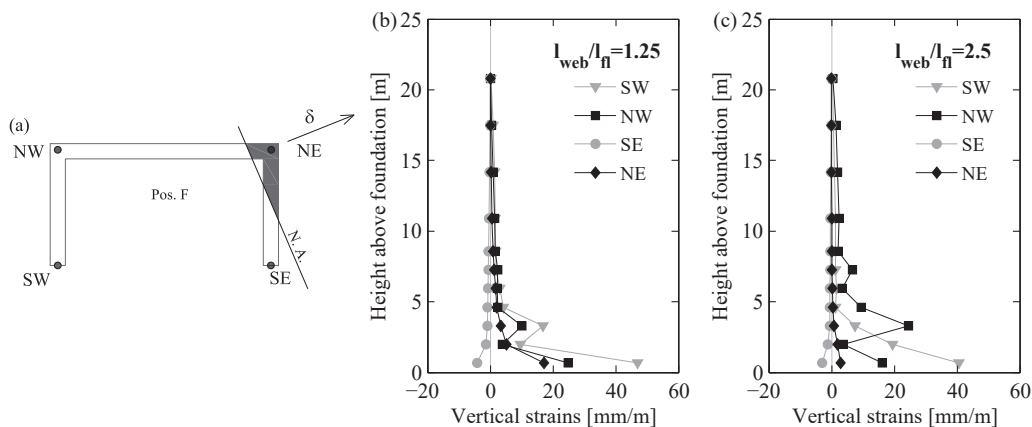


**Figure 6.38:** Vertical strain profiles over the height at position F at the edges of the mid-surface of the wall at position (a). Strains are shown for a wall with a shear span of  $H = 23.1$  m, axial load ratio of  $n = 0.06$  and with the web to flange length ratio of  $l_{web}/l_{fl} = 1.25$  (b) and  $l_{web}/l_{fl} = 2.5$  (c).

The obtained scatter of predicted to observed plastic hinge length results from predicting the plastic hinge length for all loading directions with a single equation. Only at positions C and D, the coefficient corresponding to the wall length  $l_{wall}$  are about twice as those obtained for positions A, E and F. However, the estimate of this coefficient is not very robust since the flange length was not varied within the parametric study. For positions C and D, one has therefore only one  $l_{wall}$  value. The web length, on the other hand, which was considered as wall length for the other positions, was varied between  $l_{web} = 4.5 - 9.0$  m. Having flange lengths that are larger than the web length would lead to wall geometries not commonly encountered in practice and hence their variation was not considered in the design of the parametric study.

A previous study on the plastic hinge length of columns has differentiated between the plastic hinge length associated to tension failure and the one associated to compression failure, to account for the different spread of plasticity on the tensioned and on the compressed side of the wall [GF<sup>+</sup>15]. For the walls in the parametric study presented herein, from 135 analyses results, 89 were tension controlled failures and the rest were compression controlled. The confined concrete crushing limit state was determining for all walls at position C and to walls with large axial load ratios at position E. However, it was found that the failure type (tension or compression controlled) does not influence the value of the plastic hinge length when ultimate limit strains of  $0.5\epsilon_{su}$  and  $1/3\epsilon_{cu,[MPP88]}$  are used for the steel limit strain and concrete limit strain respectively (Section 4.6).

**Table 6.2:** Coefficients for the general form of the plastic hinge length equation  $L_{ph} = (a_1H + a_2l_{wall} \frac{\tau}{0.17\sqrt{f_c}})(1 + a_3n)$  when fitting the individual loading positions.

Pos.	$a_1$	$a_2$	$a_3$	Mean $(\frac{L_{ph,predicted}}{L_{ph,numeric}})$	COV (%)
A	0.055	0.056	2.5	1.02	12
C	0.040	0.099	3.6	1.01	15
D	0.059	0.129	3.6	1.00	9
E	0.049	0.063	2.8	0.99	9
F	0.058	0.058	2.7	1.01	16

## 6.7 Conclusions

Yield curvature, yield displacements, effective stiffness ratios and plastic hinge lengths were derived from monotonic analyses of a detailed shell element model for U-shaped walls validated against experimental data. The numerical results obtained from the model were compared to several existing estimates as well as to the newly developed estimates. For each of the quantities, the following conclusions were drawn:

**Yield curvature** : New estimates for the yield curvature of U-shaped walls under any loading direction were proposed. Yield curvatures obtained from section analyses were compared to the yield curvatures obtained from the shell element model analyses and were found to match well for all analysed wall geometries.

**Yield displacement** : A new equation of the yield displacement proposed in Chapter 4 was expressed as the sum of the displacement components at yield, i.e., flexural displacements due to wall deformation and shear displacements. The new feature of the model is that it accounts for the partially cracked wall over the height at yield through an assumed bi-linear curvature profile. The new equation was verified for walls with a broad slenderness ratio  $2.6 \leq H/l_{wall} \leq 12.8$ . By comparison, yield displacement estimate based on the assumption of a linear curvature profile at yield led to rather high estimates of the yield displacement for the more slender walls ( $H/l_{wall} > 4$ ) since it overcompensated for the shear deformations, which are reduced for very slender walls.

**Effective stiffness** : Effective stiffness ratios obtained from the shell element model varied with wall geometry and loading direction were well captured by the prediction based on the new yield displacement estimate. Existing estimate by [PP92] also matched well on average the shell element model results but did not capture the influence of diagonal cracking on the cracked height and hence on the flexural flexibility. Modifying this estimate to account for the cracked height improved the match between the effective stiffness ratio estimates and the numerically obtained ones. The prediction based on the yield displacement estimate assuming a linear curvature profile led to high stiffness estimate for the walls with low slenderness ( $2.56 < H/l_{wall} < 4$ ) and to low stiffness estimate for the slender walls ( $H/l_{wall} > 4$ ).

**Plastic hinge lengths** : These lengths were found to increase with increasing axial load ratio. Unlike previous studies on the plastic hinge lengths of walls which considered that the axial load ratio is entirely applied at the top of the wall, in this study the axial load was considered to be applied at the storey levels. This modelling assumption led to spikes of inelastic curvatures just above the storey level where the axial loads were introduced, as the ratio of moment demand to moment capacity was largest above the storey level. In addition, the shear stress was found to be important in the prediction of the plastic hinge length for non-planar. For such walls, changing a wall dimension other than the shear span or the wall length in the direction of loading can modify the shear stress and hence plastic hinge length due to tension shift effects. Therefore, a new expression for the plastic hinge length was proposed for all the loading directions and it accounts for the shear stress on the wall in addition to the wall length, shear span and axial load ratio. It was found that the same plastic hinge lengths can be used for tension or the compression controlled failures as long as suitable concrete limit strains are used in section analysis to determine the ultimate curvature.



# 7. Summary, conclusions and outlook

## 7.1 Summary and conclusions

Reinforced concrete (RC) core walls are widely used as the main lateral load resisting element in mid- to high-rise buildings. Despite its popularity, studies on the seismic response of RC core walls remain scarce and their inelastic behaviour has only relatively recently been investigated through few experimental and numerical studies [RF01], [BDP08b] and [LL<sup>+</sup>13]. This study complements the previous ones by highlighting the importance of the diagonal loading direction in the analysis and design of U-shaped walls and by adapting quantities of the plastic hinge model for the analysis of U-shaped walls. The main contributions of this study are: (1) provide experimental data on the behaviour of U-shaped walls under diagonal loading, (2) evaluate the limits of applicability of plane section analysis for determining the strength and displacement capacity of U-shaped walls and (3) adapt equations for the deformation quantities of the plastic hinge model for the analysis of U-shaped walls. New or modified equations were proposed for the following quantities: yield curvatures, yield displacements, plastic hinge lengths and ultimate strain limits for section analysis for compression controlled failure. The most important findings and conclusions are discussed in the following.

### Behaviour of U-shaped walls under diagonal loading

An experimental campaign on two U-shaped walls (TUC and TUD) was presented in terms of test set-up, loading history and experimental findings in Chapter 3. The walls were tested under quasi-static cyclic loading in the directions of the geometric diagonals of the U-shaped section. The experimental results provided insights into the behaviour of U-shaped walls under diagonal loading.

### Failure modes

It was found that the flange ends are subjected to a significant longitudinal strain gradient across the flange width, which promotes out-of-plane buckling of the flange ends (failure mode of TUC).

In addition, when loading with the flange end in compression, the compression zone is very deep and extends over almost the entire flange length. Therefore, the wall is prone to brittle compressive failures over a significant part of the flange length (failure mode of TUC).

### **Influence of longitudinal reinforcement distribution**

The influence of the distribution of the longitudinal reinforcement within the section on the wall behaviour was experimentally evaluated. Distributing the reinforcement uniformly within the section was found to reduce the crack widths and as a consequence also the shear deformations. In addition, the longitudinal reinforcement distribution was found to influence the failure modes. The larger the longitudinal reinforcement content of the boundary element, i.e., the more the longitudinal reinforcement is concentrated in the boundary elements, the more susceptible the boundary element is to failure due to out-of-plane bending. The distributed reinforcement layout, on the other hand, leads to larger compression zone depths, which increases the susceptibility to concrete crushing.

### **Plane section assumption**

Finally, the experimentally determined longitudinal strain profiles along the wall perimeter confirmed the invalidity of the assumption that plane sections remain plane. This manifested itself in particular in non-linear strain profiles and additional compression zones at the intersections of web and flange .

### **Limits of application of the plane section analysis to U-shaped walls**

Despite the invalidity of the plane section assumption, it remains an analysis that simplifies analyses considerably and therefore its limitations in predicting the strength and displacement capacity of U-shaped walls were investigated. Monotonic plane section analysis was used to model a set of four U-shaped walls that were tested under bi-directional loading.

### **Strength prediction**

Plane section analysis was found to yield reasonable estimates of the wall strength for bending in the principal directions but significantly overestimated the experimentally attained wall strength for bending in the diagonal direction. The causes of this overestimation were identified by means of a shell element model validated against the experimental data and analysed for different loading histories and directions: monotonic, cyclic unidirectional and cyclic bidirectional.

The difference in strength between the monotonic and the cyclic uni-directional analyses was relatively small and was assigned to shear lag effects. For cyclic loading, the crack widths tend to be larger and upon load reversal open along the entire length of the wall. As a result, the shear deformations tend to be larger under cyclic than under monotonic loading. However, the difference between the cyclic unidirectional and cyclic bidirectional loading was more significant and indicated that capturing the loading history of the reinforcement bars was critical in predicting accurately the wall strength.

The loading history of the bars could be incorporated in a cyclic plane section analysis by including unloading and reloading rules for steel models while shear lag effects can be accounted for through effective flange widths.

### Curvature prediction

Monotonic plane section analyses predicted well the yield and ultimate curvatures for U-shaped walls. Despite the invalidity of the assumption that plane sections remain plane, the experimentally determined ultimate curvatures were well predicted by section analysis as long as suitable ultimate strain limits were used. To this purpose ultimate limit strains for confined concrete crushing were adapted for use with section analysis based on comparison with experimental results. For limit states controlled by reinforcement bars (buckling and rupture after buckling) limit strains reported in the literature yielded good results.

### Application of plastic hinge model to U-shaped walls

The plastic hinge model is very popular with design engineers because it is relatively simple to apply and it yields—if properly calibrated—robust predictions of the displacement capacity of RC members undergoing inelastic deformations. These predictions are simple to obtain and are particularly useful during early phases of the design process. Up to today, equations for yield curvatures and plastic hinge lengths have been proposed for walls with rectangular, barbelled or box-shaped cross sections. This study extends the application of the plastic hinge model to U-shaped walls by: (1) providing new yield curvatures for any loading direction because these were previously available only for the principal loading directions, (2) by modifying the yield displacement equation to account for the partially cracked height because the previous equation, which assumed a fully cracked wall at yield, was found to be too simplifying, (3) by adapting the ultimate limit strain for compression controlled failure for use with section analysis, and (4) by adapting the plastic hinge length equation to include the influence of the average shear stress on the section.

### Yield displacement

From the observation of the experimentally obtained curvature profiles at yield, a new equation for the yield displacement was proposed. The yield displacement is computed as the sum of contributions of the flexural displacement due to wall deformation and shear displacements. The novelty lies in assuming a bi-linear curvature profile at yield to account for the partially cracked height of the wall. The new equation captures well the yield displacement for walls with a wide range of slenderness ratios ( $2.6 \leq H/l_{wall} \leq 12.8$ ). The simplifying assumption of a linear curvature profile at yield results in overestimations of the yield displacements for rather slender walls ( $H/l_{wall} > 4$ ). The newly proposed approach, which is based on a bilinear curvature profile, can be extended to any wall geometry as long as yield curvatures, cracked heights, shear displacements and strain penetration lengths are well predicted.

### Ultimate displacement

The displacement capacity can be estimated using plastic hinge lengths that vary for the different loading directions combined with ultimate curvatures from section analyses. Shear displacements should be included when predicting the wall displacement capacity, since their contribution was found to be significant even for slender U-shaped walls.

## Chapter 7. Summary, conclusions and outlook

---

The results of a parametric study using the validated shell element model showed that the plastic hinge lengths of U-shaped walls depend on the wall length, the shear span, the axial load ratio and the average shear stress on the section. The influence of the loading direction was included through the wall length and through the average shear stress, which differs for the different loading positions. The inclusion of the average shear stress is novel and was found necessary in order to account for the influence of changes in the core wall geometry not accounted for through the wall length. Contrary to previous plastic hinge length equations that include the influence of the axial load on the spread of plasticity, the plastic hinge length was found to increase with increasing axial load ratio. The difference comes from the assumption on the distribution of the axial load ratio over the wall height: distributed at each storey level in this study and applied at the top of the wall in previous studies.

### **Importance of considering the diagonal loading direction**

When analysing U-shaped walls, the designer should consider besides the loading cases in principal directions of the section also the loading in the direction of the geometric diagonal of the section. The diagonal loading case is the critical one for designing the shear reinforcement in the flanges. In addition, the diagonal loading position leads to the largest compression depths for the flange ends in the experiments performed within this study and is therefore determinant when designing the confining reinforcement of the flanges.

Numerical and experimental investigations have shown that from all the investigated directions, the displacement capacity in diagonal direction is the lowest if the limit states bar fracture after buckling and crushing of the confined concrete are controlling the displacement capacity. The displacement capacity in diagonal direction can be further reduced by out-of-plane buckling of the flange end, which is promoted by a strain gradient across the flange width. This new complex failure mode experimentally observed is however difficult to capture numerically and was outside the scope of this thesis (see “Outlook” below). The diagonal direction is also determinant for the shear design of the flanges. The only failure mode that is not controlled by the diagonal loading direction is the shear failure of the web. The shear design of the web should be based on the loading direction parallel to the web, for which the shear force demand on the web is largest.

### **Recommendation for the distribution of the longitudinal reinforcement**

From the findings of the experimental campaign it is recommended to detail the walls with longitudinal reinforcement uniformly distributed in the section. While this may increase the compression depth on the flanges and therefore the susceptibility to concrete crushing failures, the shear deformations and the shear lag effects are reduced. This reduction is especially appealing for non-planar walls where shear deformations and shear lag can significantly reduce the wall strength and stiffness in flexure and shear. Distributing the longitudinal reinforcement uniformly along the wall section can also prevent sliding shear failures.

## 7.2 Outlook

This study addressed the response of isolated U-shaped walls when subjected to displacements in different loading directions and following different loading histories. Future work should address in particular open questions with regard to the torsional response of core walls, the response of core walls as elements within a structural system and with regard to the design of core walls.

**Influence of torsion on the U-shaped wall behaviour:** All U-shaped walls investigated in this study were isolated walls, for which the rotation was restrained at the wall top. The influence of a rotation at the wall head on the wall behaviour was therefore not considered within this study. Future studies should investigate (1) the effect of flexural deformations on the torsional stiffness and strength, (2) the influence of torsional response on failure modes, in particular also on the out-of-plane stability of flanges.

**Analysis of buildings with U-shaped walls:** This study focused on isolated U-shaped walls. In reality, core walls will be part of a structural system and connected to horizontal structural members such as slabs and coupling beams. The interaction with these structural members should be investigated and modelling approaches developed that are suitable for capturing this interaction.

**Design guidelines for U-shaped walls:** The design of U-shaped walls was only briefly discussed when designing the walls of the parametric study. The main issues that require further investigation are: (1) the confinement of the flange ends, (2) the shear design of the flanges and (3) consideration of out-of-plane bending when assessing the stability of the flange ends. The experimental tests have shown that diagonal loading with one flange end in compression leads to the largest compression zone depth in the flange ends and that compressive strains are non-linearly distributed along this flange. Due to the latter observation section analysis cannot capture the flange response and other simple analysis tools that allow to predict the required confinement lengths for the flanges need to be developed. Furthermore, it is at present not clear whether such elongated cross sections can be effectively confined. The out-of-plane bending of the flanges influences the stability of the flange ends but at present stability models that account for the out-of-plane bending are missing. Research on this topic is currently ongoing within the scope of the follow-up project.



# Appendix

## A.1 Introduction

This appendix provides additional information on the experimental tests carried out at structural testing laboratory at EPFL on two half-scale U-shaped walls: TUC and TUD (Figure A.1). The test objectives, test set-up, applied loading history and the interpretation of the test results have been presented in Chapter 3. The data from these two tests has been made publicly available and has been assigned DOI 10.6084/m9.figshare.3507749. The data can be downloaded using the following link:

[https://figshare.com/articles/Quasi-static\\_cyclic\\_tests\\_of\\_two\\_U-shaped\\_RC\\_walls\\_under\\_diagonal\\_loading/3507749](https://figshare.com/articles/Quasi-static_cyclic_tests_of_two_U-shaped_RC_walls_under_diagonal_loading/3507749)

This appendix presents how the data is organized and how it can be reused. When using any of the data, please cite the following reference:

R. Constantin and K. Beyer. Behaviour of U-shaped RC walls under quasi-static cyclic diagonal loading. *Engineering Structures*, 106(1):36-52, 2016. DOI:10.1016/j.engstruct.2015.10.018

## A.2 Instrumentation of the test units

The two test units were each instrumented with two different measurement systems: one composed of conventional measurement devices and one optical measurement system. Both measurement systems are described in the following.

The conventional measurement system was composed of the following conventional measurement devices that recorded continuously at a frequency of 1 Hz:

- load cells of the force actuators measuring the applied horizontal forces (Figure A.1)
- load cells measuring the applied axial force (Figure A.1)
- linear variable differential transducers (LVDTs) measuring the relative horizontal displacement of the top of the wall at  $h = 2.95$  m and  $h = 3.35$  m (Figures A.2 and A.3)
- LVDTs measuring the vertical shortening and elongation at four outer vertical edges of the wall (Figures A.2 and A.3)

## Appendix

- LVDTs measuring the vertical shortening and elongation at two inner vertical edges of the wall near the flange ends

The optical measurement system Optotrack from NDI (Optotrack Certus HD [NDI10]) was composed of the following devices that recorded continuously at a frequency of 2 Hz:

- ~ 500 light emitting diodes (LEDs) glued on the outer surface of the wall (Figures A.4 and A.5)
- three position sensors each comprising three digital cameras that recorded the x, y and z coordinates of the LEDs (Figure A.1)

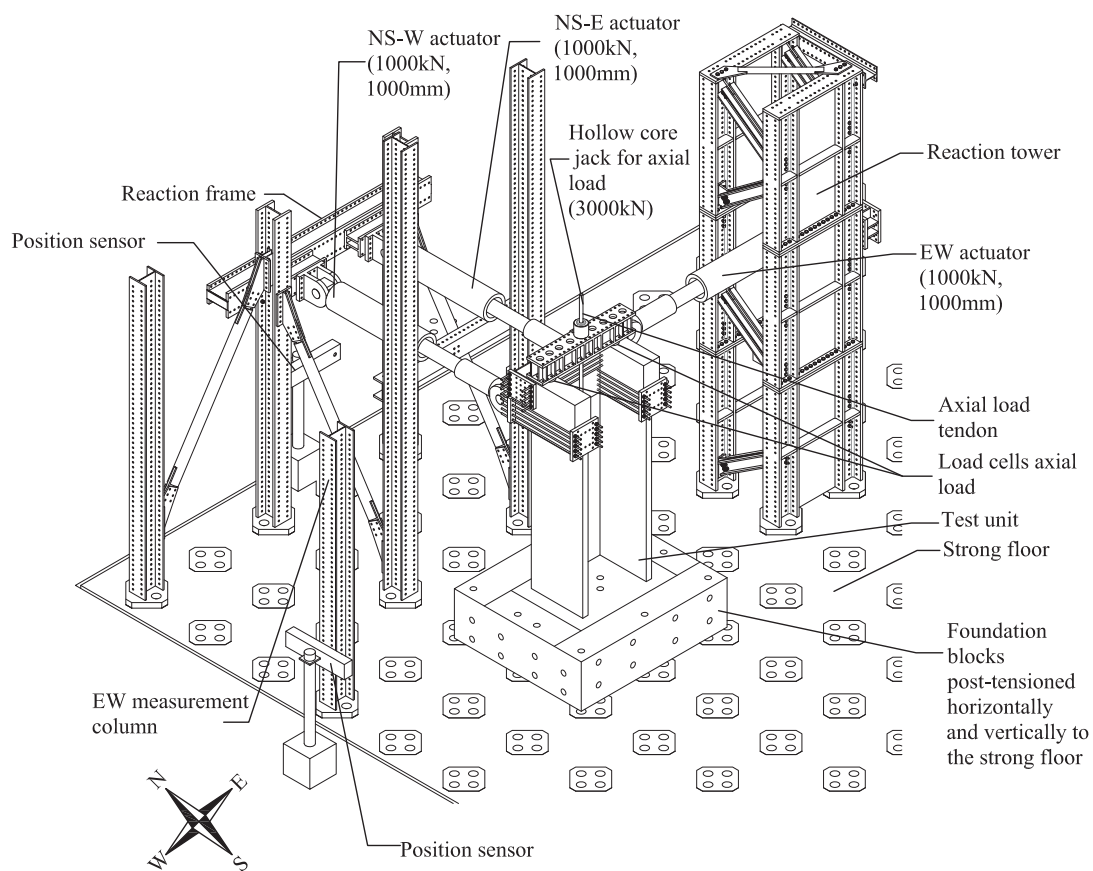


**Figure A.1:** Sketch of the test set-up



## A.2. Instrumentation of the test units

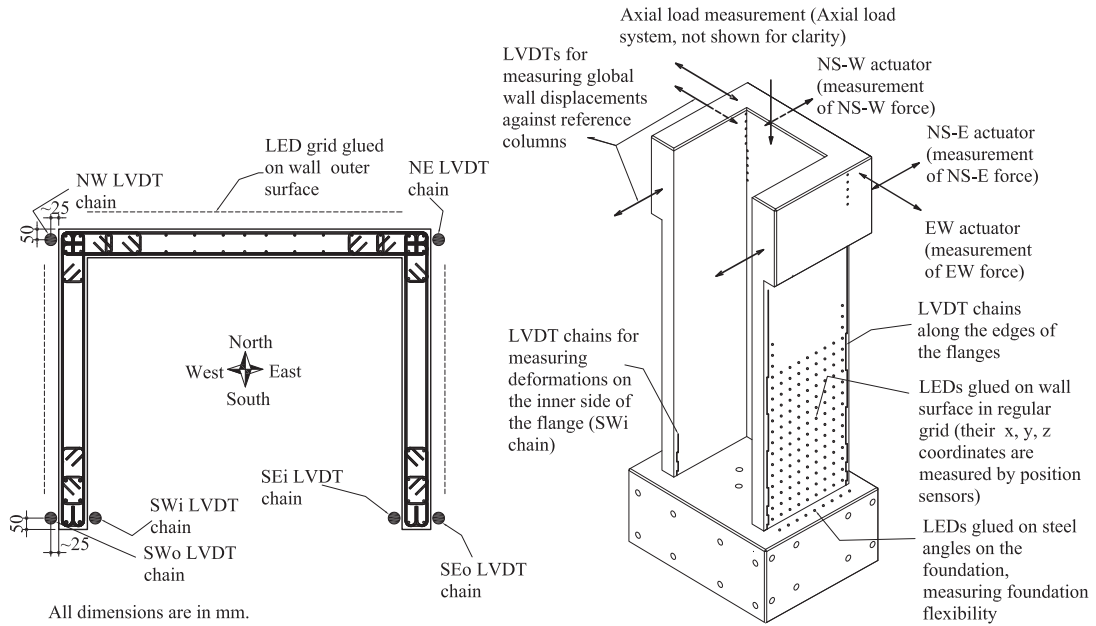


**Figure A.2:** Sketch of the measurement systems: top view (left) and 3D view (right)

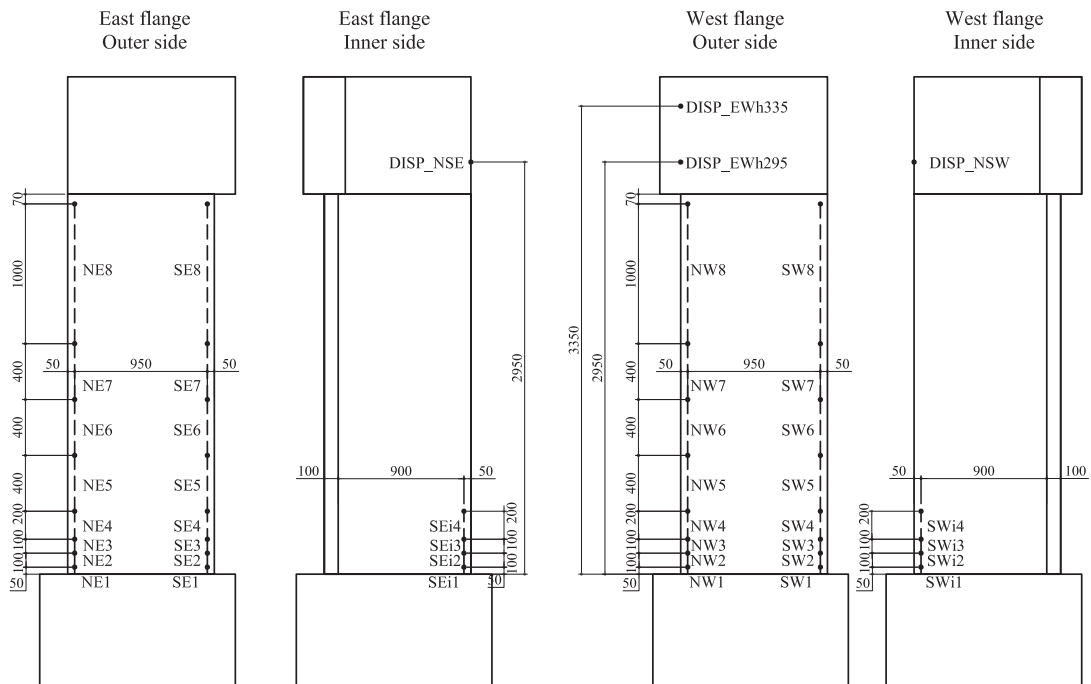
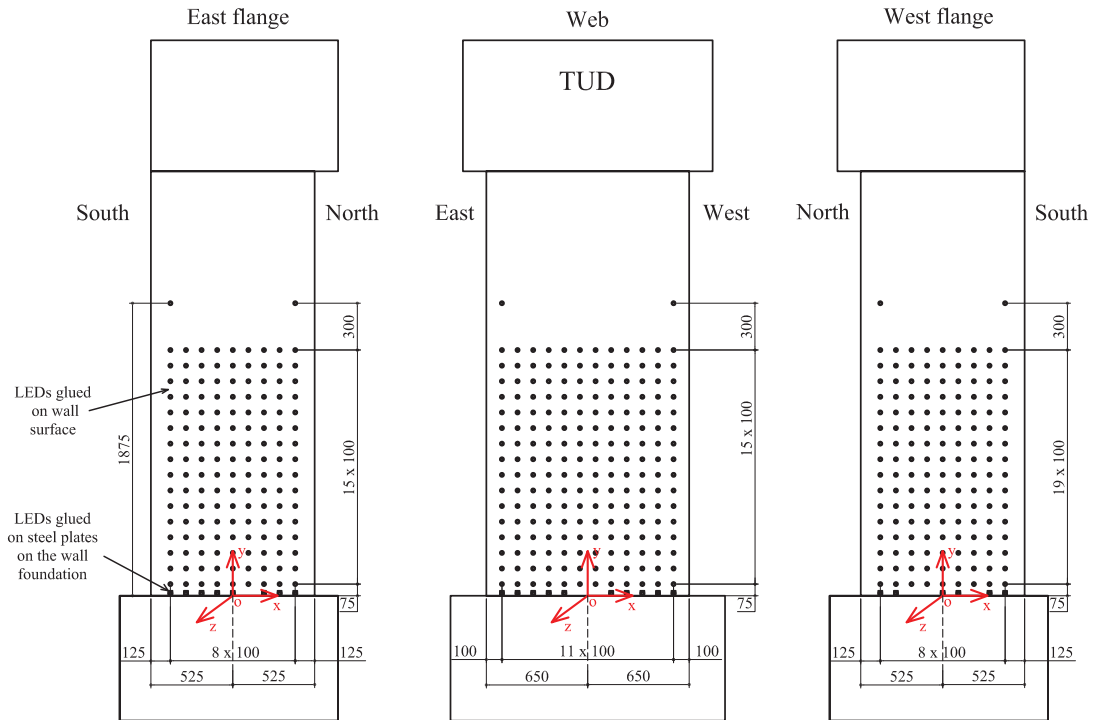


**Figure A.3:** TUC and TUD: Sketch of the LVDT chains mounted on the outer wall edges of the flanges and on the inner edge at the flange ends. In addition the positions of the LVDTs measuring the global wall top displacements are shown. All dimensions are in mm.



## A.2. Instrumentation of the test units



All dimensions are in mm.

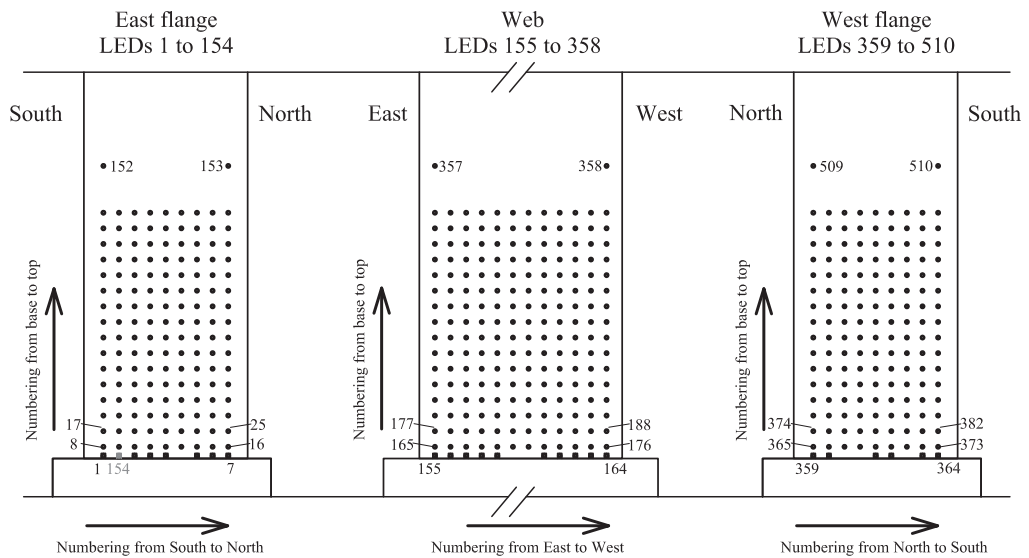


**Figure A.5:** TUD: Sketch of the positions of the LEDs glued on the outer faces of the wall, the local coordinate axes with respect to which the processed optical data is given and the numbering of the LEDs after data post-processing. Grey colour marks LEDs that are obsolete, i.e., that were not visible to the position sensors during testing.

### A.3 Loading history

The main loading cycles were applied along the two geometric diagonals of the U-shaped section: directions E-F and H-G (Figure A.6). Cycles along the principal directions were also added at small drift levels in order to check the strength capacity of the wall in these directions. The load step numbers, their corresponding loading position and the target drifts at each load step are summarised for both test units in Figure A.7. The loading for TUD was stopped at LS80.

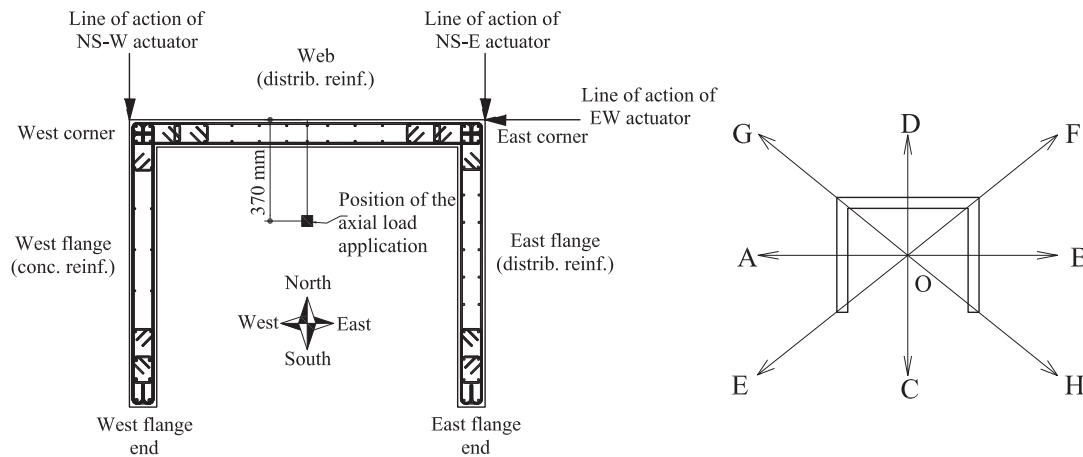


Figure A.6: Nomenclature of wall parts, cardinal orientation and loading positions

### A.4 Test data

#### A.4.1 Organisation of data



The data is organised as in Figure A.8. The data was divided into two large folders: the '01\_Documents\_and\_data' and the '02\_Photos' folders and they have been archive in a total of eight zip files. The first folder comprises a subfolder '01\_Documents\_and\_paper' which contains all the relevant documents to understanding and reusing the experimental data. Three other subfolders were included in the first folder: a subfolder containing processed and unprocessed measurements from the conventional instruments for both test units, a subfolder containing processed and unprocessed measurements from the optical system and a subfolder containing processed and unprocessed data from the material tests. A 'Metadata\_conventional\_channels.xlsx' file that provides sign conventions and information on the conventional measurement instruments used was included in the conventional measurements for each test unit.

#### A.4.2 Unprocessed data

The unprocessed data contains the original files as recorded by the measurement systems during the testing of the walls. The type of files recorded will depend on the type of measurement systems used.

## A.4. Test data

LS number	Loading position	Target drift @h=2.95 m [%]
LS0	zero measurement	0
LS1	axial load	0
LS2	C (NS)	-0.1
LS3	D (NS)	0.1
LS4	O	0
LS5	A (EW)	-0.1
LS6	B (EW)	0.1
LS7	O	0
LS8	C (NS)	-0.2
LS9	D (NS)	0.2
LS10	O	0
LS11	A (EW)	-0.2
LS12	B (EW)	0.2
LS13	O	0
LS14	E (Diag1)	-0.2
LS15	F (Diag1)	0.2
LS16	O	0
LS17	H (Diag2)	0.2
LS18	G (Diag2)	-0.2
LS19	O	0
LS20	E (Diag1)	-0.3
LS21	F (Diag1)	0.3
LS22	O	0
LS23	H (Diag2)	0.3
LS24	G (Diag2)	-0.3
LS25	O	0
LS26	C (NS)	-0.3
LS27	D (NS)	0.3
LS28	O	0
LS29	A (EW)	-0.3
LS30	B (EW)	0.3
LS31	O	0
LS32	E (Diag1)	-0.4
LS33	F (Diag1)	0.4
LS34	O	0
LS35	H (Diag2)	0.4
LS36	G (Diag2)	-0.4
LS37	O	0
LS38	C (NS)	-0.4
LS39	D (NS)	0.4
LS40	O	0
LS41	A (EW)	-0.4
LS42	B (EW)	0.4
LS43	O	0
LS44	E (Diag1)	-0.6
LS45	F (Diag1)	0.6
LS46	O	0
LS47	H (Diag2)	0.6
LS48	G (Diag2)	-0.6
LS49	O	0
LS50	C (NS)	-0.6
LS51	D (NS)	0.6
LS52	O	0
LS53	A (EW)	-0.6
LS54	B (EW)	0.6
LS55	O	0
LS56	C (NS)	-0.8
LS57	D (NS)	0.8
LS58	C (NS)	-0.8
LS59	D (NS)	0.8
LS60	O	0
LS61	A (EW)	-0.8
LS62	B (EW)	0.8
LS63	A (EW)	-0.8
LS64	B (EW)	0.8
LS65	O	0
LS66	E (Diag1)	-1
LS67	F (Diag1)	1
LS68	E (Diag1)	-1
LS69	F (Diag1)	1
LS70	O	0
LS71	H (Diag2)	1
LS72	G (Diag2)	-1
LS73	H (Diag2)	1
LS74	G (Diag2)	-1
LS75	O	0
LS76	H (Diag2)	1.5
LS77	G (Diag2)	-1.5
LS78	H (Diag2)	1.5
LS79	G (Diag2)	-1.5
LS80	O	0
LS81	E (Diag1)	-1.5
LS82	F (Diag1)	1.5
LS83	E (Diag1)	-1.5
LS84	F (Diag1)	1.5
LS85	O	0
LS86	E (Diag1)	-2
LS87	F (Diag1)	2
LS88	E (Diag1)	-2
LS89	F (Diag1)	2
LS90	O	0
LS91	H (Diag2)	2
LS92	G (Diag2)	-2
LS93	H (Diag2)	2
LS94	G (Diag2)	-2
LS95	O	0
LS96	H (Diag2)	2.5
LS97	G (Diag2)	-2.5
LS98	O	0
LS99	E (Diag1)	-2.5
LS100	F (Diag1)	2.5
LS101	O	0
LS102	E (Diag1)	0
LS103	O	0
LS104	H (Diag2)	0
LS105	O	0

 failure of TUC for the two diagonal directions  
 failure of TUD

**Figure A.7:** Load step number, corresponding loading position and target drifts. The last loadstep for TUD is LS80.

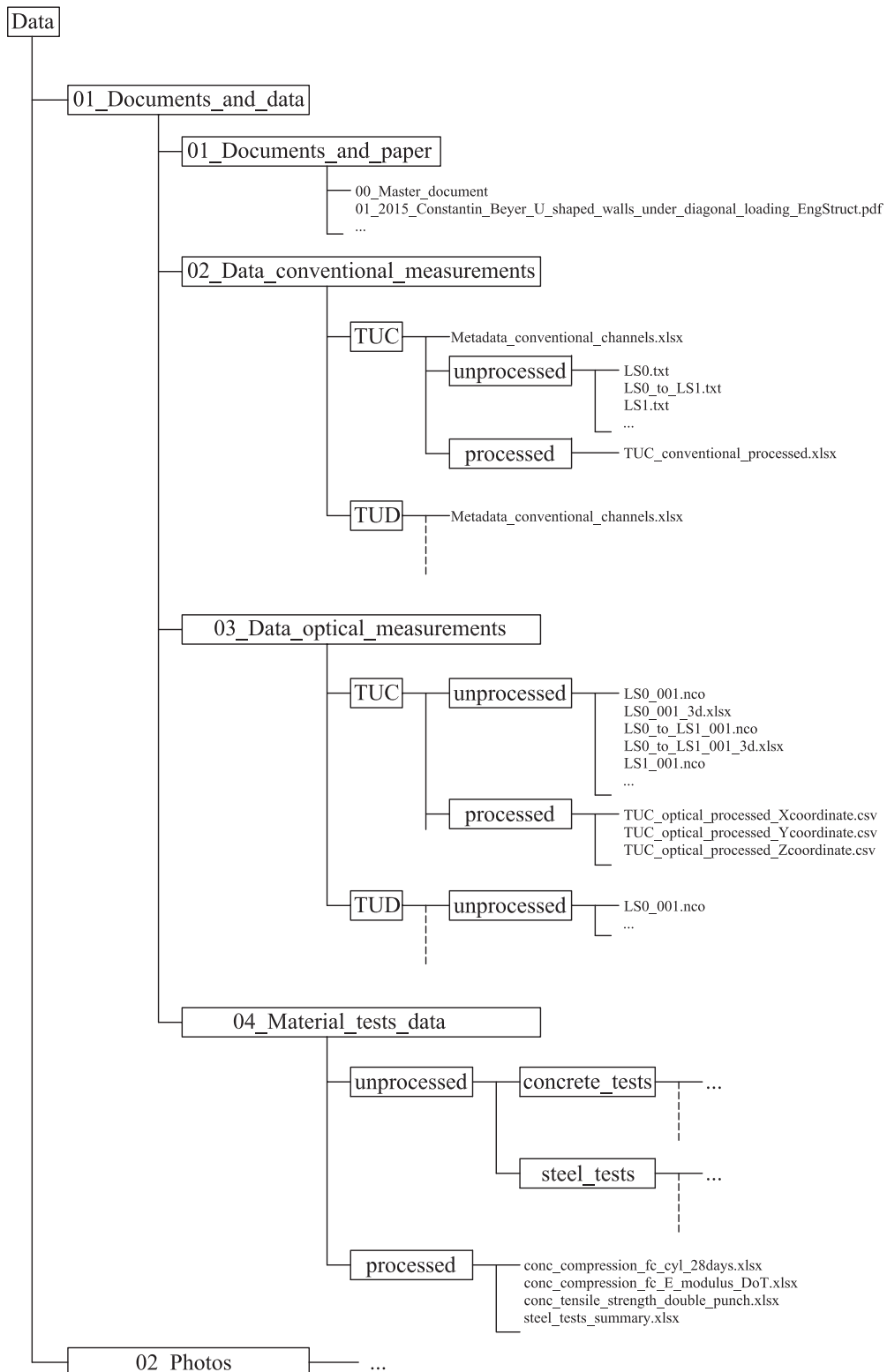


Figure A.8: Sketch of the data organisation.

### A.4.2.1 Conventional measurement data

The conventional measurements were recorded using the CATMAN software [HBM00]. This software outputs ascii files that contain the unmodified measurements as recorded by the system. A channel is assigned to each instrument of the system. The type of recorded measurements and the corresponding channel names are listed below:

- Measurement of forces and displacements of the horizontal actuators: ACTU\_FORCE\_EW, ACTU\_FORCE\_NSW, ACTU\_FORCE\_NSE, ACTU\_DISP\_EW, ACTU\_DISP\_NSW and ACTU\_DISP\_NSE
- Measurement of the applied axial forces from the two load cells placed between the top steel beam and the wall collar: F\_AX\_W, F\_AX\_E (TUC) or measurements of axial force load cell placed on the pre-stressed axial tendon: F\_AX\_1 and of pressure applied in the hollow core jack: PRESS\_AX (TUD)
- Measurements of relative horizontal displacements at the top of the wall using LVDTs: DISP\_EWh295, DISP\_EWh335, DISP\_NSW, DISP\_NSE
- Measurements of shortening and elongation of the wall edges using six LVDT chains: SWi1 to SWi4, SW1 to SW8, NW1 to NW8, NE1 to NE8, SE1 to SE8 and SEi1 to SEi4
- Voltage measurement exported from the NDI system to indicate when the optical system was recording: LED. The conventional system recording was always started before and stopped after the NDI recording. This voltage measurement was used to synchronise the conventional and the optical measurement system.
- Additional measurements to check the safety of the test set-up during loading. One LVDT fixed below the strong floor of the testing laboratory to record the vertical displacement of the strong floor during loading: DISP\_SLAB. Inclinerometers fixed on the wall collar and on the top steel beam and measuring their inclination with respect to the wall vertical axis during loading: INCLIN\_WALL, INCLIN\_BEAM (only for TUC).

The files are labelled as 'LSxx\_to\_LSxx+1.txt' to indicate measurement during loading from one load step to the next and 'LSxx.txt' to indicate measurement at load step (i.e., while holding the wall position at the target displacement).

### A.4.2.2 Optical measurement data

The data recorded from the NDI measurement system was placed in the subfolder named '03\_Data\_optical\_measurements'. For each separate recording the NDI system exports the measurement data to an Excel file. In addition an ascii file with extension 'nco' is created carrying data on the settings of the NDI system. The files are named 'LSxx\_to\_LSxx+1\_001' for measurements when loading from one load step to the next and 'LSxx' for measurements while holding the position at one load step. The Excel files are named as the 'nco' files are, plus the suffix '\_3d.xls': 'LSxx\_to\_LSxx+1\_001\_3d.xls' and 'LSxx\_001\_3d.xls'.

## Appendix

---

Each Excel file has three header lines. These lines indicate the number of frames included in the file (i.e., number of measurements values for one coordinate of a LED), the recording frequency in Hz (2 Hz for both TUC and TUD) and the units of the coordinate measurements (mm). A blank line follows the header lines, then comes the actual measurement data that is organised in columns. The first column stores the frame index that always starts from one. From the second column on, the coordinate measurements of the LEDs follow. These measurement are organised by LED number and by x, y and z coordinate. For example the second, third and fourth column which correspond to LED number 1 are labelled Marker\_1x, Marker\_1y and Marker\_1z respectively. In the unprocessed data, the numbering of the LEDs is random. If a LED was not visible to the position sensors during loading, the columns corresponding to this LED are blank.

### A.4.2.3 Measurement irregularities

Several measurement irregularities occurred during the testing of TUC and TUD. These irregularities are listed below:

- During the testing of TUC, due to a malfunction of the actuator system, loading from position H to G (LS35 to LS36) was done in steps and data files were stitched together for post-processing. In addition, when reaching LS36 one of the three actuators continued to load slightly above the target drift but at a high speed. It applied a small torsion on the wall but no important additional cracks were observed after this.
- For both TUC and TUD, the LEDs glued on the foundation originally followed a regular grid consistent with the grid of the LEDs on the wall surface. However several LEDs on the foundation were removed prior to commencing the tests as their visibility to the position sensors was obstructed by the pre-tensioning bar ends and plates. Additional LEDs were not visible during the entire testing procedure but were left in place and marked as obsolete.

### A.4.3 Processed data

Both the conventional and the optical measurement data were processed in order to reduce the amount of data and to make it easy to use. The processing consisted of: synchronising the optical and the conventional measurement data, removing any bias in the measurements not related to the actual wall behaviour (e.g., accidental touching of measurement instruments or LEDs that had fallen off but were still recording) and organising the data in one set of measurements during loading between load steps. The measurements during loading (i.e., files of type LSxx\_to\_LSxx+1) were assembled together resulting in one single continuous vector of 57110 data points for TUC and 19146 data points for TUD.

#### A.4.3.1 Conventional measurement data

The measurements of the conventional instruments have been offset so that the deformations and displacements at initial load step LS0 are zero. The measurements of the actuator forces, time channel and voltage channel were not offset.



The signs of some of the top displacement measurements and actuator forces were inverted so that they match the sign convention for the wall as described in 'Metadata\_conventional\_channels.xlsx'. In addition, the processed top displacements were modified to remove the contribution of the foundation flexibility (foundation uplift and sliding with respect to the strong floor) recorded by means of the LEDs glued on the steel plates on the foundation.

### A.4.3.2 Optical measurement data

Several processing steps were performed for the optical measurement data:

- The data was smoothed over a range of 20 data points in order to remove measurement noise. Smoothing was done using the Matlab function 'smooth' [Mat13].
- For each flange and the web, the coordinate system was rotated and shifted so that it is aligned with the local xyz coordinate system of each wall part, i.e., web or flanges. For any of the three wall parts, the local x axis is always aligned with the length of the wall part, the local y axis is aligned with the wall height and local z axis is perpendicular on the wall surface and oriented from the wall towards the position sensor (Figures A.4 and A.5). The origin of the local coordinate system is always: at mid-length of each wall part (x axis), at the base of the wall specimen (y axis) and at the outer wall surface (z axis).
- The optical measurement data was synchronised with the processed conventional measurement data. In order to have the same number of measurement values for both systems, the measurement frequency of the optical system (2 Hz) was reduced to the frequency of the conventional system (1 Hz).
- LEDs that fell off during testing were identified and the corresponding entries were replaced by NaN (Not a Number) entries.
- LEDs were renumbered starting from the base of the East flange, from left to right on the outer wall surface. Obsolete LEDs, i.e., LEDs that were not visible during testing are numbered at the end for each wall part and are shown in grey in Figures A.4 and A.5.

The processed optical measurements for all LEDs are stored in three separate csv files, one for each x, y and z coordinate. The three files are named: 'TUC\_optical\_processed\_Xcoordinate.csv', 'TUC\_optical\_processed\_Ycoordinate.csv' and 'TUC\_optical\_processed\_Zcoordinate.csv', for the case of TUC and similarly for TUD. The processed x, y and z coordinates are expressed with respect to the local axes of each of the wall parts (Figures A.4 and A.5).

### A.4.4 Photos

All the photos documenting the construction, test set-up and the damage during testing of the two specimens were saved in the second main folder '02\_Photos'. The photos documenting the damage of the walls were taken at load steps while holding the wall position at the target peak displacement. These photos are found in the '02\_TUC\_testing' and '04\_TUD\_testing' and are organised in folders 'LSxx' created for each load step numbered xx. Each 'LSxx' folder contains global photos of the wall specimen taken from the front (view of the inner wall faces), back (view perpendicular on the web), and the two sides (views perpendicular on the two flanges). These global photos are saved in 'Overview' subfolder. In addition, when damage became significant detailed photos at the damage locations were taken. These are photos were saved in the subfolder 'Detailed'.

At each load step, the cracks were traced using blue, red, black and green pens in order to render the cracks visible on photos. Each color corresponded to different loading positions: red - positions A and F, blue - positions B and E, black - positions C and H, green - positions D and G (see also Figure A.6).

## Notations and abbreviations

### Capital Latin Letters

$A_g$	Gross concrete area of a section
$A_{cv}$	Gross cross section area of wall parts (web or flange) resisting a common lateral force
$A_{cw}$	Gross cross section area of one wall part resisting all the lateral force
$E$	Elastic modulus
$E_c$	Elastic modulus of concrete
$E_s$	Elastic modulus of steel reinforcement
$EI_{cr}$	Cracked (effective) flexural stiffness
$EI_g$	Uncracked gross flexural stiffness
$F_{EW}$	Force in EW direction
$F_{NS}$	Force in NS direction
$F'_y$	Shear force at first yield
$F_n$	Shear force at nominal
$H$	Effective height of a building or the height of a wall subjected to a point load at H
$H_{cr}$	Height of the wall over which cracking extends
$H_{wall}$	Height of the wall
$K_{eff}$	Effective wall stiffness
$K_{th}$	Elastic flexural wall stiffness
$K_y$	Dimensionless yield curvature
$K_{y,fl}$	Dimensionless yield curvature for loading in the flange direction
$K_{y,web}$	Dimensionless yield curvature for loading in the web direction
$L_{ph}$	Plastic hinge length
$L_{pz}$	Height of the plastic zone (i.e., where plasticity spreads)
$L_{sp}$	Strain penetration length
$L'_{y,sp}$	Strain penetration length at first yield
$M$	Bending moment at the wall base
$M_{EW}$	Moment at the wall base due to $F_{EW}$
$M_{NS}$	Moment at the wall base due to $F_{NS}$
$M_{SRSS}$	SRSS moment at the wall base computed from $F_{EW}$ and $F_{NS}$
$M_{cr}$	Moment at the wall base at flexural cracking
$M_y$	Moment at the wall base at first yield
$M_n$	Moment at the wall base at nominal
$M_u$	Moment at the wall base at ultimate
$N$	Axial load

## Notations and abbreviations

---

$N_{stories}$	Number of stories the building braced by the U-shaped wall
$V_{nec}$	Shear force demand
$V_{nec}^*$	Shear force demand accounting for the dynamic amplification factor
$V_n$	Diagonal tension capacity
$V_{wc}$	Web crushing capacity

## Small Latin Letters

$c$	Compression depth of a section
$d_b$	Gross concrete area of a section
$f_c$	Gross cross section area of the wall section
$f_y$	Yield strength of the longitudinal reinforcement
$f_{yh}$	Yield strength of the transversal reinforcement
$f_t$	Tensile strength of concrete
$f_u$	Ultimate strength of the reinforcement
$h$	Height of one or several measuring instruments
$h_{storey}$	Storey height
$h_{EW}$	Height of load application in the EW direction
$h_{NS}$	Height of load application in the NS direction
$k_{cr}$	Factor accounting for the partially cracked wall height at yield
$k_E$	Ratio between the modulus of elasticity of steel and concrete
$l_{fl}$	Length of the flanges of the U-shaped wall
$l_{diag}$	Length of the diagonal of the U-shaped section
$l_{wall}$	Length of the wall perpendicular to the neutral axis
$l_{web}$	Length of the web of the U-shaped wall
$l_{tens,fl}$	Tensioned length of the web at yield when loading in an arbitrary direction
$l_{tens,web}$	Tensioned length of the flange at yield when loading in an arbitrary direction
$l_{tens,fl}^y$	Tensioned length of the flange at yield when loading in the direction of the flanges (bending about the web)
$l_{tens,web}^y$	Tensioned length of the web at yield when loading in the direction of the web (bending about the flanges)
$n$	Axial load ratio
$t_{wall}$	Thickness of the flanges and of the web of the U-shaped wall

### Capital Greek Letters

$\Delta_{EW}$	Displacement in EW direction
$\Delta_{NS}$	Displacement in NS direction
$\Delta_{SRSS}$	SRSS displacement at h=2.95 m of the test units
$\Delta_f$	Flexural displacement
$\Delta_s$	Shear displacement
$\Delta_{p,f}$	Plastic flexural displacement
$\Delta_y$	Nominal yield displacement
$\Delta_{y,1L}$	Yield displacement estimate assuming a linear curvature profile
$\Delta_{y,2L}$	Yield displacement estimate assuming a bi-linear curvature profile
$\Delta'_y$	First yield displacement
$\Delta'_{y,f}$	Flexural displacement at first yield
$\Delta'_{y,s}$	Shear displacement at first yield
$\Delta'_{y,sp}$	Flexural displacement at first yield due to strain penetration into the foundation
$\phi$	Curvature of a wall section
$\phi_b$	Curvature at the base of the wall determined from the curvatures above
$\phi_{cr}$	Curvature at cracking of the concrete section
$\phi_y$	Nominal yield curvature of a wall section
$\phi'_y$	First yield curvature of a wall section
$\phi_p$	Plastic curvature of a wall section
$\phi_u$	Ultimate curvature of a wall section
$\phi_{y,web}$	Nominal yield curvature for loading in the web direction (bending about the flanges)
$\phi_{y,fl}$	Nominal yield curvature for loading in the flange direction (bending about the web)
$\phi'_{y,web}$	First yield curvature for loading in the web direction (bending about the flanges)
$\phi'_{y,fl}$	First yield curvature for loading in the flange direction (bending about the web)

### Small Greek Letters

$\alpha$	Bending angle measured between the neutral axis of the current loading position and neutral axis at position C (see Figure 6.12)
$\alpha$	Ratio of cracked to uncracked flexural stiffness $\alpha = EI_{cr}/EI_g$
$\delta$	Drift at the effective height
$\delta_y$	Yield drift at the effective
$\epsilon_c$	Maximum compressive strain of a section at the location of the reinforcement bar

## Notations and abbreviations

---

$\epsilon_{cu}$	Ultimate compressive strain capacity of concrete
$\epsilon_{cy}$	Concrete compressive strain at first yield
$\epsilon_s$	Maximum tensile strain of a section at the location of the reinforcement bar
$\epsilon_{sh}$	Strain at the end of the strain hardening plateau
$\epsilon_{sy}$	Yield strain of the longitudinal reinforcement
$\epsilon_{su}$	Tensile strain capacity of a reinforcement bar
$\theta$	Rotation at the wall base
$\theta$	Crack angle with the vertical axis of the wall
$\theta'_{sp}$	Rotation at the wall base due to strain penetration into the foundation
$\theta_{pz}$	Rotation from curvature integration over the height of the plastic zone
$\mu_{\Delta}$	Displacement ductility
$\rho_h$	Transversal reinforcement content
$\rho_l$	Longitudinal reinforcement content
$\rho_{lot}$	Total longitudinal reinforcement content
$\tau$	Average shear stress on the section
$\tau_{web}$	Average shear stress on the web
$\tau_{fl}$	Average shear stress on the flanges
$\omega$	Dynamic amplification factor

## Abbreviations

$Dwf2.5$	Distributed reinforcement, web to flange length ratio $l_{web}/l_{fl} = 2.5$
LED	Light Emitting Diode
LVDT	Linear Variable Differential Transducer
NA	Neutral axis
PH	Plastic Hinge
RC	Reinforced Concrete
SRSS	Square Root of Sum of Squares
TUC	Test Unit C
TUD	Test Unit D
VT4	VecTor4 software

Remark: Notations that were introduced in the only in the literature review sections are defined when introduced and are not included in this notation list.

# Bibliography

- [AAS09] AASHTO. Aashto guide: specifications for LRFD seismic bridge design. Technical report, American Association of State Highway and Transportation Officials, Washington DC, USA, 2009.
- [ACI11] Comitee 318 ACI. Building Code requirements for structural concrete and commentary. Technical Report ACI 318M-11, American Concrete Institute, Farmington Hills, MI, USA, September 2011.
- [AIB07] P. Adebar, A.M.M. Ibrahim, and M. Bryson. Test of high-rise core wall: effective stiffness for seismic analysis. *ACI Structural Journal*, 104(5):549–559, September-October 2007.
- [ATB16] J. P. Almeida, D. Tarquini, and K. Beyer. Modelling approaches for inelastic behaviour of RC walls: Multi-level assessment and dependability of results. *Archives of Computational Methods in Engineering*, pages 1–32, 2016.
- [BA11] A. Bohl and P. Adebar. Plastic hinge lengths in high-rise concrete shear walls. *ACI Structural Journal*, 108(2):148–157, March-April 2011.
- [BDP08a] K. Beyer, A. Dazio, and M. J. N. Priestley. Quasi-static cyclic tests of two U-shaped reinforced concrete walls. *Journal of Earthquake Engineering*, 12(7):1023–1053, 2008.
- [BDP08b] K. Beyer, A. Dazio, and M. J. N. Priestley. Seismic design of torsionally eccentric buildings with U-shaped RC walls. Research Report ROSE 2008/03, ROSE School, Pavia, Italy, March 2008.
- [BDP08c] K. Beyer, A. Dazio, and M.J.N. Priestley. Elastic and inelastic wide-column models for RC non-rectangular walls. In *Proc. of the 14th World Conference on Earthquake Engineering*, Beijing, China, 2008.
- [BDP08d] K. Beyer, A. Dazio, and M.J.N. Priestley. Inelastic wide-column models for U-shaped reinforced concrete walls. *Journal of Earthquake Engineering*, 12(S1):1–33, 2008.
- [BDP11] K. Beyer, A. Dazio, and M. J. N. Priestley. Shear deformations of slender reinforced concrete walls under seismic loading. *ACI Structural Journal*, 108(2):167–177, March-April 2011.

## Bibliography

---

- [Bru09] B.L. Brueggen. *Performance of T-shaped reinforced concrete structural walls under multi-directional loading*. PhD thesis, The University of Minnesota, Twin Cities, Minnesota, USA; <https://nees.org/resources/236>, 2009.
- [BVC06] E. Bentz, F.J. Vecchio, and M.P. Collins. Simplified modified compression field theory for calculating shear strength of reinforced concrete elements. *ACI Structural Journal*, 103(4):614:624, 2006.
- [CAP10] A. Calabrese, J. P. Almeida, and R. Pinho. Numerical issues in distributed inelasticity modeling of RC frame elements for seismic analysis. *Journal of Earthquake Engineering*, 14(S1):38–68, 2010.
- [CAP15] A. A. Correia, J. P. Almeida, and R. Pinho. Force-based higher-order beam element with flexural–shear–torsional interaction in 3D frames. Part I: Theory. *Engineering Structures*, 89:204–217, 2015.
- [CB16] R. Constantin and K. Beyer. Behaviour of U-shaped RC walls under quasi-static cyclic diagonal loading. *Engineering Structures*, 106(1):36–52, 2016.
- [CCM99] D. Combescure, T. Chaudat, and A. Moutafidou. Seismic tests of ICONS U-shaped walls - Description of the experimental set-up. Main results. Rapport DMT SEMT/EMSI/RT/99-062, CEA, France, 1999.
- [CE99] Y.H. Chai and D.T. Elayer. Lateral stability of reinforced concrete columns under axial reversed cyclic tension and compression. *ACI Structural Journal*, 96(5):780–790, 1999.
- [CEN01] CEN. Eurocode8: Design provisions for earthquake resisting structures, Part 1-1: General rules, seismic actions and rules for buildings. Technical Report EN 1998-1, European Committee for Standardisation, Brussels, Belgium, 2001.
- [CEN03] CEN. Eurocode8: Design provisions for earthquake resisting structures, Part 1-1: General rules, seismic actions and rules for buildings. Technical Report EN 1998-1, European Committee for Standardisation, Brussels, Belgium, 2003.
- [CEN04] CEN. Eurocode2: Design of concrete structures, Part 1-1: General rules and rules for buildings. Technical Report EN 1992-1, European Committee for Standardisation, Brussels, Belgium, April 2004.
- [CM91] M.P. Collins and D. Mitchell. *Prestressed Concrete Structures*. Prentice Hall, edition 1997, Englewood Cliffs, NJ, 1991.
- [Com06] Computers and Structures Inc., Berkeley, California, USA. *Nonlinear Analysis and Performance assesement for 3D structures v.2.0*, 2006.
- [CY80] W.F. Chen and R.L. Yuan. Tensile strength of concrete: Double-punch test. *Journal of the Structural Division, ASCE*, (106):1673–1693, 1980.
- [Daz00] A. Dazio. *Entwurf und Bemessung von Tragwandgebäuden unter Erdbebeneinwirkung*. Dissertation IBK Bericht-254, Zurich, Switzerland, 2000.



- [DBB09] A. Dazio, K. Beyer, and H. Bachmann. Quasi-static cyclic tests and plastic hinge analysis of RC structural walls. *Engineering Structures*, 31:1556–1571, 2009.
- [FB00] R. Fenwick and D. Bull. What is the stiffness of reinforced concrete walls? *SESOC Journal*, 13(2):23–32, September 2000.
- [FB02] R. Fenwick and D. Bull. What is the stiffness of reinforced concrete walls? discussion of the paper by Richard Fenwick and Des Bull. *SESOC Journal*, 15(1):30–34, April 2002.
- [Fie15] D.C. Fields. email communication, 2015.
- [FPB83] F. C. Filippou, E. P. Popov, and V. V. Bertero. Effects of bond deterioration on hysteretic behavior of reinforced concrete joints. Technical Report 83-19, Earthquake Engineering Research Center, University of California, Berkeley, USA, 1983.
- [GF<sup>+</sup>15] J.C. Goodnight, Y. Feng, M.J. Kowalsky, and J.M. Nau. The effects of load history and design variables on performance limit states of circular bridge columns: Volume 1. Report prepared for Alaska Department of Transportation and Public Facilities Research, North Carolina State University, USA, 2015.
- [Han13] P. Hannewald. *Seismic behaviour of poorly detailed RC bridge piers*. PhD thesis, Ecole Polytechnique Fédérale de Lausanne (EPFL), Lausanne, Switzerland; <https://infoscience.epfl.ch/record/188364?ln=en>, 2013.
- [HBM00] HBM. Catman data acquisition software. Technical report, Hottinger Baldwin Messtechnik GmbH, Darmstadt, Deutschland; <http://www.hbm.com/en/menu/products/software/dataacquisition-software>, 2000.
- [HDS06] E.M. Hines, A. Dazio, and F. Seible. Structural testing of the new East Bay skyway piers. *ACI Structural Journal*, 103(1):103–112, January-February 2006.
- [HHF11] L.G. Hagsten, L. Hestbech, and J. Fisker. Energiprinsipper del 3: Betonkonstruktioner. Teori. *Lecture Notes*, 2011.
- [Hin02] E.M. Hines. *Seismic performance of hollow rectangular reinforced concrete bridge piers with confined corner elements*. PhD thesis, San Diego, USA, 2002.
- [Hir84] H. Hiraishi. Evaluation of shear and flexural deformations of flexural type shear walls. *Bulletin of New Zealand Society for Earthquake Engineering*, 17(2):135–144, 1984.
- [HK<sup>+</sup>97] J. Hoshikuma, K. Kawashima, K. Nagaya, and A.W. Taylor. Stress-strain model for confined concrete in bridge piers. *ASCE Journal of Structural Engineering*, 123(5), 1997.
- [HK<sup>+</sup>00] A. Habasaki, Y. Kitada, T. Nishikawa, K. Takiguchi, and H. Torita. Multi-directional loading test for RC seismic shear walls. In *Proc. of the 12th World Conference on Earthquake Engineering*, Auckland, New Zealand, 2000.

## Bibliography

---

- [HK<sup>+</sup>01] T. Habasaki, Y. Kitada, T. Nishikawa, K. Takiguci, H. Watanabe, and T. Korenaga. Multi-axis loading test on RC shear walls: Overview and outline of two directional horizontal loading test. In *Transactions, SMiRT 16*, Washington DC, USA, August 2001.
- [HM<sup>+</sup>14] M.A. Hube, A. Marihuén, J.C. de la Llera, and B. Stojadinovic. Seismic behaviour of slender reinforced concrete walls. *Engineering Structures*, (80):377–388, 2014.
- [HRS04] E.M. Hines, J.I. Restrepo, and F. Seible. Force-displacement characterization of well-confined bridge piers. *ACI Structural Journal*, 101(4):537–548, July-August 2004.
- [Hry13] T. D. Hrynyk. *Behaviour and Modelling of Reinforced Concrete Slabs and Shells Under Static and Dynamic Loads*. PhD thesis, University of Toronto, Toronto, Canada; [http://www.civ.utoronto.ca/vector/theses/Hrynyk/Hrynyk-PhD\(2013\).pdf](http://www.civ.utoronto.ca/vector/theses/Hrynyk/Hrynyk-PhD(2013).pdf), 2013.
- [ICC03] ICC. 2003 International Building Code. Technical report, International Code Council, Country Club Hills, IL, USA, 2003.
- [IR00] N. Ile and J.M. Reynouard. Nonlinear analysis of reinforced concrete shear wall under earthquake loading. *Journal of Earthquake Engineering*, 4(2):183–213, 2000.
- [IR05] N. Ile and J.M. Reynouard. Behaviour of U-shaped walls subjected to uniaxial loading and biaxial cyclic lateral loading. *Journal of Earthquake Engineering*, 9(1):67–94, 2005.
- [Kaz13] I. Kazaz. Analytical study on plastic hinge length of structural walls. *Journal of Structural Engineering ASCE*, 139:1938–1950, November 2013.
- [KHR69] H. Kupfer, H.K. Hilsdorf, and H. Rusch. Behavior of concrete under biaxial stress. *ACI Structural Journal*, 87(2):656–666, 1969.
- [KN<sup>+</sup>07] Y. Kitada, T. Nishikawa, K. Takiguci, and K. Maekawa. Ultimate strength of reinforced concrete shear walls under multi-axes seismic loads. *Nuclear Engineering and Design*, (237):1307–1314, 2007.
- [Kwa96] A.K.H. Kwan. Shear lag in shear/core walls. *Journal of Structural Engineering*, 122(9):1097–1104, September 1996.
- [LBMPC92] C. La Borderie, J. Mazars, and G. Pijaudier-Cabot. Shear-flexure interaction for structural walls. *ACI Special Publication*, 134:147–172, September 1992.
- [LL<sup>+</sup>13] L. Lowes, D. Lehman, D. Kuchma, A. Mock, and A. Behrouzi. Large scale tests of C-shaped reinforced concrete walls. summary report from nees project warehouse. Technical report, NEES, United States, 2013.
- [LP12] Y. Lu and M. Panagiotou. Three-dimensional nonlinear cyclic beam-truss model for non-planar reinforced concrete walls. Technical Report UCB/SEMM-2012/01, Earthquake Engineering Research Center, University of California, Berkeley, California, USA, 2012.

- [LP13] Y. Lu and M. Panagiotou. Three-dimensional cyclic beam-truss model for nonplanar reinforced concrete walls. *ASCE Journal of Structural Engineering*, 140(3), March 2013.
- [Mat13] Matlab. Matlab version 8.1.0.604 (r2013a). Technical report, The Mathwork Inc., Natick, Massachusetts, United States; <http://www.mathworks.ch>, 2013.
- [MG<sup>+</sup>12] J.P. Moehle, T. Ghodsi, J. D. Hooper, D.C. Fields, and R. Gedhada. Sesimic design of cast-in-place concrete special structural walls and coupling beams: a guide for practicing engineers. Technical Brief NEHRP Seismic Design Technical Brief No.6, National Institute of Standards and Technology, Gaithersburg, MD, USA, March 2012.
- [MHB16] B.I. Mihailov, P. Hannewald, and K. Beyer. Three-parameter kinematic theory for shear-dominated reinforced concrete walls. *ACI Structural Journal*, 142(7), 2016.
- [Min51] R. D. Mindlin. Influence of rotatory inertia and shear on flexural motions of isotropic, elastic plates. *ASME Journal of Applied Mechanics*, 18:31–38, 1951.
- [MK03] M.J. Moyer and M.J. Kowalski. Influence of tension strain on buckling of reinforcement in concrete columns. *ACI Structural Journal*, 100(1):75–85, 2003.
- [MK<sup>+</sup>06] J. Mazars, P. Kotronis, F. Ragueneau, and G. Casaux. Using multifiber beams to account for shear and torsion. Applications to concrete structural elements. *Computer methods in applied mechanics and engineering*, (195):7264–7281, 2006.
- [MMG09] S. Mazzoni, F. McKenna, and Fenves G.L. *Opensees Comand Language Manual, Opensees v.4*. University of California, Berkeley, USA, May 2009.
- [MP73] M. Menegotto and P. E. Pinto. Method of analysis for cyclically loaded RC plane frames including changes in geometry and non-elastic behavior of elements under combined normal force and bending. In *IABSE Symposium on resistance and ultimate deformability of stuctures acted on by well defined repeated loads*, pages 15–22, Lisbon, Portugal, 1973. IABSE.
- [MPP88] J. B. Mander, M. J. N. Priestley, and R. Park. Theoretical stress-strain model for confined concrete. *ASCE Journal of Structural Engineering*, 114(8):1804–1826, August 1988.
- [NDI10] NDI. Optotrak certus hd. Technical report, Northern Digital Inc., Waterloo, Ontario, Canada; <http://www.ndigital.com/industrial/certushd.php>, 2010.
- [OF84] D.R.J. Owen and J.A. Figueiras. Ultimate load analysis of reinforced concrete plates and shells. Technical report, in Hinton, E. and Owen, D.R.J. *Finite Element Software for Plates and Shells*, Swansea, UK, 1984.
- [OS<sup>+</sup>04] H. Ono, K. Shintani, Y. Kitada, and K. Maekawa. Restoring characteristics of shear wall subjected to horizontal two directional loading. In *Proc. of the 13th World Conference on Earthquake Engineering*, Vancouver BC, Canada, August 2004.

## Bibliography

---

- [Pau02] T. Paulay. The displacement capacity of reinforced concrete coupled walls. *Engineering Structures*, 24:1165–1175, 2002.
- [PCK07] M. J. N. Priestley, G. M. Calvi, and M. J. Kowalsky. *Displacement-based seismic design of structures*. IUSS Press, Pavia, Italy, 2007.
- [PG85] T. Paulay and W.J. Goodsir. The ductility of structural walls. *Bulletin of the New Zealand National Society for Earthquake Engineering*, 18(3):250–269, 1985.
- [PH89] M. J. N. Priestley and G. Hart. Design recommendation for the period of vibration of masonry wall buildings. Research Report SSRP 89/05, University of California, San Diego, California, USA, November 1989.
- [PK98] M.J.N. Priestley and M.J. Kowalsky. Aspects of drift and ductility capacity of rectangular cantilever structural walls. *Bulletin of the New Zealand National Society for Earthquake Engineering*, 31(2):73–85, July 1998.
- [Pop73] S. Popovics. A numerical approach to the complete stress strain curve for concrete. *Cement and concrete research*, 3(5):583–599, 1973.
- [PP75] R. Park and T. Paulay. *Reinforced Concrete Structures*. John Wiley and Sons, Inc., 1975.
- [PP87] M.J.N. Priestley and R. Park. Strength and ductility of concrete bridge columns under seismic loading. *ACI Structural Journal*, 84(8):61–76, January-February 1987.
- [PP92] T. Paulay and M. J. N. Priestley. *Seismic design of reinforced concrete and masonry buildings*. John Wiley and Sons, Inc., 1992.
- [PP93] T. Paulay and M.J.N. Priestley. Stability of ductile structural walls. *ACI Structural Journal*, 90(4):385:392, 1993.
- [PP<sup>+</sup>00a] P. Pégon, C. Plumier, A. Pinto, J. Molina, P. Gonzalez, P.C. Tognoli, and O. Hubert. U-shaped walls: Description of the experimental test set-up. Technical report, TMR-ICONS-TOPIC 5, JRC Ispra, Italy, April 2000.
- [PP<sup>+</sup>00b] P. Pégon, C. Plumier, A. Pinto, J. Molina, P. Gonzalez, P.C. Tognoli, and O. Hubert. U-shaped walls: Quasi-static biaxial test in the X and Y directions - Test report. Technical report, TMR-ICONS-TOPIC 5, JRC Ispra, Italy, June 2000.
- [PP<sup>+</sup>00c] P. Pégon, C. Plumier, A. Pinto, J. Molina, P. Gonzalez, P.C. Tognoli, and O. Hubert. U-shaped walls: Quasi-static test in the X direction - Test report. Technical report, TMR-ICONS-TOPIC 5, JRC Ispra, Italy, May 2000.
- [PP<sup>+</sup>00d] P. Pégon, C. Plumier, A. Pinto, J. Molina, P. Gonzalez, P.C. Tognoli, and O. Hubert. U-shaped walls: Quasi-static test in the Y direction - Test report. Technical report, TMR-ICONS-TOPIC 5, JRC Ispra, Italy, June 2000.
- [PSC96] M. J. N. Priestley, F. Seible, and G.M. Calvi. *Seismic design and retrofit of bridges*. John Wiley and Sons, Inc., 1996.

- [PV93] M. A. Polak and F. J. Vecchio. Nonlinear analysis of reinforced-concrete shells. *Journal of Structural Engineering*, 119(12):3439–3462, December 1993.
- [RA<sup>+</sup>14] A. Rosso, J.P. Almeida, R. Constantin, K. Beyer, and S. Sritharan. Influence of longitudinal reinforcement layouts on RC wall performance. In *Proceedings of the 2nd European conference on earthquake engineering and seismology*, number Paper no. 980, Istanbul, Turkey, 2014.
- [RAB16] A. Rosso, J.P. Almeida, and K. Beyer. Stability of thin reinforced concrete walls under cyclic loads: state-of-the-art and new experimental findings. *Bulletin of Earthquake Engineering*, 14(2):455–484, 2016.
- [Res93] J.I. Restrepo. *Seismic behaviour of connections between precast concrete elements*. Phd thesis, Christchurch, New Zealand, 1993.
- [RF01] J. Reynouard and M.N (Eds.) Fardis. Shear wall structures. Research Report Thematic report N<sup>o</sup>5, CAFEEL-ECOEST/ICONS, Lisbon, Portugal, September 2001.
- [SB<sup>+</sup>14] S. Sritharan, K. Beyer, R.S. Henry, Y.H. Chai, M. Kowalsky, and D. Bull. Understanding poor seismic performance of concrete walls and design implications. *Earthquake Spectra*, 30(1):307–334, 2014.
- [SEA08] SEAOC. Reinforced concrete structures, Article 9.01.010. Technical report, California, USA, 2008.
- [SIA03] SIA. Concrete structures - supplementary specifications. Building Code. Technical Report SN. SIA262/1, Swiss Society of Engineers and Architects, Zürich, Switzerland, 2003.
- [SM08] M. IJ. Schotanus and J.R. Maffei. Computer modeling and effective stiffness of concrete wall buildings. In Taylor and Francis Group, editors, *Tailor made concrete structures, Walraven and Stoelhorst (eds.)*, London, UK, 2008.
- [SML03] M. Sarkisian, N. Mathias, and E. Long. Seismic design and detailing of compound shear wall plan configurations such as I, L, C and T shaped for high-rise structures. In *Proceedings of 72nd annual Structural Engineers Association of California Convention, SEAOC*, Sacramento, CA, USA, 2003.
- [SPC12] T. Sullivan, M. J. N. Priestley, and G. M. Calvi, editors. *A Model Code for the Displacement-based seismic design of structures*. IUSS Press, Pavia, Italy, 2012.
- [SS<sup>+</sup>13] E. Smyrou, T. Sullivan, N. Priestley, and M. Calvi. Sectional response of T-shaped walls. *Bulletin of Earthquake Engineering*, 11:999–1019, December 2013.
- [SW93] C. Sittipunt and S. L. Wood. Finite element analysis of reinforced concrete shear walls. Technical report, Department of Civil Engineering, University of Illinois at Urbana-Champaign, Urbana, Illinois, USA, December 1993.
- [VC86] F.J. Vecchio and M.P. Collins. The Modified Compression-Field Theory for reinforced concrete elements subjected to shear. *ACI Journal*, 83(2):219–231, March-April 1986.

## Bibliography

---

- [VL<sup>+</sup>01] F. J. Vecchio, D. Lai, W. Whim, and J. Ng. Disturbed stress field model for reinforced concrete: validation. *Journal of Structural Engineering*, 127(4):350–358, 2001.
- [Wau09] J. D. Waugh. *Nonlinear analysis of T-shaped concrete walls subjected to multi-directional displacements*. PhD thesis, Iowa State University, Ames, Iowa, USA; <http://lib.dr.iastate.edu/etd/10525/>, 2009.
- [WV02] P. S. Wong and F. J. Vecchio. *VecTor2 and Formworks User's Manual*. University of Toronto, Canada, August 2002.
- [ZL14] Z.W. Zhang and B. Li. Evaluation of seismic performance of slender L-shaped and T-shaped RC structural walls. In *Proceedings of the second European Conference on Earthquake Engineering and Seismology*, Istanbul, Turkey, 2014.

## Curriculum Vitae

### *Personal*

Name	Constantin
First Name	Raluca-Tereza
Date of birth	October 7, 1984
Nationality	Romanian
E-Mail	raluca.constantin@gmail.com

### *Education*

01.2011-08.2016	Ecole Polytechnique Fédérale de Lausanne (EPFL), PhD
02.2009-08.2009	Institut National des Sciences Appliquées Lyon (INSA), Postgraduate project
10.2008-08.2009	Technical University of Civil Engineering Bucharest (TUCE), Postgraduate course
10.2003-08.2008	Technical University of Civil Engineering Bucharest (TUCE), Diploma

### *Work experience*

09.2010-12.2010	Internship at EPFL: design of a steel reaction frame
10.2008-09.2010	Teaching assistant at TUCE for Statics and Earthquake Engineering courses
07.2006-09.2007	Internship at Christoforos Keridis and O.E., Thessaloniki, Greece
11.2006-06.2007	Drawing technician at Infrawater SRL, Bucharest, Romania

### *Languages*

Romanian (Native); English (Proficient); French (Fluent); Italian (Basic)

### *Selected publications*

R. Constantin and K. Beyer. *Behaviour of U-shaped RC walls under quasi-static cyclic diagonal loading*, in Engineering Structures, vol. 106, num. 1, p. 36-52, 2016.

R. Constantin and K. Beyer. *Quasi-static cyclic tests on U-shaped reinforced concrete walls subjected to diagonal loading*. 2nd European Conference on Earthquake Engineering and Seismology, Istanbul, Turkey, 2014.

R. Constantin and K. Beyer. *Modelling of reinforced concrete core walls under bi-directional loading*. 15th World Conference on Earthquake Engineering, Lisbon, Portugal, 2012.

